Vrije Universiteit Brussel

UNIVERSITEIT GENT

Experimental investigation of the water entry of rigid and deformable bodies using time-resolved Particle Image Velocimetry

Graduation thesis submitted in fulfillment of the requirements for the academic degree of Doctor in Engineering

Alexandru Nila

Promotors: Prof. dr. S. Vanlanduit
Prof. dr. ir. W. Van Paepegem, co-promotor

Jury: Prof. dr. ir. Johan Schoukens, chairman
Prof. dr. ir. Hendrik Van Landeghem, co-chairman
Prof. dr. ir. Rik Pintelon, vice-chairman
Prof. dr. ir. Francesco Contino, secretary
Prof. dr. ir. Jan Vierendeels,
Prof. dr. ir. Jeroen van Beeck,
Prof. dr. ir. Raf Theunissen.

October 2014

Vrije Universiteit Brussel

UNIVERSITEIT GENT

Experimental investigation of the water entry of rigid and deformable bodies using time-resolved Particle Image Velocimetry

Proefschrift voorgelegd voor het behalen van de academische graad
van Doctor in de Ingenieurswetenschappen

Alexandru Nila

Promotors: Prof. dr. S. Vanlanduit
Prof. dr. ir. W. Van Paepegem, co-promotor

Jury: Prof. dr. ir. Johan Schoukens, chairman
Prof. dr. ir. Hendrik Van Landeghem, co-chairman
Prof. dr. ir. Rik Pintelon, vice-chairman
Prof. dr. ir. Francesco Contino, secretary
Prof. dr. ir. Jan Vierendeels,
Prof. dr. ir. Jeroen van Beeck,
Prof. dr. ir. Raf Theunissen.

October 2014

Experimental investigation of the water entry of rigid and deformable bodies using time-resolved Particle Image Velocimetry PhD thesis by Alexandru Nila

Vakgroep Toegepaste Mechanica - Faculteit Ingenieurswetenschappen
Vrije Universiteit Brussel
Pleinlaan 2, B-1050 Brussel

Vakgroep Toegepaste Materiaalwetenschappen - Faculteit Ingenieurswetenschappen en Architectuur
Universiteit Gent
Sint-Pietersnieuwstraat 25, B-9000 Gent

Contact: +32 (0)2 629 28 07 – alexnila@vub.ac.be – secr-dtw@ir.vub.ac.be

Proefschrift voorgelegd voor het behalen van de academische graad van Doctor in de Ingenieurswetenschappen

Thesis submitted in fulfillment of the requirements for the academic degree of Doctor in Engineering

Promotor:
Prof. dr. S. Vanlanduit

Co-Promotor:
Prof. dr. ir. W. Van Paepegem

Jury:
Prof. dr. ir. Johan Schoukens, chairman
Prof. dr. ir. Rik Pintelon, vice-chairman
Prof. dr. ir. Hendrik Van Landeghem, vice-chairman
Prof. dr. ir. Francesco Contino, secretary
Prof. dr. ir. Jan Vierendeels,
Prof. dr. ir. Jeroen van Beeck,
Prof. dr. ir. Raf Theunissen.

2014 Uitgeverij VUBPRESS Brussels University Press
VUBPRESS is an imprint of ASP nv (Academic and Scientific Publishers nv)
Ravensteingalerij 28
B-1000 Brussels
Tel. +32 (0)2 289 26 50
Fax +32 (0)2 289 26 59
E-mail: info@vubpress.be
www.vubpress.be

Everything flows, nothing stands still.

Heraclitus (535 B.C. - 475 B.C.)

Action and reaction, ebb and flow, trial and error, change - this is the rhythm of living. Out of our over-confidence, fear; out of our fear, clearer vision, fresh hope. And out of hope, progress."

Bruce Barton (1886 - 1967)

Acknowledgements

Every end is a beginning. So is the way of the world, so is the passing of time. But time flows the same way as everything else. It can pass by without meaning, or you can capture it, learn from it, grow with it. That is what one learns by themselves, without anybody holding their hand, without anyone telling them what to do. But every now and again, something wonderful happens. Something that defines who we are, by showing us what we can be. That special *something* is what some call love, and some call happiness. And that happiness becomes real when you can share your experience with someone else, and you feel all the wonderful emotions that define a human being. It so happens that I feel that I'm one of those lucky few who can say that I've been blessed with having so many wonderful people to learn from, to guide me, to be my friends, and to share my happiness with. And since I cannot help starting with the beginning, I need to say *Thank you!* to Steve Vanlanduit. Steve, you have been an inspiration to me, and you have taught me so much. Before coming to Brussels, I wouldn't have thought that one person can be ones' mentor and friend at the same time. Your professionalism, energy and all around positive attitude can inspire anyone and everyone to great things. And if this would already be a fantastic way for anyone to spend their PhD years, one can only imagine what happens when you have two great promoters that you can learn from. So thank you, Wim Van Paepegem, for showing me that good things do come 'in pairs'. You have been a great co-promoter, and I will always value your guidance and your kind nature.

The completion of this PhD thesis would not have been possible without the help of several people, to whom I am most grateful. Firstly, the members of the jury, who have put in a great deal of time and effort into providing me with much appreciated feedback. Undoubtedly, the quality of this thesis has improved over the past weeks thanks to your comments and our discussions, so I would like to thank you for that. Secondly, the financial support of the Fund for Scientific Research in Flanders (F.W.O.), without which, the work presented herein would not have been possible.

Of course, I cannot begin to imagine how my life would be like without my parents and family, who have given me more than I could ever repay. It's because of you I am who I am today, and without you, nothing I have done would be possible. So a big *Multumesc!* to all of you, for shaping me into the man I have become, and for being a part of me. Thank you Alina, for your patience, love and support through everything. I am fortunate to have the person next to me be the love of my life and my best friend at the same time!

There are many people that can teach you many wonderful things. Fact, not fiction! And it is a fact that I've had the good fortune of meeting fantastic people over the course of my PhD. Flavio, Roberto, Mahmoud, Christof you have been my first colleagues and friends at the VUB. I cannot express how much I enjoyed the times we've had together, the wonderful memories we've shared. Knowing you is one great plus that I can take from my time in Belgium, and I want to thank you for helping me, laughing with me, being there when I needed friends away from home. A special thank you goes to my wonderful colleagues at UGent, Diederik and Sridhar. Your help and friendship is truly appreciated. The long days that we have spent together and the good things that we have achieved together are great memories that I will take with me wherever I will go.

Thank you Ben, Galid, Tim, Alfredo, Gert, Glenn, Joe, Maarten, Luis, Abel, Innes, Cornel and Mona and to all my colleagues and friends. You have made me feel that I can always have you to count on. I have learnt a great deal from all of you, and I'm happy to have met people as great as you! I can never forget you, Adi, Cristi, Codrut, Marian, George, as you have all been the friends who I can always count on, and that made me feel safe even thousands of kilometres away. Thank you for being there and here with me at the same time.

Of course, I cannot forget all the people at VUB and UGent who have been an extraordinary help throughout my PhD. Professor Patrick Guillaume, Birgit, Jenny, Alain, Jean-Paul, and the entire technical support team at the MECH department, thank you all for your support and friendship. I am also very thankful to the technical support team at the Department of Materials Science and Engineering, and to the Department of Coastal Engineering at UGent, for making the experimental work performed there, possible.

After four and a half years in Belgium, there are many aspects that have made this the most wonderful time in my life. Both professionally and personally, there are a great number of things that I am most grateful for, and which have happened thanks to a lot of people. So thank you all, also to those who might have not been mentioned here, but who's help and friendship is most appreciated.

Summary

This PhD thesis describes the use of optical measurement techniques, namely Particle Image Velocimetry (PIV), in the study of the water impact of rigid and deformable structures. Water impact, or slamming, is a fluid-structure interaction (FSI) problem, characterized by high induced loads with a very short duration (typically milliseconds).

Following an experimental investigation of the slamming of a marine structure performed within the framework of a previous PhD thesis, several observations were made regarding the effect that hydroelasticity (deformability of the impacting body) has on the magnitude of occurring slamming loads. Based on those findings, a project funded by the FWO (Funds for Scientific Research in Flanders) was started as a collaboration between the Free University of Brussels and Gent University. The project was aimed at offering a rigorous analysis of the slamming phenomenon using both experimental investigations and numerical simulations. Three different PhD research topics were identified in order to achieve the aforementioned goal. A first thesis was aimed at developing an accurate numerical model for deformable body slamming analysis. Another PhD research dealt with the thorough experimental investigation of slamming using classical (sensor-based) measurement techniques. Finally, the goal of this dissertation is the coherent application of an alternative way to conduct experimental investigations of the slamming phenomenon, using the PIV measurement technique. In order to achieve this objective, several steps were taken within this research work, which can be identified as follows:

- The development of a custom image processing technique to calculate the fluid velocity fields during water entry, in an automated manner.
- Using the measured velocity fields to estimate fluid pressure, and consequently the slamming load acting on the impacting body.
- Conducting an extensive validation campaign to asses the accuracy of the

PIV-based estimations of slamming forces.

In Chapter 1, the main features of the slamming phenomenon are identified, based on a comprehensive literature review. It is shown that slamming has long been an interesting research topic, with the first studies dating back as far as 1929. The previous research has been carried out either by using numerical simulations or through experimental investigations, in an effort to determine the occurring structural loads as well as the flow physics. Numerical simulations of the slamming problem have long been a useful tool in the estimation of impact loads. However, current numerical models of hydroelastic slamming are subject to uncertainties caused by the coupling of fluid dynamics and structural response analysis in the simulations. These uncertainties are one of the reasons why there is a stringent need for experimental validation of the numerical results. Such experimental studies are traditionally conducted using pressure sensors, strain gauges or force transducers mounted on the impacting bodies. Nevertheless, measurements performed using such sensors, are prone to large errors caused by numerous factors including mounting precision and temperature shocks.

As previously stated, this thesis proposes an alternative to the existing techniques. Compared to classical sensor measurements, the PIV technique presents several advantages due to its non-intrusive nature. One of these advantages is the possibility to determine both the fluid flow physics, as well as the structural response during water entry.

In Chapter 2, an overview of the PIV measurement technique is given. Furthermore, the practical aspects of the application of PIV to the study of rigid body slamming are identified (using drop tests of a wedge and of a cylinder). These aspects include the requirements for particle seeding properties, camera and laser operating frequencies and post-processing procedures. Moreover, in this second chapter, original contributions to PIV processing procedures are introduced. The proposed techniques are tailored for the specific application to measurements of fluid flow in the presence of moving bodies. The results obtained from the test case measurements underline the specifics in achievable accuracy of PIV during slamming, but also the limitations of the technique with respect to its spatial and temporal resolutions.

After establishing the main aspects of the PIV measurement of fluid flow (i.e. fluid velocity), additional information about the physics of slamming, which can be recovered from the high-speed recordings, is discussed in Chapter 3. In this chapter, the techniques used for recovery of the water-air interface (free surface) profile as well as for the wetted body contour are discussed. It is shown that, using these methods to measure the water entry of deformable bodies, time-resolved

information of body displacement and free surface evolution is available. This constitutes an important advantage of the technique when compared to classical sensor measurements which can only produce information regarding load or strain or localized pressure.

Furthermore, techniques of estimating fluid pressure from PIV measured velocity fields can be implemented in order to estimate slamming loads, as it is presented in Chapter 4. A Poisson approach to recover pressure from the measured velocity is implemented in the present work (with attention to the application of appropriate boundary conditions and discretization schemes). The estimation algorithm is improved by means of temporal filtering of the raw data and through streamline-based interpolation of the velocity field in order to increase both temporal and spatial resolutions, respectively. It should be noted that the streamline-based interpolation technique is an original contribution that can be useful for a large array of applications that involve PIV-measured fluid velocity (the details of this technique are discussed in appendix A).

Chapter 5 presents the results of an extensive measurement campaign performed at the University of Gent. This campaign is used to validate the PIV processing procedures described in Chapters 2 through 4. The measurements were performed on seven cylinders of different diameter, thickness and material properties. Moreover, four different entry speeds were used, conferring a large sample of both body displacement values as well as fluid flow characteristics.

The experimental set-up used for the tests described in Chapter 5 was instrumented with load sensors and strain gauges. The focus of the validation campaign was to asses the accuracy of PIV-based estimations of the occurring slamming force on deformable cylinders. This was done by comparing PIV results with the force measured by force transducers and with the force estimated from strain gauge measurements. It should be noted that the latter results were obtained using strain-to-force conversion factors calculated from numerical simulations of the cylinder dynamic loading. These simulations were carried out within the framework of the PhD thesis of Diederik Van Nuffel (Department of Materials Science and Engineering, Gent University).

The load calculated from PIV measurements is estimated using the two commonly encountered methods in PIV-based pressure reconstruction: the Poisson approach and the direct integration of the Navier-Stokes equation. It is shown that estimation of load using the latter method offers more flexibility in the application of boundary conditions. However, the choice of integration path can lead to accumulation of measurement errors which can affect the accuracy to a higher extend than for the Poisson method. It is shown that the load estimated from PIV matches quite well with the strain-based estimations of force. At the same time, the load

cell measurements exhibit higher uncertainty due to the influence of structural vibrations of the experimental set-up.

The general conclusions of this work, as presented in Chapter 6, underline the advantages and drawbacks of using the PIV measurement technique in the study of deformable body slamming:

- PIV produces full-field measurements of fluid velocity during water entry, which is not possible with any other experimental technique. Even though the temporal and spatial resolutions of modern PIV measurements are still approximately one order of magnitude lower than current simulation resolutions, PIV results can offer a means of validating numerical models.

- The PIV measurements require careful calibration of the optical set-up as well as further analysis of the raw data with post-processing algorithms to recover fluid velocity and pressure fields. These aspects determine an increase in the total time needed to recover the magnitude of slamming loads. On the other hand, the use of intrusive measurement techniques in slamming tests is also a cumbersome procedure (especially for deformable body slamming). Pressure sensors, for instance, can not be mounted on slamming deformable cylinders because of its change in shape during water entry. This is a limitation not encountered when using PIV.

- The results obtained from PIV measurements provide a wide range of information: fluid velocity, free surface elevation profiles, body displacements, pressure and force estimations. This variety of information is currently not available when using any other method of experimental investigation. However, it should be noted that the algorithms of evaluating fluid pressure from the measured velocity can still be further improved. One of the biggest concerns when estimating the pressure field during slamming is the application of boundary conditions in the integration of the Navier-Stokes equations.

- The estimation of load using PIV results is prone to errors caused by limitations in temporal and spatial resolutions of the PIV measurement. These limitations can affect the accuracy of the pressure estimations at the wall of the impacting body, and consequently, the resulting slamming load. On the other hand, this approach eliminates measurement errors caused by structural vibrations of test set-ups, which are one of the biggest concerns for traditional slamming investigations using load cell measurements.

Samenvatting

Deze thesis beschrijft een optische meettechniek die ontwikkeld werd voor het bestuderen van de waterintrede van starre en vervormbare lichamen. Deze waterintrede, die in het Engels 'slamming' genoemd wordt, is een fluïdum-structuur interactie fenomeen dat wordt gekarakteriseerd door zeer hoge belastingen gedurende een zeer korte tijd (typische enkele milliseconden). De voorgestelde meettechniek is gebaseerd op het traceren van partikels in een fluïdum die opgemeten worden met behulp van een hogesnelheidscamera.

In een voorgaand doctoraat aan de Universiteit Gent werden verschillende observaties waargenomen met betrekking tot de invloed van de vervormbaarheid van maritieme structuren op de grootte van de optredende impact krachten tijdens slamming experimenten. Naar aanleiding hiervan werd een project opgestart tussen de Universiteit Gent en de Vrije Universiteit Brussel met financiële steun van het Fonds voor Wetenschappelijk Onderzoek (FWO) Vlaanderen. Het doel van het project bestond erin een rigoureuze experimentele en numerieke analyse uit te voeren van het 'slamming' fenomeen voor starre en vervormbare lichamen. Drie verschillende doctoraatsonderzoeken werden geïnitieerd om dit doel te bereiken. Een doctoraat focust op de ontwikkeling van een accuraat numeriek simulatiemodel voor de voorspelling van de impactbelasting. Een tweede onderzoeker had als doel om hydrodynamische impactexperimenten uit te voeren om de invloed van de vervormbaarheid op de impactbelasting te onderzoek. Hierbij werd gebruik gemaakt van kracht-, druk-, rek- en verplaatsingssensoren. Het werk dat in deze doctoraatsthesis gepresenteerd wordt heeft als doel om het gebruik van stromingsvisualisatie-experimenten te onderzoeken als werktuig bij het bepalen van de hydrodynamische drukken en krachten op lichamen bij waterimpact. In het bijzonder werd gebruik gemaakt van een partikel gebaseerde stromingsvisualisatietechniek (deze techniek wordt in het Engels aangeduid met Particle Image Velocimetry of kortweg PIV). Het onderzoek kan ingedeeld worden in drie stappen :

- Het uitwerken van een aangepaste beeldverwerkingstechniek om de snelheidsvelden in het fluïdum op een automatische wijze te berekenen.
- Het ontwikkelen van een methode om uit in de vorige stap bekomen snelheidsvelden de drukken aan het oppervlak van het lichaam te bepalen.
- Een uitgebreide validatiecampagne of de accuraatheid van de berekende snelheidsvelden, drukken en krachten in functie van de vervormbaarheid van het lichaam te bepalen.

In Hoofdstuk 1 worden de belangrijkste kenmerken van het slamming fenomeen besproken en wordt een overzicht van de literatuur gegeven. De literatuur met betrekking tot hydrodynamische impact van lichamen is reeds enkele decennia een veel besproken onderwerp met publicaties die teruggaan tot 1929. Het voorgaand onderzoek handelt voornamelijk over het gebruik van numerieke simulaties en experimenten om de optredende structurele belasting en de stromingsvelden in het fluïdum te karakteriseren. Numerieke simulaties van het slamming fenomeen zijn reeds geruime tijd een nuttige hulpmiddel bij het schatten van de impactbelastingen. Echter, de huidige numerieke modellen voor de hydroëlastische impact zijn onderhevig aan onzekerheden die resulteren uit de koppeling tussen de vloeistofmechanica en de structurele respons analyse in de simulaties. Daarom is er een sterke nood aan een experimentele validatie van de numerieke berekeningen. Deze experimentele validatiestudies worden traditioneel uitgevoerd met behulp van druksensoren, rekstrookjes en krachtsensoren die gemonteerd worden op het oppervlak van de impacterende lichamen. Echter, metingen uitgevoerd met dergelijke sensoren zijn onderhevig aan grote fouten die veroorzaakt worden door talrijke factoren, waaronder de precisie van de montering en de temperatuursschokken.

Zoals voorheen werd aangehaald wordt in dit doctoraat een alternatieve aanpak voor de studie van het waterintrede probleem voorgesteld. Hierbij worden de drukken en krachten werkend op het impacterende lichaam berekend uit stromingsmetingen die bekomen worden uit beelden van het fluïdum waarin partikels zijn toegevoegd. De voordelen van deze methode, in vergelijking met metingen met klassieke opnemers, spruiten voort uit de niet-intrusieve natuur. Verder kan door het gebruik van deze beeld-gebaseerde techniek zowel het vloeistofmechanische proces alsook de structurele vervorming gemeten worden.

In Hoofdstuk 2 wordt een inleiding tot de PIV techniek gegeven. Tevens worden de praktische aspecten bij het gebruik van PIV voor waterintrede van een star lichaam besproken (met bijzondere aandacht voor het geval van een prisma en een cilinder). De toepasbaarheid van de PIV techniek voor waterintrede-experimenten

in relatie tot de vereisten van de opstelling wordt verduidelijkt. Dit omhelst in het bijzonder de vereisten naar deeltjesconcentratie, de camera en laser frequenties en de vereiste verwerkingsprocedure van de ruwe gemeten beelden. Verder worden in het tweede hoofdstuk enkele nieuwe bijdragen besproken rond de verbetering van de PIV beeldverwerking specifiek voor de stromingsmetingen van bewegende lichamen. De resultaten van de testen die werden uitgevoerd onderstrepen de limieten van de techniek met betrekking tot de ruimtelijke resolutie, de tijdsresolutie en de nauwkeurigheid.

Nadat de belangrijkste basisbegrippen met betrekking tot de PIV techniek voor het meten van snelheidsvelden werden geïntroduceerd, wordt in Hoofdstuk 3 additionele informatie gegeven over de fysische informatie met betrekking tot slamming die uit de hogesnelheidsbeelden kan worden bekomen. In het bijzonder wordt een methode voorgesteld om het vrije oppervlak en de contouren van het impacterende lichaam te identificeren. Er wordt aangetoond dat op die manier tijdsgeresolveerde data van de verplaatsing van het lichaam en de vervorming van het wateroppervlak kan bekomen worden. Dit brengt een belangrijk voordeel met zich mee in vergelijking tot klassieke sensoren, waar deze informatie niet voorhanden is.

Bovendien kan, zoals aangetoond wordt in Hoofdstuk 4, het snelheidsveld bepaald uit PIV data gebruikt worden om de optredende krachten en drukken aan het oppervlak van het lichaam te berekenen. Een aanpak gebaseerd op de Poission vergelijkingen werd geïmplementeerd in dit werk (de keuze van de gepaste randvoorwaarden is hierbij van zeer groot belang). Het ontwikkelde algoritme werd verbeterd met behulp van een stroomlijn-gebaseerde filter en een polynoombenadering van de tijdsdomein data. Door het gebruik van deze benaderingsmethodes kan de ruimtelijke en tijdsdomein resolutie artificieel vergroot worden ten opzichte van de ruwe meetdata. Deze ontwikkelde technieken zijn toepasbaar voor slamming experimenten, maar kunnen in principe ook gebruikt worden in een veel breder kader (voor de vlotte leesbaarheid van de tekst werden de details van het algoritme in Appendix A besproken eerder dan in de tekst zelf).

Hoofdstuk 5 bevat de resultaten van een zeer uitgebreide meetcampagne die werd uitgevoerd aan de Universiteit Gent. De procedures die werden uitgewerkt in de Hoofdstukken 2 tot 4 werden hierbij toegepast op metingen uitgevoerd op zeven verschillende cilinders (met verschillende diameter, dikte of materiaal). Verder werden experimenten uitgevoerd bij vier verschillende impactsnelheden. De impacterende lichamen die gebruikt werden in Hoofdstuk 5 werden geïnstrumenteerd met krachtsensoren en rekstrookjes. Het doel van de meetcampagne die besproken wordt in dit hoofdstuk is het afschatten van de nauwkeurigheid van de PIV-gebaseerde methode voor het bepalen van krachten tijdens

slamming testen op vervormbare cilinders. Hiervoor werd het resultaat van de PIV-gebaseerde procedure vergeleken met de metingen met de krachtsensoren en de rekstrookjes. Het is belangrijk om op te merken dat deze laatste resultaten werden bekomen door het converteren van de rekmetingen naar krachten met behulp van conversiefactoren berekend uit numerieke simulaties. Deze simulaties werden uitgevoerd in het kader van het doctoraat van Diekerik Van Nuffel (Vakgroep Mechanica van Materialen en Structuren, Universiteit Gent).

De kracht die werd berekend uit de PIV metingen werd bepaald gebruik makende van twee methodes: de Poisson aanpak en de directe integratie van de Navier-Stokes vergelijking. Bij de analyse van de resultaten bleek dat deze laatste methode een grotere flexibiliteit heeft naar het opleggen van de randvoorwaarden, maar dat de keuze van het integratiepad bepalend is voor de accumulatie van meetfouten. Er werd aangetoond dat de kracht die geschat wordt uit de PIV-gebaseerde methode de berekende krachten uit de rekstrookmetingen vrij goed benadert. De krachtcelmetingen tonen een grotere onzekerheid door de invloed van de structurele trillingen van de opstelling.

De algemene conclusies van dit werk, die opgesomd worden in Hoofdstuk 6, onderstrepen de voordelen van het gebruik van de PIV meettechniek bij het bestuderen van slamming van starre en vervormbare lichamen:

- Volle veld metingen, die gebruikt kunnen worden voor het valideren van numeriek simulaties, worden bekomen. Dit is niet mogelijk met andere meettechnieken.

- Het gebruik van intrusieve meettechnieken bij slamming experimenten is een omslachtige procedure. Druksensoren kunnen bijvoorbeeld zeer moeilijk gemonteerd worden op vervormbare cilinders door de veranderende vorm van het oppervlak van het lichaam tijdens impact. Dit nadeel is niet aanwezig bij contactloze PIV-gebaseerde technieken.

- De resultaten behaald met behulp van PIV geven een breed gamma aan informatie: de snelheidsvelden in het fluïdum, de vorm van het vrije wateroppervlak, de verplaatsingen en vervormingen van het lichaam en de drukken en krachten werkend op het lichaam. Om deze informatie te bekomen met klassieke sensoren moeten verschillende sensoren en instrumenten gebruikt worden.

- Het krachtsignaal berekend uit PIV metingen is niet gevoelig voor structurele trillingen van de meetopstellingen. Dit is een van de belangrijkste praktische problemen bij het gebruik van krachtsensoren bij slamming experimenten.

Contents

Nomenclature

List of symbols

$\vec{D}_p$	Displacement of a tracer particle in the fluid domain.
Δt	Time interval between two consecutive instances.
δt	Laser pulse separation (delay) time.
$\vec{V}_p$	Tracer particle velocity.
$\vec{X}(t)$	Position vector of a tracer particle in the fluid domain.
$\vec{V}_f$	Fluid velocity.
ϵ_{lag}	Error between particle displacement and fluid displacement.
$\hat{V}_l$	Velocity lag (difference between tracer velocity and fluid velocity).
D_p	Tracer particle diameter.
τ	Relaxation time of a tracer particle.
ρ_p	Density of a tracer particle.
ρ_f	Density of the fluid.
μ	Dynamic viscosity.
d_{diff}	Minimum diffraction image diameter.
M	Magnification factor.
λ	Light wavelength.
$f_\#$	The f-number of a lens.
f	The focal length of a lens.
D_a	Aperture diameter.
z_0	Distance from image plane to the lens.
Z_0	Distance from the lens to the object plane.
d_τ	Tracer particle image diameter.
N_S	Source density.

N_I	Image density.
C	Particle density.
ΔZ_0	Light sheet thickness.
λ_p	Typical distance between particles.
W_S	Interrogation area dimension.
$\vec{X}_k$	Position vector of a tracer particle at time t.
$\vec{X}_j$	Position vector of a tracer particle at time $t + \Delta t$.
$\Delta\vec{X}$	Displacement of a tracer particle inside the interrogation volume.
$\Delta\vec{x}$	Displacement of a tracer particle image in the image plane.
I	Image intensity fields at different time t.
I'	Image intensity fields at different time $t + \Delta t$.
$I_0(k)$	Image intensity of the k^{th} particle.
$\tau(\vec{x})$	Point spread function of the imaging lens.
δ	Dirac delta function.
$C(\vec{x})$	Cross-correlation function.
$\vec{s}$	Separation vector in the correlation plane.
$R_D(\vec{x})$	Correlation peak.
$R_F(\vec{x})$	Fluctuating noise correlation.
$R_C(\vec{x})$	Correlation of the mean component of I.
$\vec{V}$	Fluid velocity.
E_R	Residual error of the measured particle displacement.
λ_m	Spatial wavelength of the displacement.
$F_i(\vec{x})$	In-plane loss of image pairs.
$F_o(\vec{x})$	Out-of-plane loss of image pairs.
IW_{of}	Interrogation window overlap factor.
Δxy	Grid spacing of PIV measured velocity.
R	Cylinder radius.
Vt	Body submergence.
V_i	Impact velocity.
U	x-component of fluid velocity.
V	y-component of fluid velocity.
W	z-component of fluid velocity.
dy_{ROI}	Region of interest dimensions used in feature identification.
V_{entry}	Water entry velocity of the impacting body.

Y/R	Water penetration depth.
E	Young's modulus.
w	Cylinder displacement (deflection).
ϵ	Circumferential ('hoop') strain.
F_{impact}	Impact force.
F_{sens}	Load cell measured force.
M_1	Impactor mass.
M_2	Combined mass of the cylinder and clamp.
f_c	Force calibration factor.
F	PIV estimated force.
$\mathbf{u}$	Fluid velocity field.
p	Fluid pressure field.
ρ	Fluid density.
μ	Dynamic viscosity.
ν	Kinematic viscosity.
$\tilde{U}$	Horizontal velocity component on staggered grid.
$\tilde{V}$	Vertical velocity component on staggered grid.
U_{GC}	Horizontal component of velocity in a ghost cell.
U_{FL}	Horizontal component of velocity in the fluid domain.
U_{Body}	Horizontal component of velocity on the solid body interface.
C_p	Pressure coefficient.
p_{ref}	Reference pressure.
p_a	Atmospheric pressure.
θ	Radial coordinate (as measured from the lowest point on the cylinder).
D	Cylinder diameter.
L	Cylinder length.
m	Cylinder mass.
d	Cylinder wall thickness.
K_c	Cylinder stiffness.
H	Drop height.
V_{ti}	Theoretical impact velocity.
V_{top}	Cylinder top velocity.
$errV$	Deviation of cylinder top velocity from the value of impact velocity.
C_S	Slamming coefficient.

List of operators

$\frac{D}{Dt}(\cdot)$ $\quad \frac{\partial}{\partial t}(\cdot) + (\cdot)\nabla(\cdot)$.

$\nabla(\cdot)$ $\quad \frac{\partial(\cdot)}{\partial x} + \frac{\partial(\cdot)}{\partial y} + \frac{\partial(\cdot)}{\partial z}$.

$\Delta(\cdot)$ $\quad \frac{\partial^2(\cdot)}{\partial x^2} + \frac{\partial^2(\cdot)}{\partial y^2} + \frac{\partial^2(\cdot)}{\partial z^2}$.

List of abbreviations

PIV	Particle Image Velocimetry.
PTV	Particle Tracking Velocimetry.
LDV	Laser Doppler Velocimetry.
LSV	Laser Speckle Velocimetry.
RHS	Right-hand side.
FOV	Field of view.
$Nd:YAG$	Neodymium-doped yttrium aluminium garnet.
$Nd:YLF$	Neodymium-doped yttrium lithium fluoride.
CCD	Charge coupled device.
$CMOS$	Complementary metal-oxide semiconductor.
SNR	Signal-to-noise ratio.
FSI	Fluid-structure interaction.
DSR	Dynamic spatial range.
MMG	Multi-material groups.
ALE	Arbitrary Lagrangian-Eulerian.
RMS	Root mean square.
DIC	Digital image correlation.
ROI	Region of interest.
WOI	Windows of interest.
PSD	Power spectrum density.
FEA	Finite element analysis.
ICP	Integrated circuit piezoelectric.
$TR-PIV$	Time-resolved PIV.
$FPGA$	Field-programmable gate array.

Chapter 1

Introduction

In this first chapter, a description of the research context is provided. An introduction to the slamming phenomenon is given in Section 1.2 along with an overview of the main studies previously performed in this field. Also, a general discussion on the main issues associated with the study of the phenomenon and the techniques used are given in Section 1.3. Finally, an outline of the thesis is provided in Section 1.4.

1.1 Research Context

This thesis is focused on the aspects concerning the fluid-structure interaction problem of rigid and deformable bodies impacting the water surface. This phenomenon, also known as slamming, is characterized by high local loads with a very short duration, which introduce high local structural stresses. Slamming is of fundamental importance in various applications related to ocean engineering, and has received increasing attention due to the high number of offshore structures being deployed. The last few decades have seen an important increase in the number of ocean engineering applications extending from classical ship engineering to new areas of interest involving offshore wind turbines and wave energy converter devices.

The first array of engineering applications that involved a thorough study of the slamming phenomenon has been the shipbuilding industry. The hull of a ship undergoes a relative motion with the sea surface, which causes it to rise above water level in rough sea conditions and to re-enter the water generating high impact loads on the structure. This is defined as the vertical or bottom slamming load, and is characterized by a duration in the order of milliseconds. These loads can cause a dynamic response of the ship and can lead to severe damage of the hull. Figure 1.1 illustrates the case of a ship just before re-entry into the water. The vertical slamming loads can occur on any number of offshore structures, and are not restricted to ships. With the increasing number of wave energy converter devices that have been deployed over the past decade, this phenomenon has posed a stringent issue in the design process of converters with moving bodies.

Figure 1.1: Ship vertical slamming (from [97])

.

The second case of slamming loads occurs when a steep wave or breaking waves impact the offshore structure. This type of loads usually have a high order of magnitude - up to 10 bar or more. The breaking wave or lateral slamming occurs on all types of offshore structures, from ships to offshore wind turbines and wave energy converters. Figure 1.2 shows an example of breaking wave slamming against a wave energy converter device.

Figure 1.2: Breaking wave slamming (from [98])

.

Taking these aspects into consideration, it is to be noted that the importance of slamming to marine applications is of high relevance from an engineering standpoint. In the next section, a brief review on the previous work done to characterize this phenomenon is introduced. It will be shown that this extensive previous research has yet to describe all aspects of slamming, and important factors such as structural properties, hydrodynamic effects or measurement instrumentation shortcomings, still play an important role in the uncertainties that exist to date in the scientific community, regarding slamming.

1.2 Slamming Phenomenon

1.2.1 Rigid Body Slamming

Research in the field of slamming has been pioneered by von Kármán [93], who developed an analytic formula to predict the maximum load occurring on a rigid body as it enters the water. His research was motivated by the necessity of adequate stress analysis of seaplane floats and of the connecting structure of the floats with the fuselage. The analytic model of von Kármán is based on a series

of experimental investigations on model and full-scale floats. The study considers a rigid wedge shape that impacts the initially calm water surface. A series of assumptions are made regarding the flow physics, namely that the flow is inviscid and irrotational and that gravity, surface tension, as well as the hydroelastic effects are neglected. The main conclusions of this study show that the force increases with the square of the impacting body's velocity and with the square root of its mass. Also, it is shown that the impacting force increases as the wedge deadrise angle - defined as the angle from the horizontal plane to the body surface - decreases, becoming infinite when the deadrise angle tends to zero.

Wagner [94] extended the method of von Kármán, to include the uprise of the water during the entry of a body, and took into consideration the effects of the flow at the spray root region. The model of Wagner was based on the assumption of small local deadrise angles, meaning an approximation of the impacting body shape with a flat disk. Although this later model did include the water uprise effects, the rest of von Kármán's assumptions were kept unchanged. However, in real-life applications, additional effects such as air entrapment, deformable structure impact, three-dimensional effects or gravity effects to name but a few, also play an important role in the estimation of slamming loads.

Several decades later, Wagner's method has been extended for different simplified shapes of impacting bodies. One example is the semi-analytic solution of the constant entry of a rigid wedge problem that was presented by Hughes [41] for the case of a weightless, incompressible and inviscid fluid. The method was successfully tested for a 90° rigid wedge impact. Miloh [54, 55] developed analytic expressions for the water entry of a rigid sphere in an inviscid and incompressible fluid.

Most of the work on slamming has deployed numerical simulations in order to test the theories of simplified solutions. Dobrovolskaya [23] developed a similarity solution of a wedge body penetrating the water surface with constant entry velocity. Later, Cointe and Armand [6] used a method of matched asymptotic expansions to resolve the problem of hydrodynamic impact of a rigid cylinder. Their method was focused on the jet formation region and demonstrated how the local solution of jet flow can be matched to an outer flow. This method was found to give good results in the case of cylinders and also wedge-shaped bodies, but still did not account for the body being deformable or air entrapment being present.

Zhao and Flatinsen [107] developed a numerical solution of the water entry of an arbitrary two-dimensional rigid body. Their approach was applicable for bodies with deadrise angles of at least 2° or 3°, thus excluding bodies with flat bottoms. Later, the same authors [108] applied a generalized Wagner method using linearised free surface boundary conditions and exact body boundary condi-

tions, without taking into account flow separation. However, their method did not account for compressibility of the fluid, nor the hydroelastic effects when dealing with deformable body slamming. Mei et al. [51] used conformal mapping to analytically solve the boundary-value problem formulated in [108], at any time instant. Using a boundary-element formulation, and under the assumption of incompressibility, Battistin and Iafrati [10] developed a numerical scheme to study the water entry of rigid, axisymmetric bodies. They validated their algorithm on test cases of a wedge and a cone with a 30 ° deadrise angle, and on a cylinder and a sphere. Their approach gave acceptable results for both two-dimensional and three-dimensional test cases, with some instabilities present in the initial transient phase. Several studies have been focused on developing numerical solutions to the water entry problem of arbitrary shaped rigid bodies - [66, 29]. Figure 1.3 presents the results of Mei et al. [51] for rigid body slamming. Free surface profiles, pressure distribution on the body as well as the force coefficient evolution during water entry are the results most relevant from the perspective of marine engineering applications.

All these aforementioned studies give a better insight into aspects of rigid body slamming, with applications in ship engineering, and probably most importantly to high-speed vessel design. However, the role that hydroelasticity plays in the study of slamming was not included in the research mentioned above, and, as we will discuss in the following subsection, this role is a key element that needs to be addressed when considering other applications in marine engineering.

1.2.2 Deformable Body Slamming

Recently, an increasing attention has been paid to one aspect of the slamming phenomenon, that had been previously neglected: hydroelasticity. The loads occurring on a deformable body that impacts the water surface have been found to differ significantly from those estimated under rigid body assumptions. In [74], an experimental validation of numerical simulations was performed using steel thin cylinders, whilst in [5], aluminium deformable cylinders were used for numerical and experimental slamming investigations. Both of these papers revealed the considerable effect that structure stiffness has on occurring loads during impact.

One of the first to discuss the effects that hydroelasticity has on an impacting body and the importance of coupling between fluid flow models and structural response analysis, was Faltinsen - [25]. In his review [26], Faltinsen addresses the difficulty in estimating the maximum structural stresses when the maximum occurring pressure is large, due to the increased influence of hydroelastic effects. Similar findings were reported in the review of Kapsenberg [44] who estimates

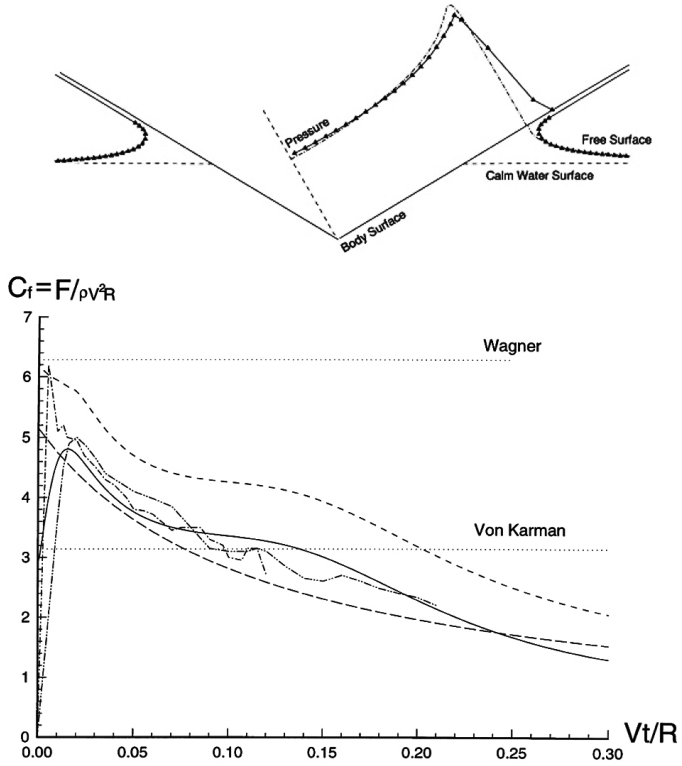

Figure 1.3: Top: Rigid wedge slamming results (from [51]): geometry of the body and free surface, as well as pressure distribution on the wedge wall (comparison between analytical (- -) and numerical (Δ) results); Bottom: Results of the force coefficient on a rigid circular section during water entry with constant velocity (from [51]): analytical results of Mei [51] through direct pressure integration (-) and using the added-mass formula (-·); experimental results of Campbell and Weynberg [14] (–) and of Armand and Cointe[6] (-·-) (-···-); theoretical estimation of Von Kármán and of Wagner (··).

that by neglecting the hydroelastic effects of deformable body slamming, the maximum stresses can be over-predicted by as much as ten times. It was shown in [12] and [64] that the effect of hydroelasticity is a function of several parameters including stiffness of the structure, local deadrise angle and entrapped air between

structure and water surface, all of which play an important role in the reduction of impact loads as opposed to the case of rigid body slamming.

In the work of [43] a generalized Wagner approach was used to calculate strain time histories of a deformable shell by incorporating the fluid-structure interaction in the calculations. Carcaterra and Ciappi [15] also studied the impact of elastic wedges by approximating the body as two rigid plates connected by a spring of constant stiffness. Korobkin published his findings in [46], a paper which deals with the unsteady 2D impact of an elastic structure with a fluid free surface. In this paper, Korobkin shows the advantage of using a generalized Wagner approach in the analysis of hydroelastic effects, by modelling a deformable wedge as two simply supported Euler beams of variable thickness. Korobkin presented results of bodies with small deadrise angles, as opposed to previous works, such as [50] where the analysis is focused on elastic wedges with moderate deadrise angles. Sun and Faltinsen [78] simulated the water entry of rigid and elastic cylindrical shells, using a boundary element method.

However, as mentioned in [73], a review of the literature on water entry problems, the existing papers have not yet succeeded in the full description of the slamming phenomenon when deformable or three-dimensional bodies are of interest. One of the causes for the inconsistencies found between results of previous research, can be accounted for by the lack of accurate experimental investigations on problems of deformable body slamming. The few works that exist on experimental testing of slamming are focused on rigid body water entry. Moreover, measurements during water entry of bodies are highly dependent on a number of parameters involving not only flow physics and structural properties, but also instrumentation precision. These parameters are very diverse, and, as we will show in the following, a clear understanding of the role they play in measuring slamming loads is missing.

1.3 Motivation and Objectives

This dissertation was performed in the framework of a joint project between the Free Univeristy of Brussels and Gent University, funded by the FWO (Funds for Scientific Research) in Belgium. The initiation of this project was determined by the conclusions of a previous PhD work [13], in which experimental investigations of the slamming of a marine structure were performed. In the aforementioned thesis, the large effects of structure deformability on occurring slamming loads were presented, and motivated the need for further research into this topic. Thus, the resulting project was intended to offer a rigorous analysis of the slamming

phenomenon, using both experimental investigations and numerical simulations. Three different research works were thus commenced, with focus on: developing accurate numerical models [91], the thorough experimental investigation of the phenomenon using classical measurement techniques [87], and the evaluation of a new technique to experimentally investigate slamming. This thesis encompasses the latter of the three aspects, and in the remainder of this section, the motivation behind this research work is given, in the context of the available state-of-the-art.

As discussed previously, the topic of slamming has been studied extensively both analytically and numerically, with generalized methods being produced for the water entry of rigid bodies with simple geometries. For the case of deformable body slamming, work has been done in recent years to improve the numerical models by including effects of hydroelasticity, and thus coupling fluid flow models with structural response analysis. However, experimental studies of the water impact of bodies are less common in literature than their numerical or analytical counterparts. Most of the measurements performed are limited to rigid bodies, and studies have shown that large scatter of data is encountered due to the sensitivity of instrumentation to various factors such as calibration, temperature shocks or mounting precision [89].

Among the first to experimentally investigate the slamming phenomenon was Chuang [16], who studied the water impact of rigid wedges with small deadrise angles (from 1 ° to 15 °). The maximum impact pressures were recorded for a range of drop velocities, at a frequency of 200 kHz. Later, Chuang and Milne [17] studied the three dimensional effects during slamming of rigid cones. Several papers - [40, 108, 66, 105, 85, 20] - have contributed through experimental investigations to a better understanding of the impact phenomenon. Obtaining consistent results has proven to be a difficult challenge because of the uncertainties in measured loads. From an experimental point of view, the only available options for determining slamming loads was the use of classical pressure sensors - [105], load cells - [85], or strain gauges mounted on the impacting body - [74, 5]. Instrumenting such experimental set-ups has proven to be a demanding and cumbersome task. As shown in the work of Van Nuffel - [88, 89] - the sensor instrumentation for impact experiments is affected by numerous factors such as: data sampling rates, temperature shocks, sensor mounting and water surface conditions. Van Nuffel has shown in his work that all these factors contribute to the scatter in registered values, and each of them can contribute to up to 50 % or more deviation of peak values. Moreover, one must account for disturbances in the flow physics that can be produced when using any type of intrusive measurement. These factors also play an important role as can be seen in all types of tests in fluid dynamics. Several instrumentation techniques, such as pressure taps or

strain gages, become even more difficult to deploy when dealing with highly deformable bodies. Because of large deformations of elastic bodies during impact, pressure or strain measurements on the surface of the object are very difficult to achieve.

Keeping in mind all the reasons described above, an alternative method of experimental investigation of the water impact phenomenon becomes desirable. This thesis proposes such an alternative approach to describe the water entry of rigid and deformable bodies. The method is based on optical measurement techniques, namely Particle Image Velocimetry (PIV). PIV is a non-intrusive technique for measuring full-field fluid velocity that presents obvious advantages to previous methods because of its lack of disturbances on the flow physics. Furthermore, the full field results can give additional information when compared with sensor instrumentation that provides simply point-wise information.

Several studies have used optical measurement techniques in the past, with application to the water impact phenomenon. Some visualization data was provided in Greenhow and Lin [31], who used high-speed images taken during the water entry and exit of rigid bodies. Their study is appreciated to be the first work that experimentally characterizes the free surface elevation and depression profiles as well as the jet formation during water entry of a cylinder. However, the focus of their paper was mainly the identification of the intersection point between the free surface and the rigid body and did not include any insight on the fluid dynamics nor on the hydrodynamic effects arising from fluid-structure interactions. Lin and Shieh [48] were able to deploy digital image techniques for capturing high-speed recordings during the water entry of a rigid cylindrical body. Based on their observations of the flow field, using particle tracking velocimetry (PTV), results of mean velocity field measurements were recovered and identification of the stages of impact of a cylinder with the water surface was done. The PTV methods deployed by Lin and Shieh were able to give information on the difference in characteristics of the velocity field distribution at two stages of water entry, i.e. before and after the water separation. However, the flow patterns identified by Lin and Shieh were not used for a quantitative analysis, and both spatial and temporal resolutions of the fluid velocity maps were very low compared to modern time-resolved PIV measurements. Figure 1.4 shows the particle tracer image and the estimated velocity distribution for the rising-up stage of the water entry, as recorded by Lin and Shieh.

It is only recently that time-resolved PIV measurements have been used in the study of slamming problems. In 2013, a part of the research work presented in this thesis, regarding slamming of rigid wedge-shaped bodies, was published in *Measurement Science and Technology* [59]. Shortly after that, Panciroli and

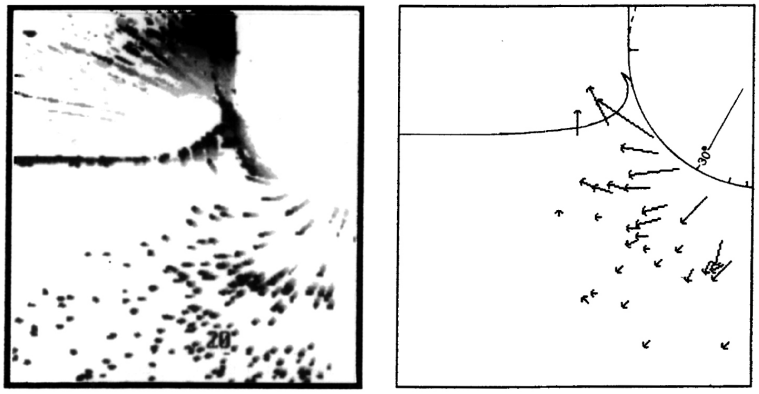

Figure 1.4: Particle tracking images during water entry of a rigid cylinder (from [47]). Left: Image of particle tracers (inverted grey levels); Right: Estimated velocity distribution.

Porfiri [65] have published their independent investigation of this phenomenon, using PIV measurements. In their work, Panciorili and Porfiri studied the water entry of a rigid wedge body with 25° deadrise angle, that is dropped from three different heights. The wedge body was allowed to free fall, and due to its positive buoyancy, it was highly decelerated when impact with the water surface occurred, as opposed to the constant water entry conditions in [59]. Panciroli and Porfiri used a high-speed PIV system to measure the fluid velocity fields, and the Navier-Stokes equations to estimate the pressure from the time-resolved fluid velocity. Their conclusions confirmed the remarks presented in [59], that PIV-based pressure measurements during slamming can provide further insight into this phenomenon. One of the most interesting application of these techniques is the study of deformable body water entry. As mentioned previously, experimental data on hydroelastic slamming problems is currently limited, and such non-intrusive measurement techniques can provide the grounds for new research in this field.

1.4 Outline of the Thesis

The aim of this thesis is to apply advantages of modern PIV systems to the study of slamming. The contributions presented herein can be categorized into two main parts. Firstly, the features of the fluid flow during slamming are identified, and fluid velocity field measurements are performed, with regard to the parameters of

classical image evaluation techniques. Secondly, the measured fluid velocity is used for pressure estimation inside the fluid domain, by making use of the Navier-Stokes equations.

The first objective is identified for PIV's most immediate result, namely full field fluid velocity measurements during water entry. Accurate results need to be obtained with high spatial and temporal resolutions. **Chapter 2** describes the operating principles of PIV measurements and its application to the water entry case. The main issues involving PIV are discussed, together with the important aspects that need to be addressed when fluid flow measurements are done in the presence of a moving body. Thus, in the second chapter, a proposed automated masking procedure is presented, which is needed for improving results accuracy when dealing with moving features on acquired PIV images.

Chapter 3 proposes a new technique of estimating loads during the water entry of deformable bodies. The masking procedure developed for rigid body movements and detailed in the second chapter, is adapted for deformable body water entry. Moreover, the high-speed images acquired during slamming are used to extract body position and shape at every time instant, and consequently, body displacements can be retrieved. An algorithm to estimate strains and forces on impacting deformable bodies, is presented. The algorithm uses information of body shape from high-speed images and finite element analysis (FEA) of the test objects.

The second part of this work is detailed in **Chapter 4**, where pressure estimation procedures using PIV velocity information are given. The procedure is applied for time-resolved data of rigid and deformable body impact. The results can be used as an estimation of slamming loads, and comparisons are made with measured force and simulations results on the same test cases.

Chapter 5 presents a complete test campaign performed on the water impact of deformable cylinders. Results using the PIV technique are compared with the results of classical sensor instrumentation on the same experimental set-up. Conclusions following this validation test campaign are presented in **Chapter 6**, with respect to the application of PIV as an alternative experimental investigation technique for water entry.

1.5 Original Contributions

The research work presented in this thesis has been focused on several innovative aspects regarding the application of PIV measurements to the investigation of slamming phenomenon. These aspects are as follows:

- A thorough description of the state-of-the-art PIV systems and PIV processing algorithms has been performed. Guidelines are given regarding the experimental slamming set-up design with respect to the deployment of PIV. Along with optimal processing schemes for PIV interrogation, an automated adaptive masking technique was implemented to improve the results of time-resolved PIV measurements taken during the water entry of rigid bodies. Wedge slamming tests and rigid cylinder slamming tests were studied using high-speed PIV measurements, and the results were compared with numerical simulations results. Part of this research work was presented at the *International Symposium on Particle Image Velocimetry, 2011* [58].

- The masking procedure elaborated for rigid bodies' water entry was further improved to be applied for deformable cylinder slamming measurements. Feature identification of the free surface and of the deformable cylinder was developed, and the results enabled further insight into the phenomenon. By tracking the evolution of the deformable body, on high-speed images taken during slamming, displacement-time histories can be recovered as well as the true immersed body wall velocity. These results, together with PIV measured fluid velocity results, provide information on both occurring loads during slamming of deformable bodies, as well as fluid flow physics. Results of PIV measured fluid velocity during the water entry of deformable bodies were presented at the *International Symposium on Applications of Laser Techniques to Fluid Mechanics, 2012* [60].

- PIV-based pressure estimation from fluid velocity maps is an important aspect that was addressed in the current work. By making use of the Navier-Stokes equation and appropriate boundary conditions, the fluid pressure maps was estimated for the water entry of rigid bodies. This part of the research work was published in *Measurement Science and Technology* [59].

- Improvements to the PIV-based estimation of pressure were considered for the case of deformable cylinders slamming. In order to achieve better estimates of the fluid pressure and consequently, of the slamming loads acting on the impacting body, techniques for improving spatial and temporal resolutions of the PIV measurements were developed. A streamline-based spatial interpolation technique for PIV grid refinement was developed and applied for the case of deformable cylinder slamming. Furthermore, temporal filtering techniques were applied to the PIV data to improve the accuracy of velocity gradients.

- A thorough experimental validation campaign of PIV-based load estimation

during slamming was conducted. The experimental campaign was used to test the estimation of loads from PIV results, and comparisons with classical sensor measurements were considered for cylinders of different sizes and material properties, and with various impact velocities. Following this validation campaign, the main advantages and drawbacks of PIV-based slamming measurements were identified. The comparison of PIV results with classical sensor results shows that the former open new possibilities in this area of research, and motivate further work to be performed on the topic of slamming using PIV.

Chapter 2

PIV Measurements During Water Entry

This chapter presents an overview of the PIV measurement technique. The background and evolution of the method are introduced, together with the general operating principles of PIV. Furthermore, the application to water entry test cases is discussed, with attention to the main issue in accurately determining fluid velocity: moving features. This chapter proposes a method of automated masking of PIV raw images before evaluation using classical processing algorithms. Results of the method are presented for the case of rigid body water entry.

2.1 PIV Background

Particle Image Velocimetry (PIV) is perhaps one of the most intuitive measurement techniques, with regard to its fundamental operating principle: observation of fluid flow. Thus, one can only imagine the first precursor of modern-day PIV, as this would probably be several centuries ago, ever since the first person observed a fluid in motion and identified a flow structure. Alongside the technical progress of the 20th century, advanced expressions of this observation principle occurred, and with it, the means of active investigation of fluid flow. The early 1900's saw scientists such as Ludwig Prandtl, able to produce in a controlled way and analyse in a qualitative manner, fluid flow. Visualization of fluid motion and identification of flow structures became a reality, and methods of estimating parameters of the flow, a goal. Development of intrusive instrumentation such as hot wire sensors became a necessity in the study of fluid velocity.

Along with the first successful experimental use of the optical pumped laser proposed by Alfred Kastler, a new era in the field of fluid flow measurement commenced. The first application of laser systems to fluid flow measurements was implemented in the form of a Laser Doppler Velocimeter (LDV) in [27]. The major drawback of LDV measurements was its restriction to point-wise measurements. This meant that measurements could not produce full field velocity data, unless a steady-state flow was being studied, in which case reproducibility of the measurement could be achieved. In the early 1980's, Meynart, a doctoral student of the Von Karman Institute in Belgium, was applying Laser Speckle Velocimetry techniques (LSV) to the study of laminar and turbulent flow [53]. The method was based on imaging of seeded flows illuminated by laser light. LSV had been previously introduced in [24, 32, 8] and was applied for quantitative measurements, even though ambiguity caused by large particle image density existed. In Meynart's work, individual particle images could be identified instead of speckles. Adrian [1] saw the potential of analysing pictures of individual particles instead of speckle patterns, and the applicability towards adequate quantitative measurements, and deemed the technique: *Particle Image Velocimetry*. This was the first step towards accurate quantitative description of full-field fluid flow.

Following the introduction of PIV, the potential of this method was recognized in the scientific community. The main advantages of the technique are its non-intrusive and full-field nature. Studies of fluid dynamics through PIV were enthusiastically received in the community, and numerous researchers as well as hardware manufacturers competed in improving all aspects of the technique.

The advancement of technological capabilities included development of more powerful laser systems, introduction of digital cameras and later the improvement

of camera resolution and frame rate. This progress made it possible for new PIV measurement methods to be developed and new areas of the technique's potential to be addressed. One such aspect is the way the flow of interest is illuminated and recorded. By using a light sheet illumination of the flow in a single plane, and one camera that records particle images, in-plane velocity field results are produced. This method is known as **2D 2C PIV** (two-dimensional two component PIV) and represents the standard PIV configuration that is still used successfully to measure flows with predominant 2D features. The potential of measuring the out-of-plane velocity component, was first explored by using two cameras (**2D 3C PIV** or **Stereoscopic PIV**) to record the 2D illuminated flow from different viewing angles. Using either mapping or warping algorithms, the third component of the flow is also recovered [67, 18, 106].

The high-speed capabilities of modern systems have facilitated the development of a new class of measurements, namely **3D 2C PIV** (three-dimensional two component PIV). The third dimension of the measured velocity can can refer to the out-of-plane component of velocity, which is recovered using multiple planar PIV measurements and reconstructing the flow volume in post-processing algorithms. However, the third dimension of the measured velocity can also refer to the temporal dimension which is recovered from time-resolved planar velocity information [36]. The PIV measurements performed in this work can be categorized as 3D 2C PIV, due to the availability of time-resolved velocity data. Furthermore, as it will be shown in Section 2.3.4, multiple planar measurements have been performed, to recover the magnitude of the out-of-plane velocity component during water entry.

Finally, several researchers have successfully performed volumetric measurements. Such PIV measurements are performed by illuminating a volume of the flow, instead of a single plane, and recording using multiple cameras - **Tomographic** or **3D 3C PIV**.

Another aspect that has received perhaps the biggest attention was the development of more accurate, more complex processing algorithms. One example of the considerable amount of work done in this regard can be found in the publications of the international PIV Challenges [75, 76, 77]. These events have been organized since 2003 to bring together research groups working on PIV. Synthetic and experimental PIV images were proposed as a means to test various algorithms and to help draw conclusions on optimal experimental as well as processing parameters. The increasing number of participants, together with the diversity in proposed methods and solutions to practical demands from PIV post-processing software, attest the importance given in the community to aspects of image evaluation techniques.

2.2 Operating Principles of PIV

Modern PIV systems are comprised of 3 main hardware components as illustrated in Figure 2.1. The first of these components are the **tracer particles** that are homogeneously distributed in the fluid flow. The particles need to be chosen appropriately depending on the working fluid at hand. Particles need to be sufficiently large in order to effectively scatter light but small enough in order to follow the flow accurately. The **light source** that is used in PIV illuminates a plane or a volume of interest in the flow field. The light source typically used in contemporary PIV set-ups is a pulsed laser system with controllable adjustment of the pulse separation time. The final hardware component of a typical PIV system is the **imaging optics**. The imaging devices used are usually CCD or CMOS sensor cameras.

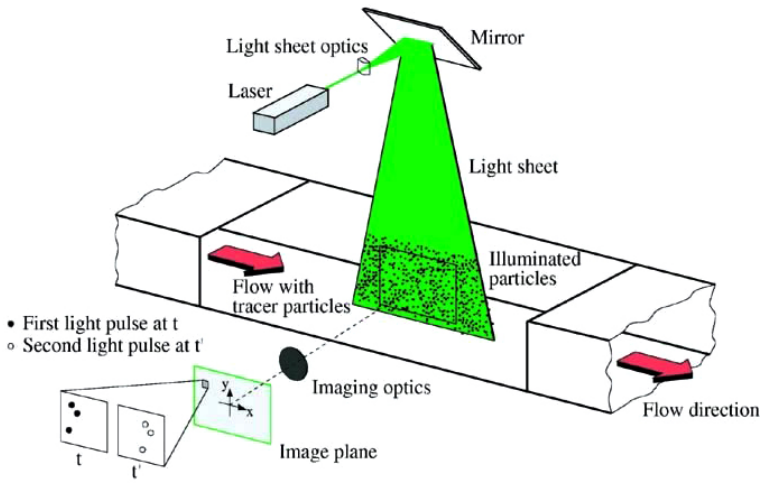

Figure 2.1: Typical PIV set-up. (from [68])

In addition to the hardware components, a **post processing** software is used for processing of the raw PIV images. Processing of two raw images of the flow facilitates the retrieval of displacements of seeding particle images. Using displacement information and by controlling the separation time between the particle images of the two frames, the velocity of the particles is determined. In the following, a detailed analysis of all the components of a PIV system is given.

2.2.1 Tracer Particles

The first task when performing PIV measurements is to chose the tracer particles that will be used in seeding the fluid flow. Depending on the working fluid at hand, the selection of particles needs to be carefully addressed. One of the biggest trade-offs that has to be made in PIV is concerning the size of the tracer particle. The most important physical criterion that is taken into consideration is that the size of the seeding particle should allow for it to follow the flow accurately.

Particle velocity lag. Given the operating principle of PIV, Westerweel [100] identified the errors introduced by measuring tracer particles instead of the actual flow. He defined the displacement measured by PIV as:

$$\vec{D}_p(\vec{X}, t_i, t_i + \Delta t) = \int_{t_i}^{t_i+\Delta t} \vec{V}_p(\vec{X}(t), t)dt \tag{2.1}$$

In equation 2.1, $\vec{D}_p(X, t_i, t_i + \Delta t)$ is the displacement of a particle in a time interval equal to Δt, and $\vec{X}(t)$ is the position vector of the particle. A distinction is made between the velocity of the tracer ($\vec{V}_p$), and that of the fluid ($\vec{V}_f$), as can be seen schematically in Figure 2.2.

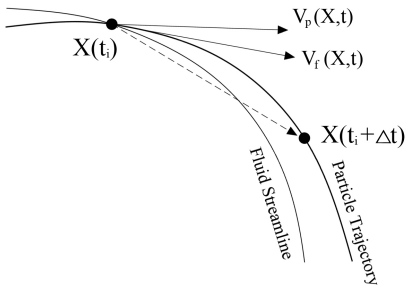

Figure 2.2: Tracer Particle Displacement [100].

Under these conditions, a difference between measured trace velocity and fluid velocity can be observed. This difference introduces an error between the displacement of the particle and that of the fluid (ϵ_{lag}) defined as:

$$\vec{D}_p = \vec{V}_p(\vec{X}(t), t) \cdot \Delta t = \vec{V}_f(X(t), t) \cdot \Delta t + \epsilon_{lag} \tag{2.2}$$

Before a PIV experiment is started, the velocity lag $\hat{V}_l = \vec{V}_f - \vec{V}_p$ needs to be studied in order to chose the appropriate particle size for the flow case of interest. Intuitively, the particles used in the seeding of fluid flow, should be very small in order to reduce the velocity lag errors. However, taking into consideration the light scattering behaviour, the particles need to have a sufficiently large diameter in order to reflect enough light on the imaging sensor. Melling [52] studied the properties of tracer particles used in PIV experiments, and derived analytic expressions for the case of a spherical particle moving in Stokes flow regime. Melling started from the equation for unsteady motion of a sphere suspended in fluid as formulated by Basset [9] and given in equation 2.3.

$$\begin{aligned}\frac{\pi {D_p}^3}{6}\rho_p\frac{d\vec{V}_p}{dt} = 3\pi\mu D_p\hat{V}_l + \frac{\pi {D_p}^3}{6}\rho_f\frac{d\vec{V}_f}{dt} + \frac{\pi {D_p}^3}{12}\rho_f\frac{d\hat{V}_l}{dt} \\ + \frac{3}{2}{D_p}^2(\pi\mu\rho_f)^{1/2}\int_{t_i}^{t_i+\delta t}\frac{d\hat{V}_l}{d\tau}\frac{d\tau}{(t-\tau)^{1/2}}\end{aligned} \tag{2.3}$$

Equation 2.3 expresses the acceleration force exerted on the particle as function of the viscous resistance defined by the first term on the right-hand side (RHS). The second term of the RHS represents a force term introduced by the pressure gradient in the vicinity of the particle, while the third expresses the resistance of the inviscid fluid to the acceleration of the particle. The final term is the *Basset history integral* which defines the resistance caused by the unsteadiness of the flow field. Under the condition of flow without shear effects or centrifugal forces, equation 2.3 was simplified by Melling considering just the first two terms, resulting in the expression for the velocity lag:

$$\hat{V}_l = \vec{V}_f - \vec{V}_p = \frac{(\rho_p - \rho_f){D_p}^2}{18\mu}\frac{d\vec{V}_p}{dt} \tag{2.4}$$

Where D_p is the tracer particle diameter, ρ_p is the density of the particle, ρ_f is the density of the fluid and μ is the dynamic viscosity of the fluid. In order to quantify the ability of the tracer particle to accurately follow the motion of the fluid, the relaxation time can be defined as:

$$\tau = \frac{\rho_p {D_p}^2}{18\mu} \tag{2.5}$$

As can be seen in equation 2.5, the relaxation time (τ) is a characteristic parameter of the seeding particle and of the fluid at hand which directly influences

the velocity lag. The relaxation time needs to be smaller than the smallest time scale of the flow, in order for the PIV measurement to be effective, and for the particle to accurately follow the fluid. For PIV experiments performed on water flows, the density values of the tracer particles used are matching the density of the water (typically around 1.1 g/cm^3). Depending on the size of the particle, the relaxation time can be as low as 0.2 μs (for an aluminum particle with a diameter of 2 μm). However, the choice of tracer particles to be used depends also on the amount of light they scatter. This characteristic is directly dependent on the particle size, as it will be detailed below.

Particle imaging. When choosing the appropriate seeding material for a PIV experiment, the factors that determine the final achievable particle image size need to be addressed. These factors concern both the *light scattering behaviour* of the particle itself (size, shape, orientation), as well as the *imaging optics* parameters (lens focal length, aperture diameter, magnification factor).

The light scattering behaviour of a PIV particle will be highly dependent on its size and shape. As shown in the previous section, the particles need to be small enough to accurately follow the flow under investigation. The implications of this requirement is that the typical size of PIV seeding particles ranges from 1 to 100 μm. Considering that these particle sizes are still larger than the wavelength of the incident light (λ = 532 nm as commonly used in PIV), the light scattering behaviour can be approximated from Mie's theory [42]. Using Mie's theory, the light scattering profile of a spherical particle of a certain dimension can be approximated. The high intensity of the light in forward scatter with respect to the incident light source, would make this direction ideal for recording particle images (180 °). However, PIV arrangements usually imply that the imaging sensor is recording perpendicular to the laser light sheet (90 °). It has been shown [68] that the intensity of the light scattered at 90 ° by a 10 μm glass particle in water is approximately seven orders of magnitude higher than that of a 1 μm particle.

Furthermore, the imaging optics parameters need to be taken into account when approximating the expected size of the particle image. As discussed in [68], the image of the particle will form a Fraunhofer diffraction pattern instead of a single point on the imaging sensor, even if aberration-free lenses are being used. The pattern of the corresponding particle image will be in the form of a circular disk (an Airy disk), which might be surrounded by Airy rings if higher exposure times are used. The Airy function is the square of the first order Bessel function and it can be used to express the impulsive response of an aberration-free lens (the so called point spread function). Using a Gaussian approximation of the Airy function and considering the characteristic of the optical arrangement, the formula of the minimum diffraction image diameter corresponding to the diameter of the

first Airy disk, can be expressed as ([68]):

$$d_{diff} = 2.44 f_{\#}(M+1)\lambda \tag{2.6}$$

where $f_{\#}$ is the f-number of the lens, defined as the ratio between focal length f, and aperture diameter D_a, M is the magnification factor of the lens and λ is the incident light wavelength.

$$f_{\#} = \frac{f}{D_a} \quad where: \quad \frac{1}{f} = \frac{1}{z_0} + \frac{1}{Z_0} \tag{2.7}$$

The terms z_0 and Z_0 in equation 2.7 represent the distances from the image plane to the lens, and from the lens to the object plane, respectively, as can be seen in Figure 2.3

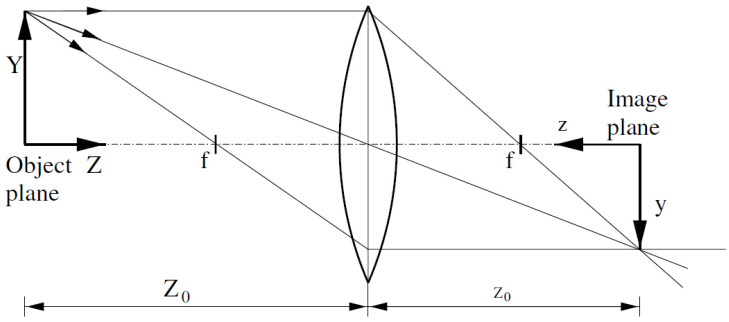

Figure 2.3: Geometrical optical arrangement (from [68]).

The approximation of the particle image diameter (d_τ) as a function of the diffraction spot diameter and particle size, can be expressed as:

$$d_\tau = \sqrt{(MD_p)^2 + d_{diff}^2} \tag{2.8}$$

The equation for the particle image diameter can thus be used to choose the appropriate optical arrangement parameters for the PIV experiment at hand. Depending on the desired field of view and particle diameter, the lens characteristics can be chosen (focal length and aperture diameter) and the corresponding magnification factor can be set by adjusting the distance from the lens to the object plane.

In practice, typical particle sizes depend on the type of flow being studied. If, for air flows, the most commonly used tracers are heated oil particles with diameters ranging from 0.5 to 3 μm [81], the seeding used in water experiments are solid particles with diameters of 2 to 100 μm. However, it should be noted that, for the reasons mentioned above, the best compromise between light scattering efficiency and velocity lag minimization involves the use of particles with diameters of approximately 10 to 20 μm (with relaxation times of a few microseconds). The commercially available particles for PIV water experiments are *polystyrene*, *aluminum* and *glass spheres*. The latter category is also the least expensive, with a price range about half that of polystyrene particles, and three times lower than the aluminum seeding [95]. Therefore, the choice of particles for the experiments performed herein is the hollow glass spheres with a mean diameter of 10 μm.

Seeding density. As mentioned previously, PIV and LSV are techniques operating on the same basic principle. However, there is one major aspect that differentiates the two methods, namely the seeding particle density. Adrian and Yao [3] defined two dimensionless parameters to distinguish between the two techniques, namely *source density* (N_S) and *image density* (N_I), expressed in equations 2.9 and 2.10, respectively. If both source and image densities are high, the seeding images are present throughout the recorded picture and overlap, corresponding to the laser speckle case. When the source density is low, but the image density is high, a typical PIV recording will be obtained, with individual particle images homogeneously distributed in the entire field of view (FOV). However, if both low image density and low source density are present, the particle images are sporadically distributed in the picture [47]. This type of recordings are deemed Particle Tracking Velocimetry (PTV), and can be used for visualization purposes, or for localized quantitative descriptions of flows. The major drawback of this technique is its shortcoming in capturing spatial velocity gradients. If high source density values are present in recordings with low image density, the data can be used purely for visualization purposes. This test case is less common and could occur in experiments meant for qualitative descriptions of a particular structure in the flow. The three cases of flow imaging depending on the seeding particle density are exemplified in Figure 2.4.

$$N_S = C\frac{\pi}{4}\frac{\Delta Z_0}{M^2}{d_\tau}^2 \approx \frac{\pi}{4}\frac{{d_\tau}^2}{{\lambda_p}^2} \tag{2.9}$$

$$N_I = C\frac{\Delta Z_0}{M^2}{W_S}^2 \approx \frac{{W_S}^2}{{\lambda_p}^2} \tag{2.10}$$

As can be seen in equations 2.9 and 2.10, the seeding and image densities are

expressed as functions of the number density of particles (C), of the magnification factor (M), and of the light sheet thickness (ΔZ_0). The factor λ_p represents the mean distance between particles, while W_S^2 is the area of an interrogation window. The interrogation window is a sub-region of the recorded image, which is used for post-processing purposes. More details on this parameter can be found in Section 2.3.2.1.

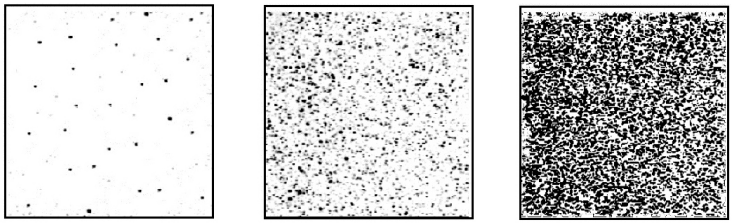

Figure 2.4: Types of Image Velocimetry Data (from [68] - inverted grey levels). Left - PTV ($N_S << 1; N_I << 1$); Middle - PIV ($N_S << 1; N_I >> 1$); Right - LSV ($N_S >> 1; N_I >> 1$).

In the experiments performed in this work, the seeding density was adjusted by increasing the concentration of tracer particles until a sufficient number of individual particle images were present in the camera FOV. The procedure was carried out to ensure a uniform distribution of particles (especially in the region close to the free surface) that determines an adequate PIV spatial resolution.

2.2.2 Light Source

For illuminating the seeded flow when conducting PIV experiments, one type of light source is currently the preferred choice: laser light. The major advantage that lasers have over other light source types, such as white light, is the emission of high energy coherent light. This aspect makes the use of lasers in PIV applications a dominant feature.

When referring to the planar PIV measurement, which is the experimental arrangement most typically encountered in practical applications, a thin laser light sheet must be produced. The illumination of a single slice of the flow of interest, eliminates errors introduced by three-dimensional projections onto a two-dimensional image when a single camera is being used. The light sheet optics are typically comprised of cylindrical and spherical lenses arrangements that turn

incoming laser beams into thin light sheets. These arrangements can be incorporated in optical guiding arms comprised either of mirror arrangements, or of fibre optics, to facilitate the laser light delivery. Since PIV measurements need to be deployed in various experimental set-ups (e.g. wind tunnels), optical access is not always straight-forward. Considering most modern high-powered laser systems are considerably bulky, the flexibility conferred by the use of optical guiding arms is necessary for delivery of the light sheet in a required test section.

The most popular laser system currently used in PIV is the Neodym-YAG (Nd:YAG) laser which operates at a fundamental wavelength of $\lambda = 1064$ nm which is turned into the visible range at $\lambda = 532$ nm. The good mechanical and thermal properties of this laser, along with its high pulse energy levels (of up to 400 mJ in commercially available systems), makes it a viable choice for PIV. Moreover, the addition of a quality switch (Q-switch), that enables operation of the laser in a triggered mode, makes the Nd:YAG laser a preferred choice. The Q-switch allows for the cavity to resonate at the most energetic point during the flash lamp cycle and facilitates the generation of short pulses (in the range of nanoseconds) of high energy levels. The usual practice for PIV system manufacturers is to incorporate double-cavity laser systems. The use of double-pulsed lasers allows for the flexibility of adjusting pulse delay times independently of the repetition rates of each cavity.

Similar to the Nd:YAG laser, the diode-pumped solid state lasers such as the Neodym-YLF (Nd:YLF) system, are a viable choice for PIV. The Nd:YLF laser operates at a fundamental wavelength of $\lambda = 1053$ nm which is turned into the visible range at $\lambda = 527$ nm, and provides the highest pulse energy and average power of the existing systems. With the ability of generating repetition rates of up to 10 kHz per cavity, the Nd:YLF laser is widely used in time-resolved PIV experiments, that require high repetition rates for description of unsteady phenomenon. Therefore, this type of system was used in the experiments presented herein.

2.2.3 Imaging Optics

Photographic Recordings. The first PIV images recorded in the early 1980's were captured on photographic films. Their availability and the high spatial resolution that they presented, provided a viable choice at the time. The exposure time of cameras using photographic films, was long enough for at least two light pulses to be imaged on the same frame. This implied that particle images of consecutive temporal instances were imaged on a single recording. This in turn, implies directional ambiguity in measured velocity vectors, particularly when the flow exhibited certain features such as vortical structures.

Digital Recordings. Along with the development of digital cameras, the application of PIV became greatly simplified and at the same time, better accuracy of the results was achieved. The immediate effect is that digital recordings allowed for a real-time adjustment of optical parameters such as focus and exposure time, with instant image availability. Another characteristic of the rapidly developing electronic imaging sensors is their high repetition rate, which, coupled with improved signal-to-noise ratios (SNR), make the use of such devices a favourable choice for PIV.

The modern PIV imaging devices are usually based either on charge coupled device (CCD) sensors architecture, or on complementary metal-oxide semiconductor (CMOS) sensors architecture. The two types of devices are widespread in the PIV community, and whilst CCD devices have enjoyed more popularity in the last two decades of the 20^{th} century, the rapid development of chip technology has facilitated the growing use of CMOS sensors. The commercially available CMOS sensor based cameras currently reach resolutions of more than 1000 x 1000 pixels, with individual sensor elements of 100 pixels/mm. The main advantage that CMOS devices present over the CCD architecture is the fact that the photodiodes can be controlled independently by MOS-FET transistors [68]. This, in turn, leads to improved SNR and resolution at high frame rates, such as those used in the present work. Therefore, CMOS sensor-based cameras were used herein, as described in Section 5.2.2. More details on performance of CCD and CMOS devices can be found in [37].

The significant sources of errors for CMOS sensors include, aside from the obvious electronic noise, thermal effects and fixed pattern noise. The fixed pattern noise includes shot noise, which is generated during the readout sequence and dark current noise. Due to these sources of noise, active cooling and internal memory solutions are standard features in PIV oriented cameras.

2.2.4 PIV Image Evaluation

One of the areas where PIV has seen major contributions since its first application to fluid flow description, is the post-processing stage. Statistical PIV evaluation has evolved from auto-correlation methods [2], to cross-correlation analysis [100] and to hybrid algorithms that include cross-correlation methods as well as particle tracking algorithms and adaptive interrogation techniques [81]. The fundamental mathematical operator that enables PIV analysis is the spatial estimator known as *correlation*. Depending on the type of PIV recordings under consideration, two respective functions can be defined as: **auto-correlation** for analysis of single exposure intensity fields, and **cross-correlation** for the evaluation

of double exposure intensity fields. Since, in the present work, single exposure recordings are analysed using the cross-correlation estimator, the details of auto-correlation will not be elaborated herein, and the reader is referred to [2] for a mathematical description of this method. In the following, a short introduction to the cross-correlation estimator is given. An in-depth analysis of the image evaluation techniques using two-dimensional correlation estimators can be found in [100, 68].

2.2.4.1 Image Intensities

In order to define an estimator for the retrieval of displacement data from PIV images, one must first identify the characteristics of the respective recorded data. The evaluation of PIV recordings is done locally, by dividing the acquired image into *interrogation windows* - or interrogation areas. Figure 2.5 exemplifies two consecutive single exposure PIV images, and the corresponding subdivision in interrogation windows. These areas are projections onto the image plane, of illuminated regions of the flow, which can be defined as *interrogation volumes*. Each interrogation volume should contain an ensemble of tracer particles. We can define the position vector $\vec{X_k} = \left\{X_k, Y_k, Z_k\right\}$ of the k^{th} tracer particle located in the flow at time t, and $\vec{X_j} = \left\{X_j, Y_j, Z_j\right\}$ the position vector of the particle at time $t+\Delta t$. The displacement inside the interrogation volume ($\Delta\vec{X}$) can thus be expressed as:

$$\Delta\vec{X} = \begin{Bmatrix}\Delta X\\ \Delta Y\\ \Delta Z\end{Bmatrix} = \begin{Bmatrix}X_j - X_k\\ Y_j - Y_k\\ Z_j - Z_k\end{Bmatrix} \tag{2.11}$$

Under the assumption of small perspective projection errors and a constant magnification factor of an aberration-free lens (**M**), the relationship between the particle displacement and the relative particle image displacement is [68, 100]:

$$\Delta\vec{x} = \begin{Bmatrix}\Delta x\\ \Delta y\\ 0\end{Bmatrix} = M \cdot \Delta\vec{X} = \begin{Bmatrix}M\Delta X\\ M\Delta Y\\ M\Delta Z\end{Bmatrix} \tag{2.12}$$

It should be noted that, if 2D-PIV measurements are deployed, the out-of-plane displacement can be recovered only if it is smaller than the light sheet thickness $\Delta Z \in \left[-\frac{\Delta Z_0}{2}, \frac{\Delta Z_0}{2}\right]$.

The relative particle image displacement ($\Delta\vec{x}$) will be recovered using spatial averaging between the two intensity fields I and I', corresponding to the respective

interrogation windows at time t and $t + \Delta t$. The intensity distributions can be expressed as:

$$I(\vec{x}) = \sum_{k=1}^{N} I_0(\vec{x_k})\tau(\vec{x} - \vec{x_k}) \tag{2.13}$$

$$I'(\vec{x}) = \sum_{j=1}^{N} I_0(\vec{x_j} + \Delta\vec{x})\tau(\vec{x} - \vec{x_j} - \Delta\vec{x}) \tag{2.14}$$

where the term $\tau(\vec{x} - \vec{x_k})$ is defined as the convolution of the point spread function of the lens ($\tau(\vec{x})$) and the Dirac delta function ($\delta(\vec{x} - \vec{x_k})$). $I_0(k)$ is the intensity level of the corresponding k^{th} particle image in the interrogation area.

2.2.4.2 Cross-Correlation Estimator

Having identified the intensity fields of the interrogation windows at two time steps, the expression of the continuous cross-correlation function can be defined as [68]:

$$C(\vec{x}) = \sum_{k,j}^{N} I_0(\vec{x_j})I_0(\vec{x_k} + \Delta\vec{x}) \int \tau(\vec{x} - \vec{x_k})\tau(\vec{x} - \vec{x_j} + \vec{s} - \Delta\vec{x})d\vec{x} \tag{2.15}$$

where $\vec{s}$ is the separation vector in the correlation plane. Adrian [2] defined three contributing parts to the total correlation estimate, as:

$$C(\vec{x}) = R_D(\vec{x}) + R_F(\vec{x}) + R_C(\vec{x}) \tag{2.16}$$

where:

- $R_D(\vec{x})$ represents the correlation of images of the same particle at the different time instances ($k = j$), and it will be referred to as *true correlation peak*
- $R_F(\vec{x})$ is the correlation fluctuating noise component of the image intensities.
- $R_C(\vec{x})$ is the correlation of the mean component of I. Both $R_C(\vec{x})$ and $R_F(\vec{x})$ are resulting from spurious correlation between different source intensities ($k \neq j$).

The final correlation peak of displacement will depend on several parameters most of which are characteristics of the PIV recording, such as image density (N_I) and window interrogation size. For a detailed description of all the parameters affecting the correlation peak, the reader is referred to the work of Westerweel [100]. The expression of the cross-correlation in discrete form can be simplified as [81, 68]:

$$C(m,n) = \sum_{k,j} I(k,j)I'(k+m, j+n) \tag{2.17}$$

where *(m,n)* represents the spatial shift of the interrogation area in the correlation analysis process, which will be elaborated in 2.3.2.

Figure 2.5 (right) exemplifies the correlation map for the chosen set of interrogation windows. The correlation peak should be noted to be the predominant feature in the correlation map, whilst the noise level correlation contribution is at least a few orders of magnitude lower.

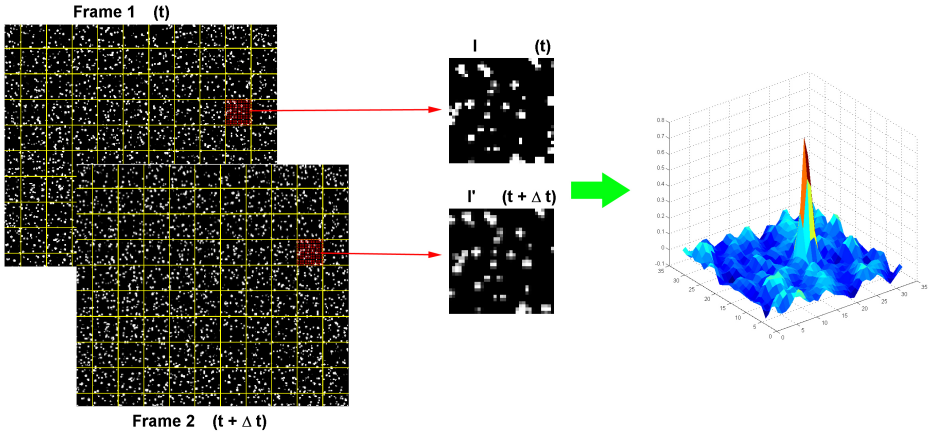

Figure 2.5: Example of PIV processing - images from third international PIV challenge [77]. Two consecutive single exposure PIV images at times: t_0 and $t_0 + \Delta t$ (left); corresponding intensity images for a chosen interrogation window (centre); the resulting *correlation map* for the chosen windows (right).

In practice, PIV raw data may exhibit high levels of noise which can affect the accuracy of the cross-correlation estimator. One way of reducing the noise

level is to use image pre-processing tools, as detailed in Section 2.3.1. In order to verify that the correlation analysis does not give erroneous results (outliers), data validation and replacement schemes are also implemented in post-processing algorithms, which are discussed in Section 2.3.2.

2.3 Slamming PIV Experiments

The PIV technique described above has been efficiently used for measurements of various fluid flow applications. The technical progress of PIV has allowed its applicability to extend to unsteady fluid flow problems of the most diverse nature. However, a thorough PIV experimental investigation of slamming problems has not been performed. As discussed in Chapter 1, the water entry problem still holds important issues that have yet to be fully described. Thus, application of PIV during water slamming can offer new insights into aspects of fluid flow, and provide solutions for validation of numerical problems of this fluid-structure interaction (FSI) problem. The prospect of time-resolved full-field fluid velocity measurements is also an interesting alternative to cumbersome point-wise measurement techniques.

The main issues that need to be addressed when conducting slamming PIV experiments are the flow physics, technical requirements of the measurement system and post-processing procedures. The flow physics aspects are mainly related to the restriction of 3D flow effects when performing 2D PIV measurements. These effects can be restricted if adequate aspect ratios of impacting bodies are achieved, and if symmetric boundary conditions are imposed to the flow. The main technical requirements of the measurement system is the high achievable repetition rate. High speed digital cameras and high-powered laser systems need to be deployed in order to capture the time scale of the flow during impact. Furthermore, optical accessibility and the repeatability of the experiment must also be taken into account.

The experimental slamming set-up for the PIV measurements that will be described in the remainder of this chapter is illustrated in Figure 2.6, and will be referred to as *Experimental set-up A*. This experimental set-up must include certain features to allow for PIV to be deployed. Firstly, optical access of the camera and laser light sheet must be achieved. For this purpose, glass panels are incorporated into the water tank. Furthermore, the free surface of the water will cause light reflections during the water entry. To resolve this issue and to restrict reflections during the experiment, light should be delivered from underneath the water tank, which means that optical guiding of the laser beam to the test section should

be used. Mirror arrangements or fibre optics bundles can be used for this purpose, whilst an arrangement of cylindrical and spherical lenses for laser light sheet generation should be incorporated as well. Secondly, a controlled movement of the impacting body and triggering of the acquisition system are preferred. Using a linear motor can provide solutions for both of these issues, as is exemplified in Figure 2.6, where the impacting body is rigidly fixed to an actuator.

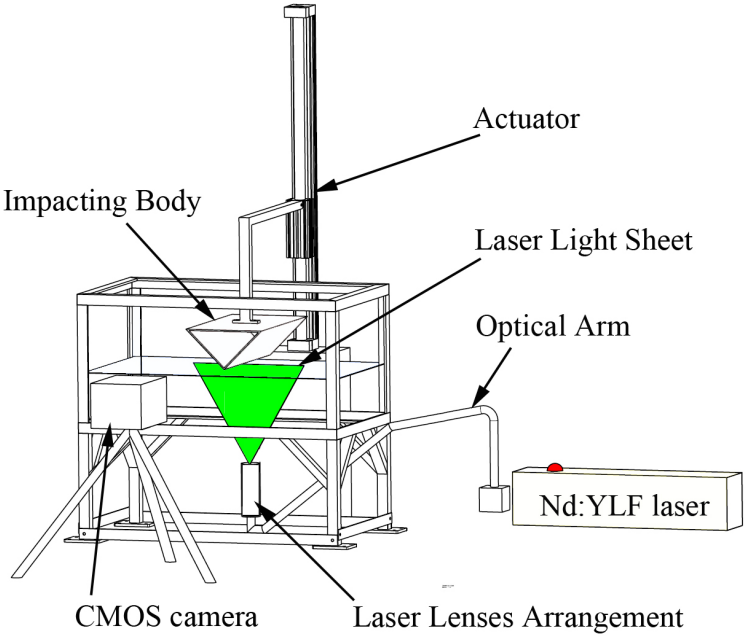

Figure 2.6: Slamming *Experimental set-up A* with PIV instrumentation (as described in Sections 2.2 and 2.3).

A third important factor in the PIV analysis of water impact is the post-processing procedure. This is perhaps the most decisive aspect that needs to be addressed because of the numerous factors that differentiate slamming from other PIV applications. In order to validate the post-processing algorithms used, and to motivate the choices taken on the processing parameters described herein, two test cases are considered in this chapter. The two test cases are PIV measurements of the water entry of a rigid wedge body and of a rigid cylinder body. The PIV-based results of fluid velocity and flow features will be presented in Section 2.3.4, and will be compared with literature results and with numerical simulations results. It should be noted that these measurements are performed using the experimental

slamming set-up A, and the PIV system features are fully described in Chapter 5.

2.3.1 Image Pre-Processing

As in many optical measurement procedures, PIV accuracy can be improved by means of an image pre-processing tool. PIV images are no exception to such techniques, and certain filters are applied to improve the SNR of raw data before evaluation of the image is performed. The filters used in the present work are chosen to maximize the SNR of the acquired digital images, whilst preventing truncation of the signal, i.e. particle image intensity. The filters considered herein include:

- Floating point data conversion.
- Dynamic threshold filter.
- High-pass filter.

A combination of some or all of these filters is used for each batch of acquired images, depending on experimental conditions. The filters are tuned according to the quality of the raw PIV images. A study of the effect of filter parameters on the cross-correlation signal-to-noise ratio is performed before commencing the PIV processing. Firstly, a **floating point data conversion** of the images is applied before other filters. This procedure converts the 8-bit raw image into a two-dimensional array of floating-point numbers in the range [0, 1]. This procedure prevents signal truncation that might occur after applying the other image filters.

The **dynamic threshold filter** is designed to increase contrast in PIV images using a percentage-based thresholding procedure. The filter imposes global, percentage-based threshold values of the histogram clipping. The upper and lower limits of the threshold are set as percentages of the sum of individual bin counts in the image histogram. The cut-off threshold is activated when the sum of individual pixels per bin exceeds the set value. The current implementation allows for an adaptive filtering through histogram analysis of a series of pictures. The advantage of using this method becomes important when considering PIV imaging in the presence of moving features. The moving features that will appear in the frame in the case of slamming measurements (body/free surface), will cause for unexpected laser light reflections with varying intensities from frame to frame. These reflections cannot be fully accounted for by using a single background subtraction procedure, or by imposing fixed threshold values. The dynamic behaviour of this filter thus becomes advantageous in a batch processing analysis.

High-pass filters are also implemented in the image pre-processing stage. The filter is designed to subtract a Gaussian low-pass filter version of the input image. This procedure leads to a reduction in noise levels of the PIV raw image, by removing low-frequency background variations. The filter kernel size should be higher than the particle image diameter to prevent loss of tracer images.

If attention is given to the way that these filters parameters are chosen, the result can be an increased SNR of the output image. Figure 2.7 exemplifies the effect of the filters described above on the SNR of the correlation coefficient. The SNR of correlation is defined here as the ratio between the square of the correlation peak and the variance of the correlation noise, expressed in dB. It should be noted that the processing parameters are kept unchanged for the two analyses of the same image pair. In the first case, the image is left unfiltered and unmasked. For the second analysis, corresponding to the right side of Figure 2.7, the filters described above are deployed. A 1 % dynamic histogram clip value is applied, and a Gaussian filter with kernel size of 3x3 pixels is used to create a low-pass version of the image to be subtracted from the original. The cylinder and air region have, as expected, the lowest values of SNR for both results. Results of correlation in the seeded water domain show a clear increase of the SNR when the filters are used in the pre-processing stage.

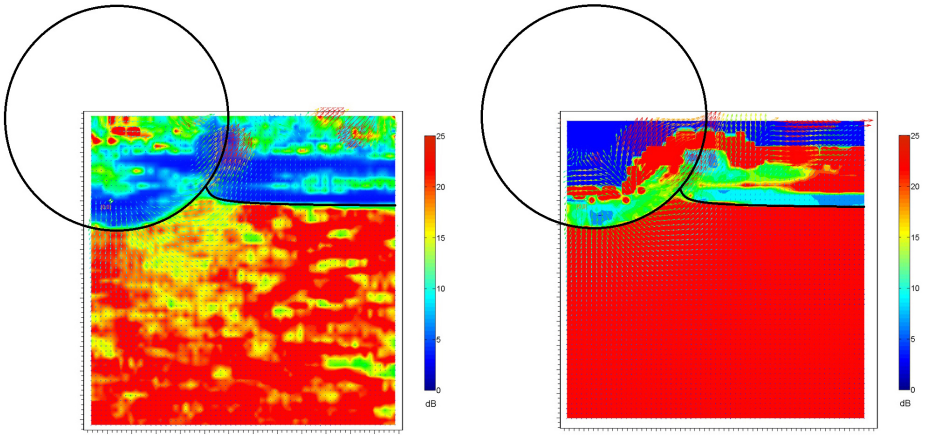

Figure 2.7: Improvement of correlation signal-to-noise ratio after image filtering. Rigid cylinder water entry example (cylinder and free surface contours schematically overlaid): Left - no image filtering; Right - results using dynamic threshold and high-pass filtered images.

2.3.2 PIV Interrogation Algorithms

In this subsection, the application of PIV processing procedures to recorded images during the water entry of bluff bodies is discussed. In order to proceed with the cross-correlation based estimation of velocity, several parameters of the processing algorithms need to be addressed. It should be noted that in this section, the choice of processing parameters is exemplified for the case of one typical PIV image recorded during slamming. These parameters are chosen to give the best overall results over a recorded sequence of several hundred PIV images that are recorded during water entry.

2.3.2.1 Interrogation Windows

The first parameter that is considered herein is the choice of interrogation windows, a notion previously introduced in Section 2.2.4. Considering the case of single exposure, double frame recordings, which is typical for digital PIV, the cross-correlation estimator as defined in equation 2.17, is used for the statistical analysis of the images. In order to spatially resolve the flow at a sufficient sampling rate that allows for an adequate physical description, the cross-correlation estimator is applied locally on subsets of the image, referred to as the interrogation windows. The way in which this analysis is performed, is by applying a shift to the interrogation window defined in the first frame that best approximates the image subset intensity distribution in the second frame. Such a shift will be the equivalent of the correlation peak as obtained from the summation of pixel-wise intensity values. The spatial shift *(m,n)* is therefore the displacement equivalent of the correlation peak. It should be noted that this procedure is standard for PIV processing, and that it involves using rigid 'blocks' (image samples), thus retrieving only linear displacements per interrogation area. As mentioned previously, several works have focused on improving aspects of correlation estimation, and alternative techniques exists which use deforming window techniques for increasing the dynamic range of measurable displacement, or even adaptive location and size of interrogation cells [81]. In Section 2.3.2.2, the adaptive window deformation and shifting techniques used in this work are explained in detail.

For the case of 2D-PIV, the choice of **interrogation window size** (${W_S}^2$) is one of the most demanding issues. Even though recurring values of this area (such as the commonly used 32 by 32 pixels) are frequently encountered in available PIV literature, the choice is still one of some debate. In the following, several aspects that dictate the selection of interrogation windows, are explained.

Particle Image Displacement. Often, in fluid dynamics studies, results are

very sensitive to both the spatial and the temporal resolutions. Resolving the high gradients that are commonly encountered in fluid flow problems, becomes a challenging issue that calls for a careful choice of the sampling rate of an experimental investigation. At the same time, one of the most important limitations of PIV is the trade-off one must resort to, between the spatial and the temporal resolutions. When referring to the temporal resolution of PIV, the most important choice is the laser pulse separation time (δt). Along with the development of hardware capabilities that offer stable, high-powered double cavity lasers, the limitations to this parameter have been greatly reduced. On the other hand, the decrease in the pulse separation time can have a negative effect on the correlation result. Raffel [68] separated the contributions to the measured fluid velocity ($\vec{V}$) into a measured particle velocity component $\vec{V_P} = \Delta\vec{x}/M(\delta t)$ and a residual error of the measured particle displacement $E_R = \epsilon_{lag}/M(\delta t)$. It should be noted that, even though the first term remains constant when decreasing the pulse separation time, the residual error becomes infinitely high when δt decreases to zero. Thus, the choice of the pulse separation time needs to be carefully addressed as it dictates the limits of the displacement values in the image plane. The choice of interrogation window size as a consequence of the particle displacement values, has been discussed in several early papers on PIV, which proposed different values of the limit of the highest possible accurate displacement result as a function of the window size. In [101], a value of $W_S/3$ has been shown to be appropriate for resolvable image displacements. However, a more conservative and widely accepted limit is that of $W_S/4$ proposed in [45], which is commonly referred to as the 'one quarter rule'.

Particle Image Density. The practical implications of correctly choosing the size of the interrogation area should be a balance between achieving the best possible PIV spatial resolution, whilst maintaining a high cross-correlation match of the particle images. In order to better understand the way in which an interrogation window is selected, a measure of the tracer pattern needs to be identified. Keane and Adrian [45] defined the term *mean effective particle image density* as a measure of the particle image pairs captured in one interrogation window. The term identifies three contributions to the accuracy of PIV, namely the in-plane loss of image pairs F_i, the out-of-plane loss of image pairs F_o and the particle image density N_I (equation 2.10). This factor can be used as a way of improving PIV performance, by relating the physical constraints to the analysis. Keane and Adrian showed that for $N_I F_i F_o > 5$, the valid vector detection probability is higher than 95 % for the case of single exposure, double frame PIV analysis.

Interrogation Window Size. Taking into account the influence of tracer image displacements and density, the size of the interrogation window can be selected. The importance of this parameter to the achievable PIV spatial resolution

stems from the filtering effect of the cross-correlation operator. Since PIV correlation analysis is, in fact, a discrete sampling of the fluid flow using interrogation spots, the measured tracer particle displacement is a value averaged over the area of one interrogation window. In order to asses this filtering effect, a theoretical sinusoidal displacement field can be considered, as suggested by Theunissen [81]:

$$u = sin(2\pi x/\lambda_m) \tag{2.18}$$

where u is the fluid displacement, x is the physical coordinate expressed in pixels and λ_m is the spatial wavelength of the displacement field. Figure 2.8 (top) shows the displacement field distribution over one interrogation window and the retrieved velocity vector using correlation analysis. It can be observed that spatial variations in the imposed displacement within one interrogation window will not be captured if the size of this window is larger than the wavelength of the flow.

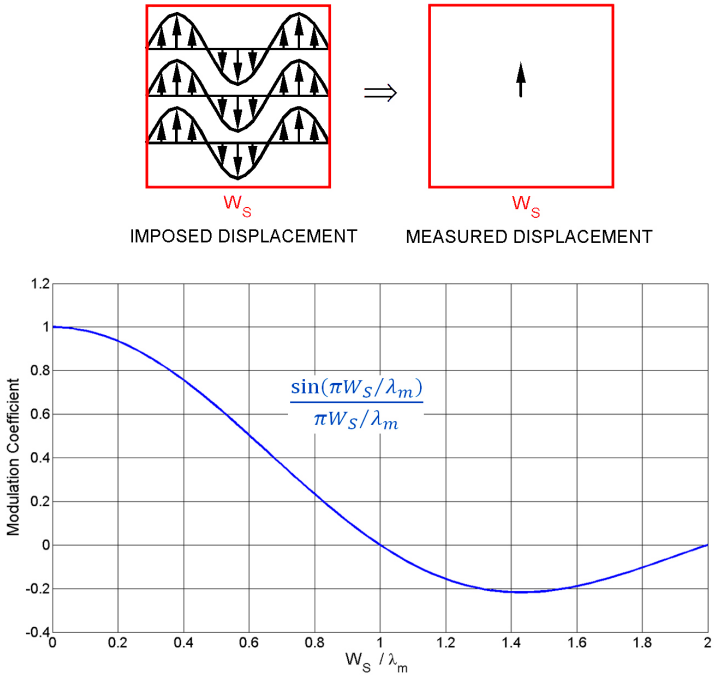

Figure 2.8: Top: Sinusoidal displacement field (equation 2.18) and the interrogation window (left); Recovered displacement using correlation analysis (right); Bottom: Spatial response of the correlation estimator to the sinusoidal displacement field.

In Figure 2.8 (bottom), the normalized amplitude of the signal is plotted as a function of the normalized interrogation window size with respect to the spatial wavelength of the velocity. It can be observed that the interrogation window size needs to be lower than 20% in order to accurately reproduce the velocity fluctuations. Therefore, five interrogation windows are needed to resolve the physical length scale of the flow with an error margin less than 10%.

Interrogation Window Overlap. After defining the interrogation area, PIV analysis requires the definition of another factor, namely the interrogation window overlap. This factor, expressed as a ratio of the interrogation window size (IW_{of}), defines the sampling rate of the vector map, and thus, the final spatial resolution. The resulting vector grid spacing can be expressed as [81]:

$$\Delta_{xy} = W_S(1 - IW_{of}) \tag{2.19}$$

The size of this overlap factor should be chosen in such a way that it ensures the sampling of the flow at a rate at least twice that of its largest frequency, resulting in a typically used value of 50 %. The final PIV grid is thus a result of window size and window overlap ratio. Figure 2.9 shows an example of working grids for rigid body water entry measurements, corresponding to a chosen interrogation window size of 32 x 32 pixels and an overlap factor of 50% for the wedge slamming case, and a 24 x 24 pixels interrogation window with 50 % overlap for the cylinder water entry measurements.

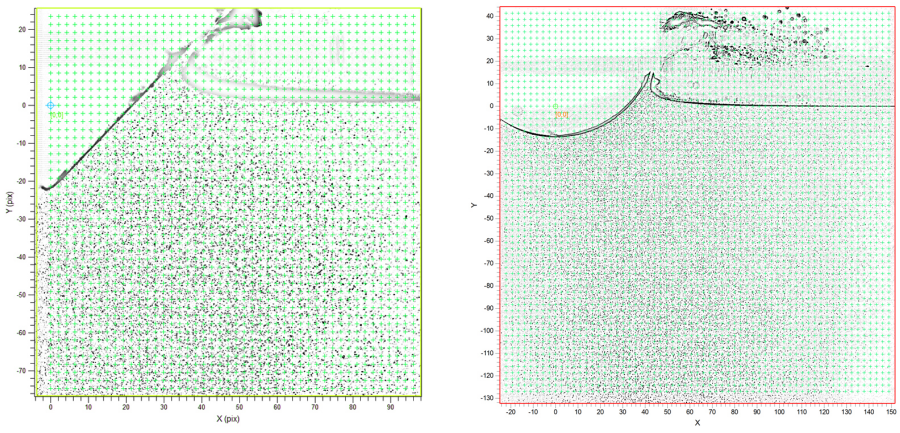

Figure 2.9: PIV grids. Left - wedge slamming: interrogation windows of 32 x 32 pixels and overlap factor 50%; Right - cylinder slamming: interrogation windows of 24 x 24 pixels and overlap factor 50%.

The PIV grids are produced after specifying a grid anchor location, which is user-defined as the horizontal and vertical coordinate expressed in pixels. This point can be arbitrarily chosen. However, in the work presented here, the anchor point is chosen at the free surface level, on the symmetry axis of the impacting body. This point represents the origin of the coordinate system in the resulting velocity maps. The limits of the PIV grid coincide with the size of the PIV image, meaning that the entire image is subjected to the correlation analysis. If desired, these limits can be decreased, if stationary artefacts such as shadows are present in all the raw images.

2.3.2.2 Interrogation Procedure

After defining the size of the working grid of the PIV analysis procedure (i.e. interrogation window size, windows overlap factor and location of grid anchor and limits), the interrogation parameters need to be defined. Various schemes can be implemented in order to increase accuracy of PIV results. The schemes used in the present work are:

- Multiple pass interrogation
- Multi-grid interrogation
- Image deformation
- Image interpolation schemes
- Multiple (repeated) correlation

These algorithms are designed to improve valid data yield from PIV analysis, by eliminating some of the limitations to the PIV results that were discussed in Section 2.3.2.1.

Multiple pass interrogation. Several iterations of the interrogation procedure can yield a higher accuracy of the results, when window offsets are used. After a first interrogation pass, the calculated displacement can be used to offset the image sample with the integer value of local shift. After each interrogation pass, a data validation criterion is used to eliminate outliers, and only valid displacement results are used in the next iteration. An upper limit to the number of passes to be performed is initially set by the user, with two or three passes being typical values used in the analysis of slamming measurements. This procedure improves results as long as the residual shifts are higher than one pixel displacement. As pointed out by Westerweel [101], the multiple pass interrogation procedure not only increases the SNR of the correlation peak (due to the decrease

of in-plane particle loss), but also reduces the measurement uncertainty when the final measured particle image displacements are less than one half of a pixel.

Multi-grid interrogation. This is an improved algorithm that incorporates the principles of the previous technique, but also allows the decrease in window size during PIV analysis. The multi-grid interrogation procedure is an iterative grid refining scheme, which uses a pyramid approach to decrease the final interrogation window size to values lower than the particle displacement, without in-plane loss of particle image pairs. In this work, the algorithm is started with an initial large value of the interrogation window (e.g. 96 x 96 pixels) that can capture the largest displacements in the frame. After data validation of this initial results, the grid resolution is increased, and the new interrogation windows are offset by values of displacements recovered from the previous step. The procedure is repeated until final grid resolution (e.g. interrogation window size of 24 x 24 pixels) is achieved. By iteratively reducing the sampling grid size, an increase of the dynamic spatial range (DSR) is achieved, and conventional limits to the PIV analysis, such as the *one quarter rule* that was previously discussed, can be overcome. The dynamic spatial range represents the ratio of the largest observable length scale to the smallest length scale, and thus determines the measurable range of velocity.

Image deformation. The image deformation schemes are particularly useful to achieve higher accuracy of the PIV results. The two algorithms previously discussed, are designed under the assumption that particle motion is approximately uniform within an interrogation window. However, in practice, the velocity gradients can exhibit large variations within a single interrogation sample, and the use of window offsets may not be sufficient to accurately determine these variations (e.g. in the spray root region of the flow). Therefore, the results of such iterative interrogation algorithms can be further improved by implementing an image deformation technique, as performed in the current research. The method uses the displacement information estimated in a previous iteration, to deform the PIV images that will be interrogated in the current step.

Image interpolation schemes. When implementing the image deformation techniques in the interrogation procedure, the image intensity map needs to be re-constructed at each iteration. Therefore, interpolation of image intensities at non-integer pixel locations needs to be performed. Although several choices of image interpolation schemes have been considered in literature (such as Gaussian or bilinear interpolation), the *B-splines* functions have been proven to offer the best balance between performance and computational cost [82, 7].

It should be noted that, in the present work, the multi-grid interrogation approach is used together with image deformation and interpolation using B-splines

functions.

Multiple (repeated) correlation. A further improvement of the interrogation procedure used herein is performed by multiplication of two correlation planes which are slightly offset with respect to each other. This approach was first proposed by Hart [38], who found that by multiplying neighbouring correlation planes with high noise content, a resulting map with a single clear correlation peak can be obtained. This finding is explained by the fact that correlation anomalies (resulting from random noise peaks) are less likely to be consistent in both the correlation maps under investigation. However, the spatial offset between the considered maps needs to be adjusted carefully, for the procedure to give good results. If this offset is too small, the random noise artefacts will be predominant in both tables, and will not be eliminated after multiplication. On the other hand, if the offset is too large, the correlation peak might be entirely lost, particularly in high gradient flows. In the present work, the repeated correlation procedure uses an offset of the interrogation windows equal to the IW_{of} of the PIV grid. This means that a typical value of 50 % overlap is used, which was also considered a viable choice in [38].

2.3.2.3 Sub-Pixel Resolution

Improved interrogation algorithms can be used to increase the accuracy of PIV estimations of displacement. Sub-pixel peak fitting is an important procedure used to determine the location of the true correlation peak with accuracy of up to $1/20^{th}$ of a pixel. Considering that the correlation analysis produces sampling of the data in a discrete way, raw results have a minimum uncertainty of one half of a pixel. There exists a variety of methods of performing this peak fit on the correlation data, and the choice between fitting functions needs to be based on the type of PIV recording at hand, as well as the characteristics of the flow being measured. In the following, the commonly used peak fit estimators are discussed.

The *peak centroid* estimator is based on the separation of the signal from background noise in the correlation plane, and it is defined as the ratio between the first order moment (or center of mass) and the zero order moment. This function requires for a way of defining the region that comprises the correlation peak. After the peak has been identified, neighbouring values of correlation (e.g. in a 3x3 kernel) can be used to calculate the first order moment. The peak centroid method performs poorly when narrow correlation peaks are encountered (which is typical for PIV images), but can give good results when broader peaks are identified. This latter situation occurs when larger particle images or larger features are present in the raw image.

Three-point estimators are probably the most commonly used type of peak fit functions, which are based on fitting a specific function to the correlation data. The function which is most frequently used is the *Gaussian peak fit* [103]. This observation is based on the fact that the properly focused particle images describe Airy intensity functions which can be best approximated by a Gaussian distribution, as mentioned previously in Section 2.2.1. The Gaussian fit function uses the four closest neighbours of the correlation peak, and fits the 3-point Gaussian curve along each of the two axes. A similar function is the *Parabolic peak fit*, which fits a parabola through the three points instead of the Gaussian curve.

Alternative peak fit estimators have been proposed, which use more than just 4 neighbouring values in the correlation plane. The first of these methods is the *2D Gaussian peak fit*, as proposed in [72]. This estimator can be used with more than the immediate neighbouring values in the vicinity of the correlation peak, and can produce better results especially when non-symmetric correlation peaks are present. Another estimator with increased complexity is the *Whittaker reconstruction* [71], which reconstructs the correlation peak value from values of correlation along the horizontal and vertical lines that cross the peak location.

In the present work, the Gauss peak fit estimators are preferred due to their robustness. The three-point Gauss fit is generally the best trade-off between computational cost and accuracy. However, when the correlation map exhibits higher levels of noise, the 2D Gauss fit is used to increase accuracy. The implementation of this estimator is performed by explicitly solving the Gaussian regression in a least squares sense, on a 3x3 area of the correlation plane surrounding the peak [61].

2.3.2.4 PIV Data Validation

The data validation schemes that are currently implemented in every PIV post-processing algorithm are basically an automated way of discarding erroneous velocity vector data (outliers). The human perception is very effective in identifying the outliers present in a processed PIV image. The main characteristics of these outliers is the inconsistency of their magnitude and/or direction compared to the neighbouring vectors. Most often, these outliers appear as single incorrect vectors, and are likely to be located at the edges of the image (due to loss of particle image pairs between the two frames), or in areas with low SNR. If an interactive elimination of these outliers can be possible when a few PIV images are to be analysed, in modern (time-resolved) PIV investigations, this is no longer feasible due to the high amount of pictures to be processed. Moreover, as discussed previously, data validation is required when iterative interrogation techniques are

being deployed. The outlier detection schemes can be categorized into two main groups, depending on the way they are defined:

- **Displacement-based tests**
- **Correlation-based tests**

The **displacement-based tests** are user-defined thresholds on the estimated displacement, that can be specified before interrogation is started. These thresholds are set based on a priori knowledge of the expected velocity distribution in the field of view. Depending on the way the thresholds are set, several tests can applied. In the present work, the following tests are used:

– *Maximum displacement test* is based on a user defined value of maximum possible displacement. This can be imposed when a knowledge of the highest measurable displacement is available before interrogation is started.

– *Displacement difference test* is a procedure that uses a threshold for the velocity gradient. The vector estimated in one interrogation window is compared against each of its surrounding neighbours (four or eight neighbours), and if the difference is higher than the specified threshold for more than half of the instances, the vector is deemed invalid.

– *Dynamic mean test* is defined in a similar way as the previous test. The difference between the two is that, in the case of the dynamic mean operator, the magnitude of the analysed vector is compared with the mean value over its neighbours. If this difference is higher than the imposed threshold, the vector is marked as an outlier.

– *Median test* is frequently used in image processing software. Its application to PIV vector data validation was found to be effective by Westerweel [99]. The working principle of this filtering procedure consists of the linear sorting of the neighbouring vector values with respect to their magnitude. The central value is recorded as the median value, and the vector under investigation is considered valid if the difference between its value and the median value is lower than an imposed threshold.

– *Normalized median test* is similar to the previous test. However, in this case, the difference between the considered vector value and the median value is normalized with respect to the median value of the residuals of the neighbouring vectors. These residuals are defined as the difference between each

vector magnitude and their median value. This test was found to produce a universal probability density function, and thus the application of a global threshold value becomes more effective in the data validation step [102].

– *Global histogram filter* is a procedure in which regions of interest in the 2D vector histogram can be constructed and used as a validation criterion. The histogram of vector data is plotted using all estimated displacement data from the PIV image. Next, rectangular and/or elliptic regions of interest can be user defined to circumscribe areas on the histogram that contain valid data information. The vectors outside these areas are considered outliers, and they are discarded. This procedure can be particularly useful in cases such as the slamming PIV measurements, where the camera FOV captures only half of the water domain (up to the symmetry axis of the impacting body). Therefore, the horizontal displacement should be strictly positive, and using this procedure, estimates of negative values are marked as outliers.

Correlation-based tests can also be implemented in order to validate vector data. However, these validation methods are less effective than the displacement-based tests because of their considerably lower detection success rate.

– *Minimum SNR* uses a minimum allowed value for the SNR of correlation to validate the data.

– *Peak ratio*. A vector is marked as an outlier if the ratio of the correlation peak to the first noise peak is lower than a certain imposed threshold.

– *Minimum correlation*. This test requires for the value of the correlation coefficient to be higher than a certain user-defined value.

A comprehensive and extensive review on the validation tests described above can be found in the book of Raffel [68], and the reader is referred to his work for further details on each of the filtering procedures.

2.3.2.5 Outlier Replacement

Following the identification and removal of erroneous vectors in the interrogation procedure, schemes of replacing these outliers need to be applied. In the work of Westerweel [99], it was shown that for a 5 % percentage of spurious data, more than 80 % of the missing data can be recovered by bilinear interpolation using

the neighbouring valid data. If the outlier vector is not isolated, and neighbouring data is also found to be erroneous, a weighted average of the surrounding valid data can be used.

In the case of some PIV processing algorithms, particularly those that use multi-grid interrogation schemes, data smoothing is also required after each iteration. As pointed out by Raffel [68], the effects of measurement noise on the experimental data can not be fully eliminated. Thus, data smoothing can be applied, especially when comparisons of PIV data with simulations data are of interest. A robust way of smoothing PIV data is by means of median filtering, a method typically used in image processing. In the work presented herein, a median filter with kernel size of 3x3 is used for data smoothing. This type of filter is particularly useful in preparation of the velocity data to be used in the pressure estimation procedures that will be discussed in later chapters.

2.3.3 Automated Masking

The procedure described in the previous section produces valid vector fields when PIV analysis is performed on regions of seeded flow, without additional artefacts such as moving body boundaries. However, in the case of slamming, the PIV images contain features of both body regions and air regions, as well as the water/air interface. Erroneous vectors that will be produced in these regions can influence the valid data at the edges of the ROI. In order to remove the negative effect of these spurious vectors, the air and body regions should be masked before processing of the pictures is begun. Because of the complex geometry of the free surface, and because of the moving body image, an adaptive masking approach is necessary. The image evaluation algorithm is adjusted to include automated adaptive masking of the body and of the air region. To achieve this, a code is written in Matlab to automate the process. The raw pictures are read into Matlab, and the automated masking procedure is done for every time step, with masking for both of the two single exposure frames. A PIV utility program (PIVview) for cross-correlation analysis, provided by PIVTEC is appended from Matlab for every time step, using the two raw pictures, a file containing the cross-correlation parameters and two mask images as input.

2.3.3.1 Masking Procedure

The masking procedure is done in two steps. Firstly, the body image is masked off using information on the actual position from the actuator controller. This approach was preferred due to the flexibility conferred by knowing the position of

the body at each time step thanks to the position encoder of the controller. Since the position and velocity information are readily available from the actuator encoder output, and considering that the body is rigid and therefore the body shape is unchanged during slamming, the body position in the raw image is reconstructed and masking of this region is performed. Figures 2.10 (a) and 2.10 (b) show a raw image taken during the water entry of a wedge body and the image with the body position masked, respectively.

Secondly, using contours of brightness levels on the picture with the masked body region, the free surface is identified on the images and masking of the air region is performed. The procedure consists of identifying contours of intensity levels of the input picture, as can be seen in Figure 2.10 (c). The resulting matrix of contour levels is used to extract the dominant feature in the picture, which will have the highest number of connected pixels with maximum intensity values. This feature will be corresponding to the laser light reflections of the free surface. Then, the lower points of this contour are chosen as the free surface elevation profile, and the pixels above this profile, which are corresponding to the air region, are masked off. It should be noted that the light reflection from the free surface has a gradual decrease of intensity in the PIV recording. However, the pixel coordinates chosen in this step present the highest values (255) of grayscale intensity, and form a contour profile with a maximum height of less than 5 pixels. This implies that the uncertainty of the free surface elevation profile as recovered using this procedure is less than 0.2 mm. The image filtering procedures applied for improvements of the free surface feature identification step, as explained in Section 3.2.1, were found to reduce this uncertainty even further.

Having recovered the pixel coordinates of both the free surface profile and the body region, a final mask is constructed and saved as a grayscale picture (Figure 2.10 (d)). This final mask is then to be used as input in the correlation analysis.

2.3.3.2 Correlation Analysis Using Automated Masking

The cross-correlation analysis is performed by taking into account the mask image obtained previously. Evidently, the correlation result on interrogation windows which contain only masked pixels is equal to zero displacement. However, considering that the PIV grid - and subsequently, the initial interrogation areas - are fixed with respect to the Cartesian coordinate system, some interrogation windows will contain both masked pixels as well as regions of the water flow. In this case, two situations can occur. If the PIV grid node (center of the interrogation window) is situated in the masked area, the resulting correlation will be zero displacement. A second case is that the grid node is in the water flow region, but

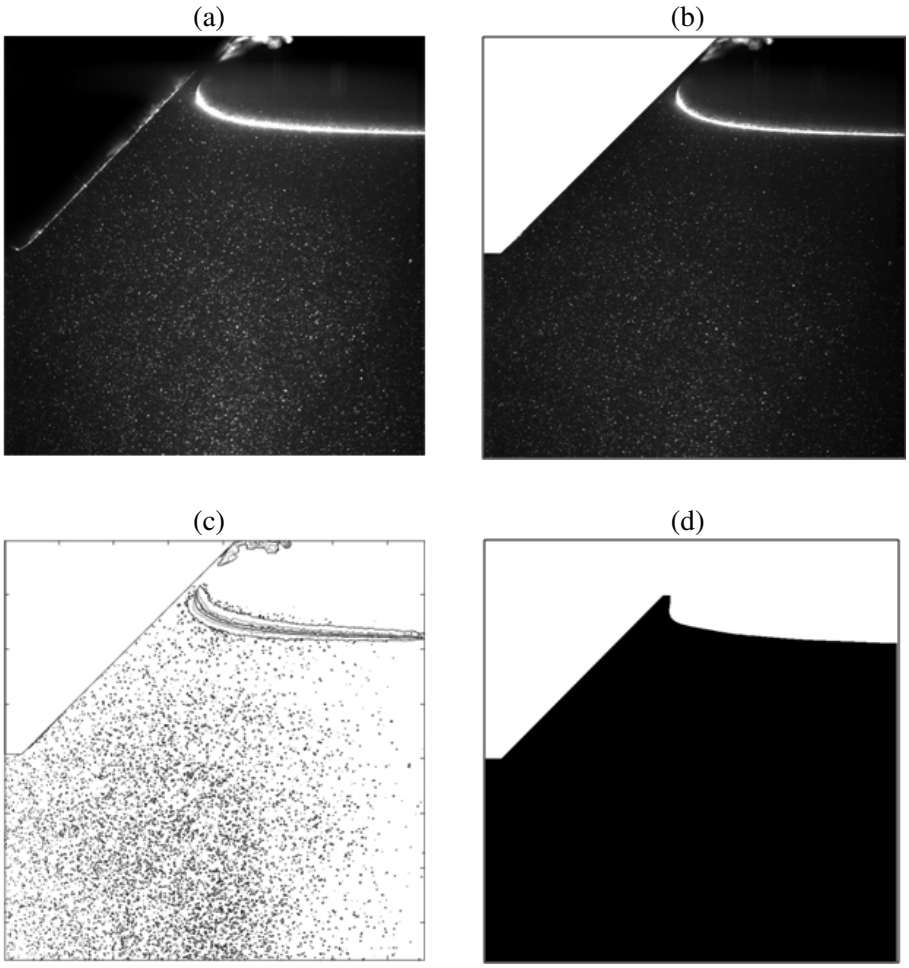

Figure 2.10: Image masking. (a) PIV raw image. (b) Body masked image. (c) Intensity contour image. (d) Final mask image.

part of the corresponding interrogation window is masked. In this situation, the correlation is performed using the available pixels (water flow). It should be noted that in this case, the available number of pixels will be smaller than the interrogation window size (i.e. 32 x 32 pixels), and that localized laser light reflections can affect the correlation estimation. If the correlation estimation does not meet the data validation criteria described in Section 2.3.2.4, the vector is replaced using

valid neighbouring data, as described in the previous section.

In order to assess the performance of the correlation analysis for the case of mask overlapping in the interrogation windows in the vicinity of the body, two theoretical flow distributions are analysed. The first case is that of a linear displacement field in the vicinity of a stationary wall, with a velocity distribution equal to $u = 0.05 \cdot x$, where x is the horizontal coordinate expressed in pixels, as depicted in Figure 2.11. The second case corresponds to a constant velocity profile with 6 pixels displacement in the vicinity of a stationary wall as shown in Figure 2.12. The two displacement distributions are used in generating PIV synthetic images that were analysed with the PIVview software. The image size used was 256 by 256 pixels, and the wall region on the frames was masked. A mean particle sizes of 2.2 pixels and a mean distance between the particles of 6.3 pixels were used, similar to the case studied in [86]. The particles size and locations were randomly distributed about their mean values, and zero-mean Gaussian white noise was added to the synthetic images, in order to simulate the conditions of experimental PIV recordings.

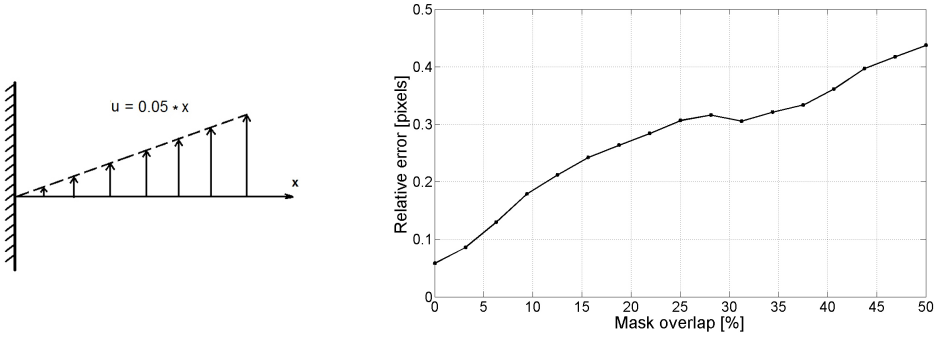

Figure 2.11: A linear displacement field in the vicinity of a stationary wall. Left: velocity distribution; Right: Relative error between PIV results and the theoretical values for different values of mask overlap in the interrogation window.

The PIV analysis was performed using 32 by 32 pixels interrogation windows with 50 % overlap. Several runs of the correlation analysis were performed, with a gradual increase of the interrogation window centre from the stationary wall location. The results of the PIV interrogation for the two considered test cases were compared with the theoretical values of particle displacement. In Figure 2.11(right) the relative error between the correlation result and the theoretical values are plotted for different values of the mask overlap of the interrogation

window. It can be observed that the values of the relative error increases with increasing mask overlap values, to a maximum of approximately 0.45 pixels when half the interrogation window is covered by the wall. Further improvements to the correlation algorithm were suggested in literature, such as vector relocation [81] in the geometric centre of the seeded part of the interrogation window, or even an extension of the particle image fields across the fluid-solid interface [84]. These improvements could lead to a reduction of the error up to 50 %, as reported by Usera [86].

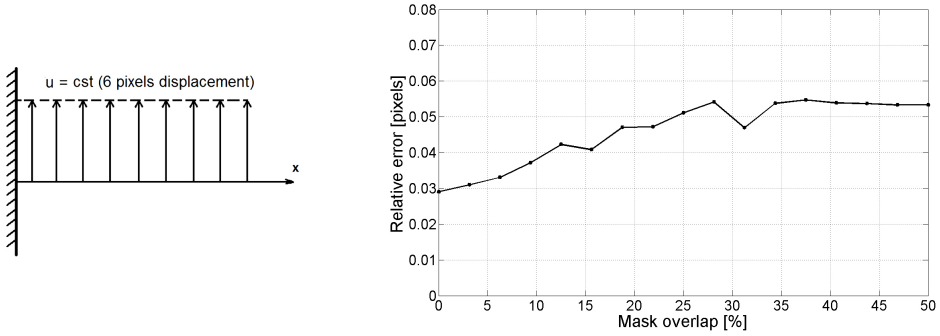

Figure 2.12: A displacement field with constant velocity in the vicinity of a stationary wall. Left: velocity distribution; Right: Relative error between PIV results and the theoretical values for different values of mask overlap in the interrogation window.

When considering the second test case, corresponding to a constant displacement profile extending up to the solid wall (similar to a free-slip boundary condition), the relative error is found to be decreased dramatically as seen in Figure 2.12 (right). In this case, the error does not go over 0.06 pixels displacement, which is approximately 1 % error of the PIV correlation analysis. Therefore, it is concluded that the application of the mask on the body wall increases the accuracy of the results within the limits imposed by the necessary particle image displacements and density, as discussed in Section 2.3.2.1. Therefore, further treatment of the wall region, aside from the application of the mask in the correlation analysis, was not considered in this work.

The application of automated masking on recordings of the water entry cases, was found to increase correlation coefficient values as well as improve outlier detection. In Figure 2.13, an example is shown for the rigid wedge water entry test case. Figure 2.13 (a) and Figure 2.13 (b) are snapshots of a typical PIV image and the processed correlation coefficient map, respectively.

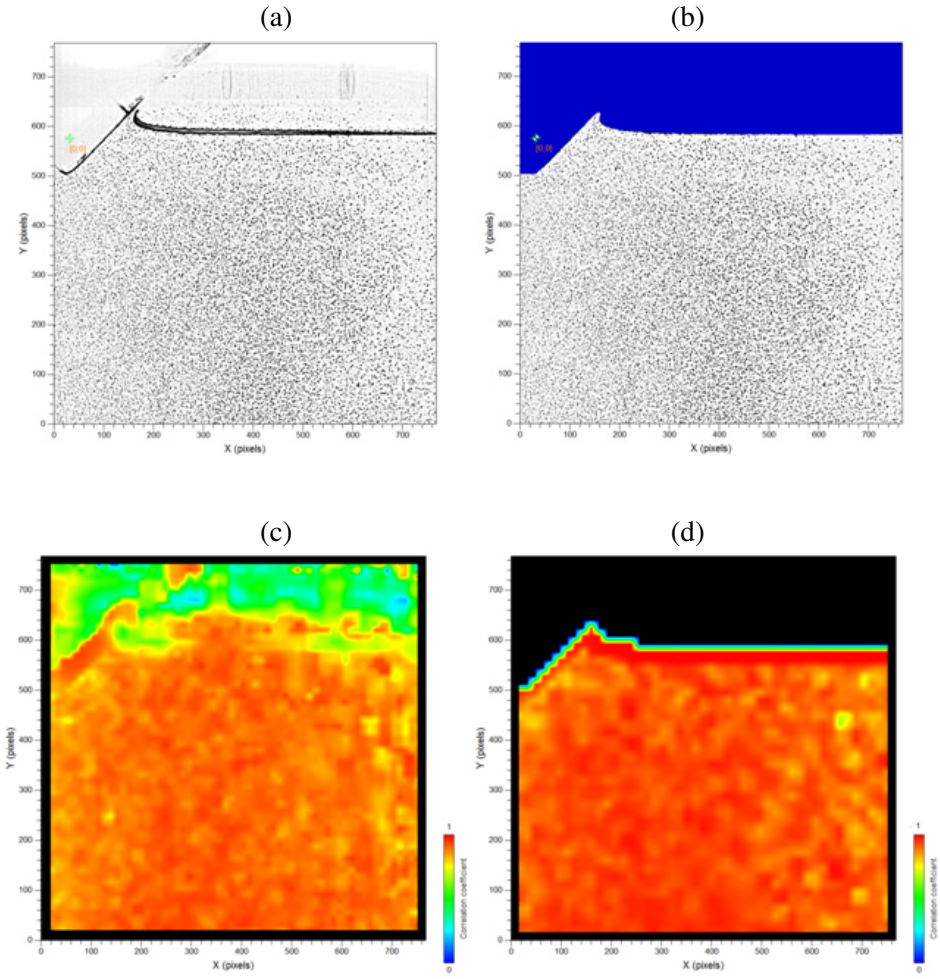

Figure 2.13: PIV images and correlation coefficients. (a) Raw image; (b) Image with mask; (c) Correlation coefficient for unmasked image; (d) Correlation coefficient for masked image; the mask is applied before image pre-process filtering is performed.

By comparing the correlation values in the region of interest corresponding to the water domain, it can be observed that using the same PIV processing parameters, but introducing the mask as well, leads to an improvement of 10% for the entire field of view (FOV). However, this increase is more substantial in the

area close to the free surface and the spray root of the water jet, which, as it will be shown in the remainder of this chapter, is a very important region of interest.

The application of the mask eliminates the artefacts that are present in the regions of the image which are not of interest, namely the body and the air region. Furthermore, the masking procedure limits the errors introduced by laser light reflections or banding noise. As a consequence, the outliers produced by false correlation outside the region of interest are eliminated. In Figure 2.13 (c) and Figure 2.13 (d) it can be observed that the correlation coefficient in the vicinity of the free surface and of the rigid body wall are higher when using the mask in the cross-correlation algorithm. In the far-field region of the water domain, the correlation values also show an improvement when using the mask. This is caused by the application of the mask before performing the image pre-process filtering that was discussed in Section 2.3.1. Because of the elimination of excessive light reflections in the image before dynamic filtering is applied, the contrast enhancement is improved, and thus the correlation coefficient values are increased further from the body and the free-surface, as well.

Another important advantage of the masking procedure is the automated nature in which it is performed. For an experiment such as slamming, where time-resolved data are required, it is important that the processing tools allow for batch analysis of the entire series of pictures (typically between 100 and 500 frames for each test). In Figure 2.14, the valid data percentages are plotted against time for measurements of rigid wedge and rigid cylinder water entries. It can be observed in this figure that the masking procedure leads to an improvement in SNR and subsequently a considerable increase of around 10% in valid velocity data measurements across the entire time series.

It is to be noted that this increase corresponds to the entire region of interest, namely the water domain, but, as shown previously, in localized regions around the free surface and rigid body, the correlation coefficients show a much higher improvement. Therefore, if a smaller field of view would be considered, with attention to these boundaries, the number of outliers in the case of measurements without masking would be even greater.

2.3.4 Water Entry of Rigid Bodies

In order to validate the operating principles of PIV measurements in the study of the slamming of rigid bodies, a wedge-shaped and a cylinder body are tested. The

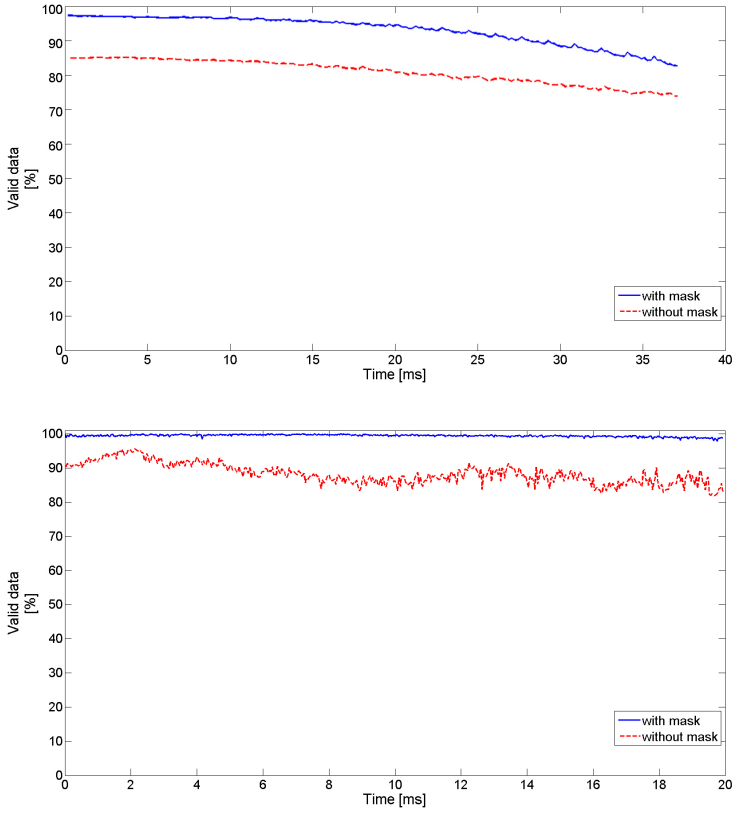

Figure 2.14: Evolution in time of valid data detection - improvement of valid data percentage by using the automated masking procedure for top: wedge body; bottom: cylinder body.

90° wedge and the cylinder (90 mm diameter) are studied during water entry with constant entry velocity $V_{entry} = 1.5m/s$. The experimental set-up A previously referred to in Section 2.3, is used for these investigations. As previously mentioned, the set-up uses a linear motor for the controlled movement of the body. The actuator is a Copley Controls XM3804S ServoTube Module with 350 μm absolute accuracy, that presents the added advantage of repeatability of the measurement, as well as precise triggering of the PIV system. Feedback is provided on actual load position, velocity and acceleration through the use of an internal oscilloscope. The actuator is operated by using programmable digital inputs in sequences of controlled movements by defining acceleration and velocity target

values. Figure 2.15 shows an example of the velocity and position information recorded by the actuator controller during operation, which is a sequence corresponding to the water entry of the rigid wedge.

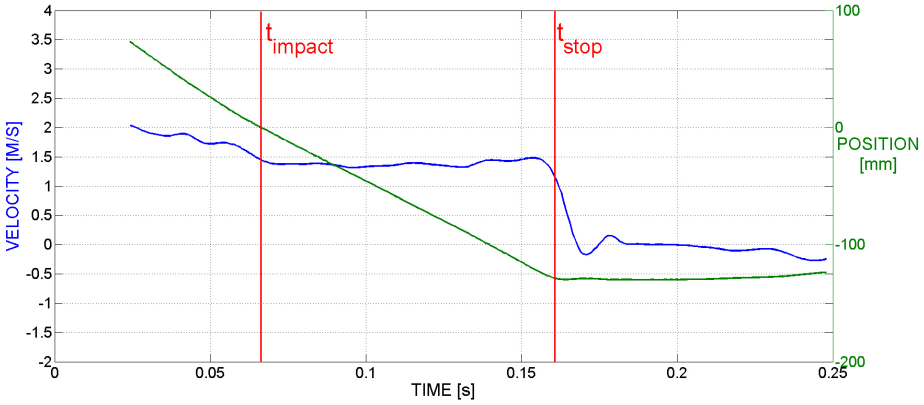

Figure 2.15: Position and velocity information recorded during water entry of a wedge rigid body. t_{impact} marks the moment of initial contact with the water surface; t_{stop} marks the moment the linear motor begins deceleration of the body.

Using the free surface contours determined in the masking procedure, free surface elevation information is extracted at each time step. The results are made dimensionless by division of the coordinates of the free surface profile with the body submergence Vt where V is the body velocity and t is the time. Therefore, the results for any time step and body velocity can be compared with the available literature results. Figure 2.16 shows the comparison between the result of free surface elevation profiles recovered from PIV and the analytical solution of [51] for a 90° wedge. Good agreement can be found, with a maximum error of around 2% at the spray root, where the PIV gives a thinner spray root region.

Figure 2.17 shows the instances of a cylinder body and of the free surface profile as measured from PIV for three time instances. The available literature results of the free surface evolution during water entry of a circular cylinder have not been included in a comparison. The reason behind this choice is that the experimental conditions used herein differ from those used in previous studies - [31, 78] - and thus the feature evolution exhibits different characteristics. The experimental conditions in the present study consist of imposing a constant velocity profile during water entry, whereas in the mentioned papers, the cylinder was tested in free-fall conditions.

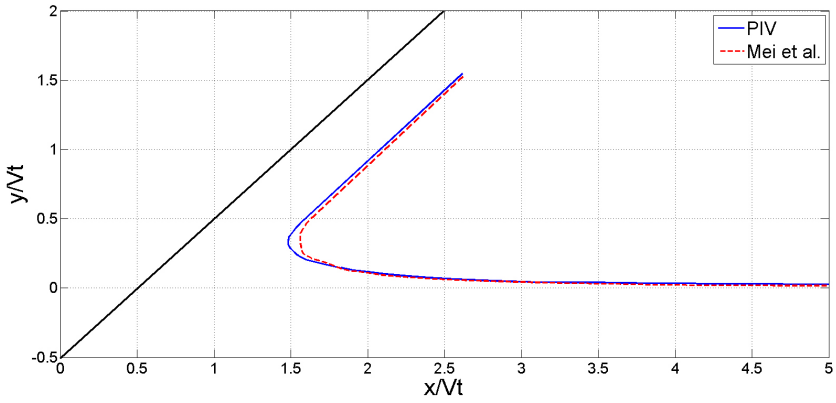

Figure 2.16: Comparison of free surface elevation for wedge impact with constant speed between PIV and the analytical solution of [51]. Vt is the instantaneous draft relative to calm water.

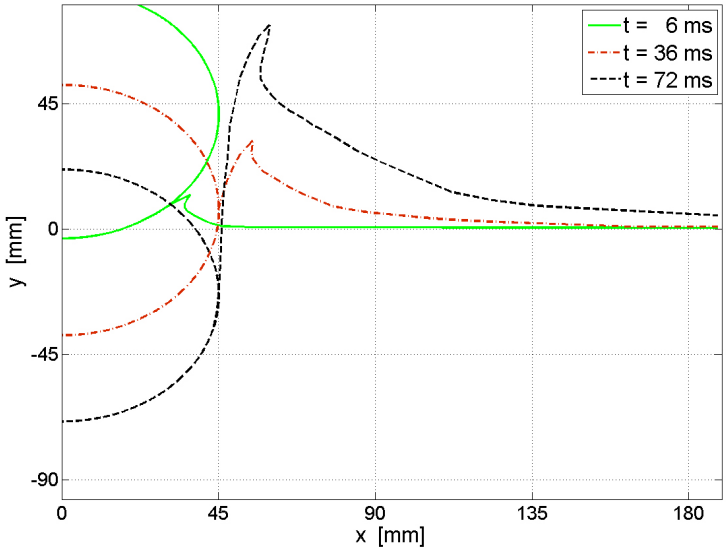

Figure 2.17: Free surface profiles during water entry of a rigid cylinder.

2.3.4.1 Numerical Simulations

The results of the PIV measurements were used for comparison with data from a numerical simulation of the same problem, performed by Vepa [91] using the soft-

ware package LS-Dyna [92]. Experimental conditions are reproduced in a quasi-three-dimensional model with only one element in thickness, and constrained degrees of freedom in this direction.

The concept of multi-material groups (MMG) is used to represent the two fluid phases, and fluid-structure interactions are modelled using a simplified cell-centred arbitrary Lagrangian-Eulerian algorithm (ALE). The algorithm calculates an explicit time step Δt based on the Courant-Friedrichs-Lewy condition using the smallest grid element size and the convective velocity. For the wedge test case, the time step used is $5 \cdot 10^{-5}$ s, while for the cylinder test, the time step is 10^{-5} s. A non-uniform grid is used for the simulations, using a domain of the same size as the tank used in the experiments (Figure 2.18). The element size is kept constant in the region of interest that is used for comparison with the PIV measurements, and it is increased away from this region. The Lagrangian boundary of the solid body is overlapped onto the fluid mesh, and a constant velocity of 1.5 m/s is prescribed for this boundary. For the wedge body impact simulations, the smallest grid element size is approximately 0.5 mm, which is four times lower than the PIV grid size. In the cylinder test case, the mesh is further refined in the vicinity of the impacting body. Thus, the final achieved resolution in the simulations is ten times higher than the PIV measurement grid.

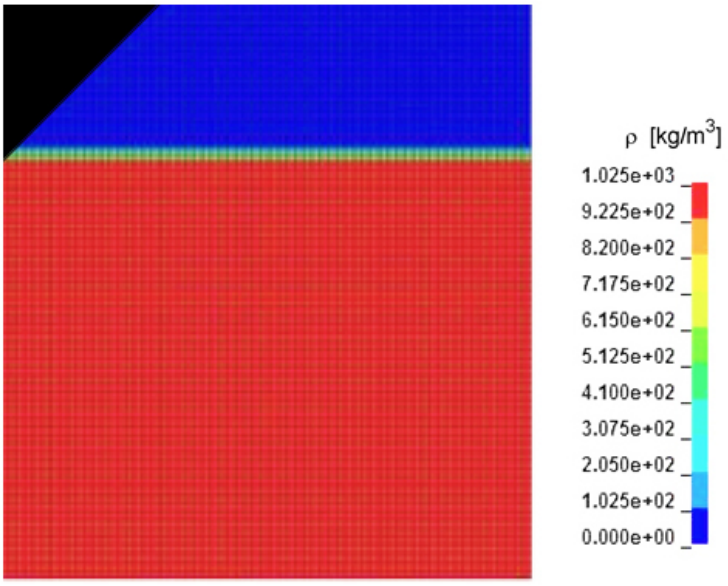

Figure 2.18: Numerical simulations grid for water entry of a rigid body, with volume of fluid density colormap.

2.3.4.2 Velocity Field Results

The PIV recordings for the two test cases under consideration herein are performed under similar conditions. In both cases, the single exposure PIV frames are illuminated sequentially by the two laser pulses corresponding to the two cavities of the laser. Both laser pulses have a width of 1 μs each, and are equally spaced in time, meaning that each laser pulse delay time (δt) is equal to the frame exposure time. This choice enables for a sequential batch analysis of the PIV recordings.

The velocity field results of the PIV measurements are compared with the numerical results from LS-Dyna for the entire time series of the measurements. In both wedge and cylinder PIV tests, a total of 1000 frames were recorded. For the wedge case, a recording frame rate of 10000 frames per second (fps) was used, and a total of 400 frames were analysed using the PIV interrogation algorithms previously described. The camera resolution in this case was of 768 x 768 pixels. To increase the particle image displacement, the two images were composed of even numbered frames and odd numbered frames, respectively (frame 1 analysed with frame 3, frame 2 with frame 4, and so on). After 40 ms of water entry, the wedge body occupies approximately half of the camera FOV, and thus PIV interrogation is stopped. However, considering that most of the dynamic behaviour of interest occurs in the first milliseconds of impact, this time sequence is sufficient for the current analysis.

For the cylinder tests, the chosen camera frame rate was of 5400 fps, and the resolution used was the maximum camera resolution of 1024 x 1024 pixels. The total number of analysed images was 432 frames, extending to 80 ms of water entry. However, the simulations results covered the first 20 ms of water entry, corresponding to the first 110 PIV frames. Since the computational time for the simulations is high, and since the important features of the phenomenon are present in the first milliseconds of impact, the 20 ms were considered sufficient for the current analysis. For more details on the technical specifications of the PIV laser and camera, the reader is refereed to Section 5.2.2.

Wedge slamming. Figure 2.19 shows the root mean squared (RMS) errors between the two velocity field results across the entire field of view, over the time series of the rigid wedge slamming experiment. The RMS errors are normalized by the range of measured PIV velocity magnitude and by the impact velocity, respectively. It should be noted that these errors are mainly caused by differences close to the solid body boundary and free surface, where PIV results are affected by reflections.

An analysis of the RMS error normalized by the range of measured veloc-

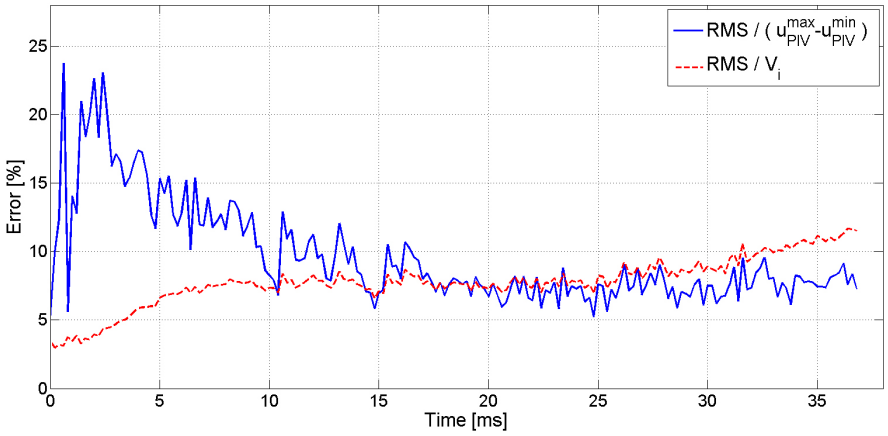

Figure 2.19: Normalized RMS errors between the PIV measured velocity field and simulation results of Vepa ([91]) for the impacting rigid wedge test case. (−) RMS error normalized by the range of PIV measured velocity magnitude. (- -) RMS error normalized by the body impact velocity.

ity values shows the importance of small velocity variations when the velocity magnitudes are also small. This effect is present in the first 5 ms of water entry, where the error reaches approximately 20 %. In this initial stage of the impact, the larger error is caused by the highly localized flow. On average, only one particle image pair is giving true velocity vector information, and therefore the PIV measurements can not capture the high local velocity gradient. On the other hand, the evolution of the RMS error normalized by the impact velocity shows that during these first milliseconds of the impact, the measured fluid displacements are very small compared to the body velocity. Another source of error between the two measured velocity fields is caused by the fact that small variations in wedge velocity are inevitable in the experimental conditions, as opposed to the constant speed imposed in the CFD model.

As mentioned previously, the PIV measurements tend to underestimate the velocity magnitude especially in the region close to the spray root and to the wall of the wedge body, where surface reflections of laser light are present, and where particle image pairs availability is limited. The measured fluid velocity fields can only be obtained in the water domain, which also implies the limitation of not being able to produce results for the water droplets in the jet and spray regions. Therefore, the cut-off of the jet implies that the results will not provide the highest

velocity magnitudes which are present in the upper parts of the jet formation.

Snapshots for two time instances 12.8 ms and 27.6 ms are presented in Figure 2.20 and Figure 2.21, respectively, illustrating the contours of horizontal and vertical velocity components measured with PIV (left column) and calculated by means of numerical simulations (right column). The measured y-component of velocity shows overall closer agreement with CFD simulation results than the x-component. This difference is attributed to the fact that gradients of the horizontal component of velocity are higher in the region of the spray root and close to the wedge wall, than gradients of the vertical component of velocity.

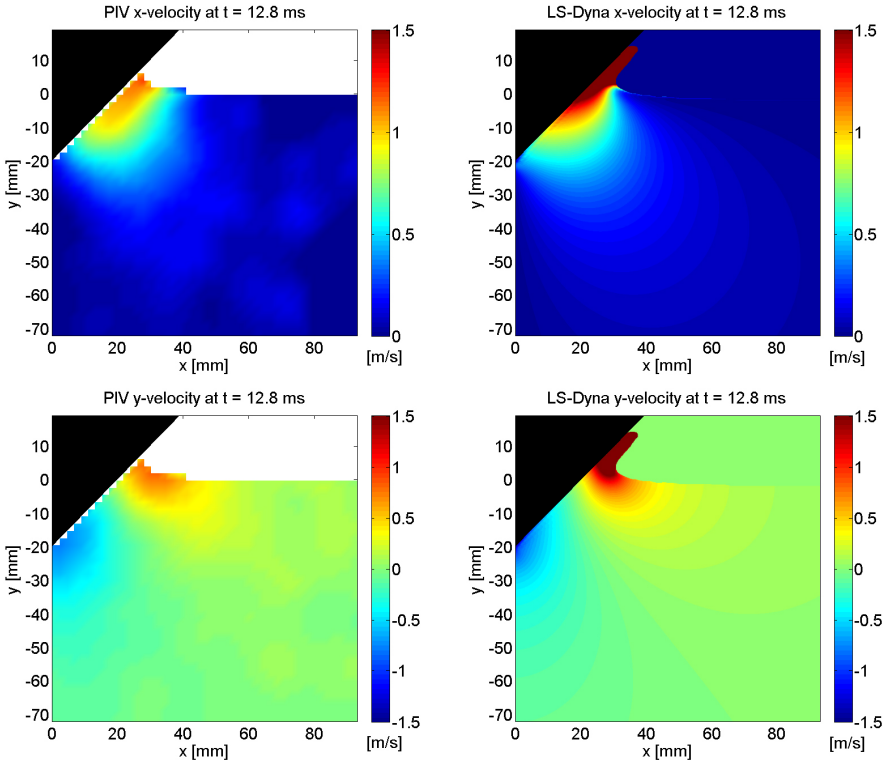

Figure 2.20: Velocity contours for the wedge body test case at time step t = 12.8 ms. Left column: PIV data. Right column: simulation results [91].

Moreover, it can be observed that for the vertical component of velocity at time t = 12.8 ms, the only region with larger error between measurements and simulations is close to the spray root, where PIV data are underestimating the magnitude. This is caused by reflections of the laser light on the wedge wall and free

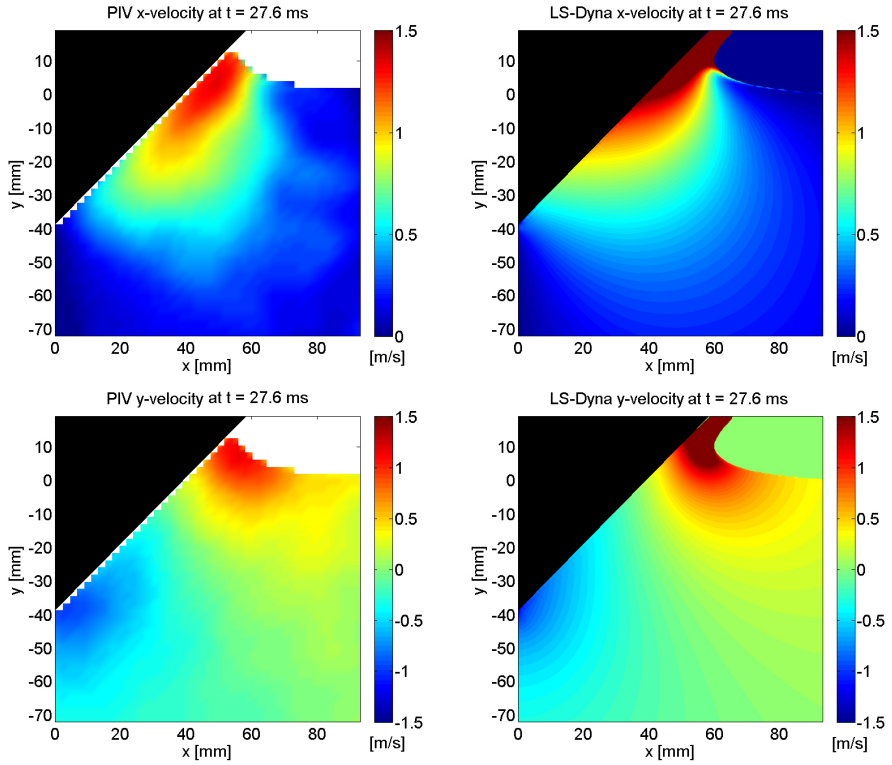

Figure 2.21: Velocity contours for the wedge body test case at time step t = 27.6 ms. Left column: PIV data. Right column: simulation results [91].

surface, and limitations to particle images pairs for correlation. Although a few particle images are present in this area, the high velocity at the spray root causes the inability to get enough image pairs in between two consecutive frames. Also, the high velocity gradients cannot be captured on such a small area, as PIV interrogation windows are still limited by the presence of enough particle image pairs.

For the later stage of water entry, at time t = 27.6 ms, the results show closer agreement, mainly because of the fact that the spray root region is wider, and more particle images are present in this high velocity gradients area. Again, close to the wall of the wedge differences are present, because of the reflections of laser light. Furthermore, in the regions of the flow further from the object, the PIV measured velocity shows a slightly higher value than the numerical simulations results. A quantitative analysis is performed in order to investigate the cause of these differences. The geometry of the impacting body and the free surface elevation profile at time t = 27.6 ms, are illustrated in Figure 2.22. Three section

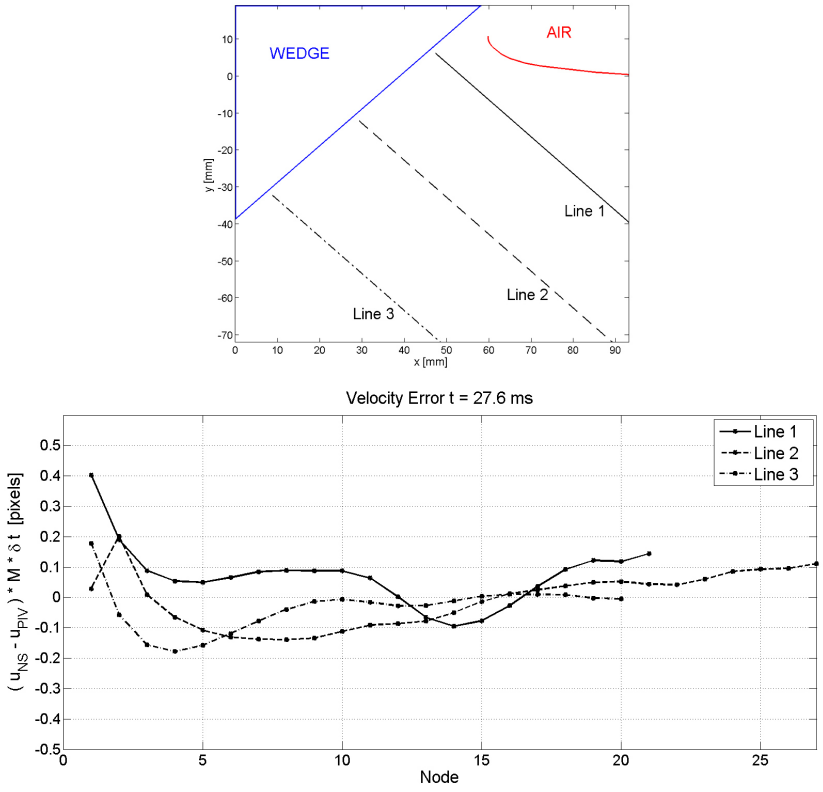

Figure 2.22: Top: PIV field of view with schematic representation of the wedge body and free surface, and three section lines at time t = 27.6 ms. Bottom: The relative error (expressed in pixels displacement) along the three section lines between PIV measured velocity magnitude and simulation results [91] at time t = 27.6 ms.

lines normal to the wedge body wall are chosen, and the values of velocity magnitude as measured from PIV and from the simulation results, are extracted along these lines. Figure 2.22 (bottom) shows the relative error between the two results, expressed in values of pixel displacement. It can be seen that the largest error is in the immediate vicinity of the wedge wall, for reasons that were explained previously. Furthermore, the highest error (approximately 0.4 pixels displacement) is found on the section line closest to the spray root of the flow. As the distance from the wall increases, the PIV measurement exhibits a fluid displacement value up to 0.2 pixels higher than in the numerical simulations. This is mainly caused by the small errors of PIV correlation analysis, but also because of the variation

of wedge velocity in the experimental conditions.

Cylinder slamming. In the cylinder slamming case, the results show the same trends as for the wedge test case. Figure 2.23 (left) shows the horizontal and the vertical components of velocity, respectively, at time t = 12 ms. The PIV results are compared with the simulations results, as illustrated in Figure 2.23 (right). One of the first features that can be observed, is the lower magnitude of the horizontal component along the normal to the cylinder wall. This is mainly caused by the lower spatial resolution of the PIV measurements (2.07 mm grid step size) compared to the fine grid used in the simulations (0.22 mm step size). Because of this difference, the velocity gradients were not captured as well in the experimental results as in the simulations. Another remark on the qualitative analysis of the velocity maps exemplified in Figure 2.23 is that the vertical component of velocity seems to be showing reasonable comparison between the two methods. However, in order to better understand the differences between the results, a quantitative analysis of the data is performed.

Three additional section lines -L1, L2 and L3 - are constructed with respect to the cylinder wall, corresponding to circles of radius R+R/10, R+R/5 and R+R/2, respectively, where R is the radius of the cylinder (45 mm). The position of the cylinder, free surface as well of the section planes are shown in Figure 2.24. It should be noted that these lines are chosen such that L1 is at a distance equal to the length of the PIV interrogation window size, L2 at twice the same distance, and so on.

In Figure 2.25, the velocity at the wall of the cylinder body and along the L2 line are illustrated. The velocities along the respective curves are calculated using a *nearest neighbour* interpolation scheme using the neighbouring fluid grid nodes. The results of fluid velocity normalized by the impact velocity (V_i), are plotted against the dimensionless body submergence parameter. From the comparison of the two results it becomes clear that the match increases considerably at a small distance from the cylinder wall. This is caused by two factors. The first is the presence of the body feature in the interrogation window that produces the fluid velocity result in the immediate vicinity of the immersed wall. This factor can introduce errors in the estimated displacement due to laser light reflections from the body surface. A second factor is the averaging nature of the interrogation procedure that uses a discrete sampling of the fluid flow along the defined interrogation windows. In order to capture the high velocity gradients that can be observed in results of the numerical simulations, the spatial resolution should be improved.

In Figure 2.26, the evolution in time of the rms errors of horizontal and vertical velocity components are plotted. Four type of rms errors of the PIV results

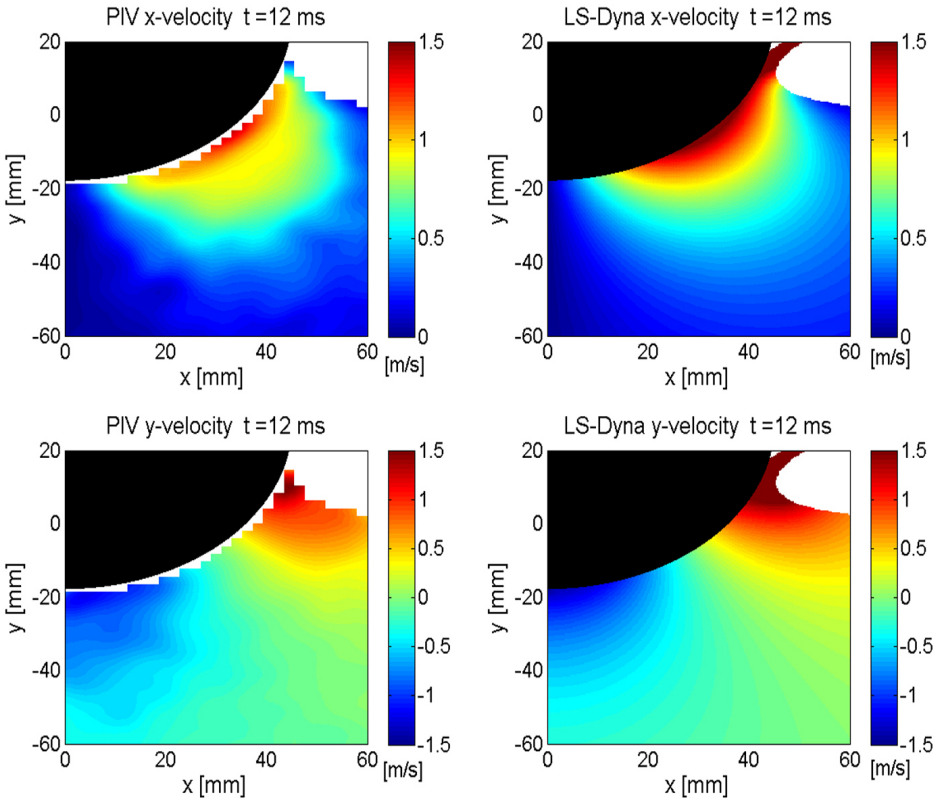

Figure 2.23: Velocity contours for the cylinder slamming test case. Left column: PIV data. Right column: simulation results [91].

with respect to the numerical results are shown. The first is the overall (full-field) error. Next, results of the rms error of velocity as extracted along the cylinder wall, along L1 and L2 are considered. It should be noted that L3 is not illustrated, as the values were very close to the full-field velocity errors. It can be seen that the highest error is present in the results along the cylinder wall, with values of up to 80 % difference for the horizontal component and 60% error for the vertical one at approximately 5 ms after impact. These values are also amplified by the presence of the jet formation along the cylinder wall, which is not measurable in the PIV experiments. These errors are seen to be decreasing as the cylinder continues its water entry, and thus the high velocity gradients present in the spray root region decrease. This phenomenon also explains why the errors along L1 are consider-

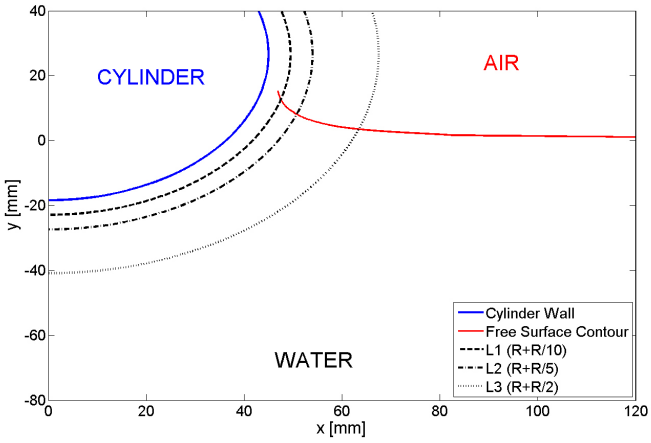

Figure 2.24: PIV field of view for rigid cylinder slamming measurements, with schematic representation of the cylinder wall and the free surface. L1, L2 and L3 correspond to section lines chosen 4.5 mm (R/10), 9 mm and 22.5 mm away from the cylinder wall, respectively.

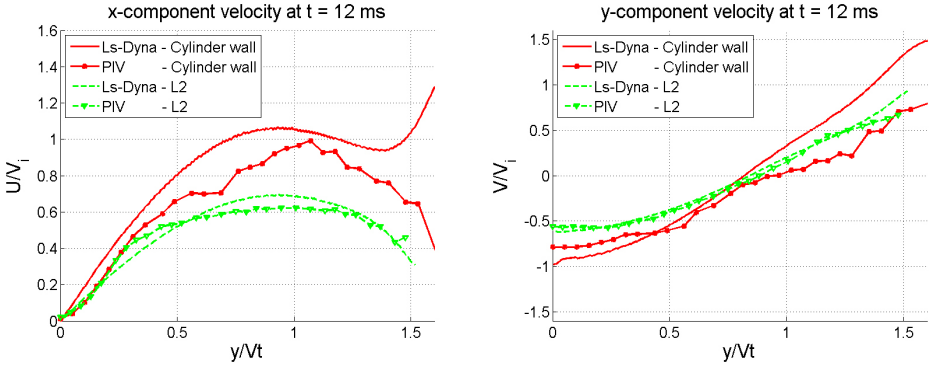

Figure 2.25: Normalized velocity ($V_i = 1.5m/s$ is the constant impact speed of the cylinder). Comparison between PIV results and simulation results in the vicinity of the cylinder wall (solid lines) and 9 mm away from the cylinder wall (L2) corresponding to approximately 2 interrogation window lengths (48 pixels).

ably lower for the entire time series, and suggests that the immediate vicinity of the body wall is an area of concern in the PIV measurements.

One other possible explanation for these errors is the presence of important

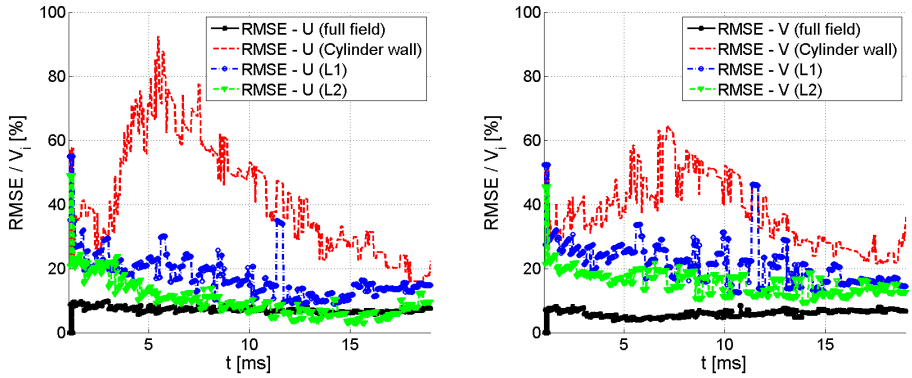

Figure 2.26: Time evolution of the RMS error between PIV measured velocity and numerical results, expressed as a percentage of the impact velocity (V_i).

three-dimensional flow components in the experiments. Since, in the case of the cylinder body, the geometry and experimental boundary conditions can influence the measured velocity to a greater extent than for the wedge body, the 3D effects need to be more thoroughly addressed. In the following, an investigation of these 3D effects of the flow is performed.

2.3.4.3 Three-Dimensional Flow Effects

One of the most stringent questions arising from the comparisons described above, is the effect that the 3D flow has on the results of the planar PIV measurement. In order to better understand if the out-of-plane component of velocity has an effect on the results obtained in the mid-plane of the cylinder, an investigation is performed using multiple-plane measurements. The light sheet illumination planes are illustrated in Figure 2.27.

Four additional planes (deemed P.1 to P.4) along the cylinder axis are chosen and PIV is performed for the same water entry velocity as in the case of the mid-plane (MP) measurement. In addition, a transversal plane is chosen along the cylinder tip (P.0). The results of measurements in this plane are shown in Figure 2.28. It should be noted that the horizontal component in the P.0 plane is corresponding to the out-of-plane fluid velocity (W) along the symmetry line in the 2D measurements performed in the middle plane of the cylinder (MP). The results suggest that this velocity component is negligible up until the end of the test tube, where the flow develops between the cylinder and the wall of the water tank. This

flow develops around the last 10 % of the cylinder length.

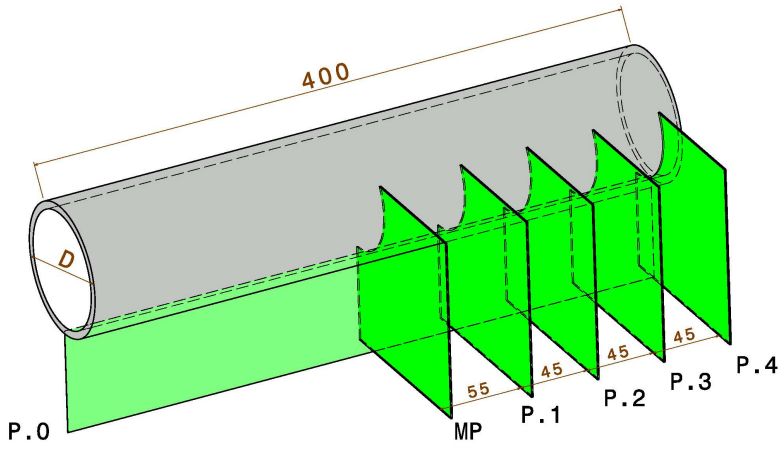

Figure 2.27: PIV Measurement planes used for investigation of 3D flow effects during water entry of a cylinder.

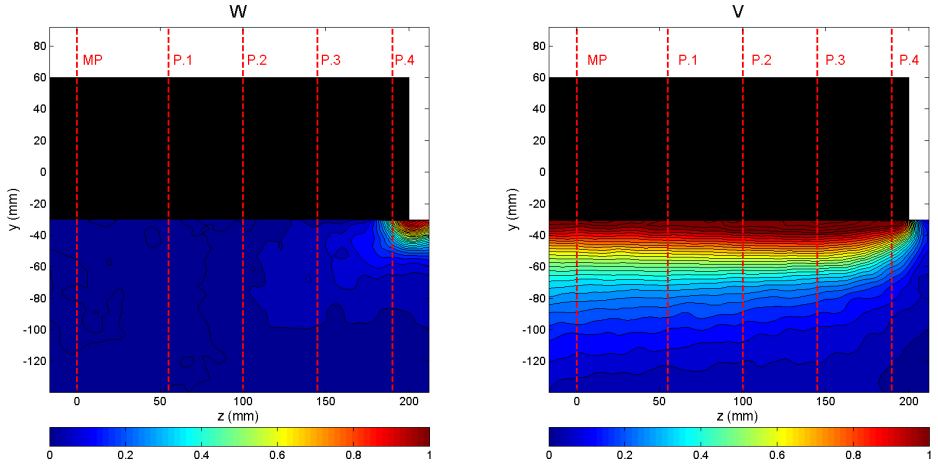

Figure 2.28: PIV measured z - component (W) and y - component (V) of velocity in plane P.0. at time t = 20 ms. The position of the additional measurement planes are indicated with dotted lines.

In Figure 2.29, the velocity magnitudes as measured in the mid plane (MP)

and in three additional planes (P.2 to P.4) are illustrated. It can be seen that the measured magnitude of velocity decreases as the distance from the mid-plane increases. This proves that 3D flow effects increase towards the end of the cylinder.

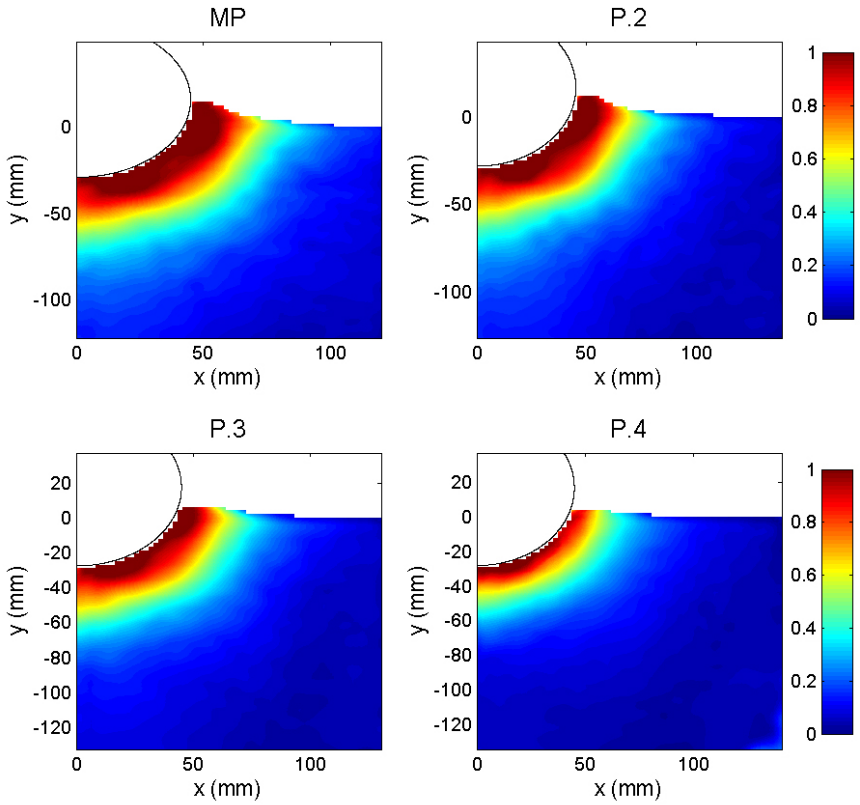

Figure 2.29: Velocity magnitude measured in four planes at time t = 20 ms.

The evolution in time of the RMS error of the measured velocity components in planes P.2, P.3 and P.4 with respect to the mid-plane measurements is shown in Figure 2.30, where the values are expressed as a percentage of the impact velocity (V_i = 1.5 m/s).

The full-field velocity error shows that the end plane P.4 exhibits the largest error (approximately 7 % for both components) at the later stage of water entry. These errors increase gradually as the cylinder penetrates the water. However, the results in plane P.2 again show that the error between the mid-plane measurements and this plane is less than 2 %.

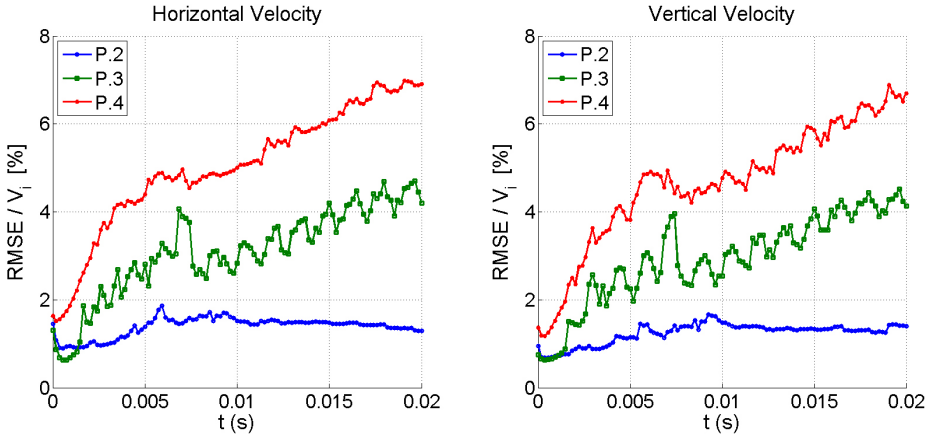

Figure 2.30: Time evolution of the RMSE of velocity (expressed as percentage of the impact velocity V_i = 1.5 m/s) measured in four planes (P1-4) compared to the mid plane measurements for both velocity components.

Based on these observations, it can be concluded that performing PIV in the mid-plane of the cylinder produces a small loss of particle pairs due to the out-of-plane component of velocity.

2.4 Conclusions

In this chapter, the general principles of the measurement technique have been introduced. The main components of a PIV system, namely the seeding particles, laser light source, imaging optics and post-processing software were described in detail. The requirements for performing PIV measurements during slamming were also identified, with attention to the necessity that these measurements should have high spatial and temporal resolutions (i.e. high magnification factors and frame rates) in order to effectively measure the impact phenomenon. It was thus concluded that a trade-off between pulse separation time and interrogation window size needs to be addressed when considering the unconventional fact for a PIV measurement, that moving features are present in the frame.

Furthermore, the choice of post-processing parameters was identified as one of the most stringent PIV requirement. In that regard, an automated adaptive masking technique was introduced, based on body position information and image intensity identification of the free surface profiles. The masking procedure showed a noticeable increase in the performance of PIV cross-correlation analysis.

The PIV processing procedure has been tested for the water entry of a wedge with deadrise angle of 45° and a cylinder with 90 mm diameter. The results were compared with results of numerical simulations performed by Vepa [91] using the LS-Dyna software and a two-dimensional model that incorporated the same boundary conditions as in the experimental set-up. The results showed good agreement, and prove that the optical measurement technique can successfully be used for water entry investigations. However, some limitations of the PIV technique were noticed, especially in the description of the spray root region of the flow. This region is situated in the vicinity of the intersection between the water surface and the body wall, and is characterized by high local gradients of the fluid velocity. These gradients can be difficult to capture because of the restricted spatial resolution of PIV and because of the laser light reflections which are present in this localized area.

Chapter 3

Adaptive Masking Using Feature Identification

In this chapter, the procedure of automated masking presented in Section 2.3.3 is adapted for deformable body water entry test cases. The study of elastic body impact requires a more flexible way of determining the body position and its shape at each time step. To achieve this goal, an algorithm for feature identification of the body is implemented in the masking process. The free surface profile detection is also improved, by using a curve fitting technique. After identification of the two features in each image, mask images are produced and used in the PIV evaluation algorithm. Due to the accuracy of body shape identification conferred by adaptive feature identification, and the tracking of shape evolution in time, loads on deformable bodies during recorded water entry can be recovered.

3.1 Introduction

The idea behind using digital image techniques to study the body deformation is derived from classical two-dimensional digital image correlation (2D-DIC). Since its development as a measurement technique for body shape and deformation in 1982, DIC has been applied in various areas of research ranging from studies of the material deformation of metals [83], plastics or even paper [79] , to scanning tunnelling microscopy [5], as well as fluid particle motion (particle image velocimetry) [59]. A comprehensive study on the various aspects concerning the theoretical concepts as well as the applications of DIC, can be found in the book of Sutton and Orteu [80]. It is to be noted that over the years, together with considerable improvements in the field of optical imaging as well as in the numerical algorithms developments, the accuracy of these techniques was proved to be exceptionally high (e.g. 1 % pixel resolution displacement accuracy). Considering the non-intrusive nature and the high accuracy of digitized imaging techniques, the method proposed in this chapter, makes use of these aspects to study the water entry problem of a deformable body. Deformation of a body contour can be followed through the sequence of digital image recordings taken during the water entry of a bluff elastic body.

3.2 Adaptive Feature Identification

During the water entry of elastic bodies, snapshots of the object and flow around it are recorded using a high-speed camera and a high-powered laser illumination of the region of interest (ROI). The high-speed nature of the recordings as well as the high resolution used, makes it possible to follow the cylinder for the first milliseconds of water penetration. A simple and robust algorithm is developed in order to effectively detect the body position and shape at every time step in an automated way. The operating principle of this algorithm is based on a minimum amount of information provided before hand, in order to effectively follow the body motion through the water. This information is regarding the identification of the two main features to be tracked in every recorded image: the body contour and the free surface profile.

Figure 3.1 shows the steps of this feature identification and tracking procedure, which are incorporated in a Matlab implementation described in the following.

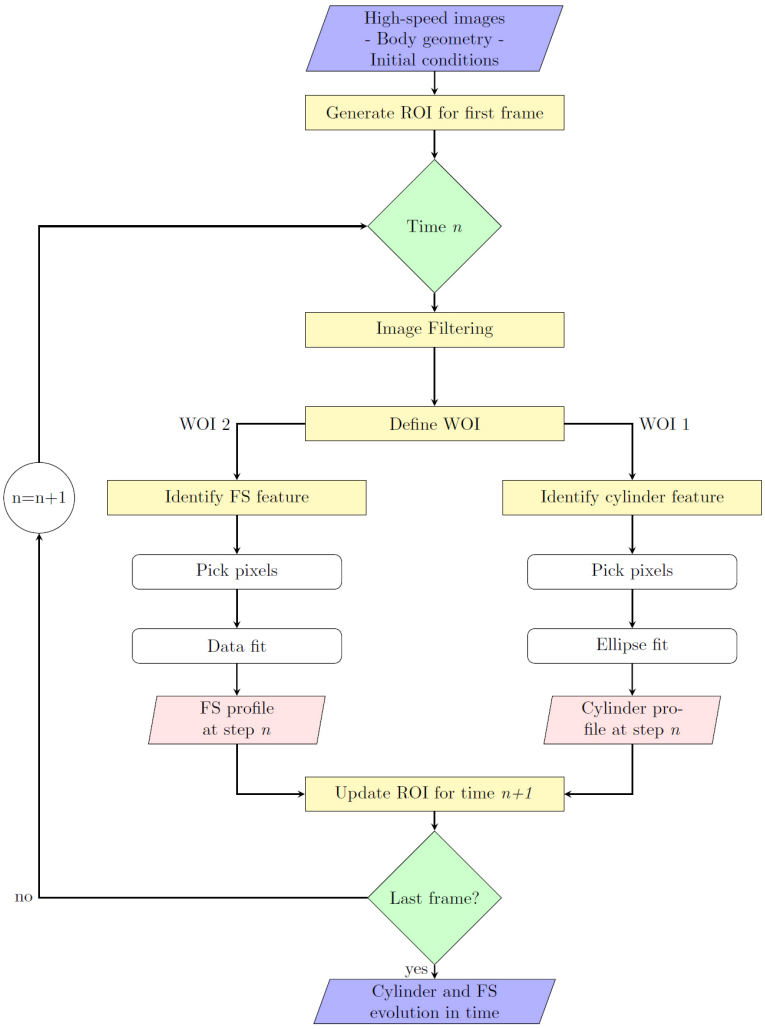

Figure 3.1: Feature tracking flow-chart.

3.2.1 Proposed methodology

Inputs. The necessary inputs of the proposed procedure, are the apriori known body shape and entry velocity, the camera magnification factor, the laser pulse delay time and the assumption that the vertical symmetry line of the cylinder is within the field of view (FOV). It should be noted that the location of the vertical

symmetry line of the cylinder, as well as the undisturbed free surface level, are identified before the tests are performed, using calibration target images. These inputs, together with the initial choice of image filters to be applied to the recorded images, are the only user required interactions with the algorithm, the rest of the procedure being fully automated.

Generate ROI for the first frame. Firstly, a ROI is generated, based on the first picture of the series, captured before cylinder penetration of the free surface, as the contour of the free surface will be the predominant feature in the frame. Therefore, the ROI will be concentrated around this main feature, and will extend above and below with a certain amount of pixels (as can be seen in Figure 3.2), determined based on the cylinder entry velocity and magnification factor, as follows:

$$dy_{ROI} = MV_{entry}\delta t \tag{3.1}$$

where: dy_{ROI} is the margin above and below the undisturbed free surface, M is the magnification factor, V_{entry} is the cylinder entry speed and δt is the laser pulse separation time. After this initial ROI is defined, all the frames of the recorded sequence are analysed as described below.

Image filtering. For each frame, the first step is to filter the image in order to reduce undesirable information for the feature identification procedure (e.g. contamination particles in the water that reflect laser light) and also noise that can be present in the picture due to excessive reflection from the cylinder body or the free surface. The following filters are applied:

- An extended maxima transform filter is applied first to the image. This is a local filter, based on an 8-neighbours scheme, that removes less significant maxima in the picture which are caused by background noise, in two stages. Firstly, a H-maxima transform filter will suppress the maxima values in the image which are less than a certain threshold value (H). This value is chosen by the user before automated processing is begun, in such a way that the white noise is reduced to its lowest value without losing valid information. Secondly, a regional maxima of the H-maxima transform is applied. The regional maxima are connected pixels with the same value of grayscale intensity, surrounded by pixels with lower intensity values. After application of this filter, a binary image is produced, that contains the significant features (wetted body surface and free surface profile) in the frame. The results of this filter are exemplified in Figure 3.3 for one typical image taken during the water entry of a circular cylinder. Figure 3.3 (top) shows

the number of white pixels in the resulting binary image, for values of the threshold H ranging from 1 to 255. It can be seen that lower values of the threshold, between 8 and 120, result in a filtered image with the features preserved and reduced background noise (*image A*). Furthermore, values of H between 120 and 200 also produce good results (*image B*), although excessive laser light reflections are not completely removed. When the batch of images analysed contains frames with localized high reflections, these will be preserved in the resulting filtered image which might cause a thicker feature profile boundary. For values of H higher than 200, the suppressed maxima values of the raw image is excessive, and thus the resulting filtered image will be unusable. It should be noted that for values of H lower than 8, background noise and out-of-focus particle images will be carried onto the filtered image, thus a slight increase in the white pixels count is observed for this low threshold values. Therefore, values of H were typically chosen to be in the range 10 to 120 depending on the illumination conditions of the test run (for batch images with higher contrast and noise, lower threshold values were considered). It should also be noted that the threshold was applied independently for the two images corresponding to the two cavities of a double-pulsed laser, thus making it effective in less than optimal operating conditions, when the two frames are not evenly illuminated.

- Next, a series of local filters are applied on the resulting binary image, in order to improve the SNR. A cleaning filter is applied in order to remove the seeding particle images from within the ROI, operating on an isolated unit value of intensity, surrounded by zero values. Also, in contrast to the first filter, a second one is used for connecting neighbouring pixels if the center pixel has more than 2 non-zero neighbours. This filter is useful for accounting for small inconsistencies in the feature contour caused by slight variations in intensity.

- Lastly, an optional erosion filter is available in the implementation, and this reduces the size of the features when excessive reflection is occurring.

The resulting image after applying this set of filters, can be seen in Figure 3.2 (middle), where the green rectangle marks the ROI.

Define WOI. After applying the image filters with the aforementioned ROI, a new set of elements is automatically generated, namely the windows of interest (WOI), which can be seen in Figure 3.2 (right). There are two windows of interest, which are defined in such a way that the feature tracking from frame to frame can be achieved. The two windows are adaptive, and change size with every frame,

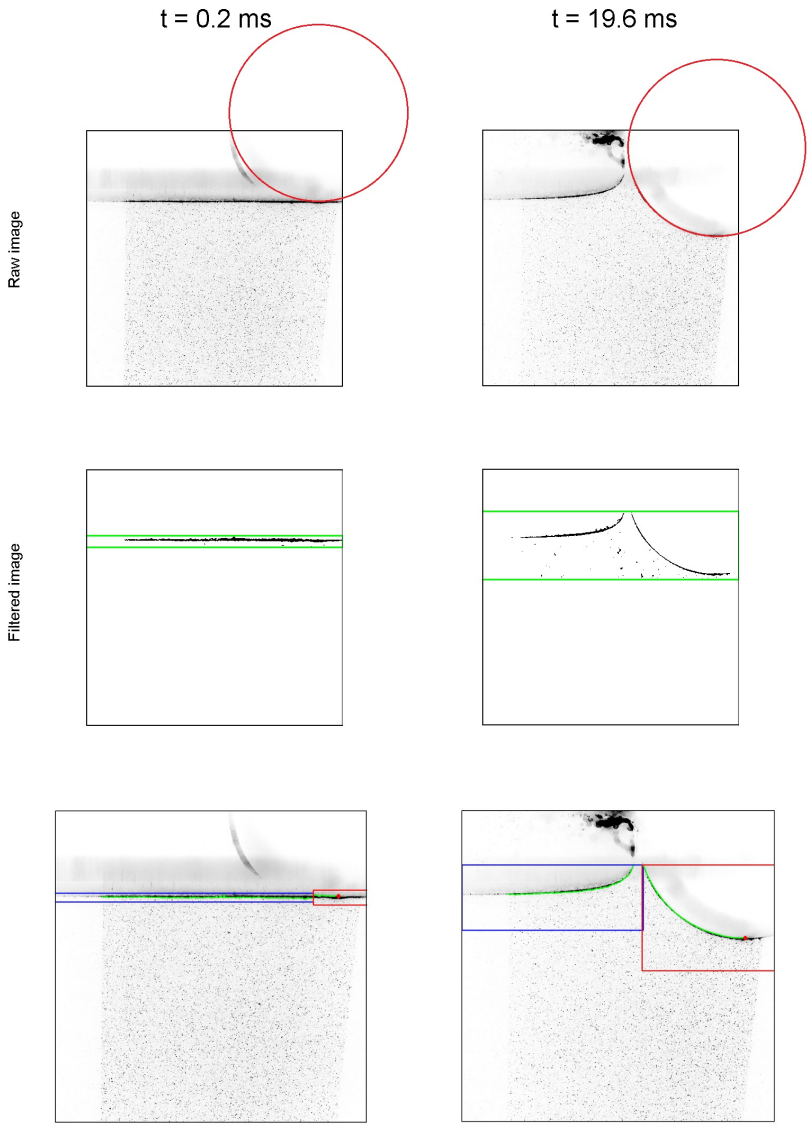

Figure 3.2: Image filtering at two time instances - 0.2 ms (left column) and 19.6 ms (right column). Top: raw images (inverted grey levels) with cylinder wall schematically shown (in red); Middle: filtered image with ROI; Bottom: raw images (inverted grey levels), WOI and feature identification contours.

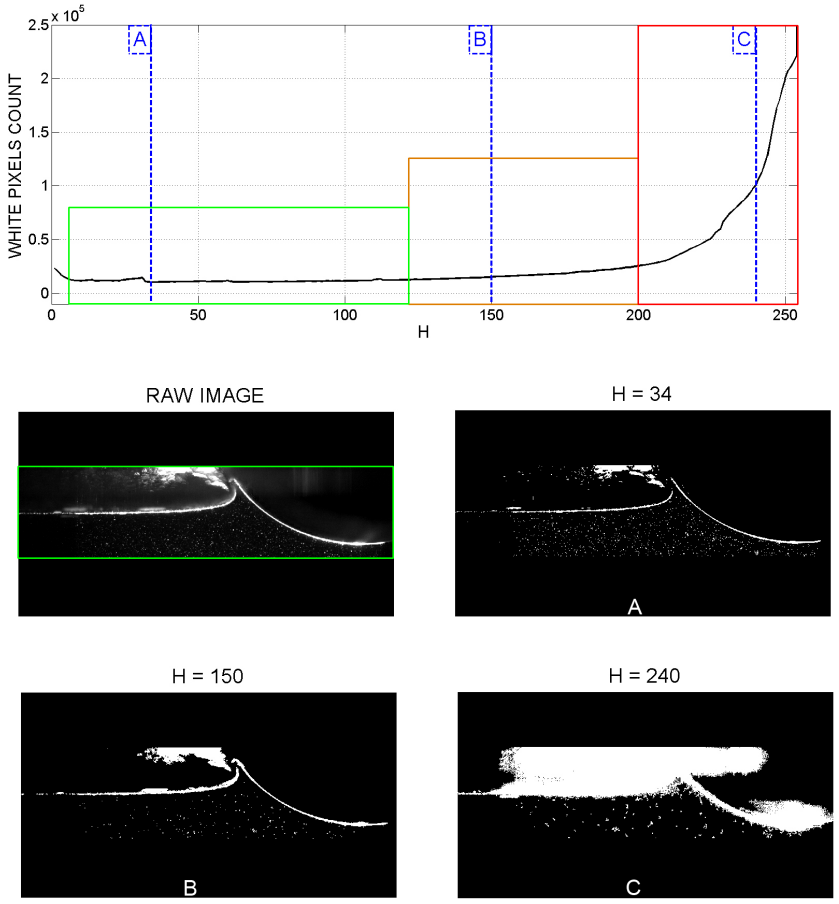

Figure 3.3: Extended maxima transform. Top: White pixels count on binary image resulting from application of the extended maxima transform; Middle: Zoom of the raw image around the cylinder and free surface (left) and filtered image for H = 32 (right); Bottom: Filtered image for H = 150 (left) and for H = 240 (right).

thus providing the initial conditions for the generation of the filtered image at the next step. The two WOI are defined as soon as the cylinder makes contact with the water surface, and can be identified in the pictures. The body contour is identified based on the body geometry and its known dimensions, consequently, the free surface is identified based on its width and height. The two WOI will serve as a

search area for the contour of each of the two features, for every frame, and results of the body movement will update the location of the ROI for the next frame of the series.

The next steps in the algorithm consist of the main procedures of feature identification and tracking based on an update of the ROI for preparation of the next frame of the series. These steps will be described in the following sections.

3.2.2 Feature identification

With the aforementioned parameters of the feature identification method in place, the identification procedure is automatically done in three steps:

- Firstly, the contour of the feature is identified as being defined by pixels of local maximum intensity in the filtered image.
- Secondly, the pixels are labelled in two categories, depending on the identified feature (body / free surface). For the free surface (FS) contour, the pixels closest to the water domain (bottom half of pixels of the contour) are marked and registered as valid. For the body contour, the pixels closest to the wall are chosen. In this way, the feature identification is less biased to errors caused by unusual reflections from the body as well as from the free surface, reflections that can occur when dealing with seeding particle clustering at the free surface level or because of scratches on the object or shape irregularities.
- Lastly, having chosen the pixels which mark the edge of the feature contour, a data fit is exerted on these points. For the example of a cylinder contour, an ellipse fit is done on the marked points. In the case of the free surface elevation profile, a least-squares data fit is applied to the raw data. In Figure 3.4, the feature contours (free surface profile and cylinder contour) can be identified.

3.2.2.1 Body Feature

The water entry studied herein is purely vertical, and thus both fluid flow as well as structural response is symmetric along the vertical axis. It was observed that, because of this axisymmetric behaviour of the flow, and because of the distributed nature of the load on the cylinder, the deformation of the body is uniformly distributed, and that an ellipse fit is an appropriate approximation of the deformed

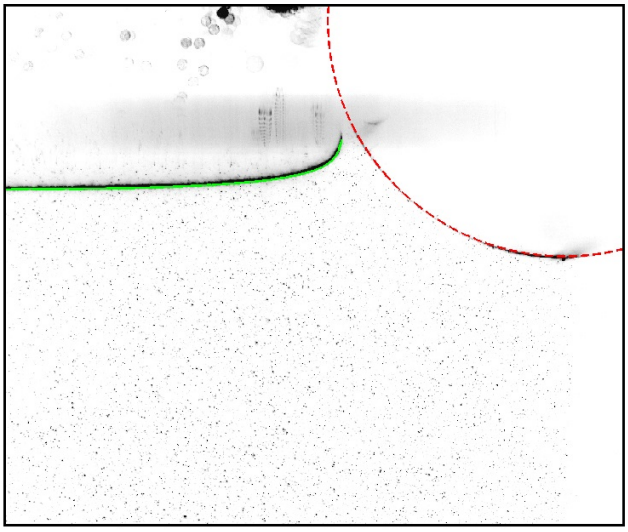

Figure 3.4: Feature identification of body and free surface features on the raw image (inverted grayscale) of the water entry of a deformable cylinder.

shape. Furthermore, the possibility of perspective projection errors was also considered. Such errors could influence the results by determining a cylinder shape to be projected on the image sensor as an ellipse. However, this possibility was eliminated after analysing the water entry of rigid cylinders, the shape of which could be well approximated by a circle on each frame, throughout the recorded sequence. Moreover, the analysis of measurements taken in additional 2D planes along the cylinder axis showed that the same ellipse fit used in the middle plane recordings, adequately captured the submerged body contour.

In the early stage of the water entry, the immersed (wetted) part of the body is restricted to a small area compared to the cylinder radius. The cylinder bottom point position is recovered from the first moment of impact, and the top point position is known from position encoder information, which means that the vertical axis of the cylinder is prescribed at the first moment of impact. Furthermore, as the cylinder enters the water, the cylinder wall reflections are used for identification of the shape and position of the body as described above. Figure 3.5 (left) shows the contour determined by the feature identification procedure for the body feature, together with an ellipse fit approximation. This approximation is based on the use of the aforementioned pixel coordinates of the immersed body wall which

are transformed into physical coordinates using the magnification factor information and the vertical position of the free surface. Using these coordinates together with the position of the cylinder top point (as recorded by the position encoder), the ellipse fit is calculated. The ellipse fit is applied by also taking into account a restriction of horizontal displacements of the vertical axis. The assumption is valid in the conditions mentioned previously of symmetry along the vertical axis, but does not apply when, for example, oblique water entry is considered. In order to improve accuracy of the ellipse fit, the cylinder contour points are mirrored along the vertical axis. Figure 3.5 shows the ellipse fit and the corresponding feature points (in red), the mirrored extension points (blue), and the cylinder top position coordinate from the position encoder measurement.

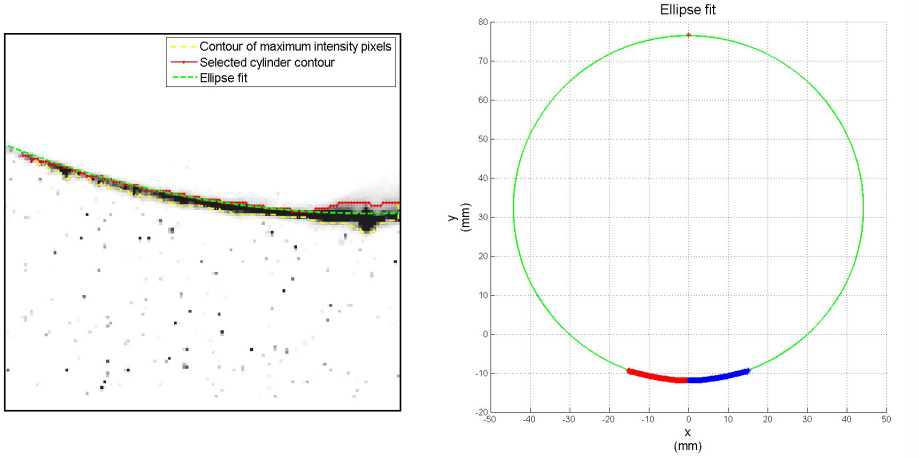

Figure 3.5: Left: Feature identification with pixel points of the body contour and the ellipse fit; Right: The ellipse fit procedure is illustrated, with the pixel points (red) of the cylinder contour and the top point from position encoder measurements.

3.2.2.2 Free Surface Feature

The fit on the free surface profile becomes a necessity when noise levels increase due to reflected laser light. In less-than-optimal experimental conditions, the high energy of the laser light can cause reflections from the smallest sized contamination particle. This can introduce large errors in estimating free surface profiles if pixel-wise approximation of its shape is performed. Due to the complex

shape of the free surface, simple estimators are found to be insufficient in capturing the local slope in the vicinity of the spray root formations. Therefore, a curve fitting approach is applied, as illustrated in Figure 3.6. The fitting is applied using a rational polynomial approximation of the pixel coordinates. The technique, which is widely used in modal analysis to model frequency response functions [34, 33], was chosen in this case to approximate the shape of the free surface. The procedure eliminates unwanted variations in the pixel-wise contour, which can be caused by localized excessive laser reflection. At the same time, the data fit needs to preserve the high slope of the free surface elevation curve in the vicinity of the spray root of the flow.

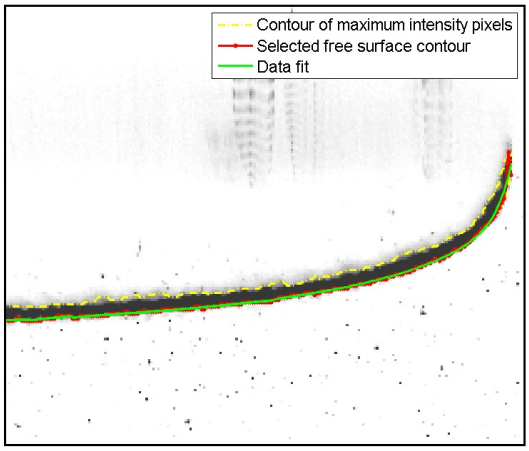

Figure 3.6: Raw PIV image (inverted grayscale) with the free surface contour and data fit.

In order to chose the best order of the polynomial approximation, a typical frame taken during water entry of a deformable cylinder is analysed. Figure 3.7 shows the selected free surface pixel coordinates and the approximations using polynomial orders from 1 to 4. It can be observed that the 3^{rd} order polynomial is a balance between smoothing out unwanted variations (or high local reflections of widths up to 3-4 pixels), and preserving the free surface feature shape. This finding was tested by analysing the RMS error between the raw pixel data of the feature and the data fit using polynomials with orders ranging from 1 to 10 as illustrated in Figure 3.7 (bottom). The analysis of the single frame results are

consistent with mean RMS values taken over a batch of 70 frames. It is shown that the error decreases below 1 pixel difference for the third order polynomial for both the single frame and for the batch analysis. This value of 1 pixels RMS error can be considered a threshold for the measure of the accuracy of the data fit approximation with respect to achieving the goals mentioned above.

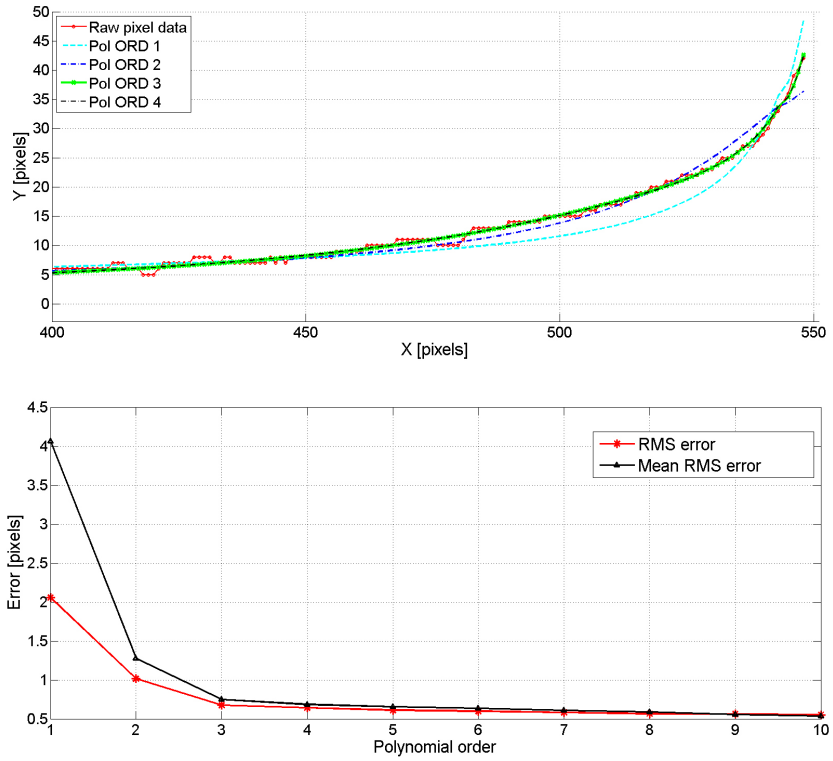

Figure 3.7: Top: Free surface profile (raw pixel data) and data fit with polynomial orders from 1 to 4. Bottom: RMS error between raw data and data fit (different order polynomial approximations) for one frame and RMS error averaged over 70 frames.

3.2.3 Tracking the feature

The feature identification technique thus provides information for every frame recorded. The steps described above are done automatically for each recorded frame, and an **update of the ROI** for the next time step $(n + 1)$ is done based on the information recovered from the previous time step (n).

Having identified the bottom point of the cylinder on the raw images, and also tracking the evolution of this point (marked in Figure 3.2) in time, the cylinder displacement can be recovered for the recorded image sequence, if the position of the cylinder top point is also known. In this current work, the experimental set-up included a position encoder, located above the cylinder, which provided information on the cylinder top position at each time step. In Figure 3.8, the evolution of these two points in time is shown for a deformable PVC cylinder with radius R=45 mm.

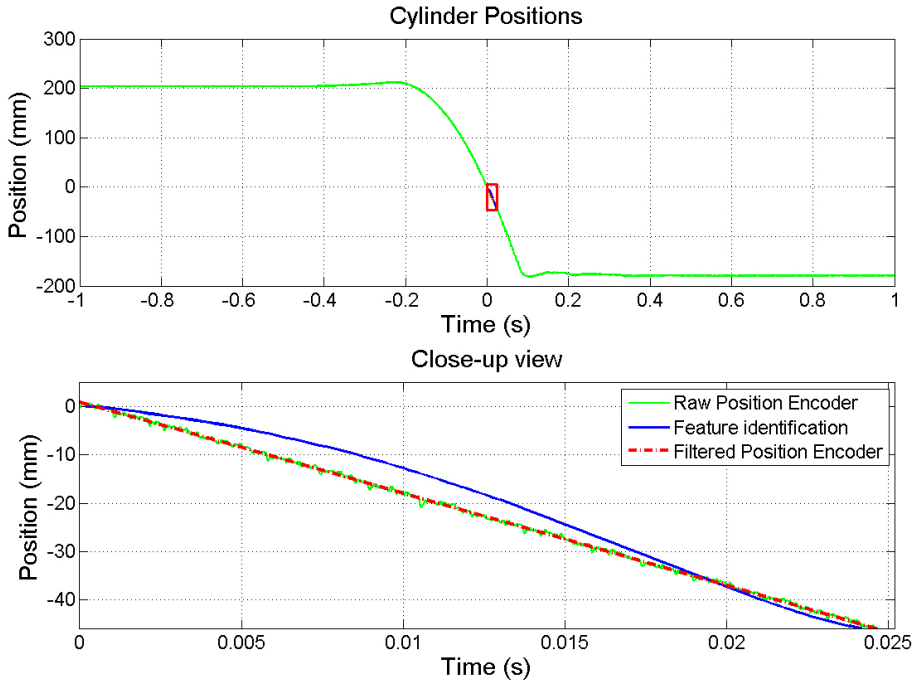

Figure 3.8: Top: Position encoder measurement during one slamming experiment. Bottom: Close-up view of the first 25 ms, with feature tracking position of the deformable cylinder bottom point (−) and position encoder measurement of deformable cylinder top point (-·). The difference between the position of the cylinder bottom point (−) and the position of the cylinder top point (-·) is caused by the deformation of the cylinder.

Figure 3.8 (top) shows the entire recording of the position encoder during the cylinder drop test. The sequence illustrated in Figure 3.8 (bottom) is corresponding to the first 25 ms of water entry of the cylinder, during which time the feature identification is performed. It should be noted that the difference between the position of the cylinder bottom point and the position of the cylinder top point (from the position encoder) is caused by the deformation of the cylinder.

3.3 Water Entry of Deformable Bodies

The procedure described in the previous section is applied for the recordings of the water entry of two deformable PVC cylinders with diameters of 90 *mm* and wall thickness 1.5 *mm* (Cylinder 1) and 3.15 *mm* (Cylinder 2), respectively. The two cylinders are each mounted on a vertical slamming set-up (*Experimental set-up B.*) consisting of a 1 m^3 water tank and an impactor that is guided on rigid rails fixed to the walls of the room. The cylinders are clamped using a line contact along the cylinder top. For a detailed presentation of the vertical slamming experimental set-up and of the cylinder material properties and geometry, the reader is referred to Section 5.2. The cylinders are dropped from 4 different drop heights - 54 *mm*, 204 *mm*, 459 *mm* and 816 *mm* as measured from the undisturbed water surface - corresponding to theoretical entry velocities of 1 m/s, 2 m/s, 3 m/s and 4 m/s. The total mass of the impactor made it possible for the velocity to remain approximately constant for the water entry time considered herein, however, due to frictional forces in the rails, the true impact velocities differed from the theoretical values. Figure 3.9 shows the velocities of the cylinder bottom point and of the cylinder top point respectively, for cylinder 1 in the case of a 204 *mm* drop height test. It can be observed that the velocity of the cylinder top point slightly increases throughout the recorded sequence of water entry. However, the increase in velocity of the top point (caused by the high mass of the impactor) is small compared to the velocity variations of the bottom point. It should be noted that the velocity of the cylinder bottom point is recovered from the feature identification and tracking procedure after the initial impact and subsequent deceleration occurs (in the first 0.2 ms of water entry). Before the impact of the cylinder with the water surface, the velocity of its bottom point is assumed equal to the velocity of its top point.

The Young's modulus for the two test tubes is determined experimentally by Van Nuffel [87], who performed compressive tests and finite element analysis of the test tubes. The material properties of the cylinders, as well as the values of the entry speeds used in the experiments are presented in Table 3.1.

The cylinders were instrumented with strain gauges at the 90° mid plane

Cylinder no.	1	2
Material	PVC	PVC
Radius [mm]	44.95	45
Length [mm]	350	350
Average wall thickness [mm]	1.5	3.15
Mass [kg]	0.304	0.42
E [Gpa]	3	2.7
Entry Velocity [m/s]	0.96	0.93
	1.83	1.81
	2.71	2.72
	3.66	3.67

Table 3.1: Cylinder Properties

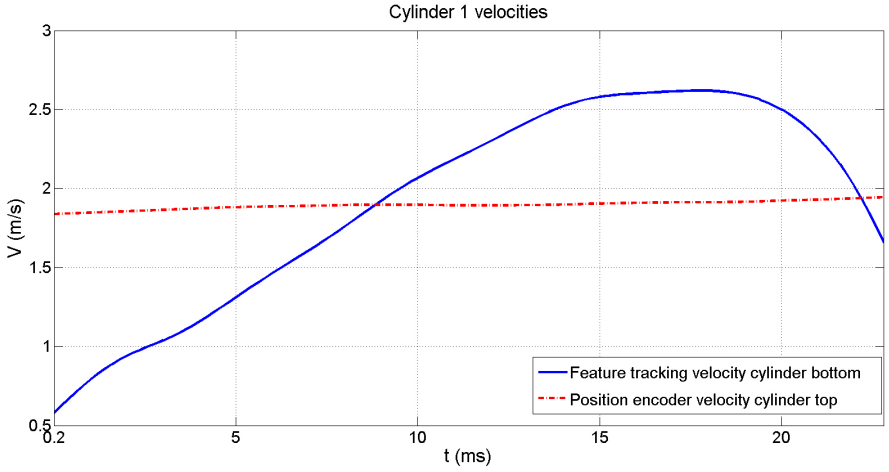

Figure 3.9: Velocities of the cylinder 1 - bottom point from feature tracking (–) and top point recovered from the position encoder measurement (-·) in the case of a 1.83 m/s drop test. The velocity of the bottom point is illustrated after the initial impact of the cylinder with the water surface (after the first 0.2 ms of water entry).

mark, on the outer surface of the cylinder, and three force sensors were included in the supporting structure, thus both strain and force were measured during the experiments as described in the work of Van Nuffel [89]. A position encoder was also included in the set-up, on the rigid impactor, on top of the cylinder. The position recorded at 100kHz was used as the position information of the top point on the cylinder, which could not be recovered on the high-speed images. High speed recordings (at 5kHz) of the water entry were performed with the use of a Photron Fastcam SA1.1, and the light source used was a Quantronix DarwinDuo Nd:YLF double-pulsed laser. The technical specifications of these components is detailed in Section 5.2.2. The magnification factor used in the experiments was 7.8 pix/mm, leading to an optical measurement uncertainty of 0.128 mm.

3.3.1 Displacements

Following the procedure presented in the previous section, the body position and free surface profiles are recovered for each time step. One example of these profiles is shown in Figure 3.10, for a water penetration depth of $Y/R = 0.14$. The deformation of cylinder 1 is obviously greater than that of cylinder 2 from the early stage of impact and throughout the time of maximum stress occurrence. The scale of this time is corresponding to the highest wet natural period of the structure, as identified in [25]. The flow physics are also changed due to this phenomenon, as can be seen in the free surface elevation profiles in Figure 3.10. Although the jet is cut-off due to the limited optical access in this region, it can be seen that the formation of the spray root differs substantially, and the water pile-up shows differences comparable to the radial deflection of the shell.

The cylinder deflections are recovered for each frame of the water entry recordings, as the difference between the position of the cylinder top point (measured by the position encoder) and the position of the cylinder bottom point (feature identification results).

The total deflection for each drop test is plotted in Figure 3.11 for cylinder 1 and in Figure 3.12 for cylinder 2. The measured displacement for cylinder 2 impacting the water at 0.93 m/s is not plotted, due to the fact that in this case, the displacements are too small compared to the uncertainty of the optical measurements. It can be seen that for cylinder 1, one oscillation period is about 40 ms, whilst for cylinder 2, the oscillation period is of 14 ms. Since the maximum strain occurs in the first half of the oscillation period, this time sequence is of interest for the current study and the focus will be on results of the first 20 ms of water entry for cylinder 1, and of the first 7 ms for cylinder 2.

For cylinder 1, the displacements for the first two entry speeds cover the first

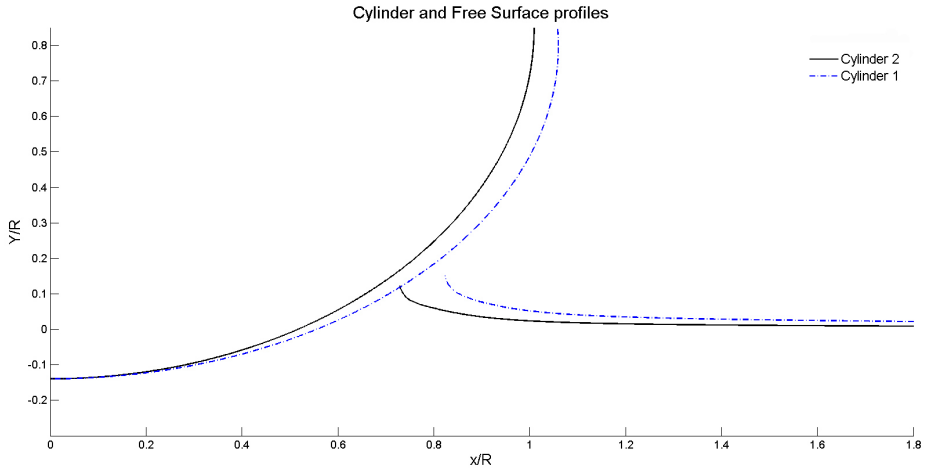

Figure 3.10: Snapshot of free surface elevation profiles and cylinder deformation for the two cylinders - drop height 204 mm (continuous line is corresponding to cylinder 2 profile and discontinuous line is corresponding to cylinder 1 profile).

half of the oscillation period, whilst for the higher entry speeds, the tracking of the body is not possible for the entire half of the period, because of the limited FOV. Due to the increased velocity, the cylinder could no longer be tracked after 17 ms for the 2.71 m/s entry speed, and after 11.5 ms for the 3.66 m/s entry speed, respectively. However, it is to be noted that the maximum displacements are recorded for each case, and range from 2.39 mm for the lowest drop height, to 18.77 mm for the highest entry velocity. The deflection of cylinder 2 is much lower than that of cylinder 1. Nevertheless, the results show the same trend as for the first test tube, with the oscillation period reduced to 7 ms. The maximum deflection recorded for cylinder 2 is 3.09 mm for the case of a 3.66 m/s entry velocity, whilst its lowest deflection, measured at 1.81 m/s entry speed, is 1.014 mm.

3.3.2 Strains

The hoop strain on the outer surface of the cylinder at the 90° mid plane mark, was calculated using the results of the shell deflection, and a polynomial approximation of the conversion from vertical displacement to hoop strain. These con-

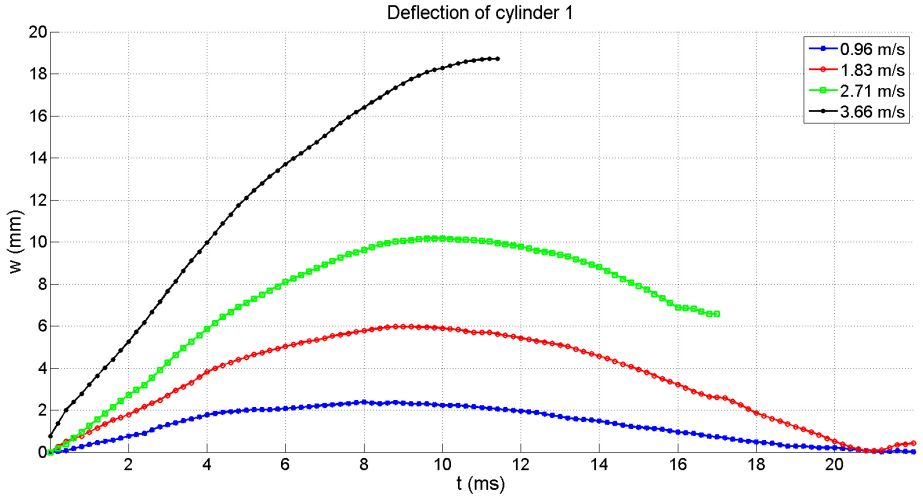

Figure 3.11: Feature tracking measured deflection of cylinder 1 at four entry speeds.

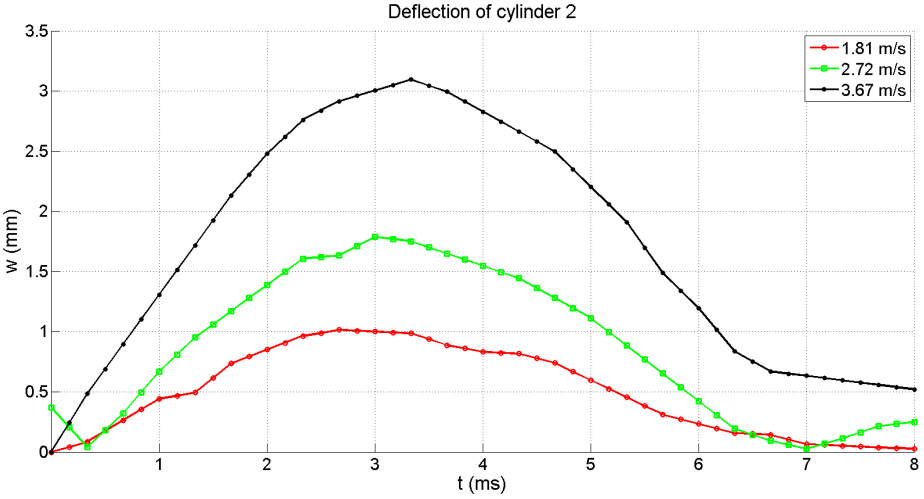

Figure 3.12: Feature tracking measured deflection of cylinder 2 at three entry speeds.

version factors were obtained by Van Nuffel [87], using static compressive tests and Finite Element simulations of the test tubes under compressive loading conditions. The numerical simulations were performed using the software package ABAQUS, and two line contact loads were applied at the cylinder top and bottom, respectively, to simulate compressive conditions. The calculations were ran for both cylinders until displacements larger than those recorded in the experiments were reached. Thus, for both cylinder 1 and cylinder 2, the relation is valid until a maximum deflection of 50 mm. For more details on the procedure of estimating the conversion factors, the reader is referred to the PhD work of Van Nuffel [87]. The polynomial approximations are given in equation 3.2 for cylinder 1 and in equation 3.3 for cylinder 2. The deflection is denoted with w_1 for cylinder 1, and with w_2 for cylinder 2, while the respective circumferential ('hoop') strains are denoted by ϵ_1 and ϵ_2, and are expressed in microstrain.

$$\epsilon_1 = -8\cdot10^{-6}w_1^6+9.7\cdot10^{-4}w_1^5-3.9\cdot10^{-2}w_1^4+6.8\cdot10^{-1}w_1^3-5.2w_1^2+472w_1; \quad (3.2)$$

$$\epsilon_2 = -1.6\cdot10^{-5}w_2^6+1.9\cdot10^{-3}w_2^5-7.8\cdot10^{-2}w_2^4+1.36w_2^3-9.15w_2^2+97.6w_2; \quad (3.3)$$

The conversion factors were applied to the deflection data as recorded from the high-speed images during impact. The results of the strain estimation from vertical deflection and the strain measured by the strain gauge instrumentation are presented in Figure 3.13 for cylinder 1, and in Figure 3.14 for cylinder 2. The raw strain data was corrected to account for any misalignment that might have occurred in the mounting of the strain gauge on the cylinder. Thus, the values measured and those estimated are both expressed for strain at the 90° angle on the cylinder middle plane.

It can be seen from Figure 3.13 that the maximum strain values match fairly well for cylinder 1. For every entry velocity studied, the peak strain calculated from measured deflection underpredicts the maximum strain measured with the strain gauges. The largest difference occurs in the case of the 2.71 m/s impact speed test case, where the measured strain is 15.5 % larger than the strain calculated from deflection, whilst in the case of the largest drop height used, the relative error is of only 2%. However, the strain time histories show a good overall agreement on the location of the occurring maximum loads. The same trends can be observed for cylinder 2 in Figure 3.14. The maximum strain as recorded by the strain gauges exhibit the same range of differences from the values determined from the measured deflection, with a relative error ranging between 9% for the highest impact speed test case to 18% for the 2.72 m/s case.

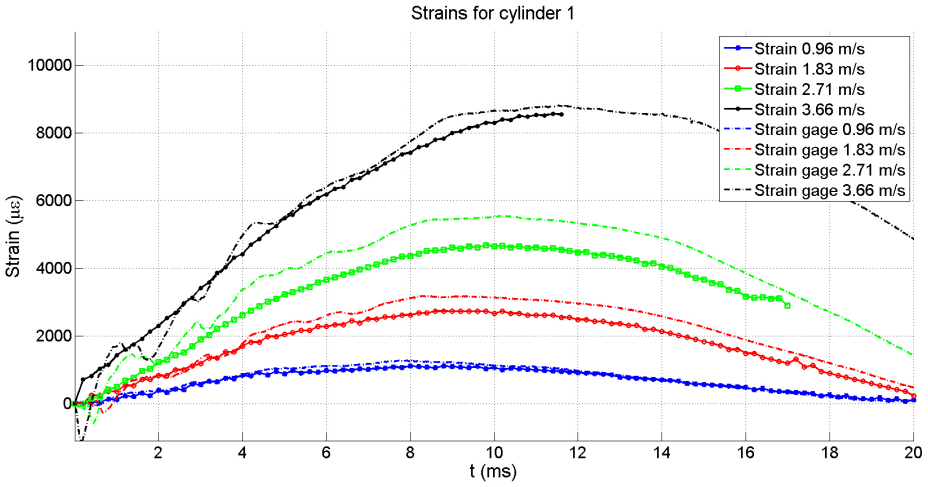

Figure 3.13: Strains on cylinder 1 at four entry speeds. Solid lines correspond to the strains calculated from feature identification results.

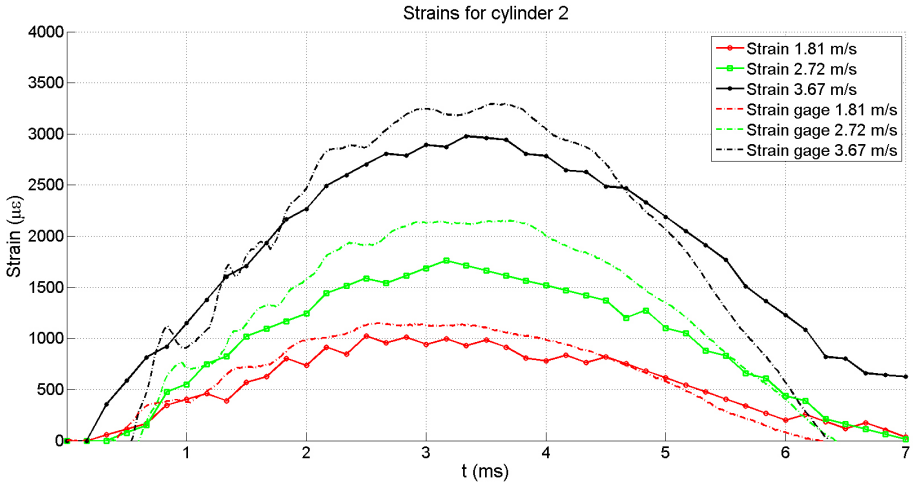

Figure 3.14: Strains on cylinder 2 at three entry speeds. Solid lines correspond to the strains calculated from feature identification results.

3.3.3 Forces

During the drop tests, the slamming forces were also measured [87]. Three force transducers were mounted between two flat plates, arranged in a triangle configurations with the centre of mass coinciding with the intersection between the cylinder symmetry line and the cylinder transversal mid-plane. The bottom plate was used for the clamp support of the cylinder, while the top plate was rigidly connected to the impactor body with L-shaped profiles. The force transducers recorded force during the water entry at a frequency of 100 kHz. The results of the three force transducers were summed to give the total force on the cylinder, and a correction was applied to include: the mass of the impactor (above the top plate), the mass of the cylinder and clamp (beneath the bottom plate) and a sensor calibration factor. The measured impact force is expressed as:

$$F_{impact} = \frac{1}{f_c}\frac{M_1 + M_2}{M_1}F_{sens} \tag{3.4}$$

where $f_c = 0.9232$ is the calibration factor of the complete force transducers arrangement, determined through calibration of the assembly using a hydraulic compression machine [87]. $M_1 = 16.7$ kg is the mass of the impactor, M_2 is the combined mass of the cylinder (given in Table 3.1) and of the clamp - which is 10.3 kg - and F_{sens} is the summation of the measured force. It should be noted that the instrumentation of the set-up and the data analysis of the force recordings was done by Van Nuffel [87].

The raw data obtained from the force sensor measurements show a lot of oscillation which are due to the structural vibrations, and which are not realistic for the actual force on the cylinder body. Thus, a low-pass filter at 200 Hz for cylinder 2 and at 60 Hz for cylinder 1 is applied to the data to determine the hydrodynamic component of the load. The filter was chosen to have the respective cut-off frequencies since a power spectrum density (PSD) analysis of the set-up showed that the first eigenfrequency of the supporting structure is located at 350 Hz and the frequency content of the cylinders is all located below 200 Hz and 60 Hz, respectively.

The load is estimated from cylinder deflection in the same manner as the strain. Equation 3.5 gives the expression of the conversion factor used for converting deflection (w_1) to force (F_1) for cylinder 1.

$$\begin{aligned} F_1 = -7.3 \cdot 10^{-7} w_1^6 + 9.2 \cdot 10^{-5} w_1^5 - 4 \cdot 10^{-3} w_1^4 + 8.4 \cdot 10^{-2} w_1^3 \\ -1.068 w_1^2 + 29.35 w_1; \end{aligned} \tag{3.5}$$

Figure 3.15 shows the comparison between the filtered measured force and the force determined from the optically measured deflection of cylinder 1. The differences here are consistent with those observed for the strains. The lowest error of 8.64% between the peak force measured by the load cell and that estimated from the vertical displacement is present for the largest entry speed considered. For the lowest drop height considered, the error is the highest, with the estimated load peak value reaching just over 65 N while the filtered measured force peaks at approximately 82 N. Again, the evolution of the force time histories are very much consistent between the two methods, and the consistency with the strain measured differences proves that the method can be applied successfully even though a certain margin of error can be expected, with the strain and force estimates being lower than the values measured with classical strain gauges and load cells.

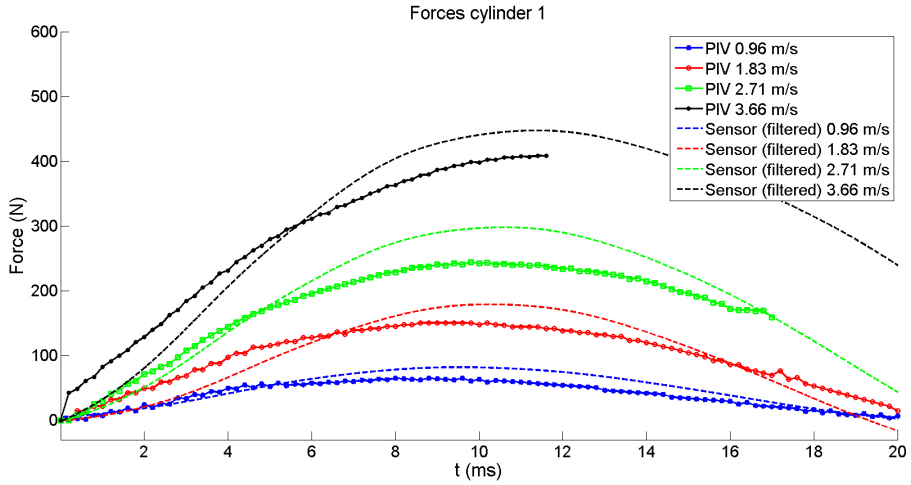

Figure 3.15: Forces on cylinder 1. Solid lines correspond to the force calculated from feature identification results and the dashed lines correspond to filtered measured forces as described in [89].

3.4 Conclusions

In this chapter, an improvement of the automated masking procedure is described. The improvements are designed to account for elasticity of the impacting body, which in turn, cause for its shape to change during the water entry. Furthermore, the feature identification technique is adapted to include adaptive filtering

of the recorded image using windows of interest defined as regions of the frame focused around the body and free surface features. All these improvements are designed to increase the accuracy of detection of the features, even when localized high intensity of the reflected laser light is present.

By using this feature identification of the deformable body shape, and tracking its evolution in time, displacements can be recovered. The algorithm was tested for two PVC cylinders of different stiffness. The results of the feature identified body displacement was compared with results of strain gauge measurement performed by Van Nuffel [87] on the same experimental test case. The comparison was enabled by the use of displacement-to-strain conversion factors obtained from the identification of the material properties of the test tubes. The same procedure was applied to convert vertical displacement to force acting on the cylinder during impact. The results showed a good agreement between the proposed method and the strain gauge and load cell measurements, suggesting that, by knowing the material properties of the impacting body, the feature identification result can produce good estimates of the occurring loads.

Chapter 4

Pressure Estimation from PIV

This chapter is a description of the methods used for pressure estimation from PIV-measured velocity. The algorithms used in this chapter are based on solving the Poisson equation for pressure. Using the fluid velocity field information extracted from PIV measurements and appropriate boundary conditions, pressure can be estimated during the water entry phenomenon. The test cases presented in the previous chapters, for a rigid wedge and a deformable cylinder water entry, are used to test the pressure reconstruction methods.

4.1 Introduction

PIV-based estimation of fluid pressure has gained popularity over the past decade. Due to the wide range of applications mentioned in previous chapters, and due to its 2D or even 3D velocity field measurement capabilities, PIV is increasingly used for fluid flow description. Along with the improvements in accuracy of PIV, new processing algorithms have been developed for extracting information on the flow. While velocity-derived parameters have been the main focus of PIV research over the years, increasing attention is paid to the possibility of pressure estimation. The estimation of pressure fields can be achieved by substituting the PIV-measured velocity fields in the Navier-Stokes equations, together with the application of appropriate boundary conditions.

Since for most of engineering applications, the integral loads and surface pressure are of fundamental interest, there have been several papers dealing with the evaluation of these loads from PIV measured velocity. One method involves the direct integration of the differential momentum equation along a path, as performed in the works of [62] and [90]. Another approach is to reconstruct the pressure field in a control volume, by solving the Poisson equation for pressure, and several studies have applied this technique with promising results [35, 22, 70]. A third method of estimating the pressure field from PIV velocity data, by using a numerical solver, was suggested in several papers [63, 39]. This iterative approach is based on the CFD predictor/corrector modelling technique. The PIV measured velocity field is introduced as initial input to the algorithm, which then solves the Poisson equation for the pressure and uses the intermediate result to correct the velocity field.

It should be noted that other research works have also dealt with the estimation of forces acting on immersed bodies, by using PIV velocity data [62, 69]. However, this latter category does not involve the explicit calculation of the pressure field, but rather the estimation of loads using the measured velocity field (and its derivatives) in a control volume (PIV measurement field of view) surrounding a fully immersed body.

As introduced above, there is a large number of research papers dealing with the estimation of pressure from PIV measured velocity. Nevertheless, many of these studies perform the evaluation of loads in steady flows [35, 28] by neglecting the acceleration term and using averaged velocity fields. Other papers [11] deal with the more complex problem of unsteady pressure field reconstruction from time-resolved PIV data, but are applied to flows surrounding immersed stationary bodies (flows around cylinders [21] and airfoils [4]). Only recently, researchers have turned their attention to PIV-based pressure estimation applied to

unsteady flows in the presence of moving features. In [19], measurements of the flow induced by a freely swimming lamprey were used to recover the pressure field by direct integration of the Navier-Stokes equations. The same method has been applied in [65] for the case of a rigid wedge water entry.

The method proposed herein uses the Poisson equation for pressure, and results of slamming test cases are compared with available analytical and numerical results. By applying a modified PIV processing algorithm to improve velocity field results, and the Poisson approach for pressure reconstruction, the results show the viability of the method and the comparison with simulations results show good agreement.

4.2 Pressure Estimation Procedure

Based on the two-dimensional velocity field as measured with PIV, instantaneous pressure field reconstruction is performed, by making use of the Navier Stokes equation. Assuming the fluid to be incompressible and inviscid, the Navier Stokes equation can be written as:

$$\frac{D\mathbf{u}}{Dt} = -\frac{1}{\rho}\nabla p + \nu\nabla^2\mathbf{u} \tag{4.1}$$

where $\mathbf{u}$ is the fluid velocity vector field, p is the instantaneous pressure, ρ is the fluid density, ν is the kinematic viscosity and D/Dt is the substantial derivative, as defined by

$$\frac{D\mathbf{u}}{Dt} = \frac{\partial\mathbf{u}}{\partial t} + (\mathbf{u}\nabla)\mathbf{u} \tag{4.2}$$

As mentioned previously, there are several approaches that can be used for the pressure reconstruction, which are based on introducing the PIV measured velocity field in the differential momentum equation. One method is to perform the direct integration of equation 4.1 over a control volume, while another is based on solving a Poisson equation for the pressure. The algorithm presented in the remainder of this chapter is part of the latter category of procedures. The Poisson pressure equation is obtained when applying the divergence operator to equation 4.1, as follows:

$$\Delta p = \nabla(\nabla p) = -\nabla(\rho\frac{D\mathbf{u}}{Dt} - \mu\nabla^2\mathbf{u}) \tag{4.3}$$

The viscous term in equation 4.3 is neglected because of its low contribution in comparison to the inertia term. Since the Reynolds numbers of the water flow studied in this work are very high ($Re > 10^5$), the contribution of the viscous term to the reconstructed pressure is negligible (more than three orders of magnitude lower than the inertia term). The final form of the 2D Poisson equation to be used is:

$$\frac{\partial^2 p}{\partial x^2} + \frac{\partial^2 p}{\partial y^2} = -\rho \left\{ \frac{\partial \nabla_{xy}}{\partial t} + u\frac{\partial \nabla_{xy}}{\partial x} + v\frac{\partial \nabla_{xy}}{\partial y} + \frac{\partial^2 u}{\partial x^2} + 2\frac{\partial u}{\partial x}\frac{\partial v}{\partial y} + \frac{\partial^2 v}{\partial y^2} \right\} \tag{4.4}$$

where (u, v) are the horizontal and vertical components of velocity, respectively, and $\nabla_{xy} = \frac{\partial u}{\partial x} + \frac{\partial v}{\partial y}$ is the in-plane divergence of the flow field.

As shown in the work of [4], the Poisson approach tends to give more stable results compared to the direct integration method, with lower noise levels especially when applying non-symmetrical boundary conditions. Thanks to the time-resolved nature of the PIV measurements performed herein, the solution of this equation can be fully determined with appropriate boundary conditions.

The pressure reconstruction algorithm implemented in this work, uses a staggered grid arrangement for the field variables, where the pressure p is calculated in the cell centre, and the fluid velocity components $\tilde{U}$ and $\tilde{V}$, which are introduced in equations 4.5 and 4.6, are located on the cell boundaries (as illustrated in Figure 4.1).

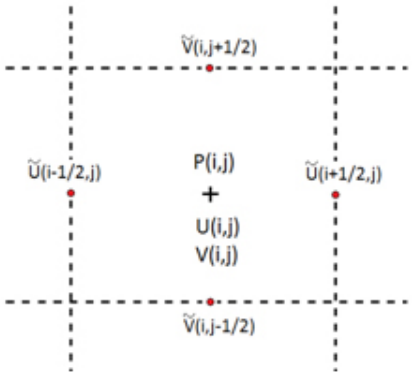

Figure 4.1: Staggered grid arrangement.

The fluid velocities as measured with PIV have the same location as the pressure, namely in the cell centre, denoted by indices i and j. The cell boundary positions are labelled with half integer values of the indices, $i \pm 1/2$, $j \pm 1/2$ and the horizontal and vertical components of velocity, respectively, are calculated as an average of the neighbouring cell-centred values:

$$\tilde{U}_{i+\frac{1}{2},j} = \frac{1}{2}(U_{i,j} + U_{i+1,j}) \tag{4.5}$$

$$\tilde{V}_{i,j+\frac{1}{2}} = \frac{1}{2}(V_{i,j} + V_{i,j+1}) \tag{4.6}$$

With the previously defined quantities, the pressure Poisson equation is discretized using a first-order upwind scheme for the time derivative of the velocity term, and a second-order central difference scheme for the remaining terms :

$$\frac{\partial u}{\partial t} = \frac{(U_{i,j}^{n+1} - U_{i,j}^{n})}{\Delta t} \tag{4.7}$$

$$\frac{\partial^2 p}{\partial x^2} = \frac{(P_{i-1,j} - 2P_{i,j} + P_{i+1,j})}{\Delta x^2} \tag{4.8}$$

$$\frac{\partial^2 u}{\partial x^2} = \frac{(U_{i-1,j} - 2U_{i,j} + U_{i+1,j})}{\Delta x^2} \tag{4.9}$$

$$\frac{\partial u}{\partial x} = \frac{(U_{i+1,j} - U_{i-1,j})}{2\Delta x} \tag{4.10}$$

The superscripts in equation (4.7) denote the time step under consideration, where n is the current time step. The partial derivatives with respect to the vertical component are treated in the same manner as for the horizontal component (equations 4.8 through 4.10).

A cell flag is introduced as well, in order to account for the position in the water domain, and for the ease of setting the boundary conditions accordingly. Figure 4.2 illustrates the different flags of cell nodes according to the position relative to the rigid wall or free surface, as well as the types of boundary conditions implemented.

The boundary conditions are applied using a ghost cells approach as typically implemented in numerical simulations models [57]. The ghost cells are cells outside of the fluid domain which are used for an easy and stable implementation of the central difference schemes in the discretization of the governing equation.

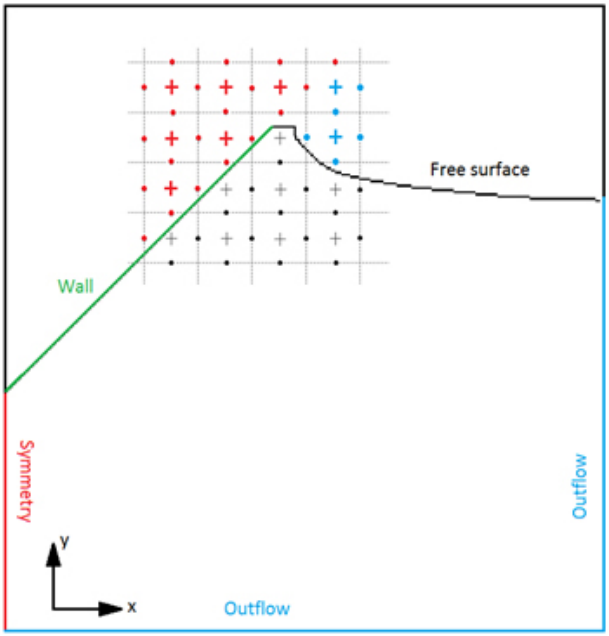

Figure 4.2: Field of view with boundary conditions and cell flag markers.

The 'wall' boundary condition is a no-slip, no penetration wall-type condition which is used for the solid body wall. This boundary condition is formulated such that the gradient of the fluid velocity normal to the wall, equals the velocity of the body at the considered wall location. Thus, the velocity in the ghost cell can be expressed as a function of the body wall velocity and the velocity in the fluid domain as $U_{GC} = 2 \cdot U_{Body} - U_{FL}$ for the horizontal component of velocity, and similarly for the vertical component. It should be noted that the velocity in the fluid domain (U_{FL}) is taken as the mirror extend of the ghost cell node along the normal to the wall body. This implies that the fluid velocity to be used is not at a grid node location, hence this value will be interpolated using the neighbouring fluid node values.

The 'symmetry' boundary condition is a free-slip wall-type boundary condition. The symmetry plane is taken on the left cells boundaries, and the boundary condition is imposed using ghost cells located to the left of the fluid cells. The components of the velocity in the ghost cells are $U_{GC} = -U_{FL}$ and $V_{GC} = V_{FL}$ for the horizontal and vertical components, respectively.

The 'free surface' boundary condition is a Dirichlet-type boundary condition. Since the current algorithm uses information of free surface elevation profiles as an input from the PIV measured free surface profiles, the Dirichlet-type condition, imposing $p = p_a$, where p_a is the atmospheric pressure, is sufficient.

The remaining boundaries, deemed as 'outflow' in Figure 4.2, are boundaries which do not represent solid walls. However, considering the flow to be irrotational, values of the pressure can be imposed on these boundaries. In the current algorithm, pressure values from the numerical results are time averaged and introduced on these boundaries. Another option of imposing boundary conditions on the 'outflow' edges in the far-field region, is to prescribe the pressure gradient as defined in the Navier Stokes equations (equation 4.1). However, this procedure was not implemented herein because of the negative effect that velocity variations in this far-field region would have on the pressure estimations. Since the PIV data used for this pressure reconstruction is time-resolved, and since the fluid displacements in the far-field region are small, the errors at the outflow locations will be in the same order of magnitude as the measured fluid velocity, as previously discussed in Section 2.3. For the deformable cylinder slamming tests presented in the following sections, an alternative to the use of these boundary conditions is preferred, by using multiple camera measurements in order to reconstruct the field of view up to solid boundaries (the walls of the water tank). Thus, for cylinder slamming test cases, the 'outflow' boundary conditions become solid wall boundaries, and are treated in a similar manner as for the impacting body wall.

4.3 Pressure Estimation During Water Entry of Rigid Bodies

Pressure field results are showing the same trends as observed in the velocity field results for the wedge body water entry, described in Section 2.3. For the initial stages of impact, a lower pressure estimation from the PIV reconstruction algorithm is found as can be observed in Figure 4.3. This observation is again attributed to the low correlation of the PIV measurements caused by the highly localized flow around the immersed body, with a reduced particle image availability in this area. However, as the wedge penetration into the water evolves, the estimated pressure results improve and closely match the results of numerical simulations. Figure 4.3 and Figure 4.4 present two snapshots of pressure field at 12.8 ms and 27.6 ms, respectively.

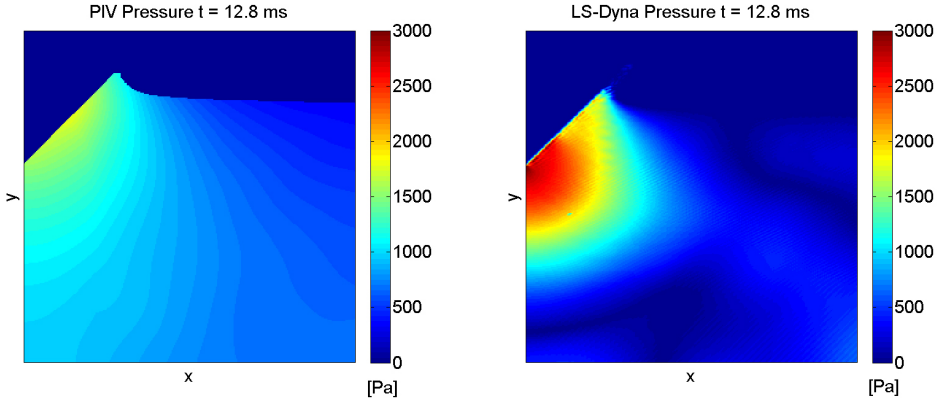

Figure 4.3: Pressure contours at t = 12.8 ms. Left: PIV-based estimations. Right: Numerical simulations result [91].

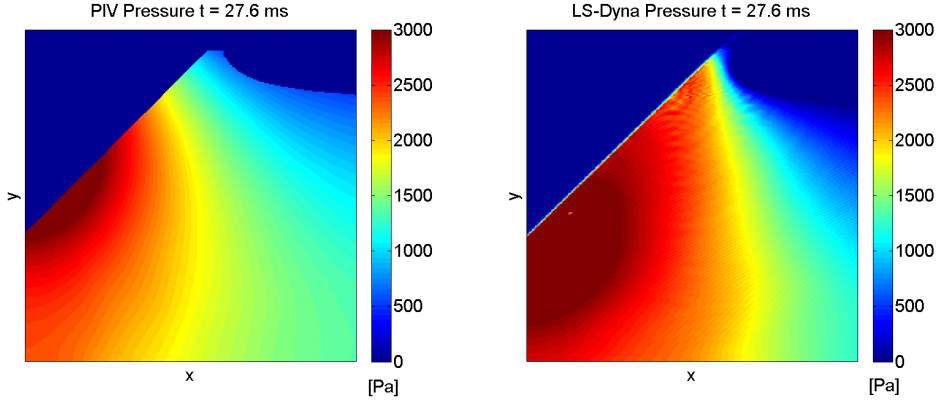

Figure 4.4: Pressure contours at t = 27.6 ms. Left: PIV-based estimations. Right: Numerical simulations result [91].

It can again be seen that the reconstructed pressure from PIV is lower in the spray root region. This result was easily predictable from the comparison of velocity magnitudes which are lower in the PIV measurements in this area. A qualitative analysis of the reconstructed pressure field from PIV shows that in the vicinity of the rigid body wall, the pressure presents a distribution closely matching results of simulations along the wedge wall, from the tip of the wedge until close to the undisturbed free surface level (corresponding to a submergence value Vt of 1). However, the pressure decreases and is up to 50% lower than the results of Vepa [91] (using LS-Dyna) at the undisturbed free surface level. For this particular test case, where a 90° wedge is used, this effect does not change the orders of magnitude of the peak pressure,which is approximately the same over the wedge wall from the tip up until the spray region, as shown in the work of [51].

In Figure 4.5, wedge wall peak pressure of the entire time series for PIV estimated pressure and simulation results are plotted. The first 2 ms of the impact are left out of this comparison, as the values of PIV reconstructed pressure were unusable because of the low resolution conferred in this initial stage. In these first milliseconds, the velocity gradients are highly localized in small regions of the fluid flow, equivalent to about one PIV interrogation window size. This means that the velocity gradients are averaged over this interrogation window. However, numerical simulations have refined grids that can closely capture the high velocity gradient change in the near wall area of the fluid, immediately after impact. This effect explains why the error between the PIV estimations of peak pressure and the numerical simulations result decreases as the rigid wedge continues its water entry. After 36 ms from the initial contact of the body with the water surface, PIV maximum pressure at the wall reaches 3.5 kPa, while in the simulations, the maximum value is around 4 kPa. An analysis of the pressure distribution on the wedge wall is also performed. For this purpose, the pressure coefficient C_p on the wedge wall, as defined in equation 4.11, is illustrated in Figure 4.6 against the dimensionless entry depth y/Vt. Values of the C_p determined from the PIV estimations and from the LS-Dyna simulations are compared with the analytical and numerical results of Mei [51] and with simulation results of Wu [104].

$$C_p = \frac{p - p_{ref}}{\frac{1}{2}\rho V_i^2} \tag{4.11}$$

The distribution of the pressure coefficient shows that the PIV estimations are in good agreement with the literature results up to values of y/Vt of about 0.7. In the region close to the undisturbed free surface level, the PIV estimations are under-predicting the maximum occurring pressure, for the reasons explained previously.

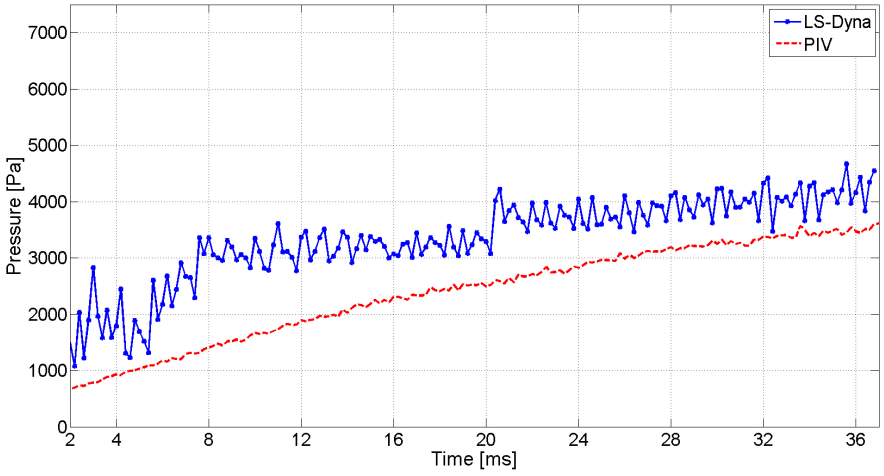

Figure 4.5: Maximum Pressure at the wall of a rigid wedge during water entry with constant velocity ($V_i = 1.5m/s$).

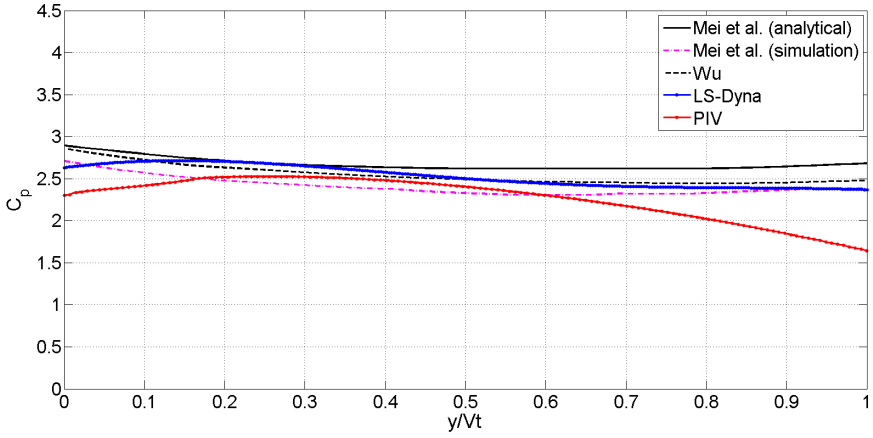

Figure 4.6: Pressure Coefficient at the wall of a rigid wedge during water entry with constant velocity ($V_i = 1.5m/s$).

4.4 Improved Pressure Estimation Algorithms

Improvements to the PIV processing algorithms described in Section 4.2 have been implemented in order to be applied to the deformable cylinder slamming test case. These improvements are represented by a vector field re-sampling and interpolation, meant to refine the temporal and spatial resolution of the velocity map results. The steps of the complete pressure estimation methodology, which are schematically shown in Figure 4.7, are presented in detail in the following:

Step 1. The PIV raw data is analysed using a **feature identification** code based on image intensities, which identifies the cylinder position and deformation, as well as the free surface profiles for every frame (Chapter 3).

Step 2. Following the feature identification procedure, an **adaptive mask** is generated for the batch of images to process, as described in Section 2.3.2. It is to be noted that the present procedure is independent from the assumption that the body is rigid, and that the body deformation is recovered for each time step.

Step 3. The raw images together with the masked images generated for each frame and a set of predetermined optimal parameters for **PIV cross-correlation analysis** are then used for batch processing. The implementation of this algorithm is done using Matlab, and the PIV cross-correlation utility program (PIVview) is appended at each time step.

Step 4. The present method includes the possibility of multiple cameras and/or multiple camera positions measurements. The repeatability of slamming tests performed herein, makes it possible for a number of separate recordings to be used to reconstruct the entire field of view (FOV) of the water domain. It is a well-known shortcoming of the PIV measurements to have limited FOV (typically in the range of a few tens of centimetres), however, the use of multiple cameras and different camera arrangements gives the possibility of overcoming these limitations. Thus, the present method proposes an optional **grid re-construction** of the entire FOV by careful calibration of spatial arrangements and time triggering of the measurements.

Step 5. The next step is to provide the user with the option of increased resolution of the velocity vector map determined by cross-correlation of the PIV images. The limited spatial resolution of a PIV grid can prove to be an important challenge when dealing with highly localized flows and high velocity gradients. Therefore, the goal of this improved algorithm is to create the possibility of vector field re-sampling in a stable way, such that the peak velocity gradients are preserved after interpolation. To achieve this requirement a vector field spatial re-sampling based on the **streamline tracing** of the flow is performed. This provides

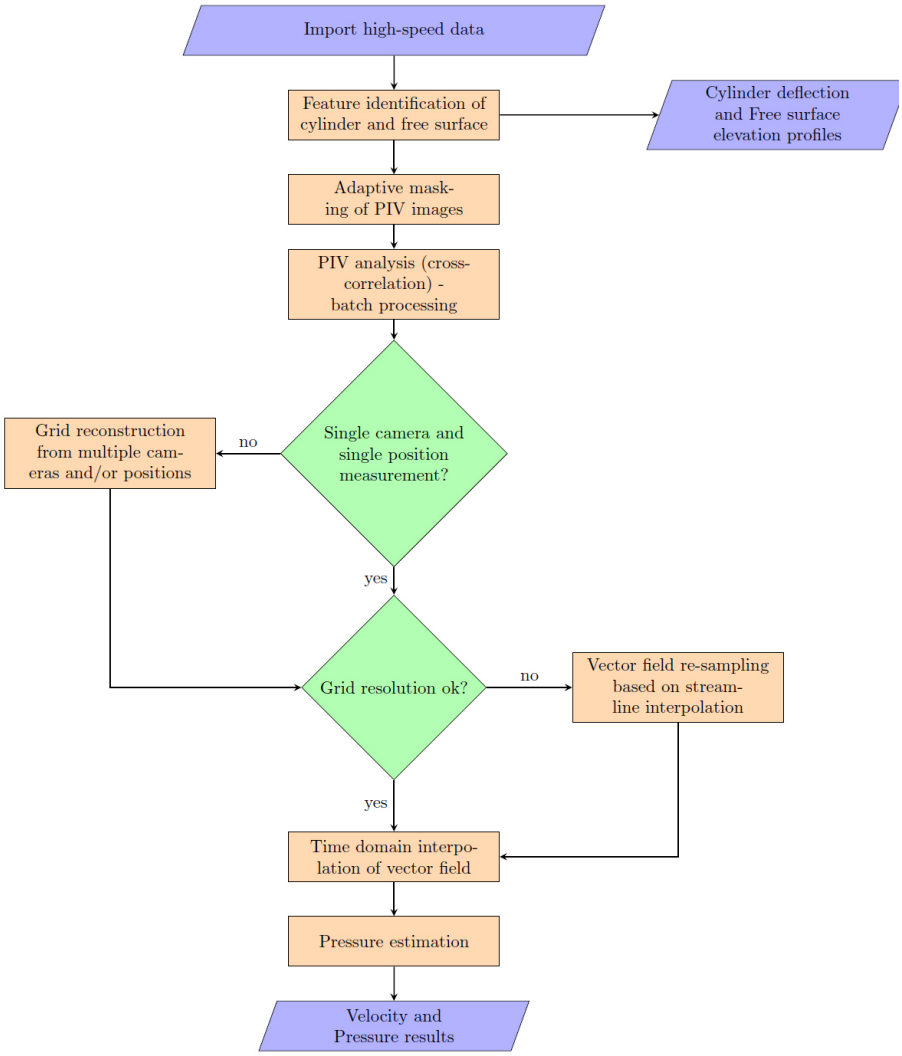

Figure 4.7: Improved pressure estimation algorithm.

an increased resolution through interpolation based on a physical interpretation of the flow. The details of this new technique are given in Appendix A.

Step 6. After the procedure described in the previous step is used to improve spatial resolution of the velocity vector map, a **time-domain interpolant** is

constructed for each grid node. This provides a measured unsteady velocity field with a lower bias by removing any outliers that might be present especially in the far-field region of the flow. The time-domain interpolation scheme is based on a 4^{th} order polynomial approximation of the velocity at each grid node. The mask generated previously for the air and solid body regions is used in the interpolation, so that only the velocity information of fluid nodes is considered. A typical velocity map is illustrated in Figure 4.8 at time t =12.4 ms. The left side of the figure shows the result of the velocity magnitude (FOV reconstructed from multiple camera measurements) after spatial streamline based interpolation, whilst on the right, the resulting map after time interpolation is shown.

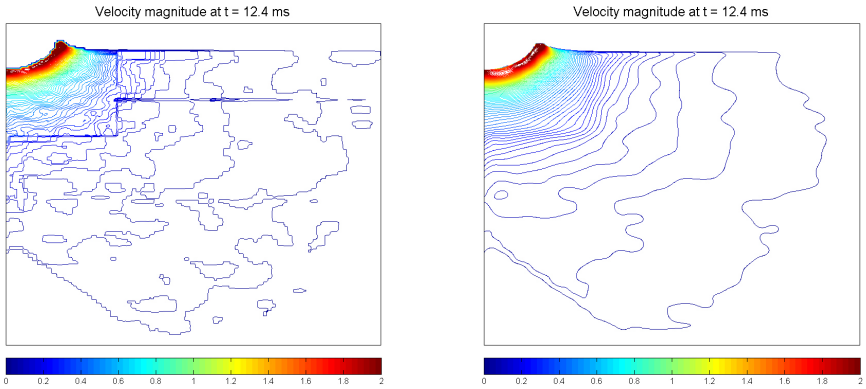

Figure 4.8: Velocity magnitude. left: before time interpolation; right: after time interpolation.

The resulting velocity map (Figure 4.8 (right)) shows a smoother distribution of the contour lines in the far-field, since the small-scale variations of velocity (with orders of magnitude around 1% of the peak velocity) are eliminated. Furthermore, the velocity map before time interpolation shows a localized error at the edge of the first camera FOV, which filters out after the procedure. The peak velocity magnitude is kept unchanged after interpolation, in spite of the fact that this region is close to the cylinder body, since the mask information is being used at each time step. Figure 4.9 shows the time history of x and y velocity component values before (black markers) and after (red markers) applying the procedure described above. The values are corresponding to a fixed spatial point with coordinates (36.9 mm, -12.3 mm), and it can be noted that after 17 ms, the point is covered by the cylinder body, as the values drop to zero because of the masking-based procedure mentioned earlier.

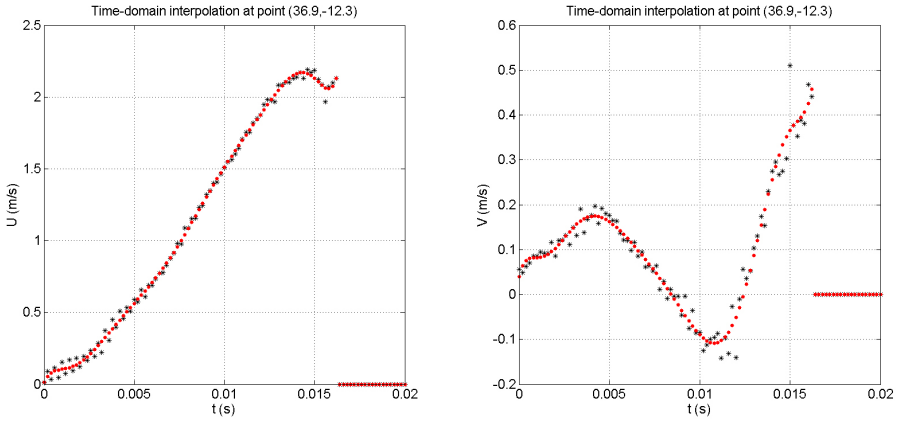

Figure 4.9: Evolution of velocity values in time, at a fixed position of coordinates (36.9 mm, -12.3 mm). Left: x-component velocity; Right: y-component velocity. Black markers denote values before and red markers denote values after time-domain interpolation.

Intuitively, the order of the polynomial approximation used for this temporal filtering procedure needs to be high enough so that peak velocity magnitudes are kept unchanged, but still sufficiently low so that unrealistic high frequency variations of the velocity are smoothed out. As mentioned previously, a 4^{th} order polynomial approximation was used to achieve this goal.

Step 7. The final step is the **pressure estimation** procedure. The velocity results obtained in the previous steps are used for pressure estimation. Neumann-type boundary conditions at solid walls such as the cylinder and the tank walls, and a Dirichlet-type boundary condition for pressure at the free surface, where the pressure is known to be equal to atmospheric pressure. The grid used is modified in a staggered arrangement to calculate pressure at the centre of one cell and the velocity components on the edges of the respective cell, as described in Section 4.3.

The procedure described above was applied to the time-resolved PIV measurements of the 1.83 m/s impact speed test of the PVC Cylinder 1. The water entry velocity was found to be approximately constant during the recorded sequence of 40 ms. However, the feature identification algorithm could only follow the cylinder for the first 20 ms, which was half of the cylinder oscillation period. The maximum occurring loads on the cylinder are found to be within this time sequence, therefore the measurement time was considered satisfactory.

It should be noted that two test runs were used for the results presented herein,

in order to enable the FOV reconstruction procedure. For this purpose, two high-speed cameras were used in the experimental set-up B, which is detailed in Section 5.2.1. The first camera, focused around the cylinder initial contact point had a FOV of 90 *mm* x 90 *mm*, and only the first run was used for the velocity map reconstruction. For the first run, the laser was at its lower position, illuminating the bottom half of the water domain. By reflecting off the mirror mounted on the bottom of the tank, the light sheet illuminated the FOV of the first camera from underneath. The spray root optical access was still limited, and a spray cut-off should be noted in the results below, as the comparison with numerical results shows the differences in root formation which is due to the measurement limitations. For the second run, the laser illuminated the upper half of the domain, and the second camera was used to measure the upper part of the far-field domain. The second camera measurements were used for the FOV reconstruction by stitching the bottom half measurement of the first run and the top half measurement of the second run to recreate the 315 *mm* x 350 *mm* water domain extending from the cylinder symmetry line to the tank wall.

The numerical simulations were performed by Vepa [91], using the software package LS-Dyna, on a 2D model of the experimental set-up, with identical boundary conditions. The drop height recorded in the experiments with the help of a position encoder, was used as an initial condition in the simulations. For more details on the simulations used herein, the reader is referred to [92].

4.4.1 Velocity Field Results of Deformable Body Slamming

The first step of the PIV processing procedure was the cross-correlation analysis of the images with adaptive masking of cylinder, air and bottom wedge. Batch processing for the two cameras was performed with different sets of parameters. The recordings of the first camera, which used a magnification factor of 7.8, were analysed with a cross-correlation interrogation window (IW) of 48 pix x 48 pix in x and y directions, respectively, and a windows overlap factor (IW_{of}) of 66 %, resulting in a final PIV grid step size of 2.0513 *mm*. The second camera recordings had a magnification factor of 2.8, an IW of 32 pix x 32 pix and IW_{of} of 62%, resulting in a PIV grid step size of 4.2857 *mm*.

After performing the grid re-construction for the entire fluid domain, the velocity vector map is interpolated using the streamline approach, to achieve a grid resolution increase from 2.0513 *mm* to 0.5 *mm*. The details of this procedure are explained in Appendix A. The final PIV velocity result is obtained after applying the temporal filter to the streamline-based interpolation result.

Figure 4.10 shows the comparison of the final measured velocity fields with

simulation results at time t =12.4 ms. It can be noted that the vertical component of velocity shows good agreement between measurements and simulation results. As explained previously, the spray root access is limited in the case of the PIV measurements, thus both velocity components show that the jet formation is visible only in the simulations. The largest error is for the horizontal component of velocity, which in the simulations increases faster than in the measurements as the y-coordinate of the cylinder wall node increases.

4.4.2 Pressure Results of Deformable Body Slamming.

The pressure from PIV measured velocity is estimated based on the Poisson equation for pressure, and it is compared with the simulations results of Vepa [91] for the same case of the 204 mm drop height test of Cylinder 1. Two representative resulting pressure maps are shown in Figure 4.11 for time t = 1 ms and t = 5 ms. The pressure field results show good qualitative agreement between the estimated pressure map and the numerical one. However, quantitatively some differences can be noticed regarding the pressure peak magnitude in the initial stages of the impact, as illustrated for the 1 ms time step. The evolution of this peak pressure wave reflected off the body surface is not as obvious in the PIV estimation as it is in the numerical results, with the maximum values up to 4 times lower in the PIV based estimation than for the numerical result. This is caused by the lower temporal and spatial resolutions of the PIV measurement, especially in the spray root and jet formation regions. The implications of this aspect are that, in the measurements, the rate of change in wetted surface is not captured as well as in the numerical simulations. This effect is more pronounced than in the case of the wedge test, as the larger deadrise angle of the wedge body does not cause for this large peak in the spray root, but for a more uniform pressure distribution on the body wall. In the case of cylinder slamming, during the initial stage of entry, the local deadrise angle tends to zero, and thus the peak pressure develops in the spray root region.

However, as pointed out by Faltinsen in his review [26], the pressure peak that can be identified in the initial stage of impact, lasting for a small period of time compared to the natural period of oscillation of the body, does not have an important effect from a structural point of view, when hydroelasticity is considered. Thus, the first milliseconds of impact - when the largest errors occur between estimated pressure and numerical pressure - can not be considered as conclusive for the comparison. Figure 4.12 shows the evolution in time of the pressure coefficient. The pressure coefficient is calculated using equation 4.11, in which p is the pressure at the cylinder wall.

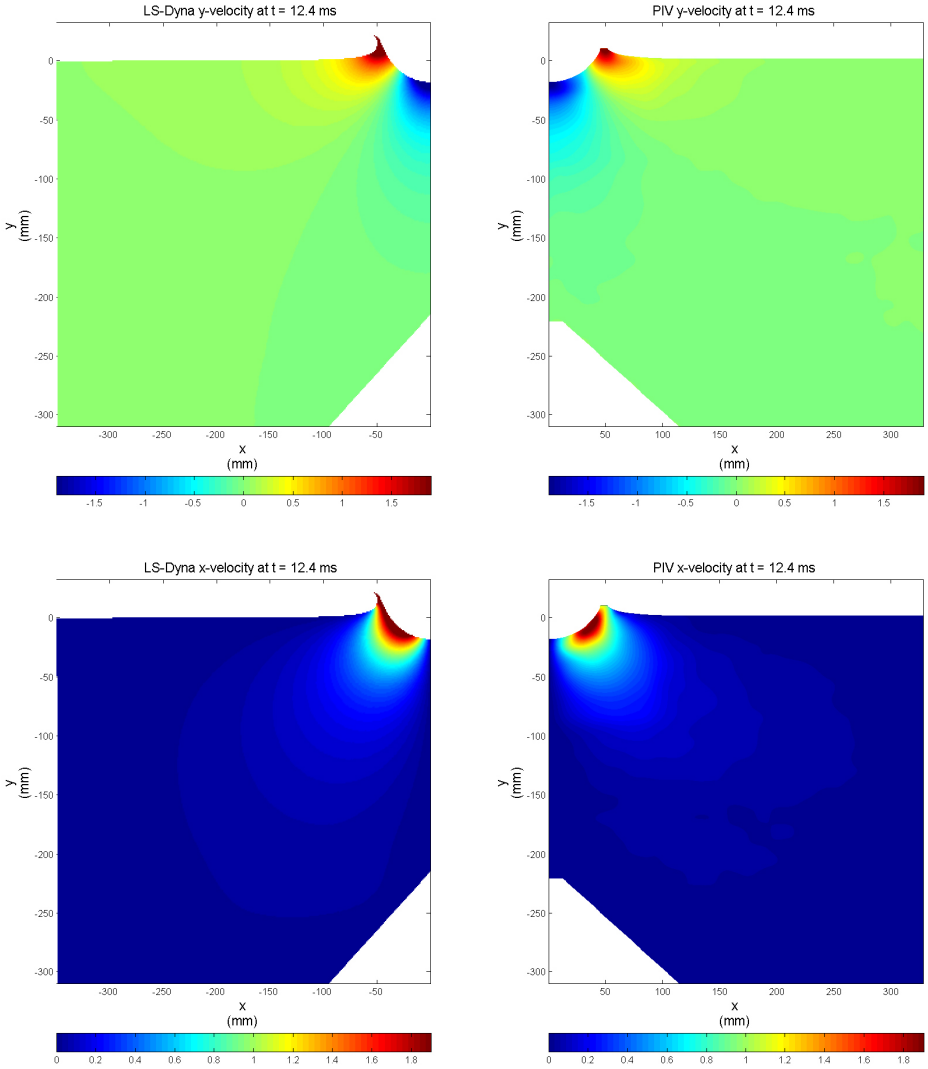

Figure 4.10: Velocity maps at t = 12.4 ms- comparison between LS-Dyna results (left) and PIV results (right). Top: y-component velocity; Bottom: x-component velocity.

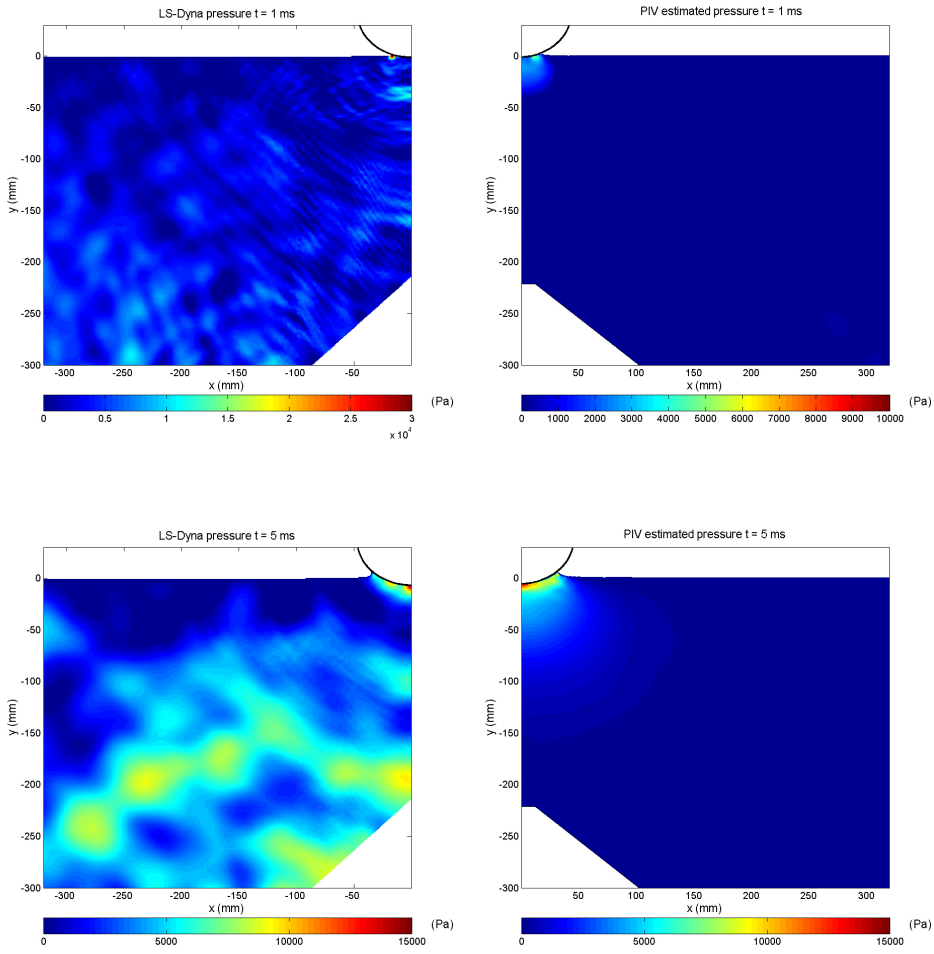

Figure 4.11: Pressure field at t = 1 ms (top) and t = 5 ms (bottom). left: LS-Dyna numerical results; right: PIV estimated pressure results.

The time history of the maximum pressure coefficient at the cylinder wall confirms the conclusions drawn from comparing the full-field pressure maps between simulations and PIV estimation. It can be observed that the high values induced by the initial impact pressure peak cause a larger relative error between the PIV result and the numerical one for the first 4 ms during entry. After the large peak has dissipated, the values of the fluid pressure at the cylinder wall are similar for the two methods. This is seen in the pressure maps results at 5 ms

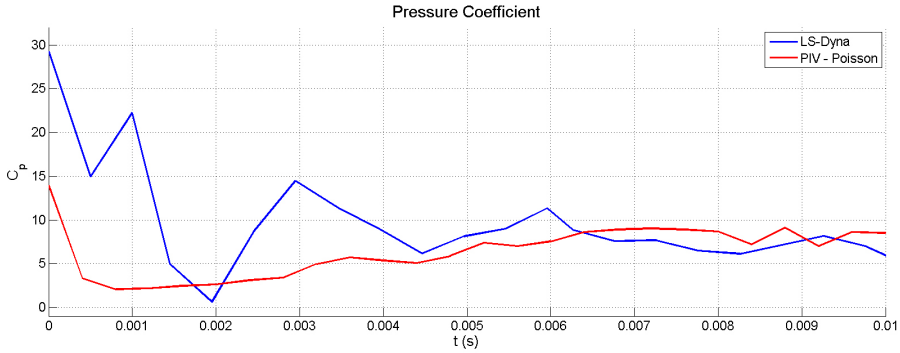

Figure 4.12: Time history of the maximum Cp at the wall. - a comparison between the values obtained from PIV pressure reconstruction using the Poisson approach, and the numerical results from LS-Dyna [91]

after impact, where the pressure distribution in the vicinity of the body is similar for PIV as it is for the LS-Dyna result. It should be noted that in the numerical results, the dynamic behaviour of the reflected pressure peak from the body and the tank walls, results in a visible pressure wave in the far-field region. This effect is not captured in the PIV results because of the lower resolution (both spatial and temporal), but it is also not relevant for the description of the slamming load.

As mentioned before, Faltinsen observed that the hydrodynamic load acting on an impacting body is not affected by high local pressure peaks. To investigate this, the total force acting on the cylinder is calculated by integrating the PIV estimated pressure along the wetted body wall. Figure 4.13 shows this result and compares it with the numerical simulations result as well as sensor measurements of Van Nuffel [87] which will be discussed in detail in the next chapter.

It should be noted that the time histories of the recorded force as estimated from PIV and the numerical simulations result match better than the maximum pressure coefficient. It is thus concluded that, even though high pressure peaks are present in the first milliseconds of the water entry, the highly localized nature of this peak means that its contribution to the total hydrodynamic load is negligible. Moreover, the match of these two results with force estimated by Van Nuffel using strain gauge measurements is also good. Therefore, it can be concluded that the PIV based estimation of loads can be used for estimating the total forces acting on slamming deformable cylinders. In the next chapter, a detailed investigation into this aspect will be presented.

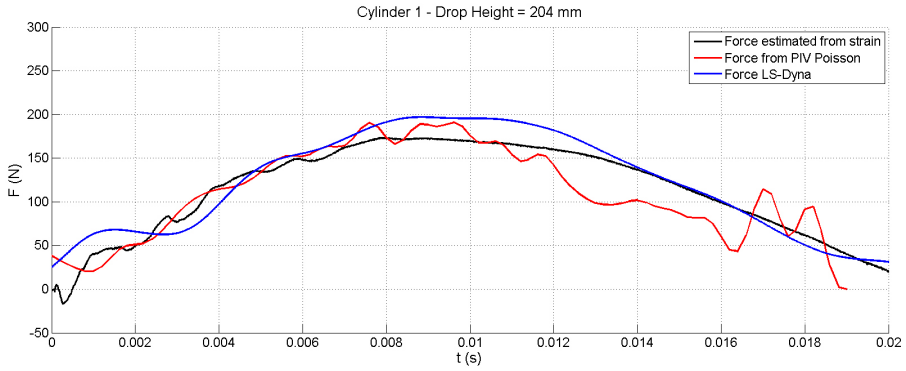

Figure 4.13: Time history of the force on Cylinder 1 - a comparison between the PIV estimated load, the numerical result of Vepa [91] and the estimated force from strain measurements on the same test case, performed by Van Nuffel [87]

4.5 Conclusions

In this chapter, the pressure estimation form PIV was detailed for the case of the wedge body and the deformable cylinder water entry tests, respectively. The comparison of PIV reconstructed pressure maps with the results of numerical simulations showed the same trends as observed in Chapter 2 for the velocity fields. The overall match of the pressure at the wall of the rigid wedge was found to be good, especially at the latter stages of water entry, while in the first milliseconds, the highly localized flow coupled with the limited spatial resolution of PIV, cause for lower values of the estimated pressure. Again, the main source of error for the PIV results is the flow in the spray root region.

In order to improve the pressure estimation procedure for the more complex test case of a deformable cylinder, streamline based interpolation for grid refinement and a time interpolation for outlier removal were deployed. The procedure was tested on Cylinder 1, for which the feature identification procedure presented in Chapter 3 was used to create the adaptive masking. The results show the same trends as in the case of the wedge. Considering that, for a cylinder body, the initial impact pressure peak is much higher than for the wedge, because of the very low local deadrise angle at impact, the underestimation of pressure from PIV is explained by the spatial resolution requirements. However, even though the magnitude of this high pressure peak is not fully captured when using the PIV measurements, it was found that it is possible to determine the hydrodynamic load

that develops over a period of time equal to the natural period of oscillation of a deformable body.

When comparing the force acting on Cylinder 1, it was found that the PIV estimations matched well with the results of the numerical simulations, as well as with the estimation using strain gauge measurements on the same set-up. This conclusion enables the further investigation of the hydrodynamic load on deformable cylinders during slamming. In the next chapter, an extensive test campaign is presented that analyses the water entry of cylinders with different stiffness and diameters.

Chapter 5

Validation of the Proposed PIV Methodology for Experimental Slamming Investigations

This chapter presents the results of a measurement campaign of slamming of deformable cylinders. PVC and composite cylinders of different dimensions and stiffness are used for drop tests with entry speeds ranging from 1 m/s to 4 m/s. The PIV measurements are performed on an experimental set-up instrumented with force transducers and strain gauges. The methodology presented in the previous chapters is applied to extract information on the cylinder response during water entry, and the measured fluid velocity fields are used for estimation of the load occurring on the test objects. The results are compared with the measurements performed using classical sensors, and the conclusions are drawn regarding applicability, advantages and limitations of the PIV-based methods.

5.1 Introduction

As mentioned in Section 1.2, the previous research done towards characterization of the loads occurring during slamming has offered a lot of insight on the topic of rigid body water entry. Well established analytical models, such as the Von Kármán method or the more general Wagner method, have been found to give consistent estimations of the occurring loads. However, one of the shortcomings of these methods is their assumption of a rigid body model to be used in the calculations. In order to effectively model a fluid-structure interaction problem such as in the case of deformable body water entry, one must resort to experimental investigation or numerical simulations that can capture the effect of the material properties of the impacting body (e.g. stiffness) on the occurring loads. As such, the existing measurement techniques that are being deployed in slamming studies are prone to errors introduced by limitations of sensor accuracy, mounting imprecisions, or even temperature shock effects on the recorded values - as shown in [89]. Numerical simulations have offered a great deal of information on the topic, with advanced algorithms and increasing computing power offering increased accuracy and higher modelling precision [26, 46]. However, numerical modelling limitations have not yet been fully eliminated, one of the biggest issues being the optimal coupling between fluid modelling and structural response algorithms.

As stated in Section 1.3, the goal of this thesis is to provide a viable alternative to the above techniques, and to introduce a new way of estimating loads on deformable bodies during water entry. The PIV measurements of fluid velocity and structural deformations, together with PIV pressure estimation capabilities, enable an alternative way of characterization of the phenomenon. In the following sections, an extensive measurement campaign of deformable cylinders slamming, is presented. The main focus in this chapter is on the aspects that are of interest in the characterization of slamming, namely the body **position and velocity**, the body **displacements**, and occurring **forces**. In the following, a detailed discussion on the advantages as well as limitations of the proposed methodology is given, and the main conclusions are drawn in comparison with well established, state-of-the-art measurement techniques that make use of force and strain sensors.

5.2 Experimental Set-up

The tests presented in this chapter have been conducted using the experimental set-up referred to, in Section 3.3, as *Experimental set-up B*. This annotation is used to differentiate from the PIV measurements presented in this chapter, and

those presented in Section 2.3, where slamming set-up *A* had been used. The PIV equipment used for both arrangements, comprising the laser, the optical arrangement, a CMOS camera and seeding particles, was identical. However, the drop tests were performed differently in the two cases. The slamming set-up *A* made use of a linear motor for the controlled movement of the impacting body, while for set-up *B*, the tests were conducted using a free-falling impactor, with strain gauge, force sensors and position encoder instrumentation mounted on the structure. Set-up *B* was designed at the Department of Coastal Engineering of Ghent University, and an in-depth analysis of the design process and instrumentation used is found in the PhD dissertation of Van Nuffel [87]. It should be thus noted, that the experimental slamming arrangement has been designed and assembled by Van Nuffel. The description given here, in Section 5.2.1, is meant as a general overview of the slamming set-up main components, with respect to the integration of the PIV equipment that is detailed in Section 5.2.2.

5.2.1 Experimental Slamming Set-up

The deformable cylinders studied in this chapter can be categorized in two, according to their respective diameters: one set of cylinders with smaller diameters ($D = 90mm$), and another with large diameter ($D \geq 315mm$). From the former category, two cylinders have already been introduced in Chapter 3, where the displacement results using the feature identification techniques were discussed. A third cylinder, manufactured from PVC as well, but with a larger wall thickness is presented herein. Regarding the large diameter tubes, results of two PVC and two composite cylinders drop tests are discussed. The material properties of these cylinders were determined by Van Nuffel [87], using compression tests, as well as simulations performed with the finite element analysis (FEA) software Abaqus. Since, in the compression tests, the cylinders were placed between circular plates that did not cover the entire length of the body, the numerical simulations were used to better approximate the relation between applied force and resulting displacement, by controlling the way the boundary conditions are imposed during compression. The material properties of the cylinders extracted from the compression tests and FEA simulations, are presented in Table 5.1, along with their dimensions. It should be noted that the composite cylinders are assumed to be unidirectional in the hoop direction, and thus the value of Young's modulus for these cylinders is expressed with respect to this direction. Moreover, the cylinder stiffness (K_c) is calculated by Van Nuffel [87] using FEA simulations, and it is the slope of the linear part of the force-displacement curves.

The cylinders were painted black, and instrumented with uniaxial strain gauges

Cylinder no.	1	2	3	4	5	6	7
Numbering in [87]	C9	C8	C7	C1	C2	C5	C4
Material	PVC	PVC	PVC	PVC	PVC	GFRP	GFRP
Cylinder diameter D [mm]	89	90	90	315	315	318.7	321.7
Cylinder length L [mm]	350	350	350	348.5	350	397.5	388
Wall thickness d [mm]	1.5	3.15	4.7	9.4	6.6	1.85	3.325
Cylinder mass m [kg]	0.304	0.42	0.615	4.25	3	1.12	2.237
Young's modulus E [Gpa]	3	2.7	2.58	3.2	3.4	22.8	18.25
Cylinder stiffness $K_c[N/mm]$	26.84	230.25	745.96	158.78	58.35	6.08	43.45

Table 5.1: Test Cylinders Properties.

of type CEA-06-250UN-350. The locations of the strain gauges differed between the small diameter and the large diameter cylinders. The small diameter shells were instrumented with strain gauges on the outer surface, in the mid-plane of the test tubes. Because of the small diameter of these cylinders, there was limited access which prevented the mounting of these sensors on their inner surface. The locations of the two strain gauges, as measured from the lowest point on the cylinder, are: $\theta = +90^\circ$ and $\theta = -90^\circ$, respectively. In the case of the large diameter cylinders, the sensors were mounted on the inner diameter of the tubes, at the mid-plane mark. The large diameter facilitated this mounting choice, and the sensors were located at the bottom ($\theta = 0^\circ$) and at the side ($\theta = 90^\circ$) of the cylinder.

Impactor assembly. The impactor assembly was designed and constructed by Van Nuffel [87]. Figure 5.1 shows an overview of the experimental set-up, as well as a close-up view of one installed deformable cylinder along with the main components of the impactor assembly. Two vertical **guiding rails** are rigidly fixed to the walls of the room, and an **impactor** is foreseen to slide between the two rails. A LIMES LI20/B1 **position encoder** with 10 μm resolution and 6.5 m/s maximum measurable speed, is also foreseen on the impactor. At the bottom of the impactor, two circular Aluminium plates include a load cell arrangement between

them, comprised of three **force sensors**. The three piezoelectric (ICP) sensors (from *PCB Piezotronics*) form a load cell with an average sensitivity factor of 14.47 N/mV and a variation coefficient of 2%. The measurement range of the load cell combination is approximately 66 kN (three load cells of 22 kN each), making it an adequate choice for the expected occurring loads.

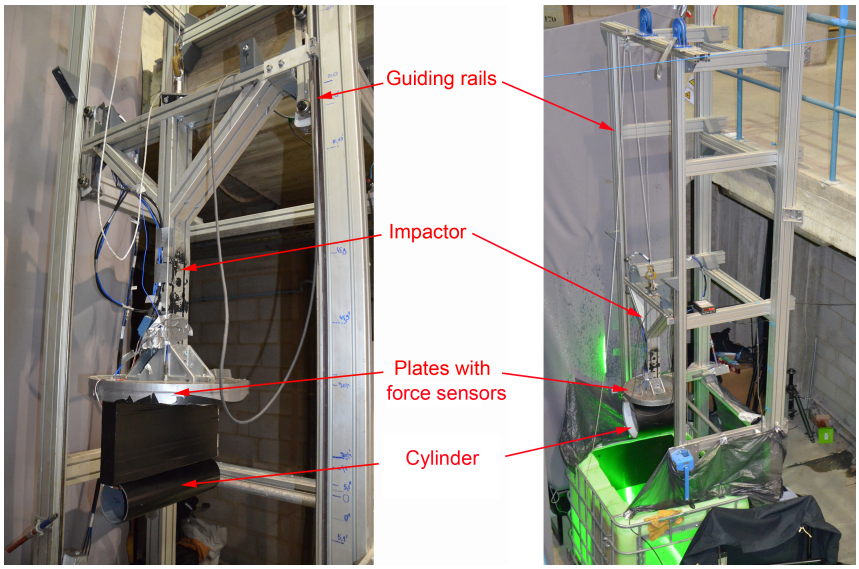

Figure 5.1: Slamming experimental set-up *B*.

The **cylinder** is fixed to the bottom circular plate, as illustrated in Figure 5.2, in two configurations, corresponding to the two types of cylinders used for the tests (small diameter and large diameter cylinders, respectively). The small diameter cylinders are connected to a beam of 200 mm height, that is fixed to the bottom circular plate. The solution of using an intermediate beam between the cylinder and the two circular plates that contain the force sensors, is motivated by the observation that, during slamming, the water jet separating from the small cylindrical body was hitting the circular plates. The water then comes splashing down on the free surface in the vicinity of the cylinder, causing unnecessary reflections and disturbances on the fluid flow. In the large diameter cylinders case, this problem was not occurring due to the fact that the circular plates diameter was in the same order of magnitude as the cylinder diameter. It should be also noted that in the second configuration, the large cylinder is fixed on the bottom circular plate, with a thin rectangular plate used between the tube and the plate, to introduce additional mass depending on which cylinder is being tested.

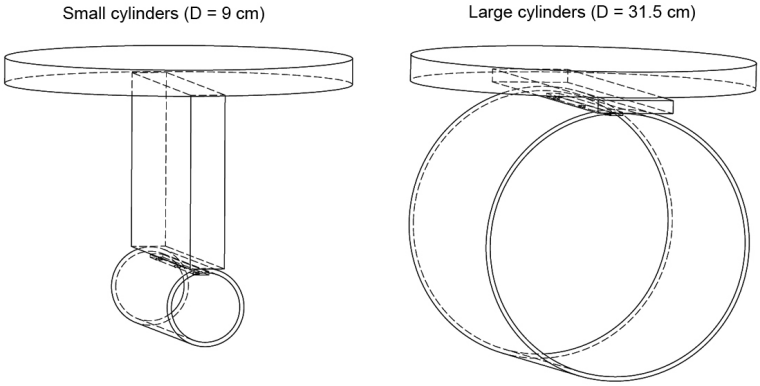

Figure 5.2: Installation of the small cylinders (left) and of the large cylinders (right) on the bottom circular plate of the impactor.

The 1 m^3 **water tank** used in the drop tests, was modified to provide the optical access needed for PIV measurements and for imposing desired boundary conditions on the flow. Firstly, two Plexiglass windows were foreseen on two of the sides of the water tank: one side-view window for access of the laser sheet perpendicular to the axis of the slamming cylinder, and one front-view window for the camera recordings of the flow field. Secondly, for the drop tests of the small diameter cylinders, a 0.7 m x 0.44 m x 0.7 m box was built and included inside the water tank. This was done in order to reduce the 3D effects that were generated predominantly at the ends of the cylinder. Therefore, the distances from the cylinder to the front and back walls were reduced considerably, and a predominant 2D flow was recreated in the mid-plane of the cylinder, where the measurements were done. Moreover, in the case of the small cylinder tests, a 90° wedge was fixed to the bottom of the box, with a mirror included on the face of the wedge oriented toward the laser head. This made it possible for the laser light sheet to be delivered from underneath the penetrating body, and to increase optical access inside the spray root region.

Two data acquisition systems were used in the present tests, to record values of the above mentioned sensors and, at the same time, to trigger the PIV measurement. The main of these two systems was a Genesis Gen5i oscilloscope, which recorded signals of the three force transducers, as well as the position encoder signal. A secondary, National Instruments C-DAQ, data acquisition system was used to record the values of the strain gauges. The Genesis oscilloscope recorded the

position encoder signal and, when a threshold value (the first contact of the cylinder with the water surface) was reached, a trigger was sent to both the secondary system and PIV synchronizer, which triggers the PIV recordings.

5.2.2 PIV Instrumentation

The PIV system used in the experiments performed in this dissertation was assembled by ILA Intelligent Laser Applications GmbH [30], and comprises the following components:

- **Laser light source**
- **Articulated mirror arm**
- **CMOS camera**
- **Synchronizer**

Figure 5.3 shows these main components of the PIV system for the case of a Cylinder 1 drop test. It should be noted that the box and mirror described in the previous section were deployed inside the water tank. This ensured optimal conditions of illumination despite the constricted optical access, as well as the application of boundary conditions to facilitate predominant 2D flow.

Laser light source. The laser used for the work presented in this dissertation is a diode-pumped Quantronix Darwin Duo Nd:YLF double-pulsed laser as illustrated in Figure 5.4. The main feature of this high-powered laser is its applicability to time-resolved PIV (TR-PIV) measurements, which is the main requirement for investigating the slamming phenomenon. The choice of Nd:YLF over the more conventional Nd:YAG lasers for conducting TR-PIV, is facilitated by the superior performance of the former thanks to its upper state lifetime, which is double that of the Nd:YAG - 480 μs compared to 230 μs.

The Aluminium enclosure of the laser head nests the pump chambers and optical resonators of two independent cavities. Q-switches are included for operation with short high-powered pulses (pulse widths in the order of nanoseconds). An external power supply cabinet contains the RF driver that provides the Q-switching mechanism, as well as a pump for the water cooling system of the laser. Table 5.2 presents an overview of the laser specifications as indicated by the manufacturer.

Before commencing the slamming experiments, a series of measurements of the laser power was conducted, and it was seen that the power showed a slight decrease from the values given by the manufacturer. The measurements were

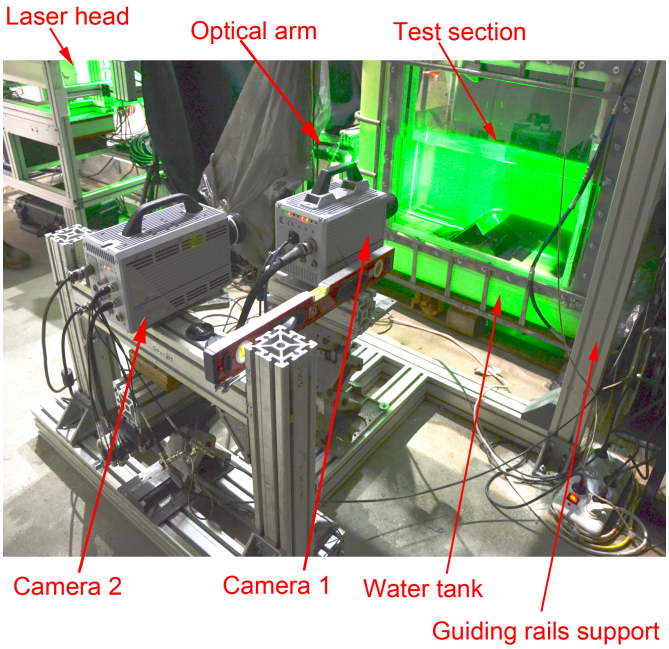

Figure 5.3: PIV arrangement for *slamming experimental set-up B*.

performed by increasing the input current intensity in steps of 2 A, for each of the cavities, individually. The operating frequency for the tests was set to 3 kHz, a value which is given as a reference in the manual from Quantronix, and which is also a common value used in the experiments presented here.

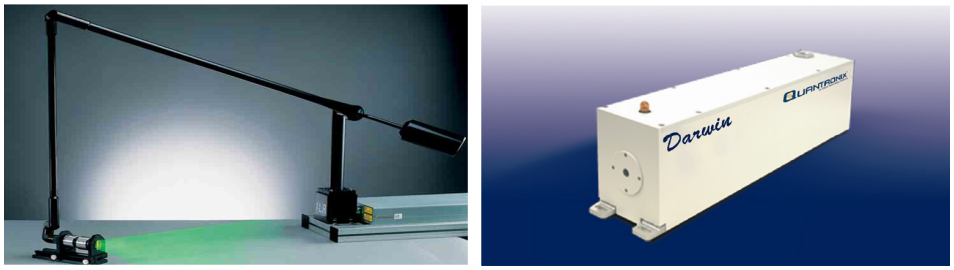

Figure 5.4: The articulated mirror arm used for laser light delivery to the test section (left) and the double-cavity Nd:YLF laser head (right) [30].

Laser Model	Darwin DUO-527-80-M
Laser Wavelength	527 nm
Frequency range	0.1 kHz - 10 kHz
Repetition rate	60 W (at 3 kHz)
Pulse energy	20 mJ (at 3 kHz)
Minimum pulse width	200 ns
Pulse-to-Pulse stability	1 % rms
Operating temperature	20 °C
Maximum current	33 A

Table 5.2: Laser Specifications.

In Figure 5.5, the results of laser power measurements are presented. The values showed a slight decrease in power of the second cavity, as compared to the first cavity, which could be compensated for in operation, due to the inclusion of a current offset setting that enables individual current intensity adjustment for each of the laser cavities. It can be seen from the graphs, that the maximum laser power at 3 kHz is 53.6 W, instead of the specified 60 W. This is caused by the second cavity having up to 22 % less energy than the first cavity. However, when operating at current intensities of up to 30 A, offsets of current on the second cavity compensate for this difference, thus resulting in an equal intensity output for the two cavities.

Also, during the measurements, a test of the optimal working temperature was conducted. A corrected value of 23 °C was found to give maximum output power, and thus this value was used further. The pulse width value used in the present tests was set to 1 μs.

Articulated mirror arm. The articulated arm illustrated in Figure 5.4 reaches 1.6 m when fully extended and offers a 360 ° orientation of the laser light sheet. The arm houses 7 mirrors oriented at 45 ° with an aperture of 16 mm. The incident laser light beam is first steered into the arm by a first user-adjustable mirror. The mirror can be adjusted on two axes, thus allowing correct alignment of the laser beam at the exit of the arm. The other end of the arm is foreseen with a lens mount, where arrangements of cylindrical lenses allow for expansion of the laser light sheet. Due to space constrictions as well as specific light delivery require-

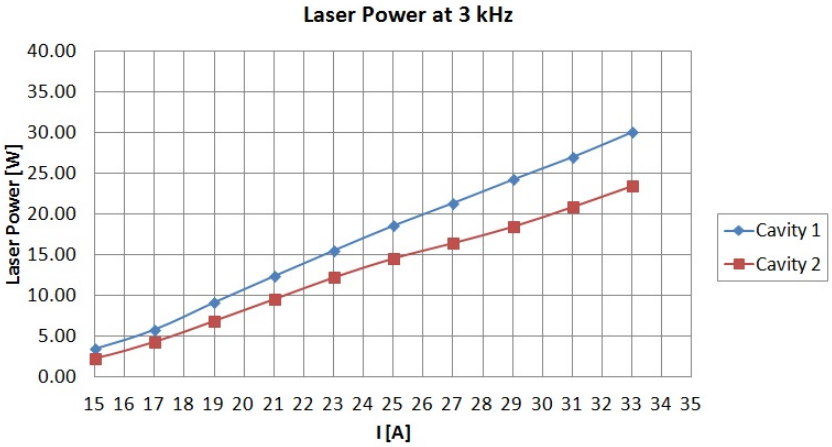

Figure 5.5: Laser power for each cavity as a function of the current intensity.

ments, the articulated arm is a useful tool for the delivery of laser light to the test section. Considering the nature of the flow for slamming experiments, the light sheet delivery is optimally done from underneath the test section (as discussed in Chapter 2). The experimental set-up *A* used for tests discussed in Section 2.3, had foreseen a glass bottom wall of the tank, which made it possible for the light sheet to be expanded from underneath the water tank, with the help of the articulated mirror arm. However, in the case of experimental set-up *B*, the slamming set-up was built before PIV experimental investigations were foreseen to be deployed. The guiding rails had been previously fixed to the walls of the room, and thus it was not possible to elevate the water tank. Therefore, the optical arm could not be mounted underneath the water tank, and it was fixed to the side of the tank, at an angle.

CMOS camera. The experimental set-up presented in this chapter included two high-speed digital cameras used for the PIV measurements. The main camera (deemed *Camera 1* and illustrated in Figure 5.6) is a 12-bit CMOS camera from *Photron*, model FASTCAM SA1.1. Camera 1 was used also in the experimental set-up A, as described in Chapter 2.

In order to increase the measured field of view of the recordings, and to reconstruct whole domain measurements as mentioned already in Chapter 4, a second high-speed camera (*Camera 2*) was included in the experimental arrangement. Camera 2 is also a CMOS sensor device from *Photron* with comparable features as the first. The specifications of the two cameras are given in Table 5.3.

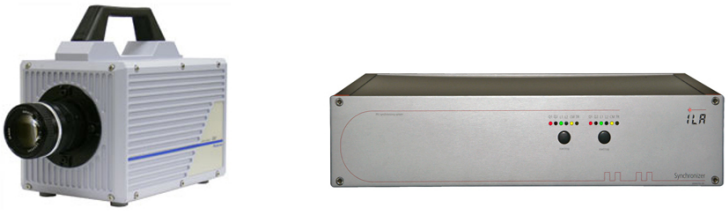

Figure 5.6: CMOS camera model Photron FASTCAM SA1.1 (left) [96]; PIV system synchronizer (right) [30].

Parameter	Camera 1	Camera 2
Sensor type	12-bit CMOS	10-bit CMOS
Pixel size	10 μm	17 μm
Minimum shutter time	1 μs	2 μs
Maximum frame rate	675000 fps	250000 fps
Maximum resolution	1024x1024 pixels (@ 5400 fps)	1024x1024 pixels (@ 3000 fps)
Built-in memory	8 GB	8 GB
Total recording time	1.01 s (@ 5400 fps)	2 s (@ 3000 fps)

Table 5.3: Camera Specifications.

The cameras record images using their built-in memory and after completion, the data transfer to a PC is accomplished via a TCP/IP connection. Furthermore, the cameras are triggered using a TTL 5Vp-p input, which is provided by the Genesis oscilloscope. The cameras also include an additional option of trigger settings, which enables the recording to be either at the end or at the beginning of a measurement sequence, or at a user-defined position. This is achieved with a two-step triggering procedure, in which the first step is to arm the cameras. This implies that the camera is running in a continuous recording state, until the actual trigger signal defines the recorded limits depending on where the trigger position was previously set.

Synchronizer. The PIV synchronizer is an in-house built system provided by ILA Intelligent Laser Applications GmbH [30]. The synchronizer is based on the Field-Programmable Gate Array (FPGA) technique, and provides the output

signals for the two laser cavities and for the CMOS camera. The synchronizer communicates with the PC via network connection (TCP/IP) and a custom-build software also provided by ILA allows for interactive user-adjustment of the PIV recording parameters (laser frequency and pulse delay times, camera frame rate, triggering options).

5.3 Small Diameter Cylinder Slamming

The first test cases examined in this section are the drop tests of cylinder 1, 2 and 3, as identified in Table 5.1. The present section is focused on the determination of cylinder velocity and induced slamming loads. The procedure described in Chapter 3 for feature identification, has already been validated on the test cylinders 1 and 2 at different entry speeds. From the information provided by the feature identification procedure, the cylinder bottom position during the recorded PIV sequence is recovered, allowing for the estimation of cylinder displacement (w). Moreover, the velocity of the immersed body wall can be recovered at each time step. The steps undertaken for pressure estimation from PIV data using the Poisson approach has also been tested in Section 4.4 in the case of a 204 mm drop height test of cylinder 1. In the following section, results of force acting on the cylinder wall during water entry, as calculated from integrating the PIV estimated pressure, are discussed for all the three small diameter cylinders. A comparison is made with the results of loads as measured by Van Nuffel on the same test cases, using load cells and strain gauge measurements. A complete description of the work performed by Van Nuffel is given in his PhD dissertation [87], and the discussion of his results is restricted in this chapter to aspects relevant to the aforementioned comparison.

5.3.1 Cylinder Velocity

The cylinder drop tests are performed from fixed heights (H), which are a priori known from the position encoder information. Theoretical impact velocities (V_{ti}) could thus be calculated as in equation 5.1. This, however, can lead to an erroneous estimate of the real impact velocity (V_i) because of the losses due to friction between the impactor and the guiding rails.

$$V_{ti} = \sqrt{2gH} \tag{5.1}$$

To correctly determine the impact speed, the position of the cylinder, as recorded by the encoder, is derived. Due to structural vibrations of the impactor,

noise is present in the position encoder signal, which causes a high error in the estimated velocity profile if the raw signal is directly derived. To eliminate this noise, a low-pass butterworth filter is applied to the resulting velocity [56]. It was shown by Van Nuffel [87] that an optimal value of the cut-off frequency of 75 Hz is appropriate for the recovery of correct velocity profiles over the entire sequence of the position encoder data. The implementation of this filter design is performed with the built-in Matlab functions *butter* and *filtfilt* for the recovery of the polynomial coefficients of the filter, and of the output zero-phased filtered results, respectively.

The filtered velocity from the position encoder is the velocity information of the impactor, which is considered to be the velocity of the cylinder, if the body is rigid. In the present case, the elasticity of the test tube needs to be taken into consideration, and thus the obtained profiles are assumed to be valid only for the position of the top point on the cylinder contour, which is clamped to the impactor.

Figure 5.7 (top) exemplifies the complete time sequence evolution of the impactor velocity in the case of a Cylinder 1 drop test from a height of 204 mm. From the moment the cylinder is released - which is marked as $t_{release}$ - until the body touches the water surface (t_{impact}), its velocity increases linearly to about 1.9 m/s. During approximately 20 ms after impact (t_{PIV}), the cylinder position is tracked using the procedure described in Chapter 3, and PIV velocity measurements are performed at 5 kHz. For the case exemplified here, the cylinder velocity keeps increasing after initial impact until the impactor structure hits the dampers - 70 ms after impact, at time t_{stop} - which brings the structure to a complete stop after approximately 100 ms. It should be noted that this behaviour is valid for all small diameter cylinders test cases, because of the large mass of the impactor structure and the low occurring loads. In the cases of the large cylinders, the velocity of the structure exhibits a slight deceleration immediately after impact, followed by a general constant velocity profile until the dampers are reached.

The lower part of Figure 5.7 shows the evolution of the cylinder top velocity only for the time sequence under consideration for PIV, for all the small cylinder cases. It should be noted that this sequence is limited by the feature identification procedure in time, as for tests with increasing entry velocity, the cylinder leaves the field of view faster. The figure shows that the velocity profiles match quite well, implying similar entry conditions, and also that the velocity does not deviate largely from a constant profile. A quantitative analysis of this deviation (Figure 5.8) shows the absolute value of the relative error of the cylinder top velocity (V_{top}) from the constant value of the impact velocity (V_i), defined as:

$$errV = |V_i - V_{top}|/V_i \tag{5.2}$$

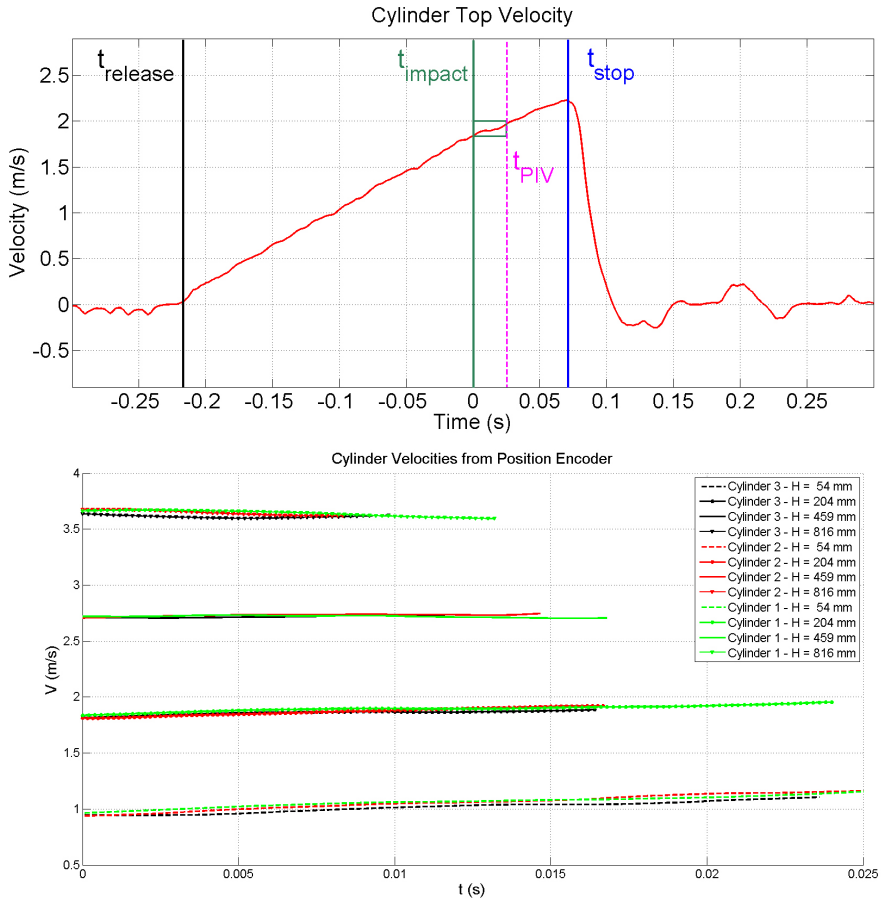

Figure 5.7: Position encoder derived velocity profiles. Top: The complete time sequence from the moment of release until full stop of the cylinder after it hits the dampers; Down: The velocity profiles for cylinders 1, 2 and 3 in the analysed time sequence corresponding to PIV measurements.

It can be observed that the largest variation of the velocity is present for all the three cylinders in the case of the lowest drop height used (H = 54 mm). For the other test cases, the variation is less than 6 % of the impact speed, thus making an approximation of constant entry velocity, a valid assumption. This consideration is based on the remarks of Hughes [40], who performed constant velocity water entry experiments on a wedge body and stated that a value of 5 % is an acceptable margin of error for the velocity to be considered constant during entry. The values

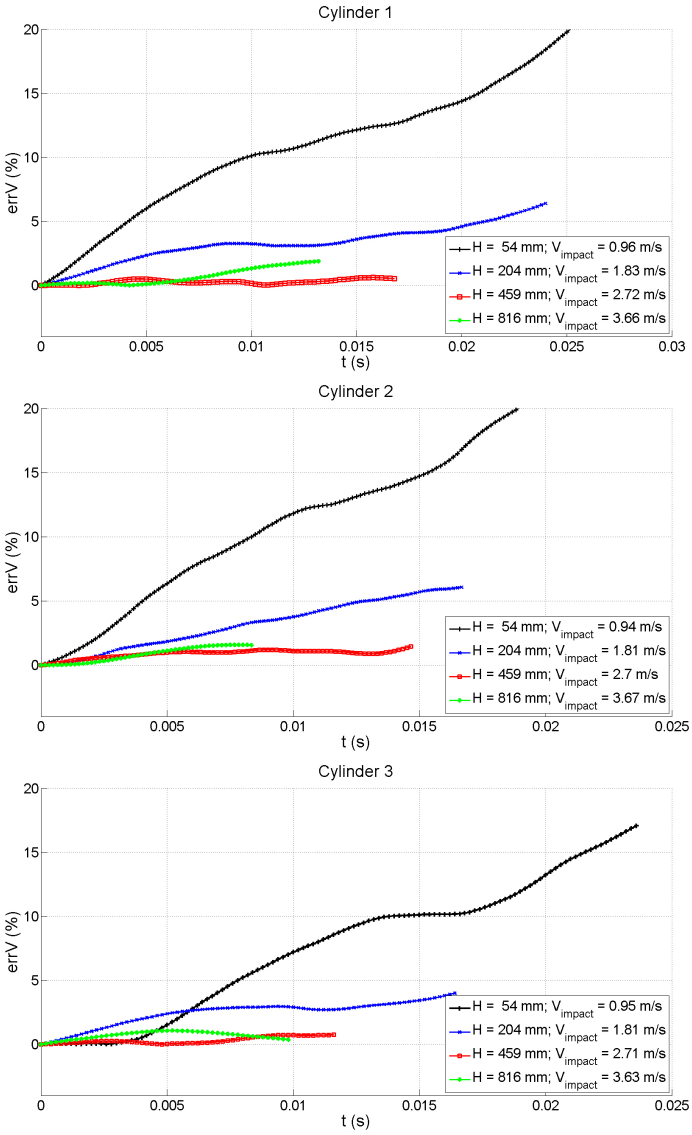

Figure 5.8: Deviation of the position encoder derived velocity from the constant value of initial impact velocity (V_i). Values for tests with drop heights higher than 54 mm present a maximum deviation of less than 6 %, which is considered an acceptable level for constant velocity water entry experiments [40].

of test drop heights, impact velocities and the maximum absolute relative error are given in Table 5.4.

	Cylinder 1		Cylinder 2		Cylinder 3	
Drop Height (mm)	V_i (m/s)	$\|errV\|_{max}$ (%)	V_i (m/s)	$\|errV\|_{max}$ (%)	V_i (m/s)	$\|errV\|_{max}$ (%)
54	0.96	27.17	0.93	27.25	0.94	17.08
204	1.83	6.38	1.81	6.05	1.81	3.98
459	2.71	0.60	2.72	1.44	2.71	0.93
816	3.66	1.87	3.67	1.57	3.63	1.06

Table 5.4: Cylinder Impact Velocities.

Having identified the velocity of the cylinder top, a similar procedure is performed on the cylinder bottom point position, as determined from the feature identification algorithm. As the results of feature identification are also prone to small errors in the recovered position, due to body surface reflections, the velocity derived from the raw position information can be contaminated with noise. This is eliminated by applying the same butterworth filter as for the velocity derived from the encoder measured position. However, the approach in this case is to filter the position information and then derive the velocity from the filtered position result. The cut-off frequencies for cylinders 2 and 3 were chosen as a function of the natural period of oscillation of the cylinders. It was observed that for a filter corresponding to one quarter of the natural period of oscillation (the occurence of maximum stress), the filter well preserved the evolution of the cylinder bottom position and eliminated any spurious values. Thus, the feature identification position results were filtered at 500 Hz for cylinder 3 and at 267 Hz for cylinder 2. For cylinder 1, however, the same procedure resulted in a cut-off frequency of 96 Hz, which was too low, as it was observed that valid information was being lost, resulting in filtered values of cylinder bottom point position which were much lower than the real values. This trend was present especially for the higher impact speed test cases. Thus, a higher cut-off frequency was used, a value of 190 Hz being found to give good results for all the impact speeds, whilst still producing smooth position results. Figure 5.9 (left) shows the fitted position results as well as the raw feature identification results for all cylinders during an impact test from H = 204 mm. It can be seen that the approximation is very good, and that the curves are almost a perfect match, with the only exceptions when spurious values of the

raw data are encountered.

On the right side of Figure 5.9, the velocity curves resulting from the filtered and unfiltered feature identification results, are illustrated. It can be seen that, even though the difference between raw and filtered position results is very small, after deriving the two data sets to obtained velocity, the differences are considerable. However, the trends are obviously kept after filtering, and, with the exception of a few spurious values given by larger differences in the position information, the magnitudes are comparable as well.

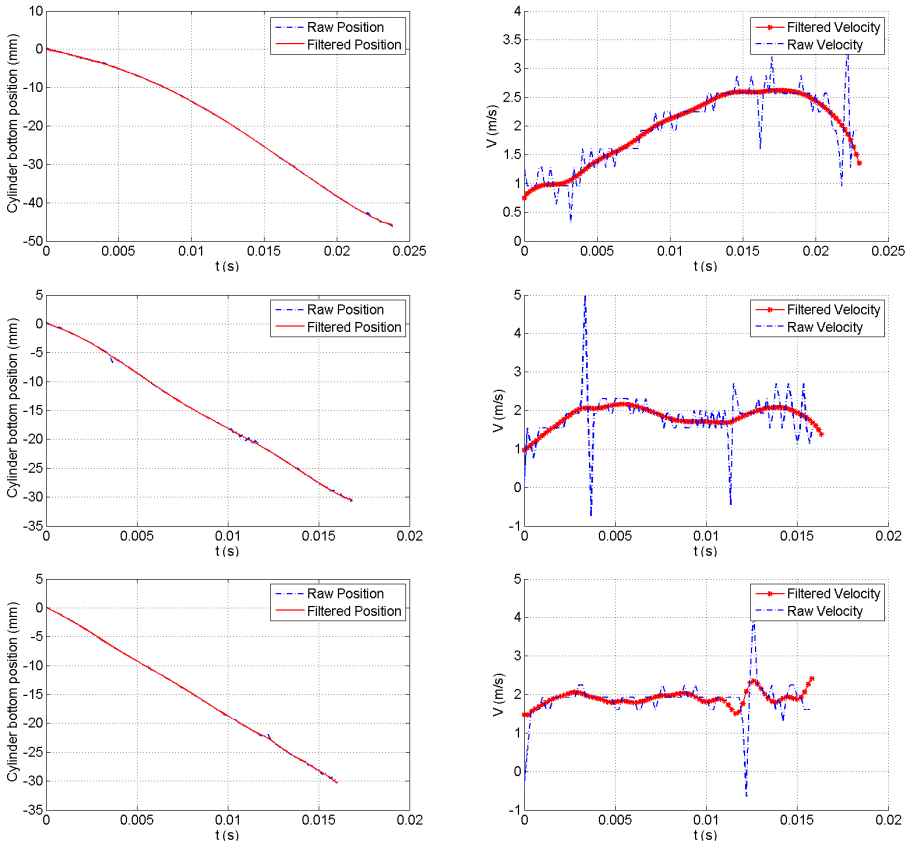

Figure 5.9: Filtered feature identification results and derived velocity of the cylinder bottom for 204 mm drop height tests - top: cylinder 1; middle: cylinder 2; bottom: cylinder 3.

In Figure 5.10, the results of the cylinder top and bottom velocities are compared for the three cylinders for all the tested drop heights. Since the cylinder

bottom cannot be tracked before it enters the water surface, its velocity profile does not show the immediate deceleration at impact. Thus, the cylinder bottom point velocity profiles derived from the feature identification procedure begins 0.2 ms after impact (corresponding to one time step). It should be noted that the cylinder bottom velocity is considered to be equal to the velocity of the cylinder top point at impact ($t = 0$) in the subsequent PIV-based load estimation procedure. Moreover, the cylinder bottom velocities could only be recovered for as long as the cylinder was tracked using the feature identification algorithm, and thus, for both cylinders 1 and 2, at a drop height of 816 mm, the profile is not captured for one entire half of the oscillation period, as for the other cases.

As soon as the cylinder is in the water and can be tracked using the feature identification procedure, the cylinder bottom begins to accelerate and, as expected, its velocity value reaches that of the cylinder top approximately at the same time that the maximum displacement occurs (see Figures 3.12 and 3.11 for comparison). The velocity continues to increase until a maximum value is reached, and then decreases to the value of the cylinder top velocity, as seen in Figure 5.10. In the case of cylinder 3, which has the highest stiffness, its bottom velocity is much closer to the top velocity, as the cylinder does not deform as much during impact.

5.3.2 Forces

The pressure estimation procedure presented in Chapter 4 is used for determining the force acting on the wetted part of the cylinder wall during water entry. By integrating the fluid pressure on the elements in the vicinity of the wall, and under the assumption of a constant distribution over the length of the cylinder, the total force acting on the cylinder body is recovered. Moreover, a second pressure estimation algorithm is tested and comparisons of results from both methods, with the force results of Van Nuffel [87] are performed.

5.3.2.1 Estimation Methods

As previously discussed, the pressure estimation from PIV measured velocity, can be done using the **Poisson** equation for pressure (as described in Chapter 4) or by **direct integration** of the Navier-Stokes (momentum) equation as given in equation 4.1. In this chapter, both methods are used for the estimation of the slamming loads. This is done in order to assess the accuracy and limitations of the two methods with respect to PIV velocity errors, the robustness of the algorithms and their applicability to slamming measurements.

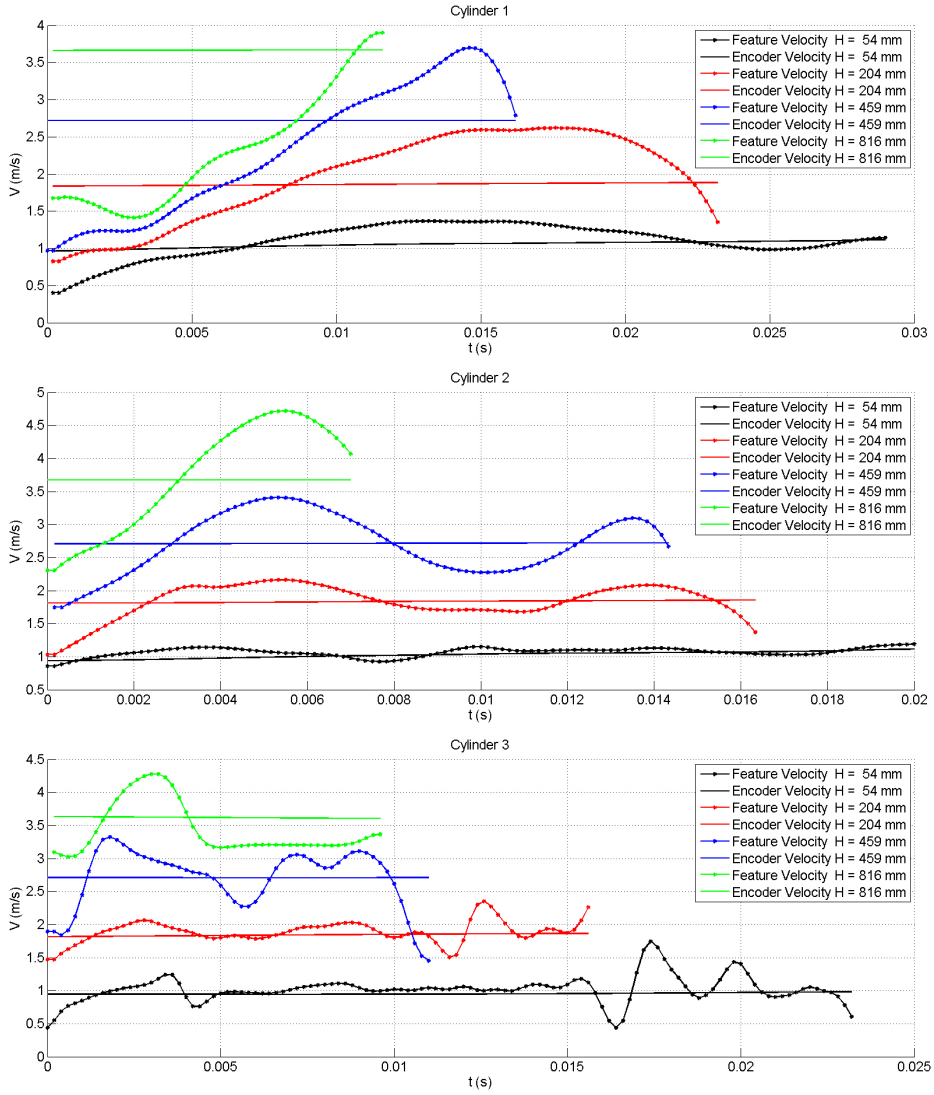

Figure 5.10: Results of cylinder top velocity (filtered from position encoder) and velocity of cylinder bottom filtered position for all drop heights test cases - top: cylinder 1; middle: cylinder 2; bottom: cylinder 3.

By estimating the pressure gradient directly from 4.1, without applying the divergence to obtain the Poisson equation, one can recover the pressure difference between two neighbouring grid points as in equation 5.3. Starting from a known value of the pressure (e.g. atmospheric pressure), and integrating along multiple paths, the pressure field is reconstructed.

$$p_x - p_{x+\Delta x} = \int_{x}^{x+\Delta x} \nabla p dx \tag{5.3}$$

When performing direct integration of the momentum equation, two aspects need to be carefully addressed. The first is the choice of integration paths. Considering that the velocity field used for calculating the pressure gradient in equation 4.1 is measured from PIV, and thus, is prone to errors, the result can be corrupted when these errors accumulate over the integration path. To eliminate these effects, an iterative approach can be adopted, as that proposed by Liu [49], where $2m(n + m) + 2n(2m + n)$ paths are averaged over a grid of m x n grid nodes. The second important aspect when adopting this technique, is the choice of boundary conditions, from which the integration is started. The implementations of these methods typically make use of prescribed boundary conditions on at least one of the edges of the domain as shown by [11], either by having the boundary on a solid wall, or by using the Bernoulli equation to estimate the value of the pressure on an edge if that edge is situated far-field.

For the work presented herein, an implementation proposed by Dabiri et al. [19] is used for the direct integration of the Navier-Stokes equation. The algorithm of Dabiri was developed for a wide range of applications, including quasi-steady state flows and unsteady flows. The robustness of the algorithm was tested in [19] for numerical simulated flows past a square cylinder as well as on PIV measurements of swimming jellyfish medusa and lamprey, with promising results. The method proposed by Dabiri differs from other algorithms in the way the integration of the pressure gradient is performed. Instead of using an arithmetic mean of many integration paths starting from each grid node, the algorithm of Dabiri makes use of the median, which is less sensitive to localized spurious results. Thus, a reduction in computational cost or even higher stability when localized errors are too high, is achieved. Furthermore, the algorithm was preferred due to its implementation of immersed boundaries treatment. The integration paths are left undefined when they cross fluid-structure interfaces, thus making their contribution to the estimated value of the pressure gradient in that node, null. This, in turn, offers the advantage of eliminating any special treatment of the pressure gradient at the solid walls, such as is necessary for the Poisson solver. The results

of pressure estimation from PIV measurements of a swimming lamprey were encouraging for the application of this algorithm in the case of PIV measurements during slamming, especially considering the treatment of the immersed boundaries. In order to avoid the limitations of this algorithm introduced by the use of non-symmetrical boundary conditions (i.e. symmetry line boundary), the PIV measured velocity field was mirrored with respect to the symmetry line. Therefore, a complete velocity field for the entire water tank was used for pressure estimation. Furthermore, to reduce the large computational time required for the integration along multiple paths, the velocity field was not re-sampled on a fine grid. This choice was made after a grid dependency study revealed that the pressure field varied with less than 1 % rms when increasing the spatial resolution by a factor of four.

5.3.2.2 Results

In the following, results of the PIV-based estimated load are compared with the results obtained by Van Nuffel for the same drop test cases. The thesis of Van Nuffel [87] explains in detail the work he performed in estimating the force from sensor measurements and from strain measurements. Therefore, the procedure will not be elaborated further here, but two observations will be made in order to stress the fact that traditional sensor measurements are also subject to careful analysis. Firstly, the *force sensor* measurements represent the unfiltered force results obtained by Van Nuffel from the three load cells he used on the set-up. However, these recordings are not simply the output of the load cells, but also include an additional mass conversion factor which is necessary in order to recover the true force acting on the cylinder body (equation 3.4), which differs from the values recorded at the force sensor locations. As described in [87], the force sensor measurements are contaminated with an important oscillatory component corresponding to the structural vibrations of the impactor. Filtering the results was proven efficient for results of tests performed on cylinders with low stiffness, such as Cylinder 1, and the filtered value of force measured with the load cell matches well with the force estimated from the strain. However, for Cylinders 2 and 3, the higher stiffness of the tubes determines a higher oscillation frequency of the measured force, that approaches the eigenfrequency of the test set-up, rendering the filtering procedure ineffective in producing the correct results without loss of real signal. Secondly, the *force estimated from strain* was calculated by Van Nuffel, as mentioned previously, using finite element simulations of cylinder dynamic loading in order to estimate strain-to-force conversion factors. This was an elaborate procedure which, corroborated with results of experimental static compression

tests, showed that strain gauge misalignments or mounting fixation imprecisions can prevent accurate application of such factors.

Figure 5.11 shows the forces on Cylinder 1 during water entry from the four drop heights used. The red and blue curves represent the results of load estimated from PIV measurements, with the Poisson and the Integral approach, respectively. The solid and dotted lines represent force on the cylinder as estimated from strain and load cell measurements, respectively. It can be seen that, for all the four drop heights used, the PIV estimated load closely matches the strain estimated load. This observation is in accordance with the remarks of Van Nuffel, who noted that the force sensor measurements need to be filtered in order to eliminate the effect of structural vibrations of the impactor.

For all the drop tests of Cylinder 1, the recorded forces are relatively small. The values estimated from strain measurements are ranging from 73 N for the 54 mm drop height test, to about 416 N for the largest drop height of 816 mm. The values of PIV estimated force, using the Poisson approach, closely match the strain estimated ones, with the largest error being 11 % at the largest entry velocity test case, but as low as 0.5 % for the smallest drop height test. In the case of the Integral approach estimations, the results show the same trends, with errors ranging from 1% for the first test case, to 15 % for the last.

Moreover, when observing the time evolution of the force obtained from these three methods, the same behaviour can be noted, with the load increasing to reach a maximum value about 8 ms after impact for the lowest drop height used, and about 12 ms after impact for a drop height of 816 mm.

When comparing these results with the measured force as recorded by the load sensors, it can be observed that the latter has a much higher deviation, with errors of about 50 % for all the drop tests analysed. This higher uncertainty can thus be eliminated only when the structural vibrations can be drastically reduced in the experimental set-up, or when filtering of the raw force measurements can successfully be applied to eliminate biased results.

In Figure 5.12, the forces on Cylinder 2 are plotted for three test cases corresponding to the drop heights of 204 mm, 459 mm and 816 mm. The same general trends are observed as for the results of Cylinder 1. The recorded forces are about 50 % higher than that of the first cylinder drop test cases. Furthermore, the force recorded from the load cells shows a higher relative error compared to the strain estimated force, over-predicting the maximum load by as much as 90 % . Thus, the strain-based estimated force is taken as a reference for the PIV estimation models. The force estimated using the PIV measurements are more consistent with the reference values, with the exception of the last test corresponding to the

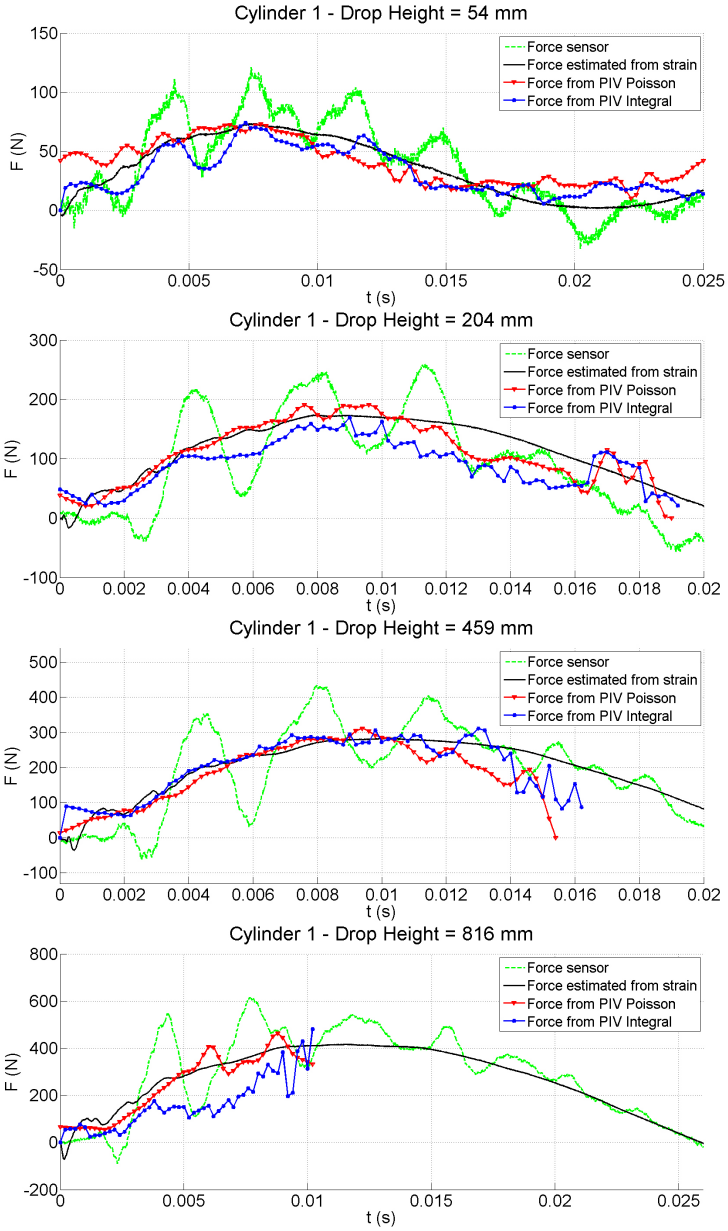

Figure 5.11: Force on Cylinder 1 - results of load cell measurements and force estimated from strain gauge measurements [87]; load estimated from PIV using the Poisson equation (PIV Poisson) and the direct integration of Navier-Stokes equation (PIV Integral) [19].

highest entry velocity. For this last case, the load estimated from PIV keeps increasing after the force estimated from strain measurements reaches its maximum and starts decreasing, about 3.5 ms after impact. Considering that this trend is observed in both PIV-based estimation methods, the errors can only be attributed to errors in velocity measurements, that lead to the shift of the force maximum to 4 ms after impact, at a value 50 % higher than the reference values. The previous two test cases show that the Integral estimation model tends to overestimate the load by less than 10 %, while the Poisson method produces maximum force values of about 20 % lower than the strain estimations.

In the case of cylinder 3, the higher occurring loads, caused by the increased stiffness of the cylinder, imply that an even higher error between strain estimated force and load cell measurements is present. Moreover, the increased oscillation frequency of the cylinder which approaches the eigenfrequency of the test set-up, implies that correct filtering of the raw data becomes difficult. Therefore, when comparing the maximum force sensor measured load with that of strain-based estimations of the load, a factor of two difference is observed for all considered test cases. This is caused by the high uncertainty of the classical sensor-based measurements of slamming force.

Figure 5.13 shows the force on Cylinder 3 for the three test cases of 204 mm, 459 mm, and 816 mm drop heights, respectively. In general, the same trends as observed for Cylinder 2 are present. The reduced oscillation period of the cylinder and the higher fluid velocity are responsible for the higher error between PIV estimations and strain-based values. The two aspects have a direct effect on the material acceleration term of the Navier-Stokes equation which is ultimately used in the pressure reconstruction algorithms. With reduced period of oscillation - 6 ms compared to 20 ms in the case of Cylinder 1 - the fluid acceleration is much higher in the first 3 milliseconds of water entry. Thus, the 5 kHz PIV recording frequency can be a limitation when trying to resolve these fluctuations. Furthermore, the pressure distribution on the stiffer cylinder body exhibits a higher peak in the spray root region of the flow, a peak that can not be captured using PIV, and which can have an effect on the integrated value of the load.

5.3.3 Slamming Coefficient

The slamming coefficient results for the small cylinders test cases are in accordance with the observations made in the analysis of force-time histories. The slamming coefficient is a dimensionless parameter defined using equation 5.4, and which is used in literature as a way to compare the slamming loads on structures with different geometries and/or entry conditions. The expression of this coef-

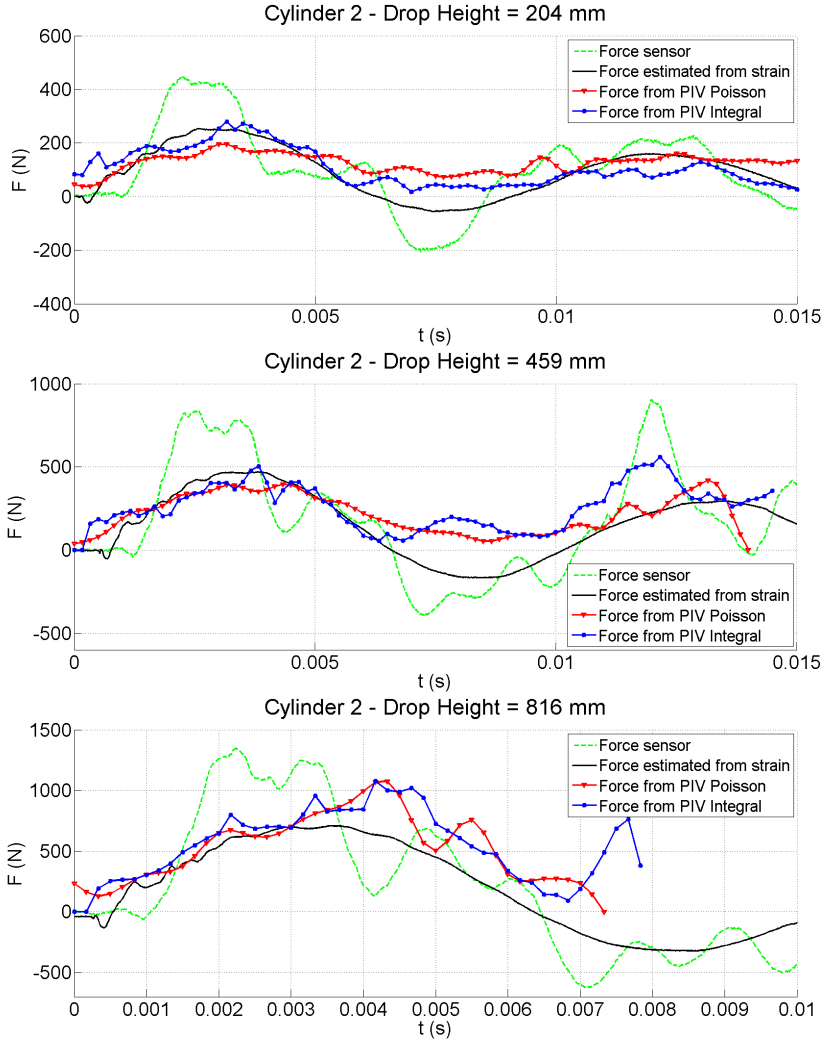

Figure 5.12: Force on Cylinder 2 - results of load cell measurements and force estimated from strain gauge measurements [87]; load estimated from PIV using the Poisson equation (PIV Poisson) and the direct integration of Navier-Stokes equation (PIV Integral) [19].

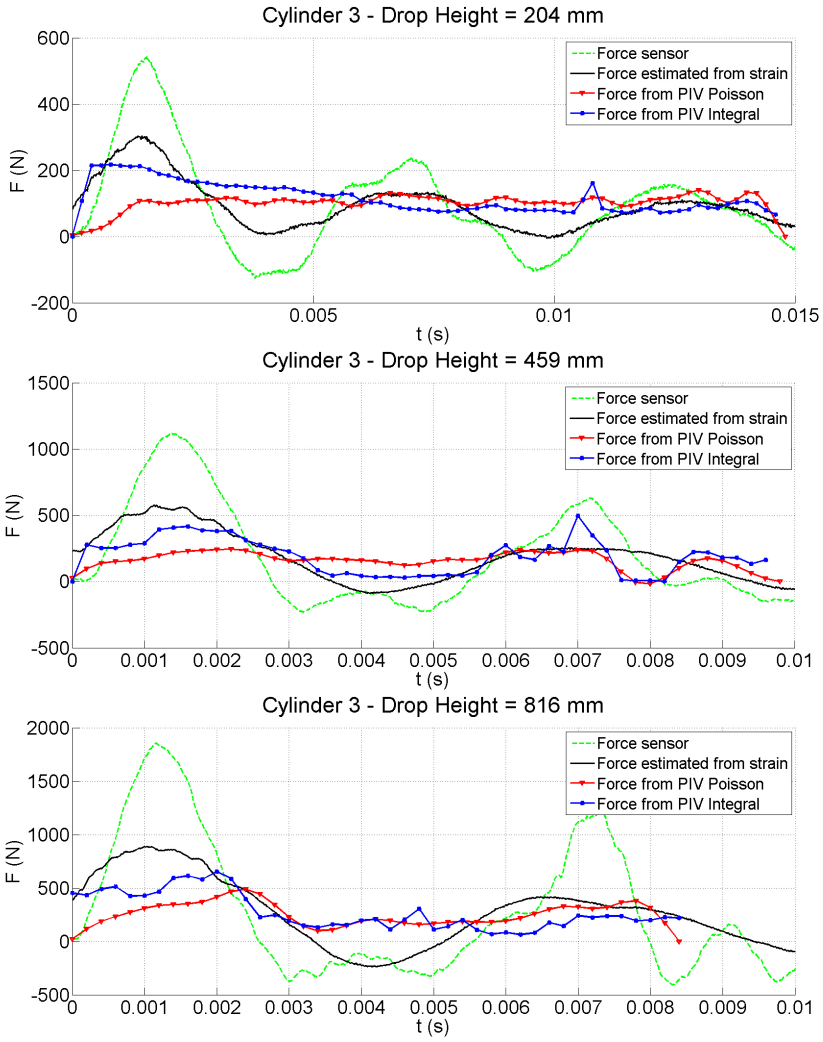

Figure 5.13: Force on Cylinder 3 - results of load cell measurements and force estimated from strain gauge measurements [87]; load estimated from PIV using the Poisson equation (PIV Poisson) and the direct integration of Navier-Stokes equation (PIV Integral) [19].

ficient is derived from the definition of the slamming load, which is the force needed to displace a certain volume of water.

$$F_{impact} = \frac{d}{dt}(mV_{entry}) = \rho RLC_s V_{entry}^2 \tag{5.4}$$

The slamming coefficient (C_s) is expressed as a function of the load (F_{impact}), fluid density (ρ), cylinder geometry - radius R and length L - and cylinder velocity (V_{entry}). As the cylinders considered here are deformable, their velocity differs for different points along the cylinder surface. Moreover, it was shown that the cylinder top point evolution in time is approximately constant throughout water entry, while the bottom point has a profile which considerably varies in time (from the deceleration immediately following the impact, to the increase up to a value of even 30 % higher than the top point velocity). Considering that the expression of the force should be dependent on the submerged part of the impacting body, the velocity of the wetted part of its circumference would need to be introduced in equation 5.4. By using the time history of the cylinder bottom velocity, results of the slamming coefficient for the Cylinder 1 are shown in Figure 5.14.

It can be observed that the distribution of the slamming coefficient differs from that of the acting load, with the maximum value shifting towards the beginning of the water entry (around 4 ms after impact, as opposed to the maximum load value occurring 10 ms after impact). If the velocity of the top point of the cylinder, which is approximately constant, would have been used in expression 5.4, this behaviour would no longer be observed.

In Figure 5.15, the maximum slamming coefficient is plotted for the three small cylinder test cases as a function of the impact velocity. The figure shows the maximum values obtained by Van Nuffel [87] (strain-based results) and those estimated from PIV using the two techniques. It should be noted that, for reasons of comparison, all the slamming coefficients are calculated using the cylinder top point velocity. It can be seen from this figure that the best results are indeed obtained for Cylinder 1, as the PIV estimations using both methods match quite well with the strain based results. For Cylinders 2 and 3, the deviation of the PIV results from the strain results is increasing, suggesting that limitations of the PIV methods occur when stiffer bodies are considered. This was again observed in the force-time histories analysis, and is mainly caused by the accuracy of the PIV measurements and estimation models.

In Figure 5.16, a comparison is made between the results obtained from strain-based estimation of load for all three cylinders. The graph shows two sets of points calculated by introducing in equation 5.4, the velocity of the cylinder top point and of the cylinder bottom, respectively. It can be seen that the decrease

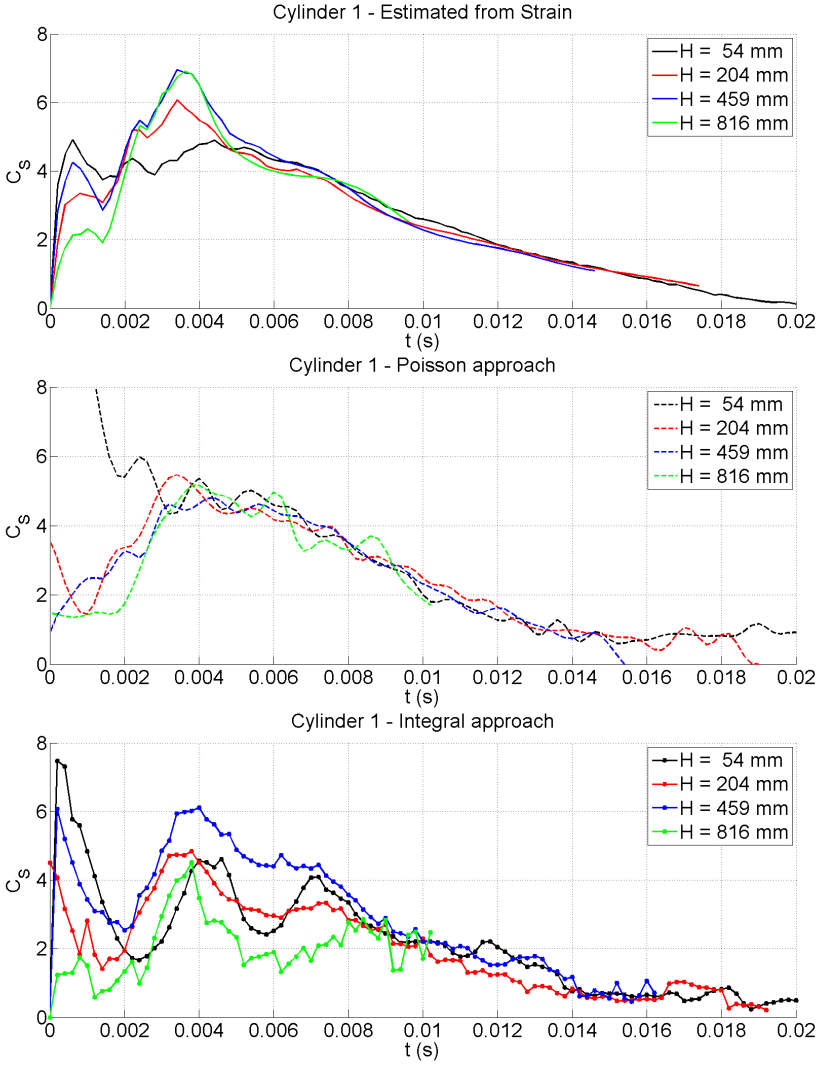

Figure 5.14: Slamming coefficient (C_S) on Cylinder 1 - top: estimated from strain gauge measurements; middle: estimated from PIV using the Poisson equation (PIV Poisson) and bottom: estimated from PIV by direct integration of Navier-Stokes equation (PIV Integral).

of the slamming coefficient values with decreasing cylinder stiffness is no longer applicable (when using the cylinder bottom velocity). It is thus believed that the C_s values should be equal when this distinction occurs. From the figure, it can be observed that this is not exactly the case. The explanation for this behaviour

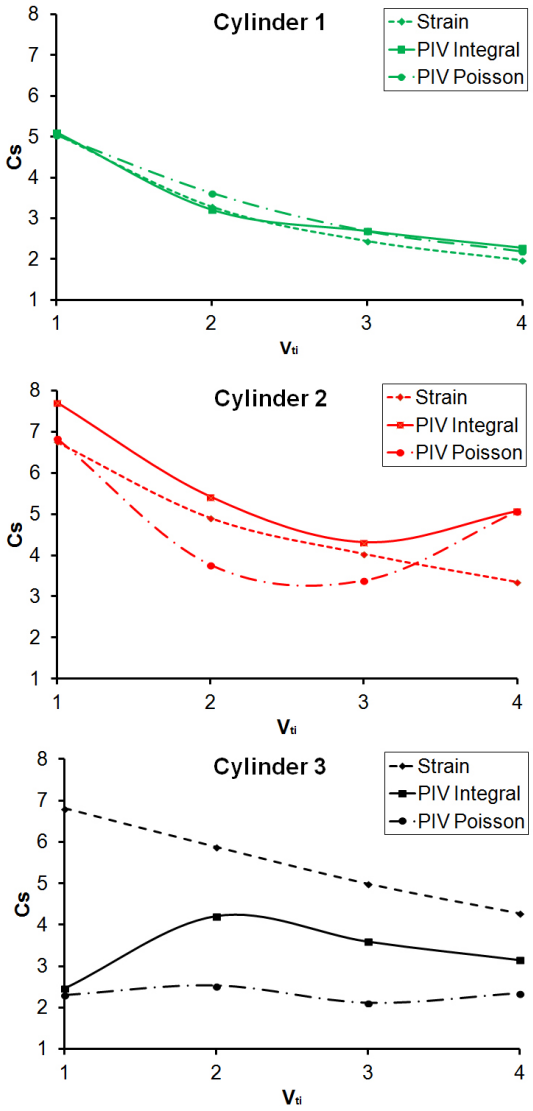

Figure 5.15: Maximum slamming coefficient values on the three small cylinders - comparison of the maximum coefficient using the cylinder top point velocity between strain-based estimations, and PIV estimation using the Poisson equation (PIV Poisson) and direct integration of the Navier-Stokes equation (PIV Integral).

must lie in the limitations in resolution of the feature identification technique, which has an uncertainty of the measured displacement of 0.128 *mm* for the used magnification factor (M = 7.8 pix/mm). Although this value is quite small, after deriving to determine the body velocity, which is then squared in the expression of the slamming coefficient, the errors are increased.

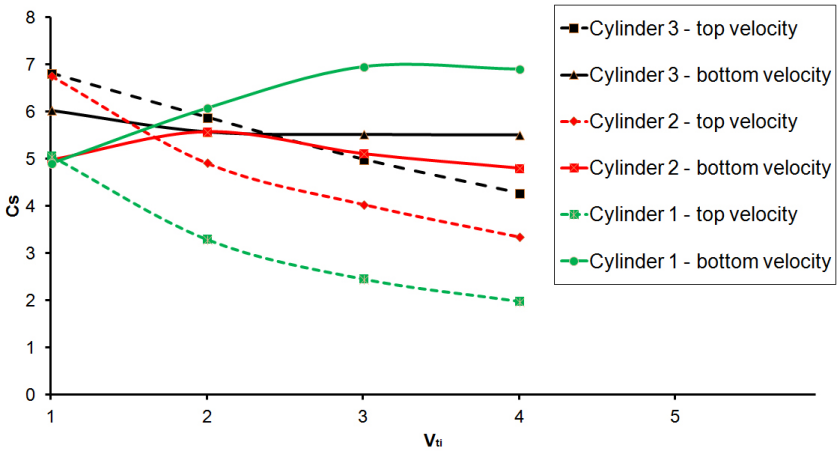

Figure 5.16: Maximum slamming coefficient values on the three small cylinders as estimated from strain gauge measurements - comparison of the results obtained using the cylinder top point velocity and using the bottom point velocity.

5.4 Large Diameter Cylinder Slamming

The large diameter cylinders, noted in Table 5.1 as Cylinder 4 through 7, were tested using the same slamming experimental set-up described above. For cylinders 4 and 5, in order to achieve a large field of view (FOV) of the PIV measurements, the two high-speed cameras were used in a side-by-side configuration. The cameras were installed on a support that was positioned at different heights in order to record different areas of the FOV. The PIV measurements were performed for each cylinder, at each drop height, three times, corresponding to three different positions of the cameras. The small error of the entry velocity profile, as well as the zero-position triggering, allowed for an accurate estimation of the velocity field using three separate measurement sets. With the help of pre-test calibrations

using a marked target, the exact position of each camera frame is recovered. In Figure 5.17 (left), the respective FOV of each camera is illustrated.

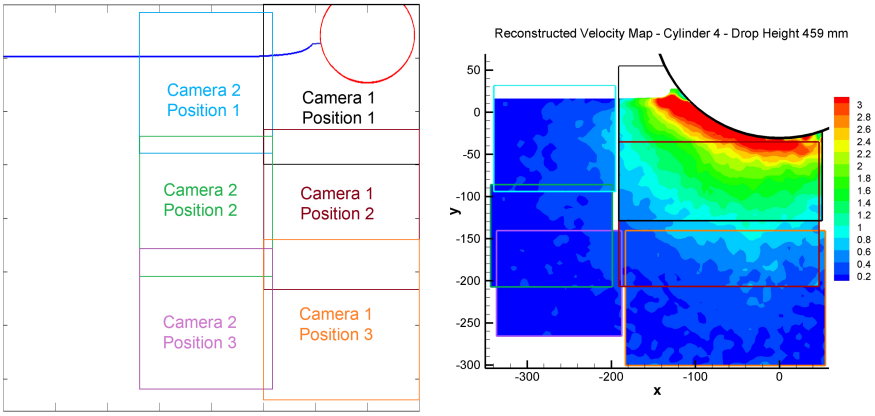

Figure 5.17: Cylinder 4 and 5 PIV measurement positions of the two cameras. Left: the three positions of the cameras are marked; Right: example of resulting velocity magnitude for Cylinder 4 (drop height H=459 mm; time step t = 15 ms).

It can be observed that the positioning of the cameras allows for an overlap that accounts for loss of information at the frame edges, as expected when performing correlation analysis on the PIV images. An example of a velocity map recorded for Cylinder 4 is shown in Figure 5.17 (right), where the recordings of each camera are overlaid on a common grid. The example depicts the added value of using such a technique for increasing the PIV measurement FOV, as well as the viability of the method when reconstructing the final large grid. The procedure thereafter is to use a *nearest neighbour* 2D interpolation of the data on a final grid, having a resolution equivalent to that of the smallest measured PIV grid. For convenience, the implementation of this procedure was performed in *Matlab*, using the built-in function *griddata*.

It should be noted that, even though the reconstructed grid did not extend up to the physical boundaries of the water tank, the domain limits were far enough to consider the flow irrotational at the boundaries. This was a choice of experimental arrangement considered with regard to the PIV pressure estimation algorithm. As discussed in the previous section, the alternative *Integral* approach suggested by Dabiri [19] presented the advantage of independence of the estimated pressure

result with respect to the imposed boundary conditions. Therefore, only the results of this algorithm will be presented in this section, and shall be referred to as PIV estimated load. Moreover, the measurements performed during the water entry of cylinders 6 and 7 did not require the additional grid reconstruction procedure, and only the first camera recordings were used.

In Table 5.5, the PIV measurements parameters are given for each of the cylinders tested. It should be noted that all of the measurements on the large cylinders were performed using a recording frequency of 6 kHz. Furthermore, to account for larger displacements at higher entry velocities the interrogation window size was varied from 24 x 24 pix to 48 x 48 pixels. These limits are given as the extreme values used in the processing of the data, with mean values of the window size being the 32 x 32 pixels choice. The window overlap factor was also varied from 50 % overlap to 62 % overlap at higher interrogation window size values.

	Cylinder 4	Cylinder 5	Cylinder 6	Cylinder 7
Camera 1 magnification [pix/mm]	4.1	4.1	3.5	3.5
Camera 2 magnification [pix/mm]	4.85	4.85	-	-
Final Grid spacing [mm]	3.9	3.8	3.43	3.33
Final Grid size [mm]	393 x 355	387 x 377	284 x 274	281 x 190
Final Grid nodes	8004	9000	6640	4312

Table 5.5: Large diameter cylinder parameters.

5.4.1 Cylinder Displacements and Velocity

Following the same steps as described for the small diameter cylinder tests, the feature identification cylinder displacements results are obtained. A fixed cut-off frequency of 100 Hz was considered for the low-pass filter applied to the feature identification result of cylinder bottom position in order to obtain the velocity profiles. The results again show that, for the higher entry velocities, the feature identification results have a time span limitation due to the cylinder leaving the

recording FOV. Even though a lower magnification factor was used in order to increase the camera FOV, the cylinder diameter was considerably larger than that of the first three cylinders, and thus the recovered information could only be extracted for a limited amount of time. It should be noted that, even though for Cylinders 4 and 5, the FOV was extended after using the stitching procedure of multiple camera positions, the feature tracking algorithm was only applied for measurements of the first camera position that captured the free surface profile in the frame. Additional use of the second and third camera position recordings in the feature identification step could have lead to an increase of the measurement time sequence.

In Figures 5.18 and 5.19, the displacement and derived velocity results of the feature identification algorithm are illustrated for the PVC large diameter cylinders. Cylinder 4, which has the largest stiffness of the large cylinders considered here, also presents the smallest recorded displacements, ranging from approximately 1 mm for the lowest entry velocity of 1 m/s, to about 6.24 mm for the 2.88 m/s drop test case. In the results presented here, the largest drop height used (H = 816 mm), is not included due to the limited time during which the cylinder is tracked. In this case, the cylinder deformation does not reach its maximum value before the feature leaves the FOV.

The cylinder bottom point velocity is also plotted along with the velocity profile of its top point, as derived from the position encoder - Figure 5.18 (bottom). It can be observed that the velocity of the cylinder bottom is consistently approaching the profile of its top point, especially when compared to the other large cylinders, for which the deceleration during water entry is much larger. This can be observed in Figure 5.19 (bottom), where the velocity profiles for cylinder 5 are exemplified for the four drop tests considered. As the cylinder displacements increase from the previous case, ranging from 3.5 mm to approximately 23 mm, the deceleration of the cylinder bottom becomes more obvious. It can be observed that, for the case of cylinder 5, the measurement time for the highest two drop heights is not sufficient to capture the peak of displacement. Also, for the case of the 204 mm drop height, the cylinder evolution is tracked until just after this peak of 9.1 mm deflection is reached. These observations explain the cylinder bottom point velocity profiles, which for the third and fourth case, does not reach the value of the encoder derived velocity.

As mentioned previously, the last two cylinders tested are composite material bodies. The results of cylinder displacements and velocity profiles are presented in a similar way as for cylinders 4 and 5, in Figures 5.20 and 5.21, respectively. Cylinder 6 has the lowest stiffness of the large cylinder bodies, and thus presents the highest recorded displacements, reaching up to 110 mm recorded deflection,

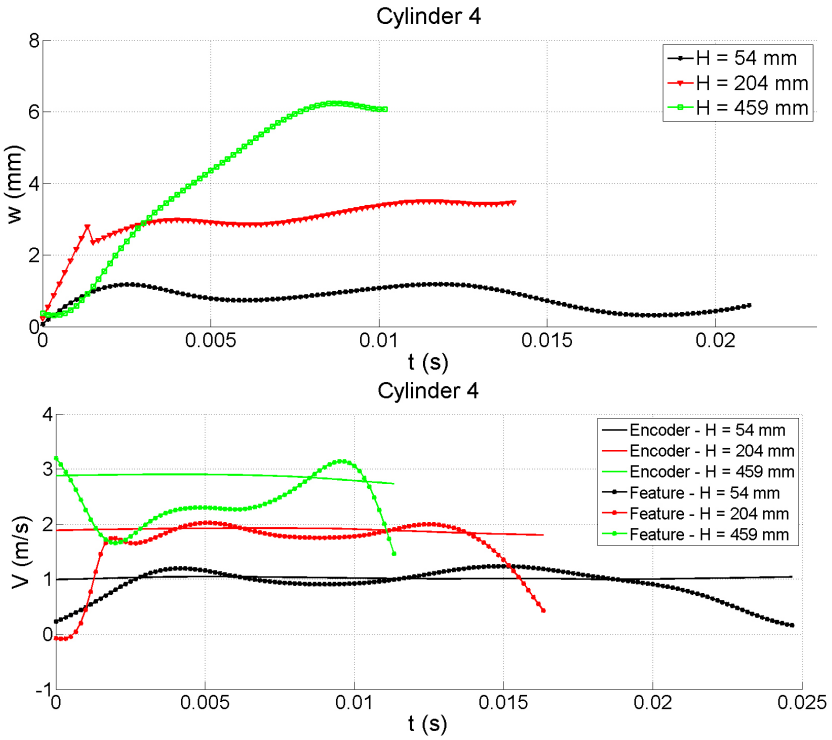

Figure 5.18: Cylinder 4 feature identification result of vertical displacement (top) and cylinder top and bottom velocities (bottom).

which is more than one third of its diameter. Due to this low stiffness, the cylinder displacement keeps increasing up to the point when the impactor structure hits the dampers. Even though in the feature identification results, this is not that obvious, raw pictures of the cylinder entry showed this to be true, and the force recordings of Van Nuffel [87] confirmed the observation, as the force time histories showed a continuous increase up until the structures stops.

In the first drop test for cylinder 6 (H = 54 mm), the cylinder displacement and recorded force seem to reach an upper limit around 40 ms after impact, but the cylinder continues its water entry for the next 40 ms without returning to its original, undeformed shape, as is the case with the other cylinders studied here. This also explains the cylinder bottom point velocity profiles, which all present the same evolution in time, without a noticeable acceleration after initial penetration. Furthermore, it was observed that cylinder 6 deforms in an unusual way for the higher drop heights used. For a drop height of 816 mm, the cylinder shape after impact evolves in a manner which can no longer be approximated using an ellipse

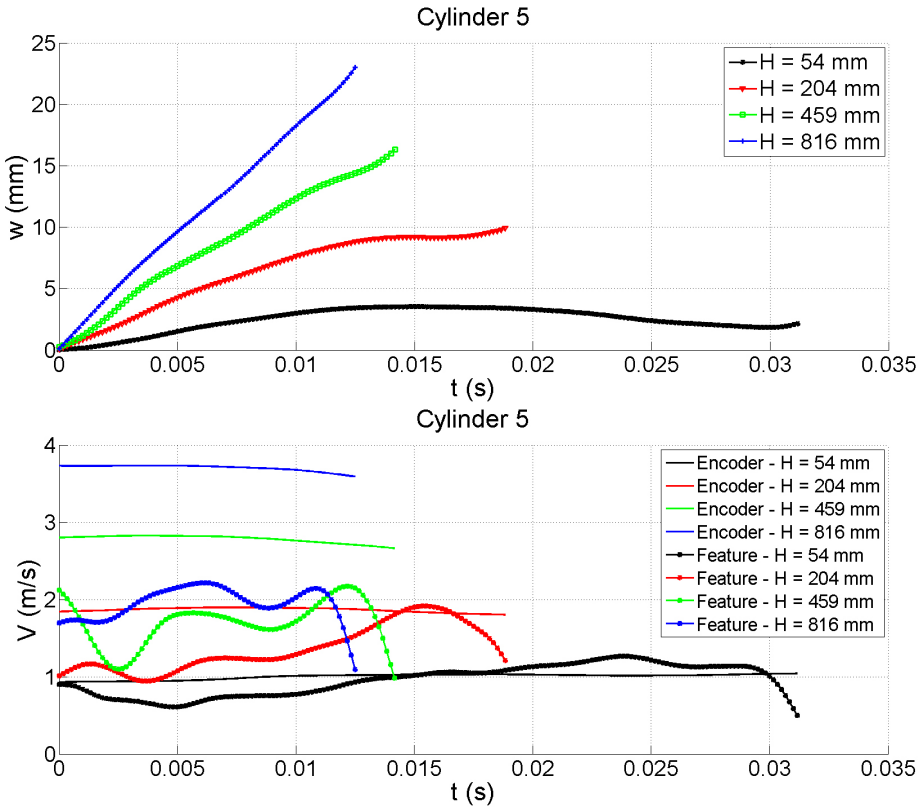

Figure 5.19: Cylinder 5 feature identification result of vertical displacement (top) and cylinder top and bottom velocities (bottom).

shape, and even though the results can still predict the position of the cylinder bottom point, the assumptions made during the feature identification stage can no longer be applicable.

The results of the cylinder 7 displacements which are shown in Figure 5.21 present similar trends as those observed for the small cylinder tests and for cylinders 4 and 5. The oscillation period for cylinder 7 is around 80 ms, with the maximum loads occurring around 20 ms after impact. Even though, for the larger drop heights, the time sequence of the feature tracking results is decreasing, it is still possible to observe the maximum displacement values, which range from approximately 6 mm to about 32 mm for the largest entry velocity. One other remark can be made on the small amplitude oscillations present in the displacement results, which are amplified in results of cylinder velocity - Figure 5.21 (bottom). This behaviour seems to be caused by the material properties of the cylinder which

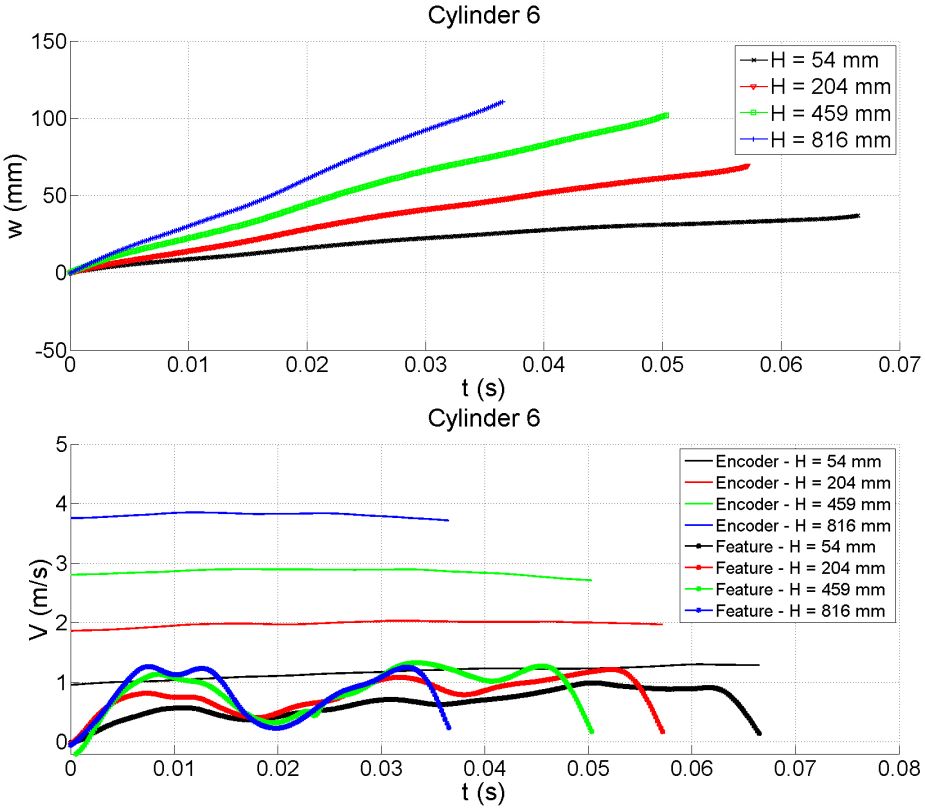

Figure 5.20: Cylinder 6 feature identification result of vertical displacement (top) and cylinder top and bottom velocities (bottom).

is manufactured using filament winding. This means that the stress distribution in the cylinder is different from that for the PVC cylinders bodies. However, the reduced amplitude of the oscillations means that there is no noticeable increase in the cylinder displacements and the results are comparable to those of cylinder 5, which has a similar stiffness.

It should be noted that, for all large diameter cylinder testing, the velocity profiles of the cylinder top point show a larger deviation from the constant value of the impact velocity. This behaviour is caused by the higher occurring forces on the large cylinders than the small diameter ones. Due to these increased loads, the structure decelerates, especially for the test cases using the larger drop heights of 459 mm and 816 mm.

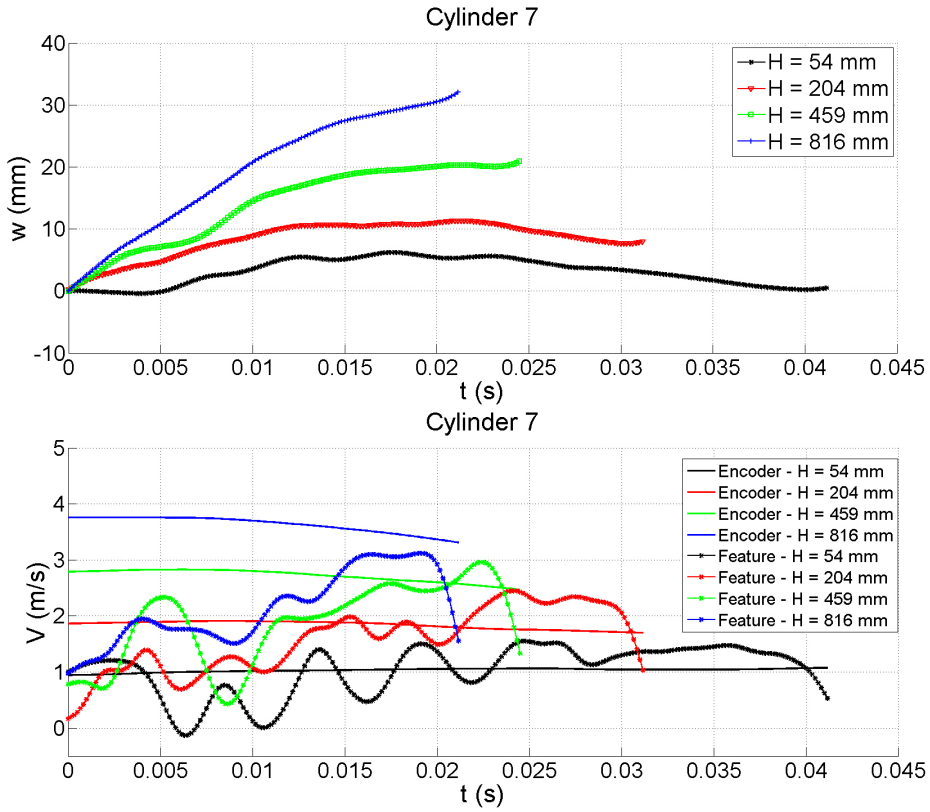

Figure 5.21: Cylinder 7 feature identification result of vertical displacement (top) and cylinder top and bottom velocities (bottom).

5.4.2 Forces

The force-time histories are obtained from integrating the pressure obtained from the PIV-based estimation on the cylinder wall, as in the case of the small cylinder tests. As mentioned previously, the Integral approach was used for this purpose, because of its flexibility regarding the specification of boundary conditions. In the following, the results are presented and compared with the results of Van Nuffel [87], as was done in Section 5.3.2. As concluded by Van Nuffel, the filtering of raw data from the force transducers, in the case of the large cylinder tests, produced more reliable results than for the small diameter cylinders. His conclusion was based on the observation of the amplitude spectrum of the force and of the strain recordings, which showed a clear separation of the peaks corresponding to cylinder deformations from those corresponding to structural vibrations of the

impactor. This enabled the use of a low-pass filter to the force sensor data, which was not as straight forward in the case of the small cylinder tests. Therefore, in the following, an inclusion of both raw measured force and filtered results is considered for the comparison of the PIV estimated load. Van Nuffel [87] considered the filtered force results as the reference for extracting the impact load values, and thus, the present analysis is focused on comparisons with these results.

In Figures 5.22 and 5.23, force-time histories for the two large PVC cylinders are illustrated for three drop heights test cases. The tests performed from a drop height of 816 mm are not included in this analysis due to the limited time history of the PIV measurement. The force estimated from PIV is compared with the force sensor raw and filtered data, and with the force estimated from strain. The strain data used by Van Nuffel to estimate force by using strain-to-force conversion factors was measured by a strain gauge located at the bottom of the cylinder (0°), on the inner surface, in the mid-plane of the tube. From Figure 5.22 a first conclusion can be drawn that, similar to the cylinder 3 tests, in the case of higher stiffness cylinders, the PIV estimated load is under-predicted when compared to the measured force. A closer look to these results leads to the conclusion that, even though the match between filtered force and strain estimated force seems to be overall quite good, an important deviation of the maximum predicted load is still present. The relative error between the two ranges from 5 % for the 459 mm drop height test to 14 % for the lowest entry velocity case, with the strain estimated load consistently higher than the filtered result. When looking at the PIV estimated load, it can be seen that the maximum values are lower than the filtered results, and increase with increasing entry velocity from about 21 % to just over 41 %. This observation supports the remarks on error sources for these results are mainly caused by increased material acceleration which occurs with increasing entry velocity, especially for stiffer bodies. However, it should also be noted that the deviation of the raw force result from the filtered one is much higher, with maximum loads of even 2.7 times higher.

For the case of cylinder 6, the comparison of the results show a different behaviour of the force-time histories. The maximum load estimated from the strain measurements, and that estimated from PIV seem to match quite well, whilst being up to 50 % lower than the filtered force sensor result. This implies one of two possible causes. On the one hand, the filtering procedure might not be very accurate for the analysis of results for this cylinder, because of a shift in the frequencies of body deformation closer to those of the structural vibrations. Another possibility might be the inaccurate results from the strain gauges due to misalignment or mounting imprecisions. This latter conclusion can be supported by the remark that during the experimental test runs, the strain gauge failed after several runs with a

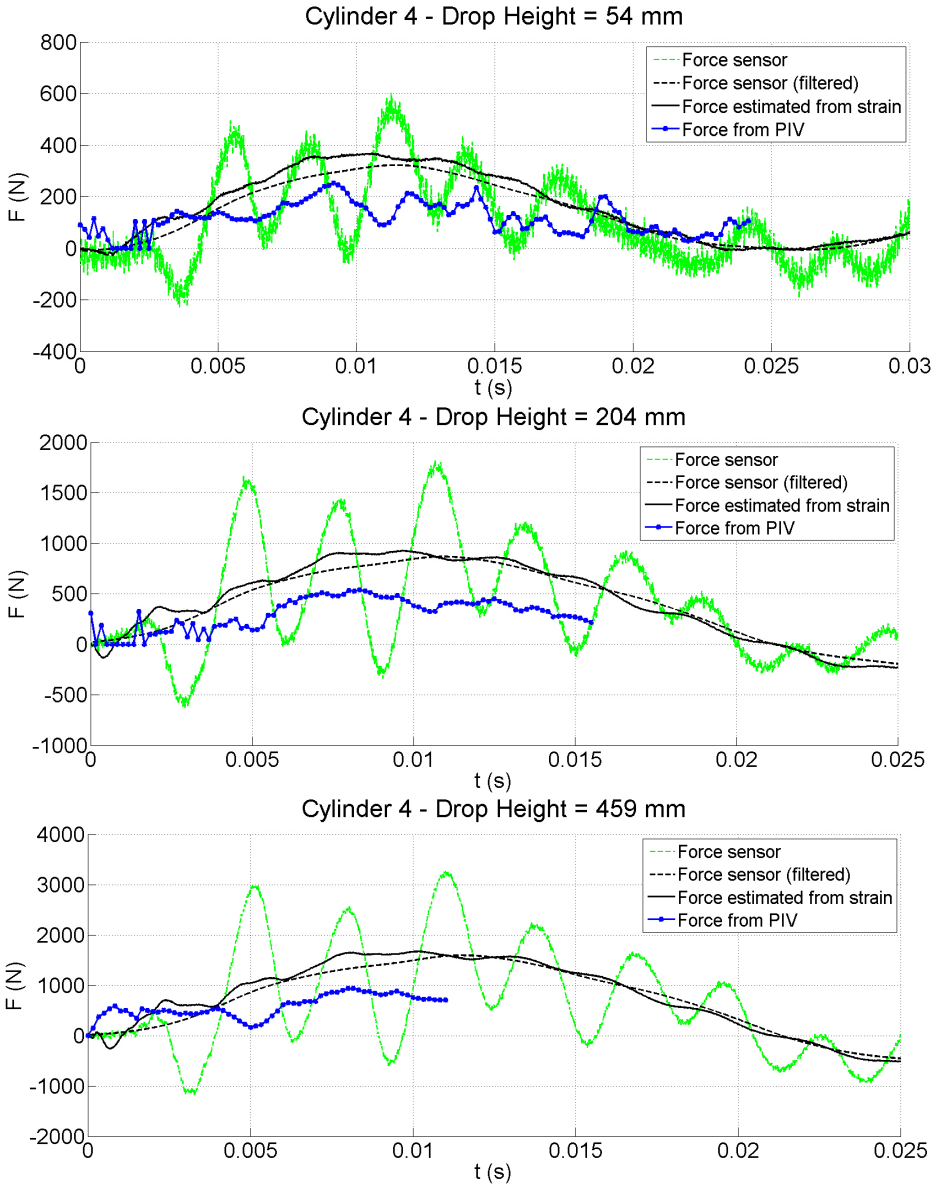

Figure 5.22: Forces on Cylinder 4 for three test cases (drop heights: H = 54 mm; 204 mm; 459 mm) . Forces obtained from PIV pressure estimation are compared with the filtered force sensor measurements and strain estimated force.

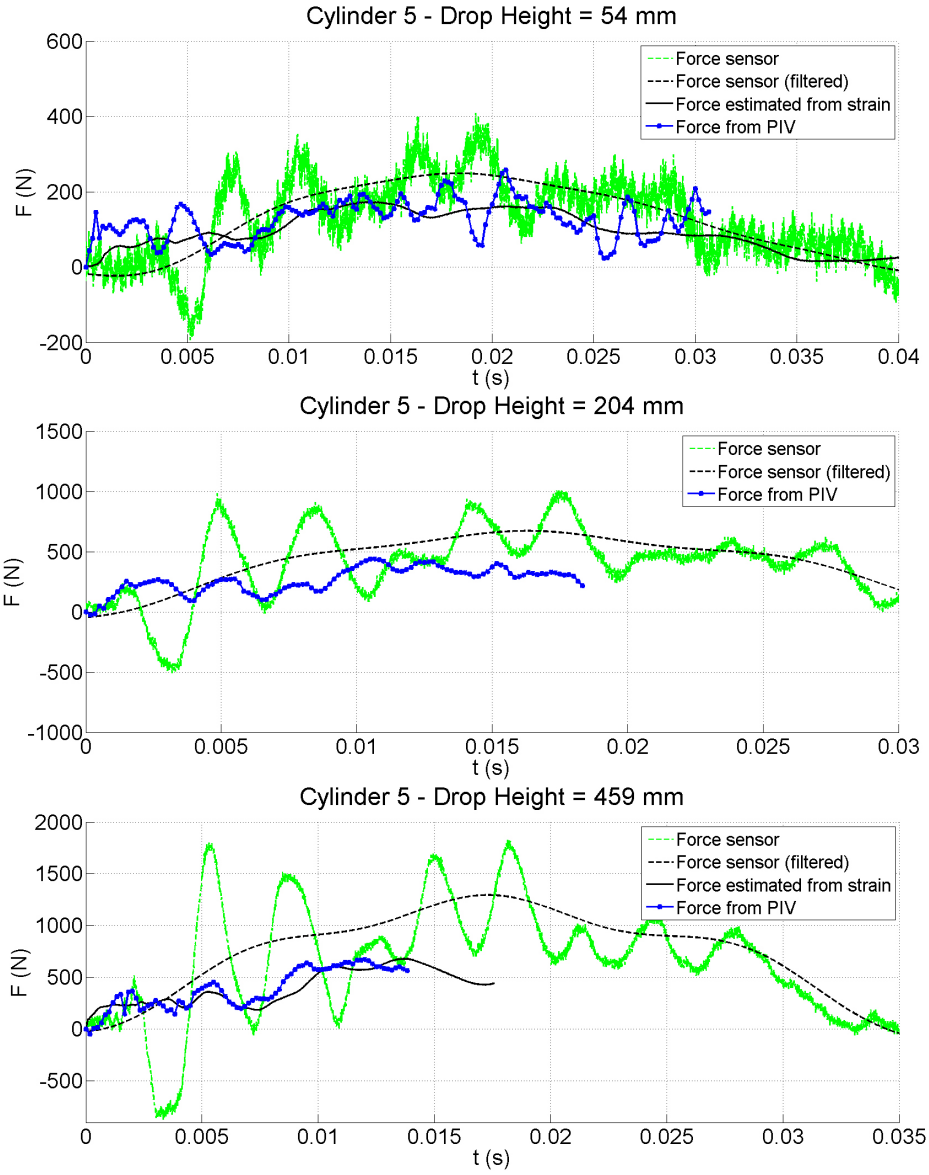

Figure 5.23: Forces on Cylinder 5 for three test cases (drop heights: H = 54 mm; 204 mm; 459 mm). Forces obtained from PIV pressure estimation are compared with the filtered force sensor measurements and strain estimated force.

higher entry velocity. This was caused by the large displacements of the cylinder which, in combination with an improper mounting of the strain gauge ultimately caused it to break. Thus, measurements before this failure occurred, could have also been prone to errors. Nevertheless, the PIV estimated load shows a maximum value 3 % higher than the filtered force for the lowest entry velocity case, but 34 % and 48 % lower for the later two cases, respectively. Again it is worth to note that the unfiltered force can produce maximum loads of up to 2 times higher than the filtered ones.

For the composite cylinders tests, the force estimated from PIV is compared with the load cell measured force and force estimated from measurements of two strain gauges [87]. The strain gauge referred to in the following as *strain gauge 1* is installed at the bottom of the cylinder, the same as in the case of the PVC large cylinders, while *strain gauge 2* is located at the side of the cylinder - 90° - on the inner surface, in the mid-plane of the tube. Figure 5.24 shows the force-time histories for Cylinder 6, for a drop test of 54 mm height.

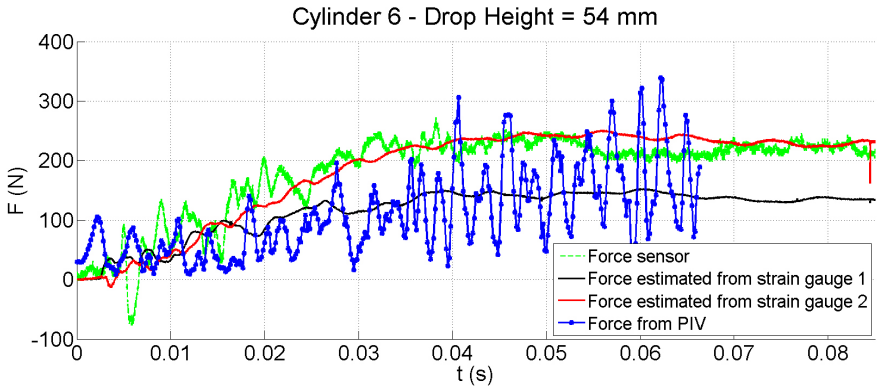

Figure 5.24: Forces on Cylinder 6 for one test cases (drop height: H = 54 mm). Forces obtained from PIV pressure estimation are compared with the filtered force sensor measurements and strain estimated force.

As mentioned previously, the flexible cylinder does not return to its undeformed shape before the impactor reaches a halt. The impact load is absorbed by the deformation of the cylinder, and for higher entry velocities the load keeps increasing for the entire 80 ms that the cylinder moves through the water. For this small drop height, a maximum force is reached approximately 40 ms after impact, and remains approximately constant before a slow decay is observed about 70 ms after impact. The result of the PIV estimated force again matches quite well with the estimation using measurements of the strain gauge located at the bottom of the

cylinder, even though a high frequency oscillation is present in the former. These oscillations can not be a physical manifestation and are attributed to the errors in PIV estimated pressure, which stem from errors of the measured fluid velocity, and which are amplified during integration.

In Figure 5.25, the force-time histories for Cylinder 7 are compared using results of the same methods as for cylinder 6. In this case, the force curves are in better agreement than for the other large cylinders. As noted previously, the displacement time history for this particular test tube showed a secondary oscillatory behaviour caused by the way in which the anisotropic nature of the composite material affects the response of the cylinder to the loading. This effect is also present in the force time history, and should be noted even though the oscillations have a small amplitude. This effect could be amplified if the cylinder stiffness is increased. The results of the 54 mm drop height test case show a strange behaviour of the force estimated from the 90° strain gauge similar to the result of the Cylinder 6 drop test. However, at the higher entry velocities, the profiles match reasonably well between the two strain gauges, as well as the PIV estimated force and the load cell measurements. The relative error between the PIV estimation of the impact force and the bottom strain gauge estimated maximum load is less than 2 % across all the three test cases. Moreover, the relative error between these two results and the filtered maximum load is less than 20 % for all cases.

5.5 Conclusions

It was shown in this chapter that the PIV method can be used for estimation of the loads acting on a deformable cylinder body during slamming. The analysis of results for various test tubes, with diameters of approximately 90 mm and 315 mm, respectively, and with various cylinder stiffness, was done. The PIV-based estimations of load were compared with the results of force sensor measurements as well as strain based estimations of the load.

One first conclusion is that the results of PIV-based methods are better when cylinders with low stiffness are considered. When the bodies are more rigid, the PIV estimated loads are lower than the expected values because of the increase in fluid acceleration that causes a larger pressure peak in the early stages of the water entry. As concluded in Chapter 4, the PIV technique presents limitations in capturing this pressure peak, thus resulting in lower values of the estimated force. However, when comparing the results with unfiltered load cell measurements and with force estimated from strain gauge measurements, it can be found that the relative error in this case is larger than that between PIV and strain estimations.

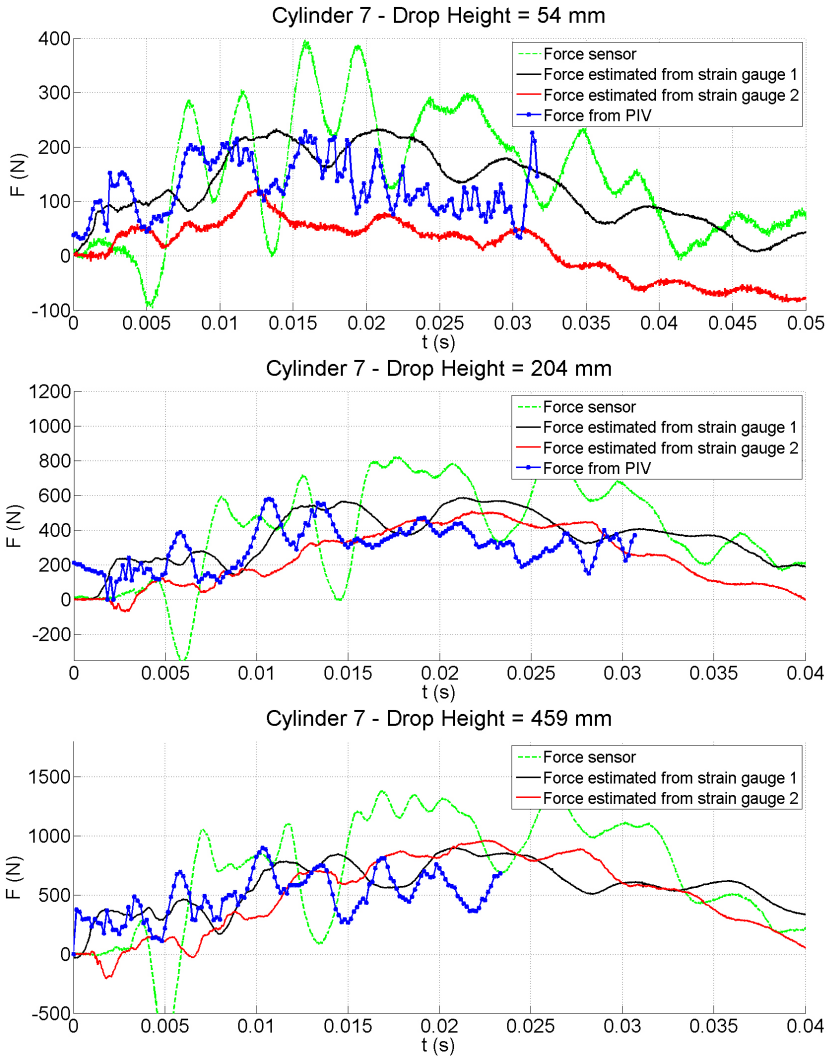

Figure 5.25: Forces on Cylinder 7 three test cases (drop heights: H = 54 mm; 204 mm; 459 mm). Forces obtained from PIV pressure estimation are compared with the filtered force sensor measurements and strain estimated force.

Therefore, it can be concluded that even though PIV does present certain limitations under particular conditions of the water entry, it does also present advantages in its application to slamming studies. The first advantage is that, by performing measurements in such a non-intrusive way, the flow physics is undis-

turbed. Secondly, the relative error between PIV results and strain based estimations is lower than the deviation of force sensor measurements. This implies that PIV can offer an alternative to experimental investigation of slamming, when vibrations of the impacting structure are large and produce biased results of load cell measurements. Furthermore, one should take into account that the estimation of force from strain is a procedure that also requires attention and effort, and that it is prone to mounting imprecisions of the sensor which can lead to erroneous results or even the failure of the sensor. This aspect should also be considered when the choice of measurement technique is made based on the flexibility that the method confers.

Chapter 6

Conclusions and Future Work

6.1 General Conclusions

This thesis presents the research work performed on the experimental investigations of water entry (*slamming*), using the Particle Image Velocimetry (*PIV*) measurement technique. The main objective of this work was to identify whether the application of the PIV technique to the study of slamming can offer further insight into this topic, especially for the case of deformable bodies slamming. According to the author's best knowledge, the use of PIV measurements in the study of deformable bodies water entry has not been previously attempted. Therefore, several steps were taken in this research work, to ensure both the feasibility of the method, as well as the interpretation of its main advantages and drawbacks compared to classical methods of experimental investigation of slamming.

Two main parts of the research presented here can be distinguished. The first part is focused on performing accurate full-field fluid velocity measurements during water entry, using PIV. In the second part, PIV-based load estimation techniques were investigated, to reveal the possibility of recovering relevant information from these measurements.

After an initial literature review on slamming investigation techniques, that offered context to the relevance of this research topic, an analysis of the main aspects of PIV was presented in Chapter 2. A comprehensive presentation of the current state-of-the-art was given in the aforementioned chapter, with respect to the components of modern (high-speed) PIV systems, as well as the post-processing techniques that are currently deployed. Several guidelines were given regarding the successful implementation of PIV instrumentation in experimental slamming set-ups. Among these, the need for optical access and for adequate seeding ma-

terial, the laser light sheet delivery methods, and restriction of 3D flow effects (when using 2D PIV measurements) were emphasized. Furthermore, state-of-the-art PIV interrogation procedures were discussed, and it was acknowledge that recent improvements in PIV post-processing algorithms have successfully complemented the technological advancements made in the manufacturing of powerful high-speed PIV systems. Therefore, it was concluded that the quality and high sampling frequency of current PIV measurements have enabled the use of these techniques in the study of a phenomenon such as slamming, which features important dynamic behaviour in a short timespan (few milliseconds).

One of the most important aspects discussed in Chapter 2 was the accuracy of PIV measurements. To improve the valid data detection during PIV interrogation, an automated adaptive masking technique was introduced. It should be noted that PIV processing algorithms are prone to erroneous results when regions of the raw image under investigation exhibit a lack of seeding particle images. Such is the case for PIV slamming recordings, where the presence of the moving body and of the air region in the field of view can hinder the accurate estimation of displacements. Therefore, the adaptive masking method was developed in order to exclude from PIV interrogation the regions of the frame which do not contain tracer images, namely the regions which do not correspond to the seeded water domain. Due to the fact that the number of acquired PIV images taken during water entry are in the order of a few hundred frames, the masking procedure needed to be implemented in an automated way. This was done using information on the position of the body at each time step, acquired using a position encoder incorporated in the experimental set-up. For the masking of the air region present in the image, a feature identification technique was implemented, to recover the free surface profile on each image. The validation of these improved PIV measurement techniques was performed using tests of a rigid 90° wedge and cylinder (D = 90 mm) slamming. The PIV results were compared to numerical simulation results for each test case. It was found that close agreement between the two methods exists. However, certain limitations in the PIV-based results are noticeable especially for the first few milliseconds (4-5 ms) of impact. This is mainly due to the fact that optical access in the spray root region of the flow is limited in the experiments, and that seeding particle availability is also reduced in this region (only about 2 particle images are present). Another factor that plays an important role in the accuracy of PIV measurements is the resolution of the grids. At present, spatial resolution of PIV is an issue that attracts a great deal of interest. Several factors affect PIV spatial resolution and the general limitations arise from the trade-off one must resort to, between optical resolution (the number of pixels per unit length) and tracer particle size and distribution. These aspects need to

be taken into account when analysing the accuracy of PIV measurements during water entry. It was shown that the strong velocity gradients which occur in the immediate vicinity of the immersed wall of the impacting rigid body can prove to be difficult to resolve with PIV. However, the overall agreement between PIV results and simulations results in the case of rigid body slamming (less than 10 % overall error) show that the former is a suitable method of experimental investigation.

In Chapter 3, improvements of the automated adaptive masking procedure previously introduced were presented. These improvements are intended for the PIV measurements of deformable body slamming. In the case of slamming of an elastic cylinder, the occurring loads cause for the body to deform during the water entry. Therefore, the use of position encoder information as previously implemented is no longer sufficient, as the assumption of constant shape of the body during impact does not apply. The algorithm developed for the feature identification of a deformable body entering the water uses the raw pictures acquired during PIV measurements. The contour of the immersed body wall is identified using the intensity levels in the grayscale image and the position encoder information to calculate an ellipse fit of the body contour. This technique thus produces the shape of the cylinder on each frame, and enables the tracking of its evolution in time. It was found that using this information, the body displacements can be estimated and with a priori knowledge of the material properties of the impacting body, strain and force results can be produced based on these measurements. This provides additional information from PIV measurements that offer further insight into slamming of deformable structures.

As mentioned previously, the second part of this thesis focuses on PIV-based methods of estimating pressure from the fluid velocity maps. Chapter 4 gives an overview of the methods applied to calculate pressure from the PIV measured velocity, by making use of the Poisson equation for pressure and appropriate boundary conditions. The algorithms used in this type of pressure estimations are found to be increasingly popular in the PIV community. However, the implementation of these methods is usually focused on the study of averaged velocity maps from batch processing of several hundreds, or even thousands of images, and they are not so common in time-resolved PIV analysis. The reason why averaged data is more often used for pressure estimation than time-resolved data is that the latter is less common in PIV studies, but also because of difficulties in pressure estimation algorithms when time-dependent data is used. The time derivative of velocity measured with high-speed PIV is prone to errors, because of the measurement uncertainty, whilst when averaged data is used, these uncertainties are reduced considerably.

The algorithm for pressure estimation based on solving the Poisson equation

for pressure is tested on the case of rigid wedge slamming and the results are compared with the numerical data. The results show that good estimation of the pressure map can be achieved, within the limits of the accuracy of PIV measured velocity data for the reasons mentioned above. It was observed that, as for the case of velocity results, the limitations in accuracy of the pressure estimations are mainly encountered in the first few milliseconds of water entry.

It should be noted that recently, another group [65] has independently performed PIV-based pressure estimation during the water entry of a rigid wedge. The test cases presented in [65] differed than the one presented in this work in both the considered body geometry as well as in the way the estimation procedure and the boundary conditions were applied. The fact that this independent research was performed and with promising results as well, is encouraging for the future application of PIV to the study of slamming.

In the same Chapter 4, the pressure estimation algorithm was applied to the slamming of deformable cylinders. In order to improve the time-resolved PIV data taken during slamming, a temporal smoothing technique was first considered. This procedure eliminates spurious results of the velocity gradients, and has a positive effect on the accuracy of pressure estimation. Another technique that was developed in this work is the streamline-based velocity re-sampling. This method is applied to the PIV velocity data in order to improve spatial resolution in a reliable way. The application of these methods to experimental investigations of deformable body slamming was tested using an extensive validation campaign presented in Chapter 5.

The experimental set-up presented in Chapter 5 was instrumented with force transducers and strain gauges, and thus the PIV measurements performed during the slamming tests were compared with synchronized measurements using these classical sensors. The goal of this campaign was to assess the performance of PIV-based load estimation in comparison with the force and strain results that are so often used in literature. Different cylinders were tested, with diameters of 90 mm and 315 mm, manufactured from different materials (PVC and composite materials), and with various wall thickness. The drop tests were performed using various impact velocities, ranging from approximately 1 m/s to just under 4 m/s. Furthermore, two cameras were used, and post-processing procedures resulted in reconstruction of the entire field of view for some of the test cases. By using the methods developed in this work, it was found that the PIV-based estimations offer good approximations of the loads occurring during slamming of deformable cylinders. One important aspect that the reader should be taking into consideration, is the findings of Van Nuffel [87]. He observed that force results of load cell measurements show a higher level of uncertainty than estimations of force based

on strain measurements, and this is caused by the effect of structural vibrations of the experimental set-up. This effect is more pronounced when the structural vibrations of the impactor are close to the resonance frequency of the impacting body. Consequently, a solution to better estimate the actual slamming loads can be to use the strain measurements and conversion factors of strain to force (when all material properties are known a priori). The PIV-based load measurements, on the other hand, show closer agreement with these strain-based estimations of load for the case of deformable body slamming. Therefore, PIV-based methods can provide a new way of measuring slamming loads without the bias caused by structural vibrations of the impactor. This, by itself, is a promising opportunity considering that currently, the most stringent problems in the field of slamming research is the effective way of separating the effects of the vibrations of the experimental set-up, from the actual slamming induced loads. Furthermore, as it was shown in this work, the information that can be extracted from PIV measurements is providing not only the means to determine slamming loads, but also insight into the flow physics (fluid velocity, free surface profiles, body displacements, etc.). This can be further used as a way to validate numerical models. Therefore, even though improved spatial and temporal accuracy is desirable, the PIV-based methods of investigation of the slamming phenomenon are an interesting prospect. And since the development of PIV over the past decade has shown remarkable progress, it should be expected that the opportunities offered by this method of experimental investigation will increase further.

6.2 Future research

The goal of this thesis was to use non-intrusive (PIV) measurement techniques in the experimental study of slamming. It was shown that PIV investigations are possible and moreover, useful in the description of the phenomenon. However, the successful implementation of these methods depends on several aspects, which can be improved in future research work.

The main aspect that needs to be considered for future work is the accuracy of PIV measurements of velocity during slamming. The main causes for uncertainties in PIV results are the spatial and the temporal resolutions of the velocity maps. One factor that should be further improved in order to achieve the aforementioned goals, is the optical resolution. The technological advancement has brought forth increasingly powerful digital cameras. Cameras with higher resolutions (currently up to 10 million pixel resolution) and even microscopes deployed for PIV measurements can be used to further increase the resolution, particularly

in the region that has been shown to be suffering from insufficient optical resolution: the spray root region. Improved spatial resolutions need to be addressed by increasing both optical resolution as well as particle seeding density.

Together with the technological advancement of PIV systems, improvements of post-processing procedures should also be addressed. One way of increasing PIV accuracy through post-processing software improvements is the used of adaptive image interrogation methods. This type of methods, such as the implementation of [81], can decrease the level of uncertainty in the velocity gradient results, and can give better estimation of displacement in the vicinity of the impacting body wall.

As it was shown in Chapter 2, multi-grid interrogation techniques were applied in this work to improve the dynamic spatial range of the measured velocity. However, new techniques using the same principle, but performing time-based iterative approaches can also be implemented. If the PIV sampling rates are to be increased further, several frames can be used for multiple correlation-based interrogation, and higher accuracy, as well as higher temporal resolution can thus be achieved.

Another aspect that should be considered in the future, is the use of fluorescent tracers, such as the Rhodamine B particles. This type of particles scatters light at a different wavelength than that of the incident laser light. If a bandpass filter is applied to the imaging device to allow for only a narrow spectral band of wavelength to be recorded (the particle images), the reflections of laser light from free surface and the body surface can be considerably reduced or eliminated altogether. This, in turn, would reduce the noise caused by unwanted reflections during water entry.

Appendix A

Streamline-Based Velocity Interpolation.

This appendix offers an overview of the streamline-bsed vector field re-sampling technique, that was used to improve the spatial resolution of velocity field results. The principles of this procedures are detailed, and results of synthetic flow test cases are given to asses the performance of the algorithm. Furthermore, the method is tested on velocity field results of cylinder slamming as measured with PIV. The PIV results discussed in this appendix have been introduced in Chapter 4.

A.1 Methodology.

A higher spatial resolution is obtained by interpolating velocity data at streamline locations which do not coincide with grid nodes, whilst the velocity vector is satisfying the condition of tangency to the streamline. The vector field resampling by means of streamline tracing and interpolation is similar to the method proposed by Thomas and Geiger [14], which used a local polynomial approximation of streamlines using each grid point as an anchor point. Firstly, the streamline is defined as:

$$\frac{d\vec{x}}{ds} = \vec{u}(\vec{x}) \tag{A.1}$$

A Matlab function was written for extracting streamline point location and velocity information at these locations. If the calculated streamline point location is (x_s, y_s), the function uses a bilinear interpolation on a 2x2 neighbourhood to calculate the coordinates as:

$$x_s = x_0 + k_s \Delta x \frac{u_s}{|v_s|} \tag{A.2}$$

Equation A.2 expresses the x_s coordinate of the streamline location as a function of the x_0 coordinate of the previous point on the streamline. The user defined step size of the streamline node location is hereby chosen as a fraction of the grid step size ($k_s \Delta x$, with $0 < k_s \leq 1$) and the interpolated velocity (u_s). Following a simplification procedure in which the local 2x2 neighbourhood is considered as a local unit coordinate system where the four grid locations are (0,0), (0,1), (1,0), and (1,1), the term u_s can be expressed in matrix form as:

$$u_s = \begin{bmatrix} (1 - x_s) & x_s \end{bmatrix} \begin{bmatrix} u(0,0) & u(0,1) \\ u(1,0) & u(1,1) \end{bmatrix} \begin{bmatrix} (1 - y_s) \\ y_s \end{bmatrix} \tag{A.3}$$

Similarly, the y_s coordinate of the streamline point location is calculated as a function of v_s. Following the procedure of determining the streamline coordinates, velocity values are estimated at streamline locations by performing a cubic downstream interpolation of the initial data. This method allows for a re-sampling of the velocity field at streamline locations, meaning that the resulting grid will no longer be a structured one. Since the methods described in this work are implemented on structured grids, a last step is taken in which the resulting streamline-based results are used as anchor points for interpolation on a structured grid. The step size of this grid is chosen to be between 2 and 4 times lower than the initial

PIV grid step size. The advantage of using this technique lies in the ability to perform interpolation on the PIV measured velocity with the option of verifying the result through a physical interpretation of the flow (the condition of tangency to the streamline). More importantly, when features such as the rigid body or the free surface are present in the field of view, the method allows for interpolating data upstream on the streamline, thus obtaining better estimates in the vicinity of the features. In the following, synthetic flows are considered, in order to assess the performance of this method.

A.2 Synthetic Flow Cases

The algorithm for streamline-based interpolation is tested on two synthetic flow test cases. The velocity fields are corrupted by Gaussian noise with varying standard deviations (σ). Results are compared against two Matlab built-in functions for 2D map interpolation - *imresize* and the *TriScatteredInterp* function. In the results presented herein, the *imresize* function performs image-based re-sampling using nearest-neighbour interpolation and the *TriScatteredInterp* function performs linear interpolation of the input datasets.

The first test case is a diverging flow, defined as:

$$U_{ij} = y_{ij}; \qquad V_{ij} = x_{ij}; \tag{A.4}$$

where U_{ij} and V_{ij} are the horizontal and vertical components of velocity, respectively. The vectors of grid coordinates x_{ij} and y_{ij} are equally spaced vectors defined as $x_{ij} = y_{ij} = \{-32, -31...31\}$. Figure A.1 shows the velocity magnitude for this first test case, with and without Gaussian noise. The vector map and a selection of streamlines is shown in Figure A.2.

For the second synthetic flow, a periodic channel flow is considered. The same domain size is used as in the first synthetic flow test case. The horizontal component has a parabolic profile in function of y_{ij}, whilst the vertical component is a sinusoidal function of x_{ij}. The expression of the vector components are given in equation A.5, where H represents the height of the channel.

$$\begin{cases} U_{ij} = 0.01 \cdot (\frac{H}{2}^2 - {y_{ij}}^2); \\ V_{ij} = 5 \sin(\frac{x_{ij}}{2\pi}); \end{cases} \tag{A.5}$$

In Figure A.3, the velocity maps corresponding to this second case are illustrated, with and without Gaussian noise.

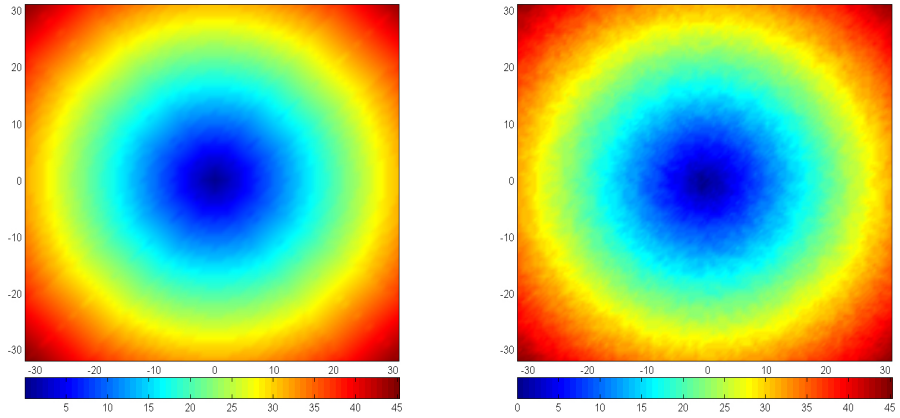

Figure A.1: Synthetic flow case 1. Left: Exact solution; Right: Vector field with Gaussian noise (σ = 1.6)

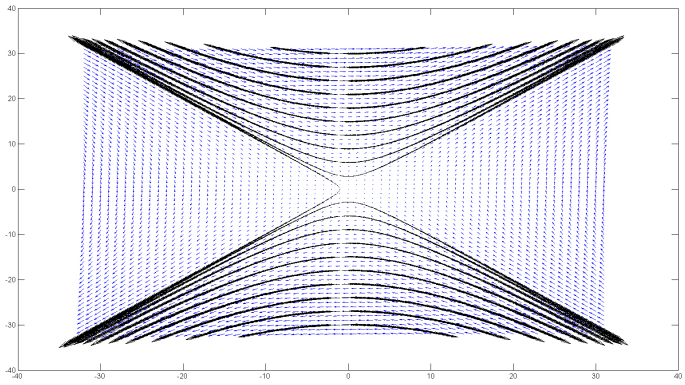

Figure A.2: Streamlines for synthetic flow case 1.

The three methods, streamline-based interpolation, the *imresize* function and *TriScatteredInterp* function are used to re-sample the vector field on a fine grid, for the two synthetic flow test cases. Results of the error of the interpolated values using the three techniques with respect to the theoretical values, are given in Figure A.4. The results prove the superiority of the streamline approach, especially for low noise values.

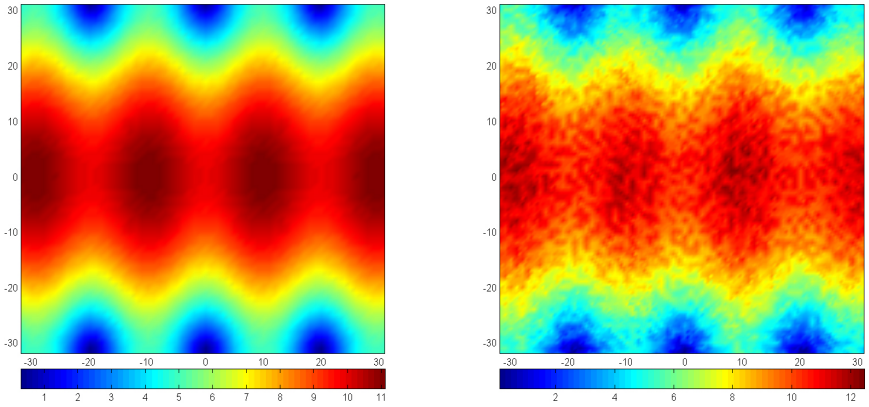

Figure A.3: Synthetic flow case 2. Left: Exact solution; Right: Vector field with Gaussian noise (σ = 1.6)

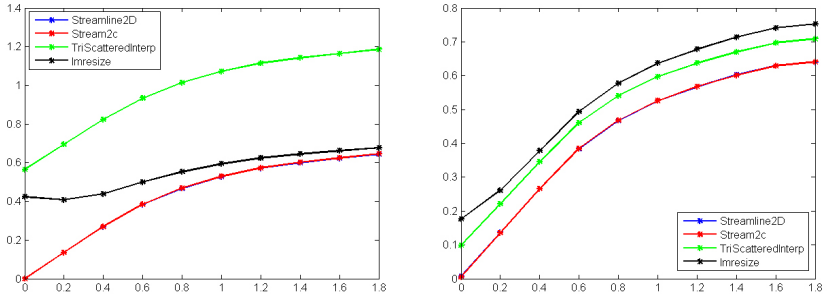

Figure A.4: Mean square error as a function of the standard deviation of Gaussian noise (σ). Left: case 1. ; Right: case 2.

A.3 PIV Slamming Measurements

The velocity data obtained from PIV measurements during slamming, as introduced in Chapter 4, is re-sampled using the streamline-based interpolation technique. It should be noted that the interpolation is performed by disregarding grid nodes which are flagged as not being in the water domain (using the mask matrix). Figure A.5 shows a typical PIV result during slamming. The velocity vectors are illustrated and one streamline is exemplified, together with anchor points (calculated on the initial grid) and the points where new velocity values are interpolated (red markers). The streamline approximation is started from the initial anchor point on the grid and the red marker points indicate new grid nodes that will be used for velocity interpolation.

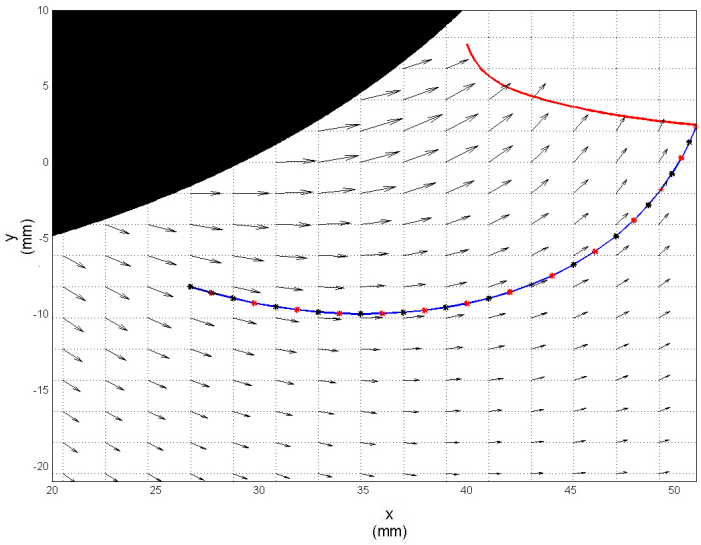

Figure A.5: Velocity vectors and streamline - black markers represent anchor points and red markers represent points used for velocity interpolation

The resolution of the final grid is increased by 4 times the initial resolution, which makes for a general achieved resolution of 0.5 mm in both in-plane directions (e.g. an initial grid of 174 x 161 will lead to a final grid of 709 x 656). Figure A.6 shows the grid before and after interpolation. The red-marked grid nodes are the fluid grid nodes used for extracting values of velocity and pressure

at the cylinder wall.

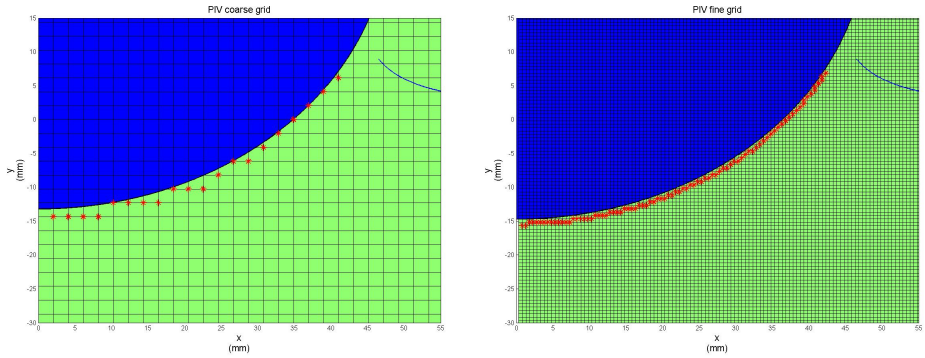

(a) (b)

Figure A.6: PIV grid. Left - coarse grid before streamline approximation; right - fine grid after interpolating based on streamline approximation

Figure A.7 shows the comparison between raw results of x and y components of velocity and interpolated ones at time 12.4 *ms* of the water entry of Cylinder 1. It can be observed that the flow features are well preserved after the interpolation, and that the peak velocity magnitudes are comparable.

An important aspect of the velocity field measurements in the case of a water impact experiment is the ability to correctly measure fluid velocity at the wall of an immersed body. The interpolation of velocity results shows good agreement with the initially measured velocity, as can be seen in Figure A.8. The vertical velocity magnitude seems to be slightly increased after interpolation at the cylinder tip, whilst for the region closer to the spray root, the interpolated values are slightly lower, especially at the early stage of impact.

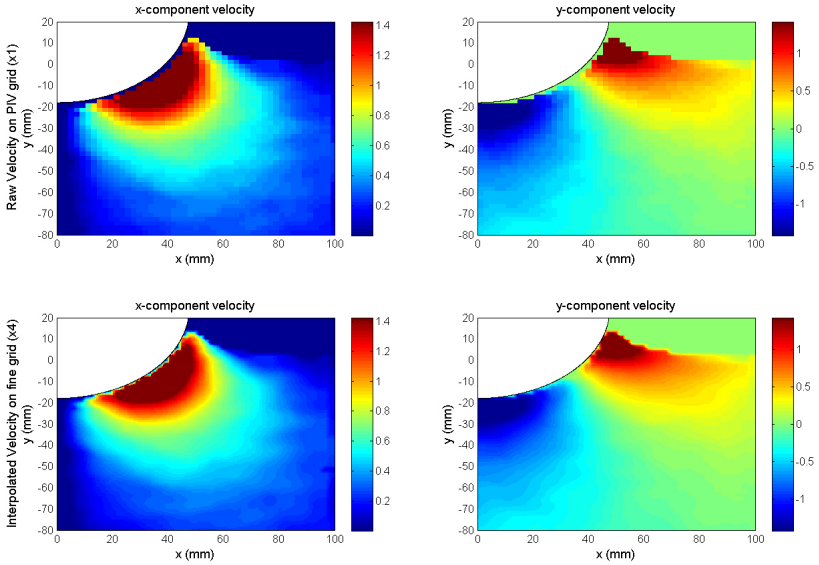

Figure A.7: Velocity field at t = 12.4 ms. upper row: raw data; lower row: streamline interpolated.

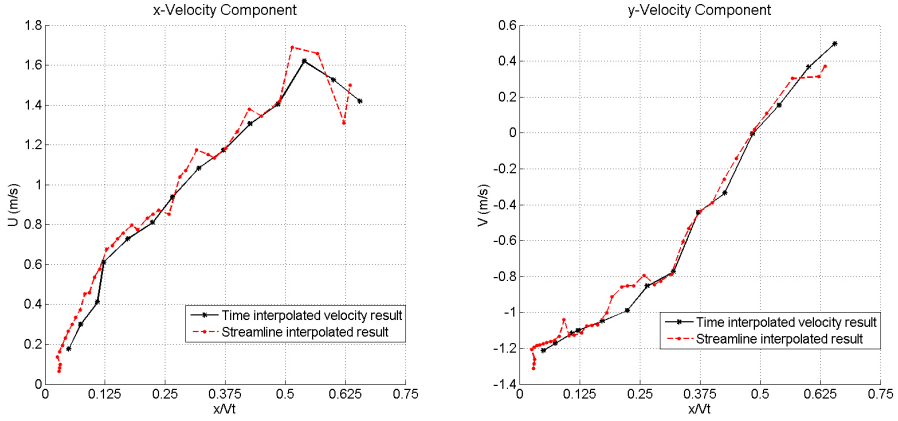

Figure A.8: Velocity values at the cylinder wall. Left: x-component velocity; Right: y-component velocity.

Bibliography

[1] R.J. Adrian. Scattering particle characteristics and their effect on pulsed laser measurements of fluid flow: speckle velocimetry vs particle image velocimetry. *Applied Optics*, 23(11):1690–1691, 1984.

[2] R.J. Adrian. Statistical properties of particle image velocimetry measurements in turbulent flow. *Laser Anemometry in Fluid Mechanics*, III:115–129, 1988.

[3] R.J. Adrian and C.S. Yao. Development of pulsed laser velocimetry (plv) for measurement of turbulent flow. *SPIE Milestone Series MS*, 99:300–300, 1994.

[4] T. Albrecht, V. Del Campo, T. Weier, and G. Gerbeth. Comparison of piv-based methods for airfoil loads evaluation. *16th International Symposium on Applications of Laser Techniques to Fluid Mechanics, Lisbon, Portugal, July*, pages 9–12, 2012.

[5] M. Arai and T. Miyauchi. Numerical simulation of the water impact on cylindrical shells considering fluid structure interaction. *Society of Naval Architects of Japan*, 182:827–836, 1997.

[6] J.L. Armand and R. Cointe. Hydrodynamic impact analysis of a cylinder. *Journal of Offshore Mechanics and Arctic Engineering*, 109 (1987): 237243, 1987.

[7] T. Astarita and G. Cardone. Analysis of interpolation schemes for image deformation methods in piv. *Experiments in fluids*, 38(2):233–243, 2005.

[8] D.B. Barker and M.E. Fourney. Measuring fluid velocities with speckle patterns. *Optics letters*, 1(4):135–137, 1977.

[9] A.B. Basset. *A treatise on hydrodynamics: with numerous examples*, volume 2. Deighton, Bell and Co., 1888.

[10] D. Battistin and A. Iafrati. Hydrodynamic loads during water entry of two-dimensional and axisymmetric bodies. *Journal of fluids and structures*, 17 (5):643–664, 2003.

[11] T. Baur and J. Köngeter. Piv with high temporal resolution for the determination of local pressure reductions from coherent turbulence phenomena. In *3rd International Workshop on Particle Image Velocimetry,(Santa Barbara, CA, USA),(1999-9)*, 1999.

[12] A. Bereznitski. Slamming: the role of hydroelasticity. *International Shipbuilding Progress*, 48(4):333–351, 2001.

[13] C. Blommaert. *Composite floating'point absorbers' for wave energy converters: survivability design, production method and large-scale testing*. PhD thesis, Ghent University, 2005.

[14] I.M.C. Campbell and P.A. Weynberg. *Measurement of parameters affecting slamming*. University of Southampton, Department of Aeronautics and Astronautics, 1980.

[15] A. Carcaterra and E. Ciappi. Prediction of the compressible stage slamming force on rigid and elastic systems impacting on the water surface. *Nonlinear Dynamics*, 21(2):193–220, 2000.

[16] S.L. Chuang. Slamming of rigid wedge-shaped bodies with various deadrise angles. Technical report, DTIC Document, 1966.

[17] S.L. Chuang and D.T. Milne. Drop tests of cones to investigate the three-dimensional effects of slamming. Technical report, DTIC Document, 1971.

[18] S.J.M. Coudert and J.P. Schon. Back-projection algorithm with misalignment corrections for 2d3c stereoscopic piv. *Measurement science and technology*, 12(9):1371, 2001.

[19] J.O. Dabiri, S. Bose, B.J. Gemmell, S.P. Colin, and J.H. Costello. An algorithm to estimate unsteady and quasi-steady pressure fields from velocity field measurements. *The Journal of experimental biology*, 217(3):331–336, 2014.

[20] G. De Backer, M. Vantorre, C. Beels, J. De Pré, S. Victor, J. De Rouck, C. Blommaert, and W. Van Paepegem. Experimental investigation of water impact on axisymmetric bodies. *Applied Ocean Research*, 31(3):143–156, 2009.

[21] R. De Kat. *Instantaneous planar pressure determination from particle image velocimetry*. PhD thesis, TU Delft, Delft University of Technology, 2012.

[22] R. de Kat, B.W. Van Oudheusden, and F. Scarano. Instantaneous planar pressure field determination around a square-section cylinder based on time-resolved stereo-piv. In *14th international symposium on applications of laser techniques to fluid mechanics. Lisbon, Portugal*, 2008.

[23] Z.N. Dobrovol'Skaya. On some problems of similarity flow of fluid with a free surface. *Journal of Fluid Mechanics*, 36(04):805–829, 1969.

[24] T.D. Dudderar and P.G. Simpkins. Laser speckle photography in a fluid medium. *Nature*, 270(5632):45–47, 1977.

[25] O.M. Faltinsen. The effect of hydroelasticity on ship slamming. *Philosophical Transactions of the Royal Society of London. Series A: Mathematical, Physical and Engineering Sciences*, 355(1724):575–591, 1997.

[26] O.M. Faltinsen. Hydroelastic slamming. *Journal of Marine Science and Technology*, 5(2):49–65, 2000.

[27] R.D. Flack. *The application of a Laser Doppler Velocimeter (LDV) in interpreting turbulent structure*. PhD thesis, Purdue University, 1975.

[28] N Fujisawa, S Tanahashi, and K Srinivas. Evaluation of pressure field and fluid forces on a circular cylinder with and without rotational oscillation using velocity data from piv measurement. *Measurement Science and Technology*, 16(4):989, 2005.

[29] P. Ghadimi, F. Chekab, A. Mohammad, and A. Dashtimanesh. A numerical investigation of the water impact of an arbitrary bow section. *ISH Journal of Hydraulic Engineering*, (ahead-of-print):1–10, 2013.

[30] ILA Intelligent Laser Applications GmbH. Available at: http://www.ila.de/, 2014.

[31] M. Greenhow and W.M. Lin. Nonlinear-free surface effects: Experiments and theory. Technical report, DTIC Document, 1983.

[32] R. Grousson and S. Mallick. Study of flow pattern in a fluid by scattered laser light. *Applied Optics*, 16(9):2334–2336, 1977.

[33] P Guillaume, P Verboven, and S Vanlanduit. Frequency-domain maximum likelihood identification of modal parameters with confidence intervals. In *Proceedings of the International Seminar on Modal Analysis*, volume 1, pages 359–366. KATHOLIEKE UNIVERSITEIT LEUVEN, 1998.

[34] Patrick Guillaume, R Pintelon, and Johan Schoukens. Robust parametric transfer function estimation using complex logarithmic frequency response data. *Automatic Control, IEEE Transactions on*, 40(7):1180–1190, 1995.

[35] R. Gurka, A. Liberzon, D. Hefetz, D. Rubinstein, and U. Shavit. Computation of pressure distribution using piv velocity data. In *Workshop on Particle Image Velocimetry*, 1999.

[36] R. Hain and C.J. Kähler. Fundamentals of multiframe particle image velocimetry (piv). *Experiments in fluids*, 42(4):575–587, 2007.

[37] R. Hain, C.J. Kähler, and C. Tropea. Comparison of ccd, cmos and intensified cameras. *Experiments in fluids*, 42(3):403–411, 2007.

[38] D.P. Hart. Piv error correction. *Experiments in fluids*, 29(1):13–22, 2000.

[39] Sigeo Hosokawa, Satoshi Moriyama, Akio Tomiyama, and Naoki Takada. Piv measurement of pressure distributions about single bubbles. *Journal of Nuclear Science and Technology*, 40(10):754–762, 2003.

[40] O.F. Hughes. Wedge penetration of a free surface. Technical report, School of Mechanical & Industrial Engineering Report No. 1971/NA/2, The University of New South Wales, Australia, 1971.

[41] O.F. Hughes. Solution of the wedge entry problem by numerical conformal mapping. *Journal of Fluid Mechanics*, 56(01):173–192, 1972.

[42] Hendrik Christoffel Hulst and HC Van De Hulst. *Light scattering by small particles*. Courier Dover Publications, 1957.

[43] M. Ionina and A.A. Korobkin. Water impact on cylindrical shells. In *International Workshop on Water Waves and Floating Bodies, Port Huron, MI, USA*, pages 44–47, 1999.

[44] G.K. Kapsenberg. Slamming of ships: where are we now? *Philosophical Transactions of the Royal Society A: Mathematical, Physical and Engineering Sciences*, 369(1947):2892–2919, 2011.

[45] R.D. Keane and R.J. Adrian. Optimization of particle image velocimeters. i. double pulsed systems. *Measurement Science and Technology*, 1(11): 1202, 1990.

[46] A. Korobkin, R. Gueret, and Š. Malenica. Hydroelastic coupling of beam finite element model with wagner theory of water impact. *Journal of fluids and structures*, 22(4):493–504, 2006.

[47] M.C. Lin and L.D. Shieh. Flow visualization and pressure characteristics of a cylinder for water impact. *Applied ocean research*, 19(2):101–112, 1997.

[48] M.C. Lin and L.D. Shieh. Simultaneous measurements of water impact on a two-dimensional body. *Fluid dynamics research*, 19(3):125–148, 1997.

[49] X. Liu and J. Katz. Instantaneous pressure and material acceleration measurements using a four-exposure piv system. *Experiments in Fluids*, 41(2): 227–240, 2006.

[50] C.H. Lu, Y.S. He, and G.X. Wu. Coupled analysis of nonlinear interaction between fluid and structure during impact. *Journal of fluids and structures*, 14(1):127–146, 2000.

[51] X. Mei, Y. Liu, and D. Yue. On the water impact of general two-dimensional sections. *Applied Ocean Research*, 21(2):1–15, 1999.

[52] A. Melling. Tracer particles and seeding for particle image velocimetry. *Measurement Science and Technology*, 8(12):1406, 1997.

[53] R. Meynart et al. Instantaneous velocity field measurements in unsteady gas flow by speckle velocimetry. *Applied optics*, 22(4):535–540, 1983.

[54] T. Miloh. Wave slam on a sphere penetrating a free surface. *Journal of Engineering Mathematics*, 15(3):221–240, 1981.

[55] T. Miloh. On the initial-stage slamming of a rigid sphere in a vertical water entry. *Applied Ocean Research*, 13(1):43–48, 1991.

[56] S.K. Mitra and Y. Kuo. *Digital signal processing: a computer-based approach*, volume 2. McGraw-Hill New York, 2006.

[57] Rajat Mittal, Haibo Dong, Meliha Bozkurttas, FM Najjar, Abel Vargas, and Alfred von Loebbecke. A versatile sharp interface immersed boundary method for incompressible flows with complex boundaries. *Journal of computational physics*, 227(10):4825–4852, 2008.

[58] A. Nila, S. Vanlanduit, K.S. Vepa, D. Van Nuffel, W. Van Paepegem, J. Degroote, and J. Vierendeels. High speed particle image velocimetry measurements during water entry of rigid bodies. In *Ninth International Symposium on Particle Image Velocimetry, Kobe, Japan*, July 21-23, 2011.

[59] A. Nila, S. Vanlanduit, K.S. Vepa, and W. Van Paepegem. A piv-based method for estimating slamming loads during water entry of rigid bodies. *Measurement Science and Technology*, 24(4):045303, 2013.

[60] A. Nila, S. Vanlanduit, S. Vepa, D. Van Nuffel, W. Van Paepegem, J. Degroote, and J. Vierendeels. High speed particle image velocimetry measurements during water entry of rigid and deformable bodies. In *International Symposium on Applications of Laser Techniques to Fluid Mechanics, Lisbon, Portugal*, July 9-12, 2012.

[61] H. Nobach and M. Honkanen. Two-dimensional gaussian regression for sub-pixel displacement estimation in particle image velocimetry or particle position estimation in particle tracking velocimetry. *Experiments in fluids*, 38(4):511–515, 2005.

[62] F. Noca, D. Shiels, and D. Jeon. A comparison of methods for evaluating time-dependent fluid dynamic forces on bodies, using only velocity fields and their derivatives. *Journal of Fluids and Structures*, 13(5):551–578, 1999.

[63] Taketoshi Okuno, Yasuhiko Sugii, and Shigeru Nishio. Image measurement of flow field using physics-based dynamic model. *Measurement Science and Technology*, 11(6):667, 2000.

[64] R. Panciroli. Hydroelastic impacts of deformable wedges. In *Dynamic Failure of Composite and Sandwich Structures*, pages 1–45. Springer, 2013.

[65] R. Panciroli and M. Porfiri. Evaluation of the pressure field on a rigid body entering a quiescent fluid through particle image velocimetry. *Experiments in fluids*, 54(12):1–13, 2013.

[66] B. Peseux, L. Gornet, and B. Donguy. Hydrodynamic impact: Numerical and experimental investigations. *Journal of Fluids and Structures*, 21(3): 277–303, 2005.

[67] A.K. Prasad. Stereoscopic particle image velocimetry. *Experiments in fluids*, 29(2):103–116, 2000.

[68] M. Raffel, C.E. Willert, and J. Kompenhans. *Particle Image Velocimetry: A Practical Guide; with 24 Tables*. Springer, 1998.

[69] D Ragni, A Ashok, BW Van Oudheusden, and F Scarano. Surface pressure and aerodynamic loads determination of a transonic airfoil based on particle image velocimetry. *Measurement Science and Technology*, 20(7): 074005, 2009.

[70] D. Ragni, B.W. Van Oudheusden, and F. Scarano. Drag coefficient accuracy improvement by means of particle image velocimetry for a transonic naca0012 airfoil. *Measurement Science and Technology*, 22(1):17003–17007, 2011.

[71] T. Roesgen. Optimal subpixel interpolation in particle image velocimetry. *Experiments in Fluids*, 35(3):252–256, 2003.

[72] O. Ronneberger, M. Raffel, and J. Kompenhans. Advanced evaluation algorithms for standard and dual plane particle image velocimetry. In *Proceedings of the 9th International Symposium on Applied laser techniques to fluid mechanics, Lisbon, Portugal, paper*, volume 10, pages 13–16, 1998.

[73] C.M. Seddon and M. Moatamedi. Review of water entry with applications to aerospace structures. *International Journal of Impact Engineering*, 32 (7):1045–1067, 2006.

[74] T. Shibue, A. Ito, and E. Nakayama. Structural response analysis of a cylinder under water impact. 1993.

[75] M. Stanislas, K. Okamoto, and C. Kähler. Main results of the first international piv challenge. *Measurement Science and Technology*, 14(10):R63, 2003.

[76] M. Stanislas, K. Okamoto, C.J. Kähler, and J. Westerweel. Main results of the second international piv challenge. *Experiments in Fluids*, 39(2): 170–191, 2005.

[77] M. Stanislas, K. Okamoto, C.J. Kähler, J. Westerweel, and F. Scarano. Main results of the third international piv challenge. *Experiments in Fluids*, 45(1):27–71, 2008.

[78] H. Sun and O.M. Faltinsen. Water impact of horizontal circular cylinders and cylindrical shells. *Applied Ocean Research*, 28(5):299–311, 2006.

[79] M.A. Sutton and Y.J. Chao. Measurement of strains in a paper tensile specimen using computer vision and digital image correlation part 1: Data acquisition and image analysis system. *Tappi Journal*, 70(3):173–175, 1988.

[80] M.A. Sutton, J.J. Orteu, and H.W. Schreier. *Image correlation for shape, motion and deformation measurements: basic concepts, theory and applications*. Springer, 2009.

[81] R. Theunissen. *Adaptive image interrogation for PIV: application to compressible flows and interfaces*. PhD thesis, TU Delft, Delft University of Technology, 2010.

[82] P. Thévenaz, T. Blu, and M. Unser. Interpolation revisited [medical images application]. *Medical Imaging, IEEE Transactions on*, 19(7):739–758, 2000.

[83] W. Tong. Strain characterization of propagative deformation bands. *Journal of the Mechanics and Physics of Solids*, 46(10):2087–2102, 1998.

[84] L Tsuei and Ö Savaş. Treatment of interfaces in particle image velocimetry. *Experiments in Fluids*, 29(3):203–214, 2000.

[85] T. Tveitnes, A.C. Fairlie-Clarke, and K. Varyani. An experimental investigation into the constant velocity water entry of wedge-shaped sections. *Ocean Engineering*, 35(14):1463–1478, 2008.

[86] G Usera, A Vernet, and JA Ferré. Considerations and improvements of the analysing algorithms used for time resolved piv of wall bounded flows. In *Proceedings of the 12th international symposium on applications of laser techniques to fluid mechanics, Lisbon, July*, pages 11–15, 2004.

[87] D. Van Nuffel. *Experimental study of the slamming induced pressures, forces and deformations experienced by quasi-rigid and deformable bodies during vertical water entry*. PhD thesis, Ghent University, 2014.

[88] D. Van Nuffel, K.S. Vepa, I. De Baere, J. Degrieck, J. De Rouck, and W. Van Paepegem. Parameters affecting the pressure measurement on the surface of a rigid cylindrical body during water slamming impact. In *Proc. 26th Int. Workshop on Water Waves and Floating Bodies (Athens, Greece,)*, pages 193–6, 2011.

[89] D. Van Nuffel, K.S. Vepa, I. De Baere, J. Degrieck, J. De Rouck, and W. Van Paepegem. Study on the parameters influencing the accuracy and

reproducibility of dynamic pressure measurements at the surface of a rigid body during water impact. *Experimental Mechanics*, 53(2):131–144, 2013.

[90] B.W. Van Oudheusden. Principles and application of velocimetry-based planar pressure imaging in compressible flows with shocks. *Experiments in fluids*, 45(4):657–674, 2008.

[91] K.S. Vepa. *Numerical study of the wave impact on rigid and deformable objects*. PhD thesis, Ghent University, 2014 (in progress).

[92] K.S. Vepa, D. Van Nuffel, W. Van Paepegem, and J. Degrieck. Numerical study of composite structures subjected to slamming loads using smoothed particle hydrodynamics (sph). In *8th International Conference on Structural Dynamics (Eurodyn-2011)*, pages 3077–3082. Ghent University, Department of Mechanical construction and production, 2011.

[93] T. Von Kármán. The impact on seaplane floats during landing. *Technical Notes - National Advisory Committee for Aeronautics*, 1929.

[94] H. Wagner. Über stoß-und gleitvorgänge an der oberfläche von flüssigkeiten. *ZAMM-Journal of Applied Mathematics and Mechanics/Zeitschrift für Angewandte Mathematik und Mechanik*, 12(4):193–215, 1932.

[95] Dantec Dynamics A/S Website. Available at: https://www.dantecdynamics.com, 2014.

[96] PHOTRON Website. Available at: http://www.photron.com, 2014.

[97] Safehaven Marine Website. Available at: http://www.safehavenmarine.com/newsletter

[98] Wave Dragon Project Website. Available at: http://ec.europa.eu/research/science-society/science-communication/casehistories04.htm, 2014.

[99] J. Westerweel. Efficient detection of spurious vectors in particle image velocimetry data. *Experiments in Fluids*, 16(3-4):236–247, 1994.

[100] J. Westerweel. Fundamentals of digital particle image velocimetry. *Measurement Science and Technology*, 8(12):1379, 1997.

[101] J. Westerweel, D. Dabiri, and M. Gharib. The effect of a discrete window offset on the accuracy of cross-correlation analysis of digital piv recordings. *Experiments in fluids*, 23(1):20–28, 1997.

[102] J. Westerweel and F. Scarano. Universal outlier detection for piv data. *Experiments in Fluids*, 39(6):1096–1100, 2005.

[103] C.E. Willert and M. Gharib. Digital particle image velocimetry. *Experiments in fluids*, 10(4):181–193, 1991.

[104] GX Wu. Numerical simulation of water entry of twin wedges. *Journal of Fluids and Structures*, 22(1):99–108, 2006.

[105] E.M. Yettou, A. Desrochers, and Y. Champoux. Experimental study on the water impact of a symmetrical wedge. *Fluid Dynamics Research*, 38(1): 47–66, 2006.

[106] J.H. Yoon and S.J. Lee. Investigation of the near-field structure of an elliptic jet using stereoscopic particle image velocimetry. *Measurement Science and Technology*, 14(12):2034, 2003.

[107] R. Zhao and O.M. Faltinsen. Water entry of two-dimensional bodies. *Journal of Fluid Mechanics*, 246(1):593–612, 1993.

[108] R. Zhao, O.M. Faltinsen, and J. Aarsnes. Water entry of arbitrary two-dimensional sections with and without flow separation. In *21st symposium on naval hydrodynamics*, 1997.

About the Author

Alexandru Stefan Nila was born on September 28^{th}, 1984 in Ploiesti, Romania. He first started his academic career in Bucharest, when he commenced his Aerospace Engineering studies within the *Politehnica Bucuresti* University in 2003.

During his bachelor program within the Faculty for Aerospace Engineering, Alexandru focused on numerical simulations aspects of fluid mechanics and structural analysis. The research work he performed for his Bachelor thesis was on numerical investigations of flow in radial seals. After successful completion of his bachelor studies in 2008, Alexandru enrolled in the Masters program of the Aerospace Engineering Faculty, with the speciality in Dynamics and Stability of Aircraft Flight. In 2010, he defended his Master thesis work on numerical simulations of flows in complex geometries, with particular focus on the treatment of *Immersed Boundary Methods*.

An additional part-time position as a Researcher within the Resistance of Materials desk at Politehnica University, which Alexandru started in 2007 in parallel to his studies, stirred his interest towards experimental work on composite materials testing. After successful completion of the Masters program for the Faculty of Aerospace Engineering with the notion *cum laude*, he decided to further his academic growth towards experimental investigations of fluid-structure phenomena.

The opportunity of joining a research project in the field of *slamming* presented itself in 2010, and so the next step was starting a joint PhD between the *Vrije Universiteit Brussel*, in the Acoustics and Vibrations group, and *Universiteit*

Gent - Department of Materials Science and Engineering. The research topic - deformable body slamming with application to sea wave energy converters - implied the development of an experimental investigation technique using *Particle Image Velocimetry* (PIV). This appealed to the author, as a great opportunity to apply his theoretical knowledge and previous experience on numerical simulations, to experimental research work of this fluid-structure interaction problem.

The challenges encountered during his 4 years as a PhD researcher contributed to an invaluable gain of insight and perspective in this field of expertise. Furthermore, working in an international group at the VUB and in close collaboration with Gent University, has offered him a great deal of professional and personal growth which is greatly appreciated by the author.

During his time as a PhD researcher, Alexandru published part of his work in international journal papers and had several contributions to international conferences, as detailed below.

List of Publications

Publications in International Journals

1. A. Nila, S. Vanlanduit, K.S. Vepa and W. Van Paepegem, *A PIV-based method for estimating slamming loads during water entry of rigid bodies*, Measurement Science and Technology, 24 (4), 2013.

2. A. Nila, S. Vanlanduit, K.S. Vepa, D. Van Nuffel and W. Van Paepegem, *Strain and Force Measurements During Hydroelastic Impact of Deformable Bodies Using Image Feature Tracking Techniques*, Submitted to Measurement Science and Technology.

3. A. Nila, S. Vanlanduit, K.S. Vepa, D. Van Nuffel and W. Van Paepegem, *An Adaptive PIV Method for Estimating Slamming Loads During Water Entry of Elastic Bodies*, Submitted to Measurement Science and Technology.

Communications at international congress / symposia

1. A. Nila, S. Vanlanduit, K.S. Vepa, D. Van Nuffel, W. Van Paepegem, J. Degroote, and J. Vierendeels, *High speed particle image velocimetry measurements during water entry of rigid bodies*, Ninth International Symposium on Particle Image Velocimetry, Kobe, Japan, July 21-23, 2011.

2. A. Nila, S. Vanlanduit, S. Vepa, D. Van Nuffel, W. Van Paepegem, J. Degroote, and J. Vierendeels, *High speed particle image velocimetry measurements during water entry of rigid and deformable bodies*, International Symposium on Applications of Laser Techniques to Fluid Mechanics, Lisbon, Portugal, July 9-12, 2012.

3. G. Van de Perre, S. Vanlanduit, and A. Nila, *Measurements of sound and flow fields in an organ pipe using a scanning laser Doppler vibrometer*, 16th. Int. Symp. on Appl. Laser Techniques to Fluid Mechanics, Lisbon, Portugal, July 9-12, 2012.

4. K.S. Vepa, A. Nila, J. Degroote, D. Van Nuffel, W. Van Paepegem, S. Vanlanduit and J. Vierendeels, *Study of Different Methods for the Simulation of Vertical Water Entry of Rigid Wedge*, Fourth International Conference on the Application of Physical Modelling to Port and Coastal Protection, Ghent, Belgium, 2012.

Experimental Investigation of the Water Entry of Rigid and Deformable Bodies Using Time-Resolved Particle Image Velocimetry

Alexandru Nila

This doctoral thesis is focused on the use of optical measurement techniques, namely Particle Image Velocimetry (PIV), in the study of the water impact of rigid and deformable structures. Water impact, or slamming, is a fluid-structure interaction problem, characterized by high induced loads with a very short duration (typically milliseconds). Previous research on this topic has been carried out using numerical simulations and experimental investigations for determining the occurring structural loads and the flow physics. Numerical simulations of the slamming problem have long been a useful tool in the estimation of impact loads. However, uncertainties in the numerical modelling and coupling of fluid dynamics with structural analysis, cause the need for experimental validation of the results. Such experimental studies are conducted using pressure sensors, strain gauges or force transducers mounted on the impacting bodies. Measurements performed using such sensors, are prone to large errors caused by numerous factors including mounting precision and temperature shocks.

The present thesis proposes an alternative to the existing techniques, by using PIV measurements for description of the water entry problem. The advantages of this method arise from its non-intrusive nature. By using such imaging techniques for experimental investigation it is possible to accurately determine both the fluid flow physics, as well as the structural response during water entry. The first part of the thesis is focused on the fluid flow physics and the improvements of PIV processing algorithms for accurate fluid velocity measurements, free surface elevation profiles and body shape evolution. In the second part of the thesis PIV-based pressure estimation models derived from the Navier-Stokes equations are implemented to recover slamming loads from PIV measurements. Finally, results of an extensive experimental campaign, using various deformable impacting bodies, are presented and discussed.